



UNIVERSITAT
POLITÈCNICA
DE VALÈNCIA



UNIVERSITAT POLITÈCNICA DE VALÈNCIA
DEPARTAMENTO DE COMUNICACIONES

Architectures and Novel Functionalities for Optical Access OFDM Networks

***“Arquitecturas y Nuevas Funcionalidades
para Redes OFDM de Acceso Óptico”***

Ph.D. THESIS

Maria Morant Pérez

Supervisor: Dr. Roberto Llorente Sáez

Valencia, December 2011

Ph.D. THESIS

Maria Morant Pérez

"Architectures and Novel Functionalities for Optical Access OFDM Networks"

"Arquitecturas y Nuevas Funcionalidades para Redes OFDM de Acceso Óptico"

Universitat Politècnica de València

Draft submitted on 13th December 2011

Accepted on 3rd February 2012

Defense on 1st March 2012

A la meua família i amics

ABSTRACT

“Architectures and Novel Functionalities for Optical Access OFDM Networks”

A clear increase in the deployment of fibre-to-the-home (FTTH) optical access networks around the world has been experienced in the recent years. FTTH is a flexible, future-proof access technology that enables the provision of Gbit/s data rates per user. Several studies indicate that FTTH will become the key differentiator between competing operators. In addition, FTTH is the only technology capable of creating new revenue streams from high bit-rate applications, e.g. high-definition entertainment (HD-video, HD-games, etc). On the operator side, an important advantage with FTTH is that it permits enhanced operational efficiencies compared with other access technologies. Primarily by reducing maintenance and operating costs. Also, it reduces the operational requirements of the central office equipment, and consequently leads to lower energy consumption. This Ph.D. Thesis aims to extend these advantages beyond the simple FTTH concept by the inclusive integration of the in-building optical distribution path with the final short/medium range wireless link, so providing an integrated end-to-end FTTH network architecture. In this way, the benefits of reduced operational costs and higher efficiencies are fully extended to the end user of the network, the final customer.

In this Thesis, we propose an optical-radio integrated access network architecture employing orthogonal frequency division multiplexing (OFDM) signals for the provision of different services such as Internet, phone/voice, HDTV, wireless and home security. OFDM signals are incorporated in radio standards such as ultra-wide band (UWB), WiMAX, LTE, WLAN, DVB-T or DAB. These formats take advantage of the intrinsic characteristics of OFDM modulation such as relative immunity to multi-path fading. This Thesis includes the proposal and demonstration of multi-standard bi-directional radio-over-fibre transmission of triple-play services (3PLAY) using OFDM-based UWB (for high-definition television), WiMAX (for internet data) and LTE (telephone service) in coexistence over passive optical networks (PON). This technique permits an increase in the overall capacity of the system; providing for triple-play services. Moreover, radio-over-fibre transmission allows using standard equipment at both ends of the architecture like low-cost UWB receivers, mobile devices using LTE and equipment using in-built WiMAX receivers.

Different network architectures for OFDM-based radio-over-fibre transmission are proposed. This permits a cost effective and fully centralised network architecture enabling transmission impairment compensation and network management to be carried out only at the central office. No further compensation, regeneration or format conversion is required along the network. This technique permits the avoidance of many of the conversion stages, so providing cost, space and energy savings.

Also, streaming of audio and video has become one of the main applications of UWB technology. The key market opportunity of UWB radio is the cable replacement in personal area networks using wireless universal serial bus (WUSB) technology. Since UWB offers high capacity and can coexist with other wireless services, UWB is becoming a strong candidate for the connection of high-bitrate demanding devices (e.g. external hard disks) and high-definition video streaming for in-home networks. For these reasons, the viability of UWB-over-fibre transmission is further investigated in this Ph.D. considering the end-to-end architecture comprising the access network, the in-home optical network and the final wireless transmission at customer premises.

Different photonic techniques to improve the performance of radio-over-fibre transmission are also proposed and investigated. The transmission of OFDM-based signals in polarization multiplexing is investigated for increasing the capacity of the network. This is demonstrated in the case of UWB and WiMAX signals transmission in coexistence.

For the management of pico-cells, the UWB-over-fibre distribution in in-building optical networks employing different media (single-mode and multi-mode) is investigated. In addition, the optical technique based on photonic analog-to-digital converters is proposed and demonstrated for sensing the high-bandwidth radio spectrum (up to 10 GHz). The localization and management of UWB pico-cells using this technique is also investigated.

As the radio-over-fibre transmission of several wireless services in coexistence through the same optical network requires electro-optic modulators (EOM) with excellent dynamic range and an extensive linear regime, linearization techniques have been also investigated in this Ph.D. Multi-carrier signals with large number of sub-channels like multi-band OFDM-UWB signals have large peak-to-average power ratio (PAPR) which joint with the high bandwidth of each UWB channel (528 MHz) is the main limitation of intensity-modulation systems. Here, we evaluated the performance of new modulators developed by Photline Technologies based on a Y-coupled architecture and a dual-drive modulator in radio-over-fibre applications.

After this, different architectures for the combined distribution of 3PLAY signals simultaneously in radio-over-fibre networks are proposed and evaluated: (i) a reflective architecture based on a reflective electro-absorption transceiver (R-EAT) to avoid using unacceptably powerful lasers at user premises, and (ii) a bi-directional coarse wavelength division multiplexing (CWDM) architecture using Mach-Zehnder electro-optical modulators with one wavelength for uplink data and another wavelength for downlink information. Within these networks the maximum optical reach is investigated. Also, the integration of the wireless path after the access network and different optical media for in-home optical distribution are investigated.

Finally, impairment compensation techniques for multi-format OFDM-based radio-over-fibre transmission in optical networks are proposed and studied. An impairment compensation subsystem is proposed based on using extra RF-pilots in the free-spectrum of the multi-OFDM signal to extract the network channel information to be applied on a pre-distortion equalizer.

The usage of these techniques in the different levels of the optical network is interesting for the proper evolution of the Information Society, which is the main objective of this Ph.D thesis.

RESUMEN

“Arquitecturas y Nuevas Funcionalidades para Redes OFDM de Acceso Óptico”

En los últimos años ha habido un gran aumento en el despliegue de redes de acceso ópticas de fibra hasta el hogar (FTTH, del inglés *fibre-to-the-home*). FTTH es una solución flexible, una tecnología de acceso de futuro que permite proporcionar tasas de datos del orden de Gbit/s por usuario. Diversos estudios indican que FTTH se convertirá en la diferencia clave entre los operadores más importantes. Además, FTTH es la única tecnología capaz de crear nuevas fuentes de ingresos de aplicaciones de alta velocidad, como por ejemplo entretenimiento de alta definición (vídeo y juegos de alta definición...). Desde el punto de vista del operador, una de las ventajas importantes que proporciona FTTH es que permite una mayor eficiencia operativa en comparación con otras tecnologías de acceso, principalmente por la reducción de costes de mantenimiento y de operación. Además, FTTH reduce los requisitos de los equipos de las centrales. Esta Tesis Doctoral tiene como objetivo extender estas ventajas más allá del concepto FTTH mediante la integración de la red óptica de distribución desplegada dentro del hogar así como el enlace radio final de corto o medio alcance inalámbrico. Esto proporciona una arquitectura de red FTTH integrada de extremo a extremo. De este modo, los beneficios de la reducción de costes operativos y mayor eficiencia se extienden hasta el usuario final de la red.

En esta Tesis Doctoral, se propone una arquitectura de acceso integrada óptica-radio basada en la multiplexación por división ortogonal de frecuencia (OFDM, del inglés *orthogonal frequency division multiplexing*) para proporcionar diferentes servicios al usuario como Internet, teléfono/voz, televisión de alta definición, conexión inalámbrica y seguridad en el hogar. Las señales OFDM se utilizan en muchos estándares inalámbricos como las señales de banda ultra-ancha (UWB, del inglés *ultra-wide band*), WiMAX, LTE, WLAN, DVB-T o DAB. Estos formatos aprovechan las características intrínsecas de la modulación OFDM como su mayor inmunidad ante desvanecimiento multi-camino. Esta tesis incluye la propuesta y la demostración experimental de la transmisión simultánea y bi-direccional de señales OFDM multi-estándar en radio-sobre-fibra proporcionando servicios *triple-play* basados en OFDM como UWB para televisión de alta definición, WiMAX para datos de Internet, y LTE para el servicio telefónico. Utilizando esta técnica se consigue un aumento de la capacidad general del sistema con el suministro de múltiples servicios simultáneos. Además la transmisión radio-sobre-fibra permite usar dispositivos estándar en ambos lados de la arquitectura como receptores UWB de bajo coste, dispositivos móviles con LTE y equipos de datos como portátiles con receptores WiMAX integrados.

Para ello, se proponen diferentes arquitecturas de red para la transmisión radio-sobre-fibra basada en señales OFDM. Esto permite una arquitectura de red centralizada que permite la compensación de los efectos de la transmisión así como la gestión de red que se llevarán a cabo sólo en la oficina central, simplificando de esta manera el equipamiento necesario en casa del usuario. Con este método no se necesitará compensación adicional, ni regeneración o conversión de la señal. Esta técnica evita la necesidad de diversas etapas de conversión proporcionando así reducción de coste, de espacio y ahorro de energía.

Además, la transmisión de flujo de audio y vídeo se ha convertido en una de las principales aplicaciones de la tecnología UWB. La oportunidad de mercado que ha encontrado la tecnología UWB radio es el remplazo de los cables de conexión entre dispositivos de redes de área personal inalámbrica mediante WUSB (del inglés, *wireless universal serial bus*). Como UWB ofrece una gran capacidad de datos y puede coexistir con otros servicios inalámbricos dada su baja emisión de potencia, UWB se está convirtiendo en un fuerte candidato para la conexión de dispositivos de alta velocidad (por ejemplo, discos duros externos) y para la provisión de flujos de vídeo de alta definición en redes para el hogar. Por estos motivos, también la viabilidad de la transmisión UWB-sobre-fibra

se investiga en esta Tesis Doctoral, teniendo en cuenta la arquitectura extremo a extremo incluyendo la red óptica dentro del edificio y la transmisión inalámbrica en casa del usuario.

En esta Tesis también se proponen distintas técnicas fotónicas para mejorar el rendimiento de la transmisión radio-sobre-fibra. La transmisión de señales basadas en OFDM usando multiplexación en polarización se estudia para aumentar la capacidad de la red. Esta técnica se demuestra experimentalmente con la transmisión de señales UWB y WiMAX en coexistencia.

Para la gestión de pico-celdas se estudia la distribución de señales UWB-sobre fibra en redes ópticas dentro del edificio (del inglés *in-building*) mediante fibra monomodo y multimodo. Además se propone una técnica óptica basada en conversor analógico a digital fotónico (o *photonic analog-to-digital converter*) que se demuestra para la detección del espectro radioeléctrico de banda ancha (hasta 10 GHz). La localización y gestión de pico-celdas UWB usando esta técnica también se investiga en esta tesis.

Como la transmisión radio-sobre-fibra de varios servicios inalámbricos en coexistencia a través de la misma red óptica requiere moduladores electro-ópticos con un excelente margen dinámico y un gran régimen lineal, esta Tesis también estudia técnicas de linealización para los moduladores. Las señales multi-portadora como las señales multi-banda OFDM-UWB tienen una gran relación potencia pico-potencia media PAPR (del inglés *peak-to-average power ratio*), que junto con el gran ancho de banda de cada canal UWB (528 MHz) son las principales limitaciones de los sistemas de modulación de intensidad óptica. En este caso, se ha evaluado experimentalmente el comportamiento y la mejora alcanzada con nuevos moduladores desarrollados por la empresa Photline Technologies, basados en arquitecturas en forma de Y acopladas y en un modulador *dual-drive* para aplicaciones radio-sobre-fibra.

Después de esto, se proponen diferentes arquitecturas para la distribución conjunta de las señales OFDM de forma simultánea proporcionando servicios *triple-play*: (i) una arquitectura reflectiva basada en el dispositivo R-EAT (*reflective electro-absorption transceiver*) para evitar el uso de láseres de alta potencia en casa del usuario, y (ii) una arquitectura bi-direccional basada en multiplexación por longitud de onda CWDM (del inglés *coarse wavelength division multiplexing*) utilizando moduladores Mach-Zehnder con una longitud de onda de subida y otra de bajada. En estas redes se obtendrá el alcance de fibra máximo que se puede alcanzar con los diferentes servicios OFDM en coexistencia. Además, también se considera la integración del enlace inalámbrico después de la red de acceso y de diferentes medios ópticos para redes ópticas dentro del hogar para obtener el máximo alcance radio que se puede conseguir con las diferentes señales.

Por último, se propone y estudian técnicas de compensación de los efectos de la transmisión radio-sobre-fibra de señales multi-formato OFDM. En esta Tesis se propone un subsistema de compensación basado en el uso de portadoras adicionales en la porción libre de espectro entre los diferentes servicios. Estas portadoras sirven para extraer la información del canal de la red que se aplicará a las señales OFDM mediante pre-distorsión.

El uso de estas técnicas en los diferentes niveles de la red óptica es interesante para la evolución adecuada de la Sociedad de la Información, que es el objetivo principal de esta Tesis Doctoral.

RESUM

“Arquitectures y Noves Funcionalitats per a Xarxes OFDM d'Accés Òptic”

Un gran augment en el desplegament de fibra fins la llar (FTTH, de l'anglès *fibre-to-the-home*) s'ha experimentat a tot el món en els últims anys. FTTH és una solució flexible, una tecnologia d'accés que permet proporcionar taxes de Gbit/s per usuari. Diversos estudis indiquen que FTTH serà el diferenciador clau entre els operadors competidors. A més, FTTH és l'única tecnologia capaç de crear noves fonts d'ingressos de noves aplicacions d'alta velocitat, com per exemple, entreteniment i vídeo d'alta definició. Des del punt de vista de l'operador, un dels principals avantatges de la FTTH és que permet una major eficiència operativa en comparació amb altres tecnologies d'accés. Principalment per la reducció de costos de manteniment i d'operació. A més, redueix les especificacions necessàries dels equips de l'operador. Aquesta Tesi Doctoral té com a objectiu estendre aquests avantatges més enllà del concepte FTTH gràcies a la integració de la xarxa òptica de distribució a casa i l'enllaç ràdio sense fils, el que proporciona una arquitectura de xarxa FTTH integrada d'extrem a extrem. D'aquesta manera, els beneficis de la reducció dels costos operatius i una major eficiència s'estenen fins a l'usuari final de la xarxa.

En esta Tesi es proposa una arquitectura d'accés de integrada òptica-ràdio emprant senyals amb multiplexació per divisió ortogonal de freqüència (OFDM, de l'anglès *orthogonal frequency division multiplexing*) per aconseguir la prestació de diferents serveis com Internet, telèfon/veu, televisió d'alta definició, connexió de dades sense fils i seguretat a casa. Les senyals OFDM son emprades per molts estàndards ràdio, com les senyals de banda ultra-ampla (UWB, de l'anglès *ultra-wide band*), WiMAX, LTE, WLAN, DVB-T o DAB. Aquests formats s'aprofiten dels avantatges de les característiques intrínseques de la modulació OFDM com és la major immunitat front a esvaniment multicamí. Aquesta Tesi inclou la proposta i la demostració experimental de la transmissió bi-direccional de senyals OFDM multi-estàndard emprant ràdio-sobre-fibra per proporcionar serveis *triple-play* mitjançant UWB per a televisió d'alta definició, WiMAX per a Internet i LTE per al servei telefònic. Aquesta tècnica permet un augment de la capacitat general del sistema amb el subministrament de diferents serveis simultanis. La transmissió ràdio-sobre-fibra permet l'ús d'equipament estàndard comercial en ambdós extrems de l'arquitectura com per exemple receptors UWB de baix cost, dispositius mòbils amb LTE i equips com ordinadors portàtils que disposen de receptors WiMAX integrats.

En esta Tesis, es proposen diferents arquitectures de xarxa ràdio-sobre-fibra basades en senyals OFDM. Açò permet una arquitectura de xarxa centralitzada que permet la compensació plena dels efectes de la transmissió sobre fibra així com la gestió de xarxa que es duren a terme només a l'oficina central de l'operador, simplificant l'equipament necessari a casa de l'usuari. D'aquesta manera no es necessita cap conversió ni compensació addicional a la xarxa, ni la regeneració de la senya. Esta tècnica permet evitar moltes de les etapes de conversió, proporcionant un estalvi en costos, espai i energia.

A més d'açò, la distribució d'àudio i vídeo s'ha convertit en una de les principals aplicacions de la tecnologia UWB. L'oportunitat clau de mercat de UWB és el reemplaçament de cables en xarxes d'àrea personal emprant la tecnologia WUSB (de l'anglès *wireless universal serial bus*). Com UWB ofereix una gran capacitat de dades i pot coexistir amb altres serveis sense fil degut a la seua baixa potència d'emissió, UWB s'està convertint en un fort candidat per a la connexió de dispositius d'alta velocitat com, per exemple, discs durs externs, i per a proporcionar vídeo d'alta definició en xarxes personals. Per estes raons, la viabilitat de la transmissió UWB-sobre-fibra s'ha investigat en esta Tesi, tenint en compte l'arquitectura d'extrem a extrem que comprèn la xarxa òptica d'accés, la xarxa òptica en l'edifici i la transmissió final sense fils en casa de l'usuari.

En esta Tesi també s'investiguen diferents tècniques fotòniques per millorar el rendiment de la transmissió ràdio-sobre-fibra. La transmissió de senyals basades en OFDM emprant multiplexació en polarització s'estudia per augmentar la capacitat de la xarxa. Esta tècnica es demostra experimentalment amb la transmissió de senyals UWB y WiMAX en coexistència.

Per a la gestió de pico-cèl·lules s'estudia la distribució de senyals UWB-sobre-fibra en xarxes òptiques dins d'edificis (de l'anglès *in-building*) mitjançant fibra monomode i multimode. A més, la tècnica òptica basada en convertidors analògic a digital fotònics és proposada i demostrada per a la detecció de l'espectre radioelèctric de banda ampla (fins a 10 GHz). La localització i gestió de pico-cèl·lules UWB usant aquesta tècnica també s'ha investigat en aquesta Tesi.

Com la transmissió ràdio-sobre-fibra de diversos serveis sense fil en coexistència a través de la xarxa de fibra òptica requereix moduladors electro-òptics amb un excel·lent marge dinàmic i un gran règim lineal, també s'han estudiat i analitzat tècniques de linealització per als moduladors. Les senyals multi-portadora com la senyal multi-banda OFDM-UWB tenen una gran relació potència de pic-potència mitja PAPR (del anglès *peak-to-average power ratio*), que conjuntament amb el gran ample de banda de cada canal UWB (528 MHz) són les principals limitacions dels sistemes de modulació d'intensitat. En aquest cas, s'avalua experimentalment el rendiment dels nous moduladors desenvolupats per l'empresa Photline Technologies, basats en una arquitectura Y-acoplada i un modulador *dual-drive* per a aplicacions ràdio-sobre-fibra d'aplicacions.

Després d'això, es proposen diferents arquitectures per a la distribució conjunta de senyals OFDM de manera simultània proporcionant serveis *triple-play*: (i) una arquitectura reflectiva basada en el dispositiu R-EAT (*reflective electro-absorption transceiver*) que evita l'ús de làsers de gran potència a casa de l'usuari, i (ii) una arquitectura bi-direccional emprant modulador Mach-Zehnder i multiplexació per longitud d'ona (CWDM, de l'anglès *coarse wavelength division multiplexing*). Es gasta una longitud d'ona de pujada i una altra longitud d'ona de baixada i s'investiga quina és la màxima longitud de fibra que es pot obtenir amb els diferents serveis OFDM en coexistència. A més, la integració de l'enllaç ràdio després de la xarxa d'accés i de diferents tipus de fibra per a la xarxa òptica dins de casa també es considera.

Finalment, es proposen i estudien tècniques de compensació dels efectes de la transmissió ràdio-sobre-fibra de senyals multi-estàndard OFDM. En esta Tesi es proposa un subsistema de compensació basat en l'ús d'unes portadores addicionals situades en l'espectre lliure entre els diferents serveis. Estes portadores serveixen per extreure la informació del canal de la xarxa que s'aplicarà a les senyals OFDM mitjançant pre-distorsió.

L'ús d'aquestes tècniques en els diferents nivells de la xarxa òptica és interessant per a l'adequada evolució de la Societat de la Informació, que és l'objectiu principal d'aquesta Tesi Doctoral.

INDEX

CHAPTER 1. INTRODUCTION	1
1.1. Motivation and state-of-the-art	1
1.1.1. <i>Radio-over-fibre state-of-the-art</i>	2
1.1.2. <i>UWB technology main characteristics</i>	6
1.2. Framework and objectives of this Ph.D.....	8
1.2.1. <i>Research topics and outline</i>	9
CHAPTER 2. UWB RADIO-OVER-FIBRE IN FTTH ACCESS NETWORKS	13
2.1. Introduction	13
2.2. Simulation evaluation of UWB radio-over-fibre transmission	14
2.3. Comparison of OFDM-UWB and IR-UWB signal performance in radio-over-fibre distribution	17
2.4. OFDM-UWB signals performance in radio-over-fibre distribution	22
2.4.1. <i>Multi-channel OFDM-UWB radio-over-fibre evaluation</i>	22
2.4.2. <i>Impact of pilots in OFDM-UWB signals over fibre</i>	28
2.4.3. <i>Hybrid wireless-optical access evaluation</i>	34
2.5. Polarization division multiplexing radio-over-fibre over PON.....	38
2.5.1. <i>Effect of multi-channel PM-UWB</i>	40
2.5.2. <i>Maximum reach evaluation for UWB signal transmission</i>	41
2.5.3. <i>Distribution of different OFDM-based services using polarization multiplexing</i>	43
2.6. Conclusion.....	48
CHAPTER 3. UWB RADIO-OVER-FIBRE IN IN-BUILDING OPTICAL PICO-CELL CLUSTER NETWORKS.....	51
3.1. Introduction	51
3.2. Optical media evaluation for in-building pico-cell provision of UWB radio-over-fibre signals	52
3.2.1. <i>OFDM-UWB performance in in-building networks</i>	53
3.2.2. <i>OFDM-UWB and IR-UWB performance in in-building networks</i>	59
3.3. Photonic-ADC architecture for sensing UWB radio signals	65
3.3.1. <i>Single-channel photonic-ADC performance</i>	69
3.3.2. <i>Multichannel photonic-ADC including localization and fingerprinting functionalities</i>	74
3.3.3. <i>UWB radio-over-fibre transmission and simultaneous sensing with photonic-ADC</i>	80
3.4. Linearized electro-optical modulators.....	84
3.4.1. <i>Dual-parallel Y-coupled Linearized Modulator</i>	85
3.4.2. <i>Dual-drive Mach-Zehnder linearized modulator</i>	91
3.5. Conclusion.....	95

CHAPTER 4. COEXISTENCE IN MULTI-STANDARD OFDM-OVER-FIBRE TRANSMISSIONS	97
4.1. Introduction	97
4.2. Optical access architectures evaluation for multi-standard OFDM transmission ...	99
4.2.1. <i>Simulation studies of optical architectures</i>	100
4.2.2. <i>Experimental demonstration of bi-directional reflective architecture using R-EAT</i>	103
4.2.3. <i>Experimental demonstration of bi-directional conventional Mach-Zehnder architecture</i>	108
4.3. Access and wireless transmission evaluation.....	112
4.4. Access and in-home distribution evaluation	115
4.4.1. <i>In-building ultra-bendable and plastic optical fibre media comparison</i> ...	116
4.4.2. <i>In-home POF reach evaluation</i>	120
4.4.3. <i>In-home POF and wireless distribution</i>	123
4.4.4. <i>Access, in-home POF and wireless distribution</i>	128
4.5. Conclusion.....	132
CHAPTER 5. IMPAIRMENT COMPENSATION TECHNIQUES FOR MULTI-STANDARD OFDM RADIO-OVER-FIBRE TRANSMISSIONS	135
5.1. Introduction	135
5.2. Evaluation procedure	137
5.3. Broadband impairment compensation performance.....	138
5.3.1. <i>Performance vs. Number of pilots evaluation</i>	139
5.3.2. <i>Performance vs. Transfer function order</i>	141
5.3.3. <i>Effect of extra RF-pilots on UWB signals</i>	144
5.4. Impairment compensation proof-of-concept.....	144
5.4.1. <i>Downstream path using external modulation and pre-compensation</i>	145
5.4.2. <i>Upstream path using DML and post-compensation</i>	151
5.5. Conclusion.....	154
CHAPTER 6. CONCLUSION AND FURTHER WORK	157
6.1. Main conclusions	157
6.2. Further work.....	158
6.3. Acknowledgements.....	159
ANNEX A. PUBLICATIONS	161
A.1. Original publications	161
A.1.1. <i>International peer-reviewed journals</i>	161
A.1.2. <i>International conferences</i>	161
A.1.3. <i>Book chapters</i>	164
A.2. Technical Reports.....	164

ANNEX B. LOCALIZATION ALGORITHMS AND PERFORMANCE.....	169
B.1. Localization of UWB signals approach	169
<i>B.1.1. Building the weight vector.....</i>	<i>170</i>
<i>B.1.2. Predictive delay estimator.....</i>	<i>171</i>
B.2. Simulations for position computation	172
B.3. Position of the sensors evaluation	173
ANNEX C. ELECTRO-OPTIC MODULATOR DESIGN AND CHARACTERIZATION.....	177
C.1. Y-coupled electro-optical modulator	177
<i>C.1.1. Fabrication process.....</i>	<i>178</i>
C.2. Dual-drive electro-optical modulator with chirp management.....	180
<i>C2.1. Chirp measurement.....</i>	<i>180</i>
REFERENCES	185
LIST OF ACRONYMS	191
LIST OF FIGURES	195
LIST OF TABLES	205

CHAPTER 1. INTRODUCTION

1.1. Motivation and state-of-the-art

In this Ph.D. thesis, different techniques for the optical transmission of wireless signals on orthogonal frequency division multiplexing (OFDM) modulation are proposed, analysed and demonstrated experimentally with the aim of further develop the transmission technology to increase the single-user and overall capacity in access networks and in in-home optical-radio user networks.

OFDM modulations are employed in several radio standards such as ultra-wide band (UWB), WiMAX, LTE, WLAN, DVB-T or DAB, due to the intrinsic characteristics of OFDM modulation which is capable to cope with severe channel conditions and multi-path fading.

From these wireless technologies, UWB is currently receiving special attention from industry and academia for the deployment in a very broad range of applications: from computer peripheral integration over wireless USB to home multimedia streaming. UWB wireless is a radio technology targeting high-bit rate short-range indoor data communications, potentially exceeding 1 Gbit/s [1], and vehicular short-range applications, involving outdoor communications, also known as car-to-car and infrastructure-to-car [2], and radar sensors [3]. This technology exhibits unique characteristics, such as very low power transmission and consumption, high tolerance to multi path fading, low probability of interception and low cost devices [4].

UWB is considered a complementary communication solution within the future integrated networks beyond 3G. The ultimate target of UWB systems is to use broadband unlicensed spectrum (from 3.1 to 10.6 GHz [5]) by emitting noise-like signals. The major UWB advantages are potentially low complexity and low power consumption that implies that UWB technology is suitable for broadband services in the mass markets of wireless personal area networks (WPAN).

Inherently, the high data rates of UWB communication (480 Mbit/s) are available over short-range of less than 10 m. This is simply derived from the constraints on allowed emissions and fundamental limits of thermal noise and Shannon limits. In many cases the 10 m range is too short for many residential applications so we propose to extend the range of UWB communications using radio-over-fibre transmission. The transmission of UWB signals in FTTH is a natural step forward in the evolution of the access network.

The radio-over-fibre transmission of multi-format OFDM-based signals in optical fibre-to-the-home (FTTH) networks allows increasing the overall capacity of the system providing enough bitrate for the multiple services such as high bitrate data (e.g. GbE or WiMAX), telephone service (e.g. LTE), and high-definition television broadcasting (which can be provided by UWB technology).

WiMAX, meaning Worldwide Interoperability for Microwave Access, is part of the fourth generation (4G) of wireless communications used for wireless local area networks (WLAN). WiMAX has different implementations for fixed and mobile service under the specifications of the IEEE 802.16 family [11]. LTE, coming from Long Term Evolution, is a standard developed by the 3rd Generation Partnership Project (3GPP) for radio communication of high-speed data for mobile phones [12]. It is based on the GSM/EDGE and UMTS/HSPA network technologies, increasing the capacity and speed using new modulation techniques. The combination of UWB, WiMAX and LTE in the same FTTH network provides triple-play services to the end user, including high-definition video, high-speed data and telephony.

In this Thesis, coexistence studies for the simultaneous transmission of 3PLAY services are developed for different FTTH network architectures. Finally, an impairment compensation technique for this kind of networks based on channel sounding and proper equalization is also proposed and evaluated.

The techniques developed in this Ph.D. thesis will provide solutions for increasing the reach of the wireless signals thanks to the optical network transmission and also improve the capacity of the network enabling the coexistence of different OFDM-based services. These techniques are proposed and demonstrated in the three different levels of application: user network, including the radio path, local network and also in access network.

The usage of these techniques in the different levels of the network is good for the proper evolution of the Information Society which is the main objective of this Ph.D thesis.

1.1.1. Radio-over-fibre state-of-the-art

In the last twenty years, many techniques have been developed in the field of radio-over-fibre systems. These can be classified in optical signal processing techniques, including photonic analogue-to-digital converters, photonic-microwave filters, millimetre-wave and THz signal generation, beamforming and imaging. Nevertheless, from these applications the most successful relies on the use of optical fibre links to distribute wireless signal. This application leads to the so-called hybrid fibre-radio (HFR) transmission systems [13]. The HFR concept is similar to the distribution of cable-TV signals over a hybrid-fibre coaxial (HFC) network, as described in [14]-[15].

The optical distribution of the wireless signal already in a format suitable for to be radiated at the end of the fibre allows centralizing the complex functions needed for RF signal processing in the central office. A simplified schematic of the proposed radio-over-fibre application is shown in Figure 1.

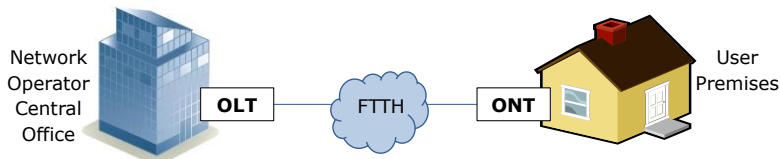


Figure 1. Simple concept of radio-over-fibre application in FTTH networks

At the central office (network operator premises), different wireless signals are generated in their native format. The wireless signals are distributed in both upstream and downstream directions. Different lights at different frequencies, i.e. wavelengths, can be employed to transmit the wireless signal intended for different users (downstream), or to provide the return channel (upstream). This arrangement is called wavelength-division multiplexing (WDM). Depending on the spectral separation of the optical channels, these are called coarse- or dense-wavelength division multiplexed systems, named CWDM and DWDM respectively. The specific case of DWDM system and the special requirements to minimise the crosstalk between the different lights is addressed, for example, in [16].

It is worth to note the availability of polarization-multiplexed (PM) systems which employ two orthogonal polarizations per wavelength, each transporting a given wireless signal that will be also investigated in this Ph.D. Thesis. This approach maximizes the spectral efficiency and was first proposed in [17].

In the state-of-the-art, analog transmission over fibre links has been demonstrated for frequencies up to 120 GHz [18]. The huge bandwidth of the optical fibre link and the availability of wireless commercial devices facilitate the standards-independent optical transmission and multiservice operation for existing cellular systems. Several transmissions of different wireless standards using radio-over-fibre techniques have been demonstrated so far, such as GSM[19], UMTS [20], wireless-LAN WiFi 802.11 a/b/g/n [21]-[23]), and WiMAX [24].

The proposal of network configurations for efficient signal transmission between the central office and the end user has been subject of continuous investigation. Mobile operators are investigating several radio access interfaces such as HSDPA, LTE, WIMAX, or UWB, not only from the technology point of view but also taking into account CAPEX and OPEX minimisation. It is not clear at this moment, which technology will dominate, as they are in a different stage of development and standardization. Moreover, the coexistence and compatibility features of all these radio services are under the research scope of the principal operators and are another of the main objectives of this Ph.D. Thesis.

Taking into account this heterogeneous environment, huge efforts are made to develop convergent infrastructures able to cope with increasing bandwidth demand. This integrated and converged infrastructure must be able to offer multi-standard transmission capabilities and to provide integration with both the transport network and wireless backhaul solutions in order to increase the network flexibility and the dynamic adaptation to changing traffic conditions.

This market is growing very fast as several market analysts have recently predicted. ABI Research estimates that the penetration of radio-over-fibre in-building systems will grow from 18% of the total in-building market in 2003 to 46% in 2009 [25]. ABI states that distributed-antenna systems will make a significant impact in larger buildings because they offer multi-service broadband capabilities.

The deployment of optical fibre in an access network can be achieved in multiple ways. In fact, many access technologies are commonly referred to as FTTx when in fact they are simply combinations of optical fibre and twisted pair or coaxial cable networks. This has created some confusion though as FTTx covers several different architectures and protocols.

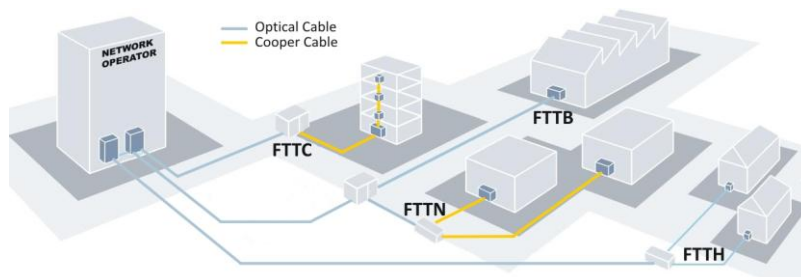


Figure 2. Different FTTx deployments

In fact, some of digital subscriber lines (DSL) and HFC networks have been qualified as FTTx networks due to their use of fibre in the access, as a passive optical network does. Hence, it is best when referring to a deep fibre penetration network to specify its actual architecture. The most common architectures depicted in Figure 2 are: FTTH, Fibre-to-the-Building (FTTB), FTTCurb (FTTC) and FTTNode (FTTN) [26].

The growth of FTTx is expected to continue at a very fast pace with the number of FTTx subscribers expected to grow to over 100 million by the end of 2012. Today FTTx broadband comprises 7.5% of all broadband users and is expected to comprise 16% of all broadband users by end of 2012 [27].

For these reasons, the use of radio-over-fibre technologies is expected to be deeply used for indoor deployments due to the flexibility of the radio-over-fibre system able to transmit multi-standard wireless signals over the same system with transparency and providing unlimited bandwidth thanks to the fibre-based architecture.

The main key elements of any radio-over-fibre system are the devices with electro-optical and opto-electric conversion functions. An electro-optic conversion is needed to up-convert

the wireless signal to optical frequencies to be transmitted through fibre to the remote user, and afterwards an opto-electric conversion recovers the radio signal from the optical carrier to be transmitted wirelessly to the end user. These functions are illustrated in Figure 3.

The main systems for electro-optic conversion are broadband optical sources either based in direct or external modulation. Once the signal is adapted to the optical domain, it is transmitted over a suitable transmission media such as standard single-mode fibre (SSMF), specialty fibre (e.g. Terlight), multi-mode fibre (MMF), or plastic optical fibre (POF). Finally, the signal is converted to the electric domain using broadband photodetectors or photoreceivers [28]-[29], and filtering.

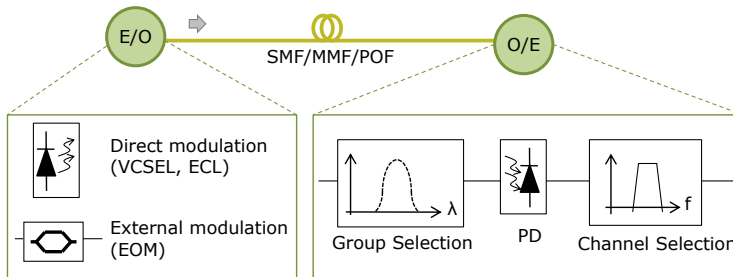


Figure 3. Main elements in a radio-over-fibre link. Only one direction of communication (downlink/uplink) is shown for simplicity

As it was commented previously, two main approaches can be used for electro-optic conversion functions [29]: direct modulation of a laser or a continuous wave laser with an external modulator. To point out the main advantages and disadvantages of both electro-optic conversions, it is worth to say that external modulation provides more bandwidth, with low drive voltage and good linearity.

External modulation is usually performed using Mach-Zehnder electro-optic modulators (EOM) and electro-absorption modulators [30]. On the other hand, the cost of external modulators is nowadays more expensive than direct modulation devices, and for this reason this second method is usually preferred for low-cost radio-over-fibre systems deployments.

Concerning direct modulation techniques, the modulated signal changes the intensity of the laser output. In this case, the modulation bandwidth, the optical wavelength and the efficiency have to be considered. Since the first proposals of direct modulation [31] considerable work has been done devoted to the increase of the direct modulation bandwidth and semiconductor lasers at 1550 nm. For example, in [28], a modulation bandwidth greater than 30 GHz has been demonstrated.

When the wireless signal to be transported over the radio-over-fibre system is limited to a frequency range between 800 and 2500 MHz, the detector/modulator can be achieved using waveguide electro-absorption modulators [32] or polarization independent asymmetric Fabry-Perot modulators [33]-[34]. For the frequencies used in the major part of the current wireless standards as GSM, WiFi 802.11 a/b/g, UMTS and WiMAX, which can be up to 5-6 GHz, directly modulated semiconductor lasers are preferred [35] because these lasers have a lower production cost. At higher frequencies, only externally modulated transmitters can satisfy the required performance for adequate wireless transmission. Recently, important research efforts have been carried out targeting the development of low-cost/high-performance transmitters, for instance uncooled lasers [36]-[37] or vertical-cavity surface emitting lasers (VCSEL). In the last years, VCSELs have been proposed for low-cost direct modulation [20]-[21]. These VCSELs operate in a single longitudinal mode using a very small cavity length (around 1 μm). These devices provide efficient coupling

with optical fibre and have low cost production, which are very interesting features for the implementation of cheap radio-over-fibre systems. However, nowadays VCSEL is not a mature technology and usually present lower output power and bandwidth than the devices used for external modulation. Additionally, VCSEL are mainly available at wavelengths of 850 and 1310 nm, although devices at 1550 nm (the usual wavelength band for telecommunication applications) are beginning to be commercially available with increasing direct modulation bandwidth.

The second key element of the radio-over-fibre system is the optical fibre. There are several types of fibres such as standard single-mode fibre (SSMF), multimode fibre (MMF) and plastic optical fibre (POF). The most suitable media for long-haul radio-over-fibre transmission links is SSMF while for indoor applications MMF or POF are preferred due to its easier installation and reduced cost. The main difference between the different media is the fibre core radius (typically around 9 μm in SSMF and 62.5 μm in MMF) which results in the propagation of a single or multiples modes through the fibre. POF is made of plastic instead of glass and shows larger core radius than MMF. The main benefit of POF is that the cost is lower than glass fibres (which is an attractive solution for indoor applications), although the insertion loss and dispersion is higher.

SSMF is usually selected by operators for long haul links of optical communication core networks. This kind of fibre provides huge capacity, with capacity per distance products up to 41 Petabit/s.km as was demonstrated in [38]. On the other side, MMF and POF is intended for short links inside buildings, airports, shopping malls and corporate office premises. Due to its low cost and ease of handling this types of fibre can be installed in-building with typical lengths of up to 300 m. Recent advances in photonic crystal and microstructure fibre geometries suggest that tight light confinement (i.e. making it ultrabendable fibre) may be possible whilst maintaining a low modal order, i.e. exhibiting a relatively low v number, similar to that of SMF. The latest advanced were presented in February 2008, ClearCurve fibre from Corning [39], in September 2009, EZ-Bend fibre from OFS [40] and BendBright-XS fibre from Draka Comteq [41] and in January 2009 the ClearCurve multimode fibre [42].

Finally, the opto-electronic conversion is performed by a photodetector (PD) [43], which key requirements are high quantum efficiency and bandwidth. High-speed photodetectors in the 1310-1550 nm bands have been reported in the literature with 3-dB bandwidths up to 300 GHz [44]. Nowadays there are commercially available devices that operate at frequencies up to 100 GHz.

According to the scheme shown in Figure 3, both optical links (down-link and up-link) present a similar configuration. The detected signal power at the output of the photodiode in the wireless signal extractor from the down-link path is calculated in [43].

An important technology issue in radio-over-fibre is the coexistence between different wireless standards when transmitted through fibre. Coexistence of WiMAX with over wireless signals, e.g. UWB or UMTS, when transmitted through the fibre usually does not pose a problem. The different licensed or un-licensed wireless services are allocated at different transmission bands and a careful design of the optical transmission system can minimize interference.

The impact of UWB interference on WiMAX at 3.5 GHz band is a relevant research topic and raise regulatory concerns [45]. For this reason, the coexistence problem of UWB radio with narrowband systems such as UMTS, GSM, GPS, etc. has been investigated in the literature [46]. WiMAX and UWB coexistence is a key issue in indoor scenarios. Indoor fibre installations are typically based on MMF and VCSELs operating at 850 nm, and low-cost receivers [47][48].

The study of simultaneous radio-over-fibre transmission of WiMAX and UWB on MMF was carried out in [49] to identify the transmission impairments in a spectral overlapping situation.

Moreover, radio-over fibre transmission has to deal with the optical fibre attenuation (around 0.2 dB/km in SSMF at 1550 nm) and other transmission impairments which limit the transmission reach, for this reason the impairment compensation of radio-over-fibre transmission is also targeted in the Ph.D. thesis.

1.1.2. UWB technology main characteristics

UWB signals occupy huge bandwidths (0.5 to 7.5 GHz) and with extremely low spectral power density, at the level of parasitic emissions in a typical indoor environment. The effective isotropic radiated power (EIRP) defined by FCC part 15 is of -41.3 dBm/MHz from 3.1 to 10.6 GHz according to Table 1 [5].

Table 1. Maximum EIRP levels stated by FCC for UWB emissions [5]

Frequency (MHz)	EIRP (dBm/MHz)
960-1610	-75.3
1610-1990	-53.3
1990-3100	-51.3
3100-10600	-41.3
Above 10600	-51.3

UWB is defined as a radio signal with 20% fractional bandwidth or, at least, 500 MHz [5]. UWB is an unlicensed wireless service allocated in the 3.1 to 10.6 GHz band for indoor applications as stated in current regulation ECMA-368 [6], ETSI regulation [7] and WiMedia standard defines signals based in multi-band OFDM modulation [8] which deeply commercially exploited for indoor applications.

The International Communication Union (ITU) is deeply studying the compatibility between devices using UWB technology and the mobile and satellite services, as UWB emissions spread over a very large frequency range and therefore may affect several radio services. The European Commission asked the European Telecommunications Standards Institute (ETSI) to produce of Harmonized Standards for UWB to. ETSI's standardization activity for short-range devices currently includes these UWB applications such as communications, ground- and wall probing radar and automotive radar applications. The generic Harmonized European Standard for UWB Communications (ETSI EN 302 065), published in February 2008, uses frequency ranges from 3.1 to 4.8 GHz and 6 to 8.5 GHz for implementation in road or rail vehicles. Detect-And-Avoid (DAA) specifications as a mechanism for the protection other radio services, are defined for UWB in 3.1 to 4.8 GHz and 8.5 to 9 GHz bands has been published in June 2008 (ETSI TS 102 754). The automotive radar group is developing the 77-81 GHz Harmonized European Standard for the anti-collision radar application (ETSI EN 302 264). The 24 GHz Harmonized European Standard (ETSI EN 302 288) was amended in Feb. 2008.

ECMA-368 regulation employed by WiMedia devices divides the UWB spectrum from 3.1 to 10.6 GHz in 14 bands according to Figure 4. Currently most of the market available devices [9][10] work in the band group #1 comprising the three first UWB channels from 3.1 to 4.8 GHz depicted in Table 2.

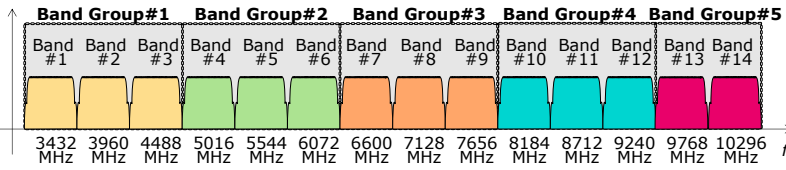


Figure 4. Multi-band OFDM channelization defined by ECMA-368 [6]

Table 2. ECMA-368 frequency information of band group #1 channels

Band Group	Band_ID	Lower Freq	Centre Freq	Upper Freq
1	1	3.168 GHz	3.432 GHz	3.696 GHz
	2	3.696 GHz	3.960 GHz	4.224 GHz
	3	4.224 GHz	4.488 GHz	4.752 GHz

ECMA-368 regulation also defines different time frequency codes (TFC) for the transmission. We can classify in two types: (i) time-frequency interleaving (TFI) codes where the information is transmitted interleaved over three different bands (known as TFI1) or over two bands (TFI2), and (ii) fixed frequency interleaving (FFI), where the information is transmitted on a single band. Support for both types is mandatory on the standard devices and most of the devices currently available at the market implement TFC1 to TFC7 with hopping patterns depicted in Table 3.

Figure 5 shows an example of the difference between TFC1 with time-frequency interleaving in the three UWB channels following $f_1, f_2, f_3, f_1, f_2, f_3$; and TFC5 with fixed frequency in the first channel band $f_1, f_1, f_1, f_1, f_1, f_1$.

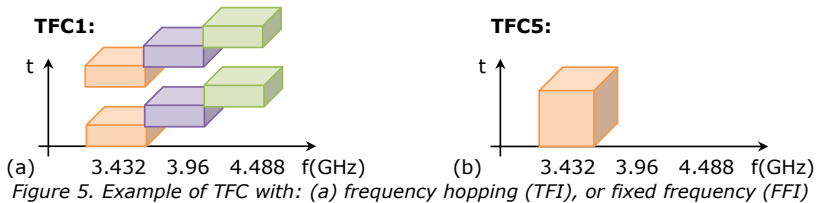
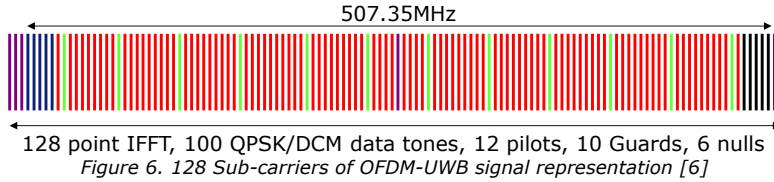


Table 3. ECMA-368 time frequency codes for band group #1

TFC Number	TFC Type	Band_ID order for TFC					
1	TFI	1	2	3	1	2	3
2	TFI	1	3	2	1	3	2
3	TFI	1	1	2	2	3	3
4	TFI	1	1	3	3	2	2
5	FFI	1	1	1	1	1	1
6	FFI	2	2	2	2	2	2
7	FFI	3	3	3	3	3	3
8	TFI2	1	2	1	2	1	2
9	TFI2	1	3	1	3	1	3
10	TFI2	2	3	2	3	2	3

Each OFDM-UWB signal consists in 128 sub-carriers comprised by null sub-carriers (specified at the band edges in order to relax electrical filter requirements), pilot sub-carriers, guard sub-carriers, and data sub-carriers as represented in Figure 6.



The OFDM symbol period is 312.5 ns and the data as shown in the OFDM encoder of Figure 7 is transmitted in 242.42 ns. The guard-time is 70.1 ns which comprises 60.61 ns for the cyclic prefix [6]-[8] as represented in Figure 8. The sub-carrier frequency spacing is 4.125 MHz and the total OFDM-UWB signal bandwidth is 528 MHz (128×4.125 MHz).

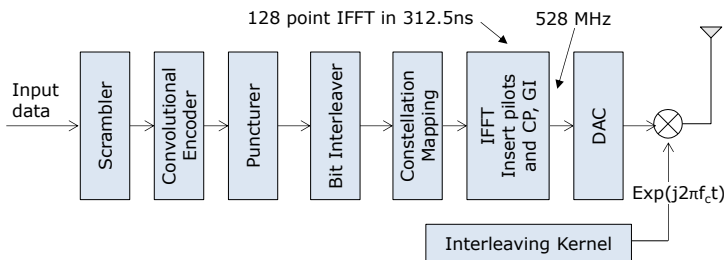


Figure 7. OFDM encoder block diagram

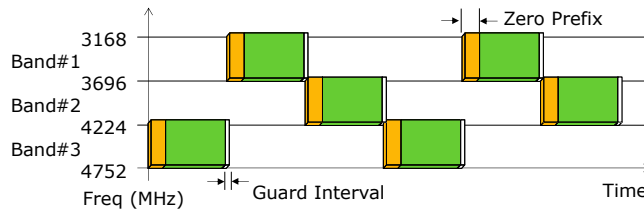


Figure 8. Band Interleaving, zero Prefix and guard intervals of MB-OFDM UWB signal [6]

1.2. Framework and objectives of this Ph.D.

This Ph.D. thesis was developed in the research group of the Wireless-Photonics Area of the Nanophotonics Technology Center (NTC) of the Universitat Politècnica de València (UPV). In the NTC, the research line called "Optical Access and Next-Generation Networks" coordinated by Dr. Roberto Llorente investigates novel architectures and technologies for networks based on optical fibre such as FTTH. Techniques to increase the capacity of optical networks, such as sub-carrier multiplexing, dense wavelength division multiplexing (DWDM), or polarization-division multiplexing are also being researched.

During the realization of this Ph.D. thesis, I have collaborated in different projects. I started collaborating in 2007 with the FP6-2005-IST-5-033615 UROOF Project which was focused on photonic components for Ultra-wideband Radio over Optical Fibre (www.ist-uroof.org). In the framework of this project, the investigation of UWB signal distribution on optical network was investigated. Also, I collaborated with the network of excellence (NoE) FP6-IST 26592 ISIS for "Infrastructures for broadband access in wireless /photonics and integration of strengths in Europe", FP7-ICT-2007-1-216863 BONE "Building the Future Optical Network in Europe" and FP7-ICT-2007-2-224402 EUROFOS "Pan-European Photonics Task Force: Integrating Europe's Expertise on Photonic Subsystems".

In 2008, the European project FP7-2007-ICT-1-216785 UCELLS "Ultra-wide band real-time interference monitoring and cellular management strategies" started (www.ict-ucells.eu). This project was coordinated by UPV and run from January 2008 to the end of December 2010. In UCELLS project, the main objective was the demonstration of UWB radio sensing by photonic analog-to-digital converter (ADC) architecture. The application of this photonic technique was evaluated in this thesis and also the requirements to perform UWB sensing in linearized modulators was investigated. In addition, a fibre-to-the-home UWB signal distribution feasibility analysis was performed in this Ph.D. because, although UCELLS addressed the distribution of UWB signal in-home, the UWB signal could also be provided from the operator premises. It was the interest of UCELLS to assess the possible in-home distribution of UWB signal that have been already transmitted through a fibre-to-the-home optical access network.

Also the project FP7-ICT-2009-4-249142 FIVER was coordinated by UPVLC, which started in January 2010 and will finish by the end of December 2012 (www.ict-fiver.eu). This project proposes and evaluates a fully-converged integrated optical-wireless access architecture for quintuple-play services provision. In 2010, also the national I+D+i Spanish project ULTRADEF started for the optical distribution of ultra-high definition video (UHDV) in wavelength multiplexing using ultra wideband modulation.

1.2.1. Research topics and outline

The research topics covered by this Ph.D. thesis can be summarized as:

- **UWB-over-fibre in FTTH access networks:** The study the radio-over-fibre transmission of UWB signals in optical access FTTH networks is reported in Chapter 2. The results to be obtained at this point are the development and demonstration of solutions for the transmission of UWB signals transmission over optical networks. The objective is to reach from 10 to 100 km optical fibre networks (also called long-reach passive optical networks or LR-PON), which means that the UWB connectivity at high bitrate is range extended. This approach employs the FTTH optical links to optically distribute the UWB signal in its native format from a central location to the remote customer premises for its further wireless transmission. This access technique exhibits several advantages: (i) The optical distribution of UWB signals in the band from 3.1 to 10.6 GHz enables the provision of a large number of UWB channels employing only one light. (ii) UWB is cost-efficient. The signal transmitted to user premises is received by commercially available low-cost UWB devices. (iii) Optical reception and radio transmission is flexible. As re-modulation and/or frequency up-conversion are not needed, the customer-side receiver is agnostic regarding the frequency band and the specific modulation employed. Both UWB implementations based in impulse-radio and OFDM signals will be studied in first place. In this objective, the evaluation of the wireless path after the optical network will also be addressed, as it is important to analyse the impact of the optical transmission in the final application at customer premises. Also, the optical techniques for maximizing the capacity of the access network are evaluated in this topic. In Section 2.5, the performance of polarization-multiplexing in access networks for doubling the capacity of the system is evaluated for UWB signals and also for the multi-format radio-over-fibre distribution of OFDM-based signals (WiMAX and UWB signals) without mutual interference.
- **UWB radio-over-fibre in optical pico-cell cluster networks.** This research objective includes radio-over-fibre transmission techniques for managing UWB pico-cell cluster network. In first place, the analytical study and experimental demonstration of UWB-over-fibre transmission in in-building networks for UWB pico-cell service provision were performed.

Once the UWB pico-cell cluster networks are active in a given area, it is important to be able to manage the UWB pico-cells. So, another objective of this Ph.D. was the evaluation of cognitive radio techniques using optical networks. Cognitive radio technologies are expected to be a key solution to the foreseen spectrum scarcity problem due to the ever increasing number of subscribers and data rates. Cognitive radio systems rely on first getting the knowledge of the radio environment (sensing stage). The data are then processed and used to maximize the user capacity and to mitigate the possible interference between sharing applications by adapting the transmission parameters [50]. Sensing radio signals is a challenging task when both a large bandwidth and high sensitivity must be achieved. Radio measurement in a large frequency span is typically done using a spectrum analyser and a frequency down-conversion stage sweeping the desired frequency range. The spectrum analyser is synchronized with a sampling digitizer in order to capture the entire spectrum. These techniques become more complex and expensive as the power of the sensed signals decreases and as their frequency range increases. So in this topic, optical techniques for sensing high-bandwidth spectrums investigated and demonstrated in Section 3.3. This includes the demonstration of control strategies of UWB signals in a cellular environment.

In order to be able to sense the full spectrum including all the radio signals, optical devices with very good dynamic range are needed. In Section 3.4 the investigation on linearized modulators to cover the full UWB band with improved performance is included.

- **Coexistence study of multi-standard OFDM radio-over-fibre transmission.**

In a real FTTH development it is expected that the operator provides multi-service to the user using different signals, so it is very important to check the coexistence between the different services not only in the radio environment but in the optical transmission. For example, in a network providing triple-play services, radio-over-fibre can be applied for the distribution of LAN connectivity provided by WiMAX, cellular phone connectivity provided by LTE, and HDTV provided by UWB wireless signals. About this topic, Chapter 3 evaluates the coexistence between the different OFDM-based signals in radio-over-fibre transmission.

Different optical network architectures are proposed and evaluated. The first FTTH proposed architecture consists of providing point to point communication to several users employing two wavelengths as known by conventional wavelength-duplexed distribution architecture. The electrical UWB signal alongside the other wireless signals are distributed through the FTTH network in an optical carrier and broadcasted at the user premises. A second architecture is based on the data transmission in the upstream path from user premises to the central office employing a reflective electro-absorption transceiver (R-EAT). These coexistence studies also include the evaluation of different in-building optical media and the radio link at customer premises.

- **Impairment compensation techniques of multi-standard OFDM radio-over-fibre transmissions**

are also investigated in the last Chapter of this Ph.D (Chapter 5). According to the results obtained in the radio-over-fibre transmission, it was observed that the reach of the FTTH network could be extended if we apply compensation techniques in the network. An impairment compensation subsystem is proposed based on using extra RF-pilots in the free-spectrum of the multi-OFDM signal to obtain the network channel information. The performance of this impairment compensation technique is evaluated and demonstrated in a multi-standard OFDM quadruple service including GbE, LTE, WiMAX and UWB signals.

As a result of these technical objectives, another objective of this Ph.D. thesis is the dissemination of the results with the scientific community through publications in specialized peer-reviewed international journals such as IEEE Journal Lightwave Technology [Mor09a], IEEE Photonics Technology Letters [Mor09b], OSA Optics Express [Mor11a], IEEE Transactions on Microwave Theory and Techniques [Llo10a], IEEE Journal on Selected Areas in Communications [Llo11a]; and high-impact conferences in optical topics such as OFC [Mor09c], [Mor11b-e], [Mor12a] and ECOC [Llo10c][Llo11e]. The original contributions obtained during this Ph.D are listed in Annex A.

The workplan of this Ph.D. thesis started on 2008 with the M.Sc. thesis about UWB radio over fibre transmission in optical networks. In the last years, it has been possible to develop further on this topic and propose the different research objectives of this Ph.D. thesis following the quality parameters of the Doctorate program of Telecommunications from the Departamento de Comunicaciones of the Universitat Politècnica de València.

CHAPTER 2. UWB RADIO-OVER-FIBRE IN FTTH ACCESS NETWORKS

2.1. Introduction

UWB wireless is a radio technology targeting high-bitrate short-range indoor data communications. UWB is defined as a radio signal with 20% fractional bandwidth or, at least 500 MHz. UWB communication is a wireless service allocated in the 3.1 to 10.6 GHz band with EIRP levels of -41.3 dBm/MHz as shown in Figure 9 [5].

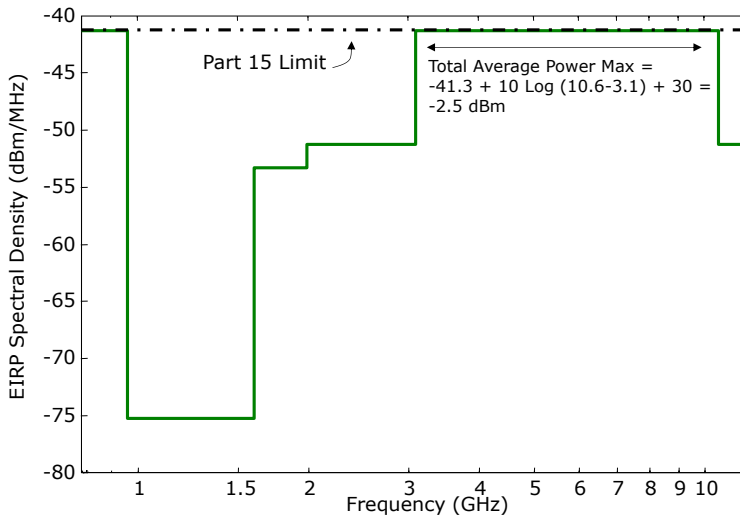


Figure 9. Spectral mask defined by FCC [5]

UWB has been indicated as one of the most promising techniques to be used in wireless communication networks. The growing interest in this technique is due to its low self-interference, tolerance to multi-path fading, low probability of interception and capability of passing through walls while maintaining the communication [4]. Nowadays, UWB is appointed for high bit-rate wireless communications at picocell range, namely as a replacement of high definition (HD) video/audio cabling [51].

Hybrid wireless-optical access based on the transmission of UWB signals in FTTH networks is a natural step forward in the evolution of the access network. This approach employs the FTTH optical links to optically distribute the UWB signal in its native format from a central location to the remote customer premises for its further wireless transmission [Llo08a]. This approach exhibits several advantages:

- (i) FTTH networks provide bandwidth enough to distribute a large number of UWB signals, as each one of them can occupy up to 7 GHz in current UWB regulation [5].
- (ii) The optical distribution of UWB signals in the band from 3.1 to 10.6 GHz enables the provision of a large number of UWB channels employing a single wavelength.
- (iii) No trans-modulation is required at user premises. HD audio/video content is transmitted through the fibres in UWB native format with intrinsic support of video.
- (iv) No frequency up-conversion is required at customer premises. The UWB signals are photo-detected, filtered, amplified and radiated directly to establish the wireless connection.
- (v) FTTH networks are transparent to the specific UWB implementation employed. Optical reception and radio transmission is flexible. As re-modulation and/or frequency up-conversion are not needed, the customer-side receiver is agnostic regarding the frequency band and the specific modulation employed.

(vi) UWB is cost-efficient. The signal transmitted to user premises is received by commercially available low-cost UWB devices, which range in lower than \$100 market price [9][10].

Two specific UWB implementations are mainstream nowadays: Impulse-radio (IR-UWB), which transmits data by short impulses (monopulses), and OFDM-UWB (also called multi-band OFDM) which divides the UWB spectrum into 14 channel bands of 528 MHz bandwidth following ECMA-368 regulation [6] as it was shown in Figure 4.

The optical distribution of IR-UWB and OFDM-UWB signals in FTTH networks was first proposed in [Llo08a]. Mathematical modelling was performed for both UWB signals in [52] and UWB-over-fibre has been studied by simulation as reported in Section 2.2. Section 2.3 includes the comparison of IR-UWB and OFDM-UWB radio-over-fibre transmission in FTTH. The results indicated that OFDM-UWB signals are better suited for optical transmission as IR-UWB signals are more sensitive to nonlinear distortion [53] so in the further sections a deeper study on OFDM-based UWB radio-over-fibre transmission is done in Section 2.4 including the evaluation of multi-channel transmission, number of pilots employed for demodulation and also the integrated wireless-optical end-to-end transmission of OFDM-UWB signals in radio-over-fibre.

Finally, in Section 2.5 proposes and analyses the distribution of polarization-multiplexed (PM) UWB signals as a suitable technique for the provision of wireless connectivity to a large number of users. The radio-over-fibre polarization-multiplexed technique is demonstrated experimentally with UWB signals and also for WiMAX signals without mutual interference.

2.2. Simulation evaluation of UWB radio-over-fibre transmission

As a first step, a simulation analysis was performed to evaluate the maximum reach in standard single mode fibre (SSMF) of UWB-over-fibre transmission using the two mainstream UWB implementations IR-UWB and OFDM-UWB. External modulation by a Mach-Zehnder electro-optic modulator (MZ-EOM) and direct-modulation by a vertical-cavity surface-emitting laser (VCSEL) are considered in this study.

Figure 10 shows the two UWB radio-over-fibre implementations schematics considered. The analysis targets to evaluate the SSMF reach achieved for OFDM-UWB and IR-UWB at the maximum bitrate defined in ECMA-368 standard, i.e. 480 Mbit/s. The analysis was done employing a commercial split-step Fourier simulation tool, VPI Photonics [54].

The MZ-EOM employed is a chirp-free LiNb X-cut modulator. Modulation index has been optimised in every configuration analysed to maximize UWB reach in every case. This allows a fair result comparison. Table 4 summarises the parameters employed in the analysis for the elements shown in Figure 10.

Table 4. UWB radio-over-fibre simulation parameters

<i>PIN</i> parameter	value	<i>MZ-EOM</i> parameters	value
Responsivity	0.7 A/W	E/O BW	20 GHz
Thermal noise	10 pA/ $\sqrt{\text{Hz}}$	V_n DC	5 V
<i>VCSEL</i>	value	V_n RF	5.5 V
Core radius	2×10^{-6} m	Insertion losses	6 dB
Active region thickness	0.3×10^{-6} m	Thermal freq shift	-10^{-12} df/dJ
Confinement factor	0.03	Extinction ratio	35 dB

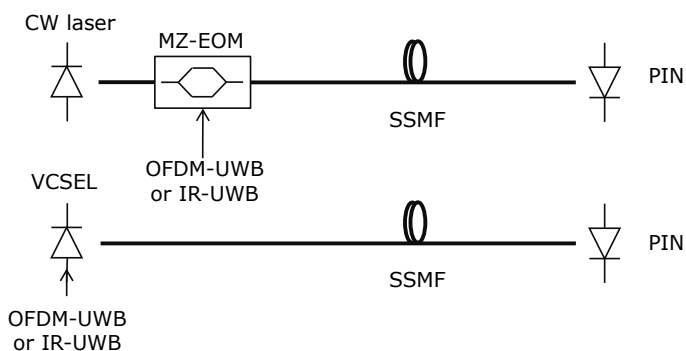


Figure 10. UWB radio-over-fibre optical link analysis configuration: (a) Mach-Zehnder external modulation. (b) VCSEL direct modulation

Figure 11(a) shows the voltage-current characteristics of the VCSEL at 24 °C in the analysis. The impulse-radio UWB base-band signal consists of a Gaussian monocycle pulses as shown in Figure 11(b). This waveform exhibits 1.94 ns T_{fwhm} width and the equivalent spectrum has 525 MHz bandwidth at -3 dB, which fits with the 528 MHz bandwidth of the OFDM signal. The OFDM simulated bears 480 Mbit/s and is composed of 128 carriers modulated in quadrature-phase shift keying QPSK.

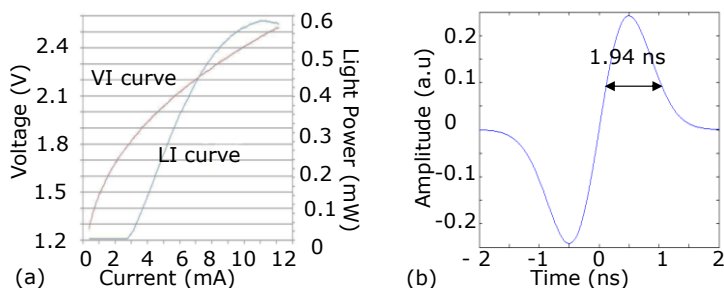


Figure 11. (a) VCSEL characteristics. (b) IR-UWB monocycle

Figure 12 show the bit-error rate (BER) achieved by IR-UWB radio-over-fibre transmission on SSMF optical media.

From these simulation results we can observe that external modulation on SSMF give a maximum reach of 50 km, at error-free ($BER < 10^{-9}$) operation, with 7 dBm optical power launched in the fibre. Direct modulation on SSMF gives a maximum reach of 75 km with 6.5 dBm optical power launched in the fibre.

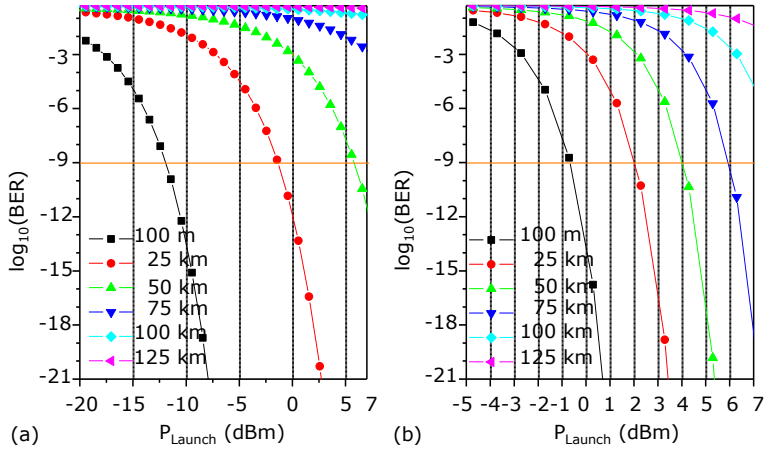


Figure 12. BER vs. launch power vs. SSMF length in IR-UWB at 480Mbit/s bitrate for (a) external modulation, and (b) direct modulation

Figure 13 show the analysis results for OFDM-UWB case. Performance of OFDM-UWB transmission is given by the error vector magnitude (EVM). The EVM is a measure of the signal divergence from its reference and is defined by equation (1). EVM is widely used in wireless digitally modulated communication systems measurements. The EVM root mean square (RMS) is computed directly from the demodulated constellation using [55]:

$$EVM_{RMS} = \sqrt{\frac{\frac{1}{N} \sum_{n=1}^N |S_n - S_{0,n}|^2}{\frac{1}{N} \sum_{n=1}^N |S_{0,n}|^2}} \quad (1)$$

where S_n is the normalized n^{th} symbol in the stream of measured symbols, $S_{0,n}$ is the ideal normalized constellation point of the n^{th} symbol and N is the number of transmitted symbols. The bit error ratio could be calculated, if desired, from the EVM measurements shown, as described in [55].

However, in order to compare with IR-UWB performance, the BER of the OFDM-UWB signal is calculated from the EVM. Assuming that additive white Gaussian noise dominates the system performance, the relationship between EVM and BER is given by [55]:

$$BER = Q\left[\sqrt{2}/EVM\right] \quad (2)$$

where $Q(x)$ is defined by:

$$Q(x) = \frac{1}{\sqrt{2\pi}} \int_x^{+\infty} e^{-\lambda^2/2} d\lambda \quad (3)$$

From the results shown in Figure 13(a), external modulation on SSMF gives a maximum reach of 100 km with 8 dBm of input optical power for OFDM-UWB signals.

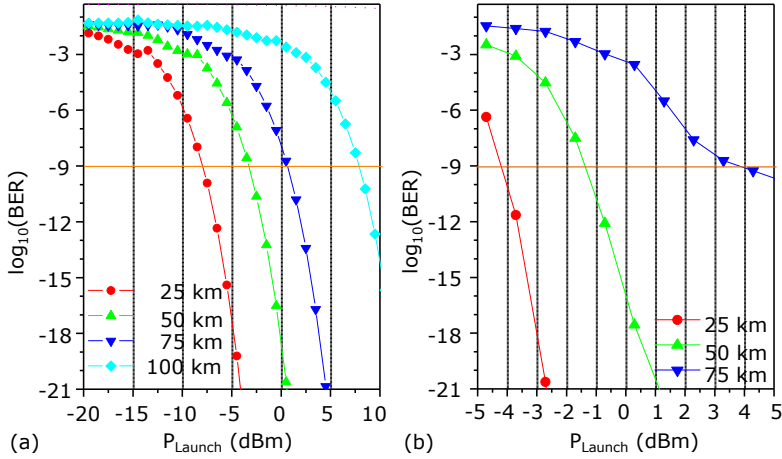


Figure 13. BER vs. launch power vs. SSMF length in OFDM-UWB at 480 Mbit/s with (a) external modulation and (b) direct modulation

Table 5 summarises the UWB radio-over-fibre reach all configurations. From the simulation results OFDM-UWB achieves the highest range to 100 km SSMF with a high launch power level and external modulation. IR-UWB can achieve a reach of 75 km in uncompensated SSMF at lower launch power level than OFDM-UWB.

Table 5. UWB radio-over-fibre simulated reach summary

Technology	Fibre reach	Launch power
IR-UWB External modulation	50 km	6.6 dBm
IR-UWB Direct modulation	75 km	6 dBm
OFDM-UWB External modulation	100 km	11.5 dBm
OFDM-UWB Direct modulation	75 km	5 dBm

Those results indicated for the first time the UWB-over-fibre was a potential solution for optical access networks in SSMF. This simulation study will be validated experimentally in the next section.

2.3. Comparison of OFDM-UWB and IR-UWB signal performance in radio-over-fibre distribution

The proposed technique for UWB radio-over-fibre transmission is depicted in Figure 14(a). This figure shows a central node (head-end) which generates UWB signals transporting HD content. These signals are distributed through the FTTH network to a number of subscribers. At the subscriber premises, the received UWB signals are photo-detected, filtered, amplified and radiated to broadcast the HD content to an UWB-enabled television set or computer.

Figure 14(b) shows the sub-carrier multiplexing (SCM) channelization proposed for the FTTH transmission. The channelization consists in several 528 MHz-wide channels (each one in accordance with [5]) forming a SCM group which modulates an optical carrier. Different optical carriers can be wavelength division multiplexed to increase the number of UWB channels delivered by each fibre of the FTTH network. Each UWB channel bears one HD audio/video stream, which is extracted at the customer premises by an UWB wireless extractor (UWE).

Figure 14(c) shows the proposed architecture for the UWE. Operation is as follows. A given SCM group is first selected by optical filtering, and then the group is photo-detected and filtered in electrical domain to select the specific UWB channel transporting the desired HD contents. The selected UWB channel is then amplified and radiated. The proposed UWE architecture does not require demodulation or frequency translation of the UWB signal, and is transparent to the specific modulation employed.

In this section, the signal degradation due to the fibre transmission impairments experienced in the FTTH link is analysed.

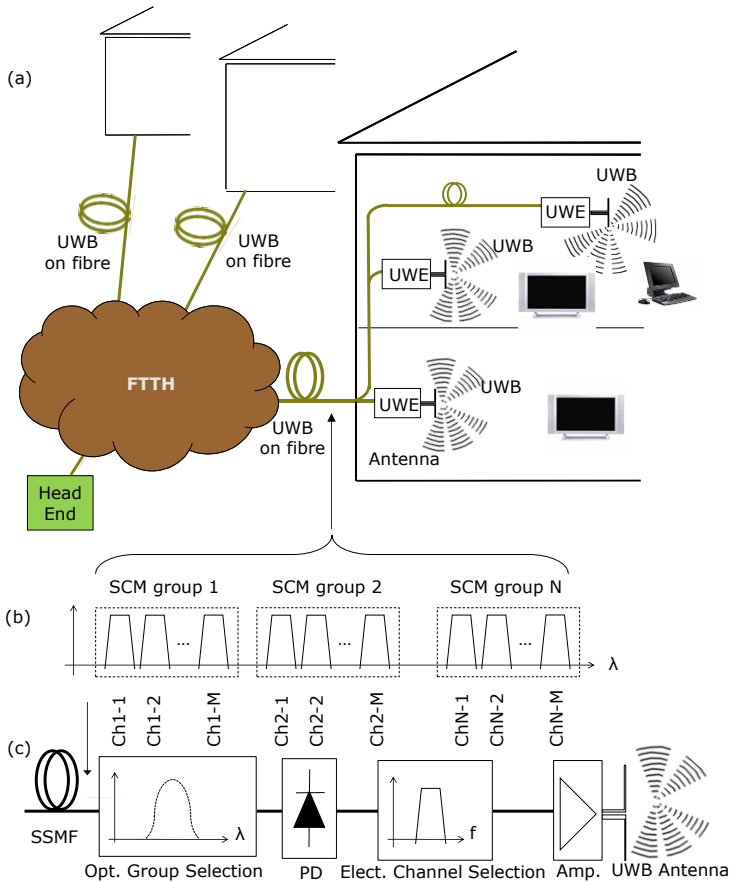


Figure 14. (a) Concept of UWB on FTTH for distribution of high definition audio/video. (b) Proposed sub-carrier multiplexing (SCM) channelization. (c) Proposed UWB wireless extractor (UWE) architecture

Figure 15 shows the experimental set-up to evaluate the UWB signal degradation due to fibre transmission. The two UWB versions are implemented for performance comparison: IR-UWB and OFDM-UWB as in current regulation [6].

The UWB signal bit-rate is 1.25 Gbit/s in both cases, adequate for uncompressed $1920 \times 1080 \times 18 \text{bpp} \times 60 \text{ Hz}$ video [56]. The UWB signals are transmitted along different SSMF links, ranging from 25 km to 60 km corresponding to conventional FTTH transmission paths.

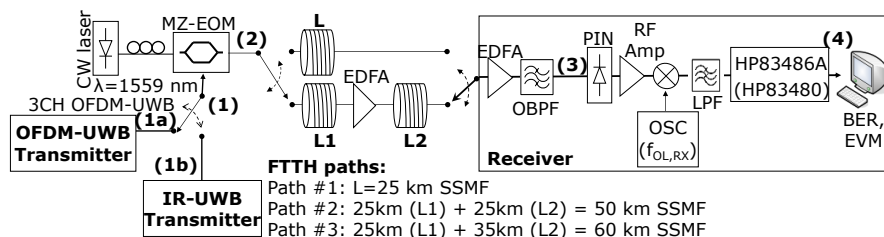


Figure 15. UWB on FTTH demonstrator setup block diagram. The receiver emulates the UWB wireless extractor

The OFDM-UWB transmitter depicted in Figure 16 consists in three OFDM channels with an aggregated bit-rate of 1.25 Gbit/s, forming a SCM group. Each OFDM channel has 128 carriers, each QPSK-modulated, including pilots. Separation between carriers is 4.11 MHz. The channel under study (labelled CH2 in Figure 15) is located at $f_{OL2} = 2.5$ GHz and is surrounded by two adjacent channels centred at frequencies $f_{OL1} = 1$ GHz and $f_{OL3} = 4$ GHz. The bandwidth (BW) at -10 dB of the OFDM-UWB SCM group is 3.51 GHz [see Figure 17(a)].

The average optical power after modulation and before transmission [point (2) in Figure 15] is -2 dBm. The three OFDM channels are generated by an AWG6030 arbitrary waveform generator with 1.25 Gsamples/s.

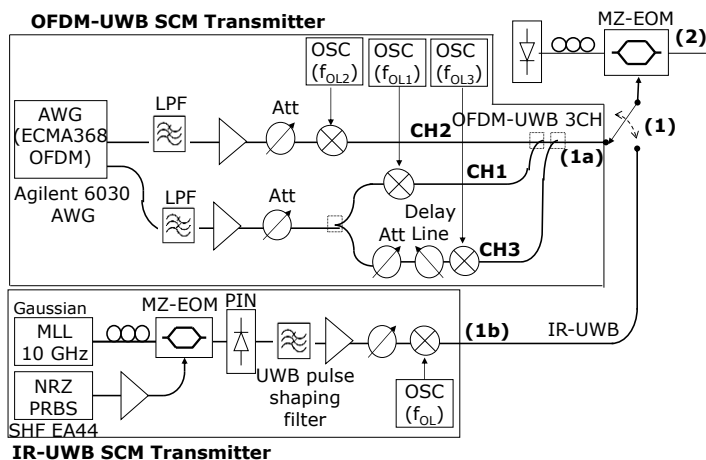


Figure 16. OFDM-UWB and IR-UWB transmitter block from Figure 15

The IR-UWB signal is generated as shown in Figure 16, in accordance with the FCC UWB spectral mask between 3.1 and 10.6 GHz. The IR-UWB monopulses are obtained from a 10 GHz Gaussian pulse ($T_{fwhm} = 2.8$ ps) train generated by a mode-locked laser. The pulse train is gated by a Mach-Zehnder electro-optical modulator (MZ-EOM) with 1.25 Gbit/s PRBS data. The gated optical pulses are photo-detected, shaped to monopulses with $T_{fwhm} = 283$ ps by a pulse-shaping filter and up-converted to $f_{OL} = 6.6$ GHz for fibre transmission. The overall -10 dB bandwidth of IR-UWB signal is 3.2 GHz [see Figure 17(b)] and occupies the band from 5 GHz to 8.2 GHz, following actual regulation [5]. The average optical power at point (2) in Figure 15 is adjusted to -2 dBm.

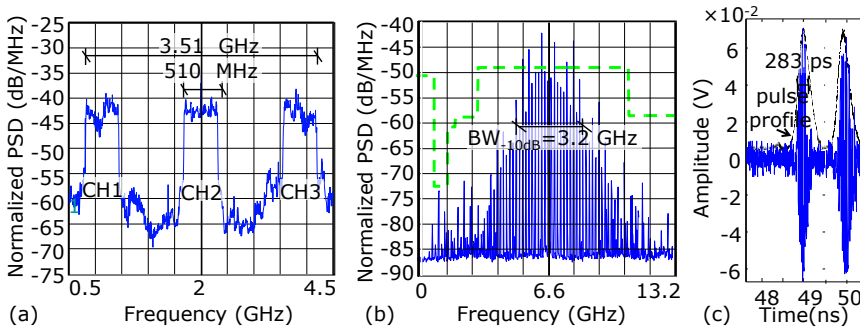


Figure 17. (a) OFDM-UWB electrical spectrum at point (1a) of transmitter in Figure 15; (b) IR-UWB RF spectrum (RBW=1 MHz), and (c) Electrical IR-UWB signal and pulse profile at point (1b) of Figure 15

The two UWB versions modulate a 20 GHz BW MZ-EOM at quadrature-bias point and are transmitted through the three FTTH paths shown in Figure 15. After transmission, the signals are filtered by a 0.8 nm @ -0.5 dB optical filter (SCM group selection) and photo-detected by a PIN photodiode (0.65 A/W, 50 GHz BW) as in the UWE architecture proposed in Figure 14(c). In order to evaluate the performance of the UWB channel under study, the photo-detected signal is converted to baseband and sampled by an HP83486A module (20 GHz BW). Performance is evaluated with received optical power ranging 0 – 10 dBm at the photodiode. These levels translate to -51.8 – -31 dBm/MHz (50 Ω) power spectral density over the 3.2 GHz BW. These values would meet the wireless EIRP limits [5] employing a 0 dBi antenna.

In the OFDM-UWB case, after sampling the received channel, the channel under study is equalized from pilot information, demodulated and the error vector magnitude (EVM) is measured. Bit-error ratio (BER) of the OFDM-UWB signal is calculated from the EVM according to equation (2) for QPSK signals.

In the IR-UWB cases, the monopulses are demodulated, low-pass filtered and the Q-factor is measured by the HP83480 instrument in Figure 15. BER is then calculated from the Q-factor for equally probable data symbols assuming Gaussian noise, as given by:

$$BER = 0.5 \cdot \operatorname{erfc}(Q / \sqrt{2}) \quad (4)$$

The measurements have been done in back-to-back and for three FTTH transmission paths: Path#1=25 km SSMF, Path#2= 25 km SSMF + amplification + 25 km SSMF (50 km reach) and Path#3= 25 km SSMF + amplification + 35 km SSMF (60 km reach). These paths are depicted in Figure 15. Inline amplification is realized by a 23 dB gain, 4 dB noise figure erbium doped fibre amplifier EDFA (Keopsys BT2C-13). The receiver includes a 4.5 dB noise figure, 19 dBm saturation power EDFA (Exelite SFA-19).

Figure 18(a) shows the OFDM-UWB received constellation after equalization employing pilot tones information, at point (4) of Figure 15. Figure 18(b) shows the IR-UWB received eye diagram, at point (4) of Figure 15. Constellation and eye diagram shown in Figure 18 are obtained at point (3), at 9 dBm received power and 50 km of SSMF. Figure 18 shows that the received signal presents good quality for both IR-UWB and OFDM-UWB signals; therefore, good performance is expected for both UWB implementations.

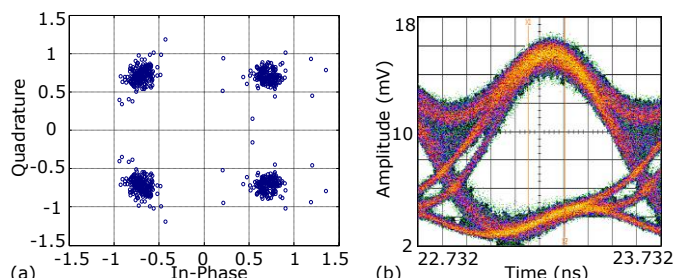


Figure 18. (a) Received OFDM-UWB (QPSK carriers) constellation (784 symbols shown) after pilot compensation, at point (4) of Figure 15. Aggregated bit-rate 1.25 Gbit/s. (b) IR-UWB received eye diagram, at point (4) in Figure 15

The BER achieved by OFDM-UWB and IR-UWB are shown in Figure 19 for all the FTTH paths between 25 km and 60 km and back-to-back versus the received power, measured at point (3) in Figure 15. These experimental results demonstrate the feasible distribution of 1.25 Gbit/s UWB signals achieving $BER < 10^{-9}$ operation at 50 km with both IR-UWB and OFDM-UWB implementations. Figure 19 shows that the IR-UWB technique exhibits performance degradation in comparison with OFDM-UWB. This is due to the different modulation schemes. OFDM-UWB channels are generated independently and up-converted to generate a SCM group. The IR-UWB signal does not follow this channelization, and to provide a bit rate of 1.25 Gbit/s, a single IR-UWB signal with 3.2 GHz bandwidth @ -10 dB was generated. IR-UWB suffers from the non-perfect operation of up- and down-converting mixers over such wide bandwidth. Figure 19 also shows that OFDM-UWB degrades quickly with fibre length, due to the carrier suppression effect originated from the SSMF chromatic dispersion [63].

The bandwidth occupied by the 3 channels in OFDM-UWB (3.51 GHz), that ensures the accumulated bit-rate of 1.25 Gbit/s, leads to an equivalent spectral efficiency of 0.36 bit/s/Hz. The IR-UWB bandwidth (3.2 GHz) for the same bit-rate gives a spectral efficiency of 0.39 bit/s/Hz. This similar spectral efficiency combined with the improved performance obtained for OFDM-UWB suggests that the UWB-over-fibre implementation should be accomplished with OFDM signals.

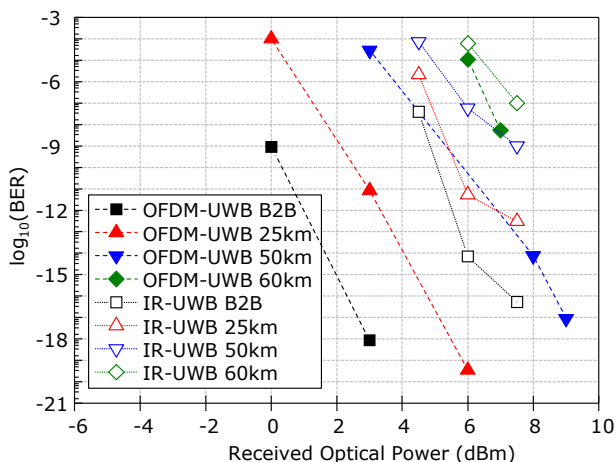


Figure 19. Experimental BER comparison of UWB implementations at 1.25 Gbit/s for the three FTTH SSMF paths. Filled symbols and dashed lines: OFDM-UWB three channels SCM group (QPSK per carrier); Blank symbols and dotted lines: IR-UWB signal results

2.4. OFDM-UWB signals performance in radio-over-fibre distribution

From the results obtained in the comparison between IR-UWB and OFDM-UWB it was decided to further study the performance of OFDM-UWB radio-over-fibre distribution, considering the end-to-end architecture comprising the access network, the in-building optical distribution and the wireless radiation at customer premises. Also the multi-channel effect of OFDM-UWB transmission and the impact of the number of OFDM pilots used for the demodulation of the UWB signal was investigated.

2.4.1. Multi-channel OFDM-UWB radio-over-fibre evaluation

The UWB-on-fibre distribution in FTTH networks approach was depicted in Figure 14(a). This figure shows an optical line termination (OLT) which distributes HD audio/video content from the core network to a number of users through a FTTH network. The OLT generates OFDM-UWB signals as defined by ECMA-368 [6]. These signals are transmitted to the subscriber premises, where are received by a wireless extractor (UWE) system. The UWE extracts the UWB signal from the FTTH fibre and transmits the UWB wireless signal to an UWB-enabled TV set [58] or computer [59]. The UWE performs the photodetection of the transmitted signal, electrical filtering and amplification and directly radiates the resulting signal to establish a standard UWB communication.

The UWB-on-fibre radio spectral mask is allocated between 3.1 and 10.6 GHz, providing 14 channels with 528 MHz bandwidth [6], as shown in Figure 20. The electrical UWB signal is distributed through the FTTH network in a single wavelength and broadcasted in the user premises. Multicast or unicast operation is possible increasing the number of UWB channels available. This can be done employing different wavelengths in a wavelength-division multiplexing (WDM) configuration.



Figure 20. Diagram of the band group allocation in ECMA-368 [6]

In this experiment, two different OFDM-UWB multichannel configurations are compared. First, a three-channel quadrature-phase shift keying OFDM (QPSK-OFDM) configuration is implemented and its transmission performance is evaluated. Second, a five-channel binary-phase shift keying OFDM (BPSK-OFDM) configuration is also implemented and its performance is evaluated. Both configurations transport a 1.56 Gbit/s aggregated bitrate signal. Their performance is compared to identify the best performing system-level implementation.

Also, following the description of Section 2.2, two FTTH configurations have been studied in this experiment. The first one is labelled "FTTH configuration A" in Figure 21(a) and consists in a conventional passive optical network (PON) architecture with a 'trunk' link connecting the OLT with the UWE at the subscriber base [60]. The second is labelled "FTTH configuration B" and is depicted in Figure 21(b). This configuration simulates a FTTH link with intermediate optical amplification, comprising a 'trunk' link that connects the OLT with the remote node and an 'access' link to reach the UWE at subscriber premises [61]. Configuration B is commonly used to provide triple play services with the addition of carriers incorporating local or regional programming and also voice and data services.

The fibre link distance in the direct connection case shown in Figure 21(a) can range up to 60 km. The long 'trunk' links shown in Figure 21(b) interconnect distribution hubs (DH) towns which can be up to 100 km apart. The 'access' links shown in Figure 21(b) connect the DH to the final subscriber, which can be up to 60 km apart.

The target of the analysis is two fold: first, to demonstrate the feasibility of multi-channel OFDM-UWB on FTTH networks at 1.56 Gbit/s aggregated bitrate – adequate for HD uncompressed $1920 \times 1080 \text{i} \times 24 \text{bpp} \times 60 \text{ Hz}$ video transmission [56]; second, to investigate the trade-off between the number of channels and their modulation index at system level.

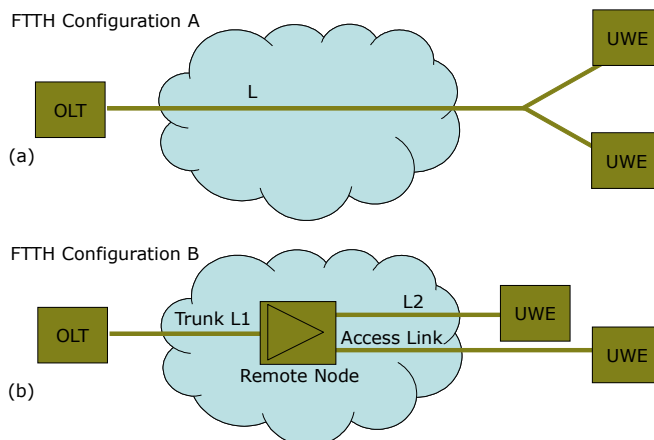


Figure 21. FTTH architectures: (a) configuration A (fibre path without optical amplification) [60], and (b) configuration B (fibre paths with inline optical amplification) [61]

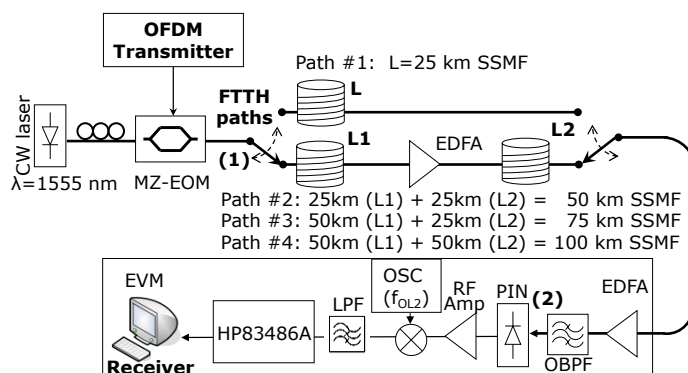


Figure 22. Experimental set-up for OFDM-UWB transmission over four different FTTH paths: Path #1 = 25 km, Path#2 = 50 km, Path#3 = 75 km and Path#4 = 100 km

The experimental analysis set-up is shown in Figure 22. Two different OFDM-UWB transmitters are implemented as shown in Figure 23 for three-channel QPSK-OFDM UWB and in Figure 24 for a five-channel BPSK-OFDM UWB configuration. The bandwidth of each channel is 528 MHz. These two configurations are implemented by an Agilent 6030 AWG with 1.25 GS/s sampling rate. The OFDM-UWB signals are generated at baseband and up-converted to the 6.5 GHz central frequency for analysis. The baseband OFDM signal was generated offline in advance and sent to the AWG. Two output channels are available in AWG6030, which will be further employed to generate uncorrelated side channels.

The signal generated by the OFDM-UWB transmitter block modulates externally a continuous-wave 1555 nm laser using a MZ-EOM with 20 GHz BW at quadrature-bias (QB) point. The average power in optical domain after modulation and before transmission, point (1) in Figure 22, is set to -2 dBm to ensure linear transmission into the optical link.

The resulting optical signal is then transmitted through the four FTTH paths shown in Figure 22, composed by different SSMF lengths ranging from 25 km to 100 km, corresponding to conventional FTTH transmission paths [62]. Optical amplification with EDFA is used when necessary. After back-to-back configuration, the first analysed path (Path #1) has 25 km of SSMF, simulating FTTH configuration A described in Figure 21(a). The second path (Path #2), with 50 km reach, is obtained using two fibre sections with 25 km of length each, with an EDFA between them. The third path (Path #3) with 75 km of reach is composed by two fibre sections with length of 50 km and 25 km and an EDFA between them. The last studied path (Path #4) has a reach of 100 km, and is composed by two fibre sections of 50 km with an EDFA between them. Paths #2, #3 and #4 simulate a FTTH link using configuration B described in Figure 21(b). The optical amplification is done by a 23 dB gain, 4 dB noise figure EDFA (Keopsys KPS). The receiver includes a 4.5 dB noise figure, 19 dBm saturation power EDFA (Exelite XLT) used for adjusting the received optical power level measured at point (2) in Figure 22.

After transmission, the signals are filtered by a 0.8 nm @ -0.5 dB optical filter and photodetected by a PIN photodiode (0.65 A/W responsivity, 50 GHz bandwidth). In order to evaluate the performance of the UWB channel under study, the photodetected signal is down-converted to baseband and sampled by an HP83486A module (20 GHz bandwidth). Once sampled, the channel under study is equalized from the pilot sub-carriers information, demodulated and the EVM is evaluated directly from the received constellation. The maximum permissible relative constellation error is set to a root mean square (RMS) EVM of -17 dB [6].

Figure 23 shows the experimental set-up for the 3-channel QPSK-OFDM UWB transmitter. The transmitter generates a three-channel OFDM configuration comprising 128 carriers per channel, including pilots. In this configuration, the 128 sub-carriers distribution is as follows: 82 information sub-carriers, 42 pilot sub-carriers and 4 null sub-carriers. Each sub-carrier is modulated in QPSK with an aggregated bit rate of 1.5689 Gbit/s. The three channels form a SCM signal. The central channel —labelled CH2 in Figure 23 and Figure 25— is located at $f_{OL2} = 6.5$ GHz and used for performance evaluation. This channel is surrounded by two adjacent channels centred at frequencies $f_{OL1} = 5$ GHz and $f_{OL3} = 8$ GHz respectively. The SCM signal bandwidth (SCM BW) is 3.5 GHz at -10 dB for the QPSK-OFDM-UWB SCM group. Two QPSK-OFDM-UWB channels are generated by the AWG and the third one is obtained from one of these ones after delay line de-correlation and electrical losses compensation (due to the power divider and the electrical time delay).

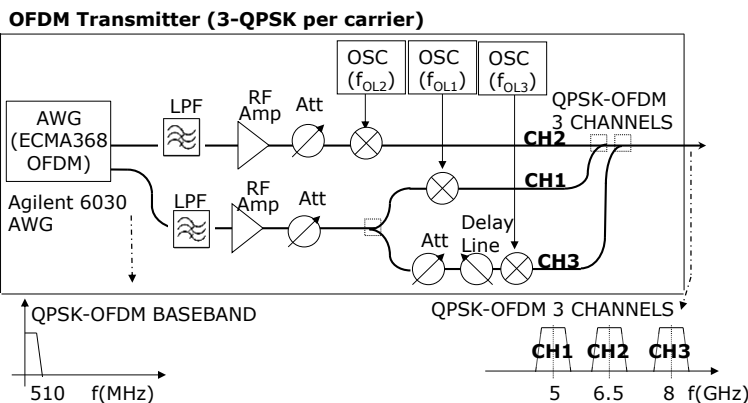


Figure 23. Experimental set-up of the 3-channel QPSK-OFDM transmitter. The centre channel is centred at $f_{OL2} = 6.5$ GHz and is surrounded by two adjacent channels centred at frequencies $f_{OL1} = 5$ GHz and $f_{OL3} = 8$ GHz

OFDM Transmitter (5-BPSK per carrier)

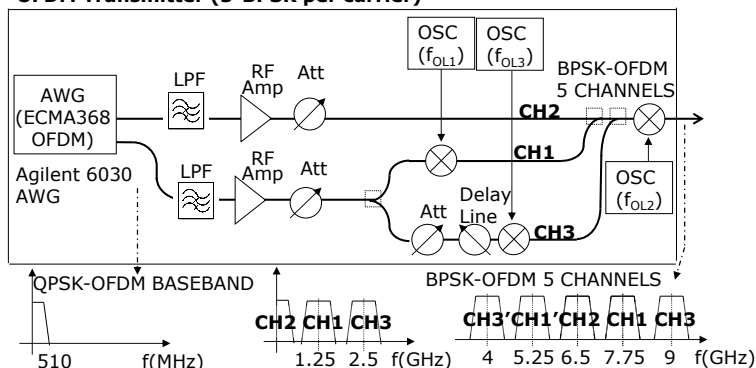


Figure 24. Experimental set-up of the five-channel BPSK-OFDM transmitter where the centre channel is centred at $f_{OL2} = 6.5$ GHz. Using mixer frequencies $f_{OL1} = 1.25$ GHz and $f_{OL3} = 2.5$ GHz, neighboring channels centred at frequencies 4 GHz, 5.25 GHz, 7.75 GHz and 9 GHz are obtained

Figure 24 shows the transmitter of the five-channel BPSK-OFDM-UWB configuration. In this case, each UWB channel has 128 sub-carriers distributed in 98 information sub-carriers, 26 pilots sub-carriers, and 4 null sub-carriers. Each sub-carrier is modulated by BPSK with an aggregated bit rate of 1.5625 Gbit/s. The central channel is located at $f_{OL2} = 6.5$ GHz and is used for performance assessment. Neighbouring channels are centred at frequencies 4, 5.25, 7.75, and 9 GHz, using two up-conversion processes with initial mixer frequencies of $f_{OL1} = 1.25$ GHz and $f_{OL3} = 2.5$ GHz and then, the resulting signal is up-converted to 6.5 GHz.

Figure 25(a) shows the transmitted electrical spectrum measured for the three-channel QPSK configuration at MZ-EOM input. The transmitted signal spectrum at MZ-EOM input for the five-channel BPSK-OFDM-UWB configuration is shown in Figure 25(b). In Figure 25, the electrical spectrum distortion is due to the frequency limitations of the electrical devices.

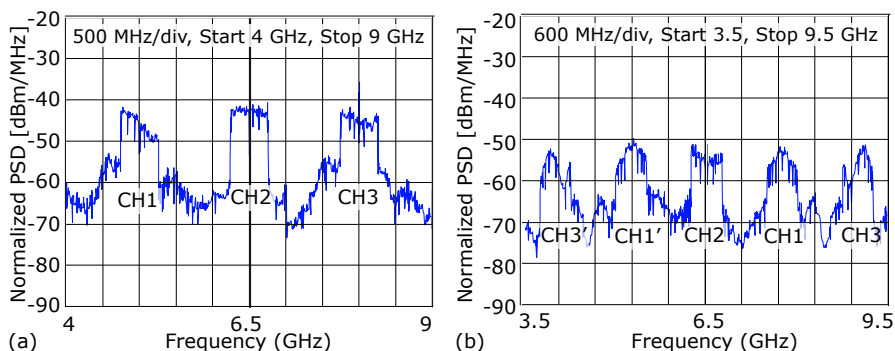


Figure 25. Electrical spectrum for (a) 3-channel QPSK-OFDM and (b) 5-channel BPSK-OFDM configuration (RBW=1 MHz)

The received signal is down-converted to baseband and a low-pass filter (-3 dB bandwidth of 1 GHz) is used to select the channel under study (channel located at 6.5 GHz). This signal is re-sampled and equalized from pilot compensation. This is possible due to the insertion of the pilot subcarriers in the OFDM-UWB signal. These dedicated subcarriers transmit known pilot symbols to assist the phase estimation, whereas the remaining subcarriers transmit information symbols.

Pilot compensation is performed on the received signal using the information from the known module and phase of the inserted pilots to estimate the module and phase error induced by the transmission channel. After, the compensation of these errors along the channel bandwidth is accomplished using the performed pilot-based estimation. The estimation is achieved by least squares adjustment.

The radio-over-fibre link performance is analysed from the evaluation of the EVM of the received baseband OFDM signal, as it is shown in Figure 22. The EVM is a figure of merit commonly used in wireless digitally modulated communication systems. EVM is a measure of the departure of signals from its ideal reference and thus it allows concluding about the system degradation.

It is common to see the values of EVM expressed in % (according to expression (1)) or in dB (according to (4)). In this case, we are going to express the values of EVM in dB. In order to calculate the EVM value from the % value:

$$\text{EVM(dB)} = 20 \cdot \log_{10}(\text{EVM}_{\%}/100) \quad (5)$$

In this experiment, two sets of measurements have been done on four FTTH SSMF transmission paths depicted before in Figure 22, and for different optical received power levels measured at point (2) in Figure 22.

Figure 26(a) and (b) show the corresponding received constellations after fibre transmission along Path #3 (75 km length with amplification) with 6 dBm of received optical power level for BPSK and QPSK, respectively, and Figure 26(c) and (d) the resulting constellations after equalization using pilot tones information.

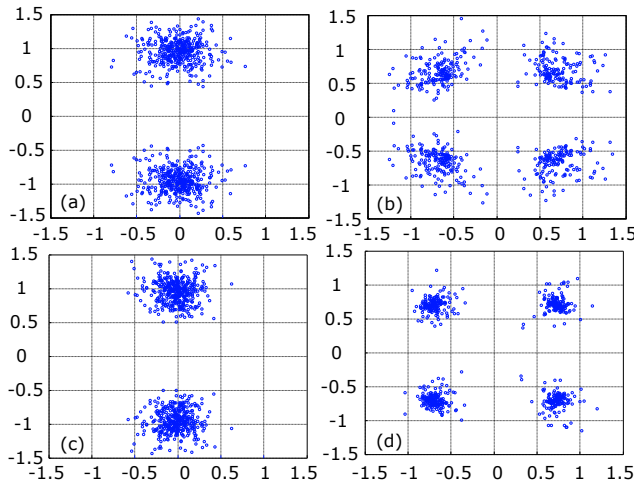


Figure 26. (a) Received BPSK constellation, (b) received QPSK constellation (both for 6 dBm received optical power after 75 km fibre transmission (Path#3)), and the resulting constellations after equalization for (c) BPSK and (d) QPSK

The experimental results of EVM for the 3-channel QPSK and 5-channel BPSK configurations are shown in Figure 27 and Figure 28, respectively. In each figure, the EVM results obtained for the four FTTH paths shown in Figure 22 are represented. The EVM threshold for successful UWB communication of -17 dB [6] is shown as a dashed horizontal line in Figure 27 and Figure 28.

Comparing the EVM results in Figure 27 and Figure 28 for the four FTTH paths, it can be observed that performance degrades when transmitting along longer optical transmission

paths. The degradation is mainly due to the fibre dispersion-induced power fading [63]. Additional degradation occurs because longer distances lead to higher optical noise power originated by the optical amplifiers. Higher optical noise power levels lead to EVM degradation.

Figure 27 shows also that the EVM of the 3-channel QPSK configuration follows approximately a linear dependence of the EVM on the measured received optical power. However, for large optical powers, a significant saturation effect of the EVM dependence on the received optical power can be noticed. In fact, in the saturation zone, the EVM tends to stabilize, and its reduction with the increase of the received optical power is very small.

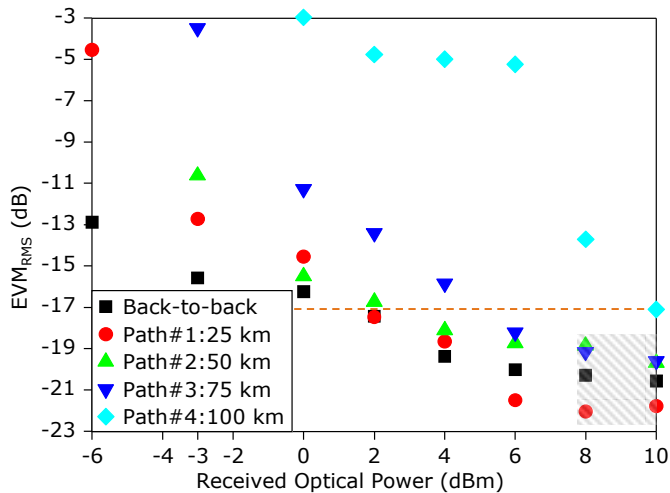


Figure 27. EVM experimental results: three channels QPSK-OFDM in B2B and after 25 km, 50 km, 75 km and 100 km SSMF transmission. Dashed line indicates the EVM threshold and Greyed area indicates the saturation zone

The saturation behaviour can be attributed to the dominance of optical noise with respect to electrical noise at high optical power levels received at the PIN input. In case of dominance of optical noise, no performance improvement can be achieved by increasing the received optical power at the PIN input through the optical pre-amplifier gain increase. Figure 28 shows a similar linear dependence for the EVM of the 5-channel BPSK configuration and a stronger saturation effect. The saturation zone is marked in grey in Figure 27 and Figure 28.

From the experimental results, it can be also seen that 3 channel QSPK-OFDM UWB exhibits better performance than the 5-channel BPSK-OFDM UWB configuration. This is due to the multi-channel effects, more intense in the five-channel configuration due to the higher number of channels and the smaller channel spacing in the BPSK configuration.

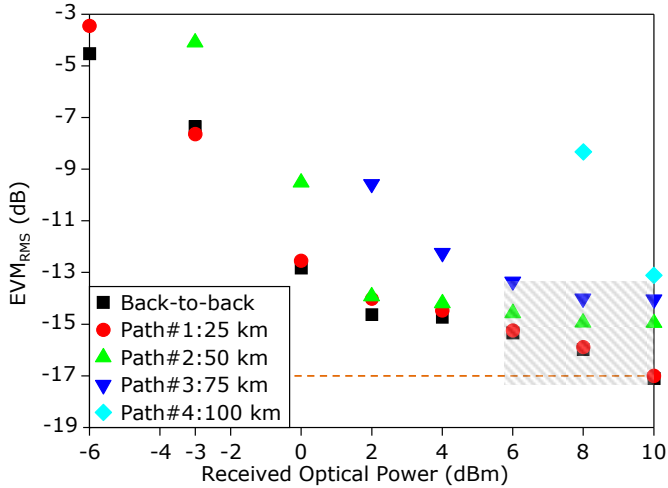


Figure 28. EVM experimental results: five channels BPSK-OFDM in B2B and after 25 km, 50 km, 75 km and 100 km SSMF. Dashed line indicates the EVM threshold and greyed area the saturation zone

From this study, we can conclude that a feasible distribution of OFDM-UWB at $EVM_{RMS} < -17$ dB [6] achieves 100 km reach in a three-channels QPSK-OFDM UWB configuration, and with 25 km reach in a five-channels BPSK-OFDM UWB configuration.

2.4.2. Impact of pilots in OFDM-UWB signals over fibre

As it was commented before in the OFDM modulation, a few subcarriers are defined as pilot subcarriers in order to estimate the wireless channel-induced distortion along the OFDM-UWB bandwidth. Thus, FTTH OFDM-UWB based networks can also use these pilots subcarriers to estimate the optical link induced distortion.

This section investigates the dependence of the reach and performance of multichannel OFDM-UWB signals over fibre transmission systems on the number of pilot subcarriers used for distortion equalization. The experiments comprise an UWB transmission system supporting 1-, 3- and 5-channel configurations. The transmission performance on four different FTTH links up to 100 km is evaluated for different number of pilot-tones.

Figure 29 shows the experimental setup used in the OFDM-UWB transmission over FTTH. This set-up generates an OFDM time domain signal employing an Agilent 6030 AWG at 1.25 GS/s sampling rate with 15 bits vertical resolution.

The OFDM signal generated follows the WiMedia ECMA-368 standard and comprises 128 carriers distributed in: 98 information carriers, 4 null carriers and a different number of pilots is allowed to evaluate the impact of the number of pilot subcarriers on the transmission performance. The carrier separation is 4.125 MHz and each carrier is BPSK modulated, giving 312.5 Mbit/s transmission bitrate.

The signal generated by the OFDM-UWB transmitter block modulates externally a continuous-wave 1555 nm laser using a MZ-EOM with 20 GHz BW at QB. In order to guarantee linear transmission in the optical fibre, the average optical power level after external modulation –point 1 in Figure 29– is set to -2 dBm.

The UWB signals are transmitted on different SSMF links ranging from 25 km to 100 km, in the same way as in Section 2.4.1: Path #1: L=25 km fibre, Path#2: L1=25 km fibre + amplification + L2=25 km fibre (50 km reach), Path#3: L1=50 km fibre + amplification + L2=25 km fibre (75 km reach) and Path#4: L1=50 km fibre + amplification + L2=50 km fibre (100 km).

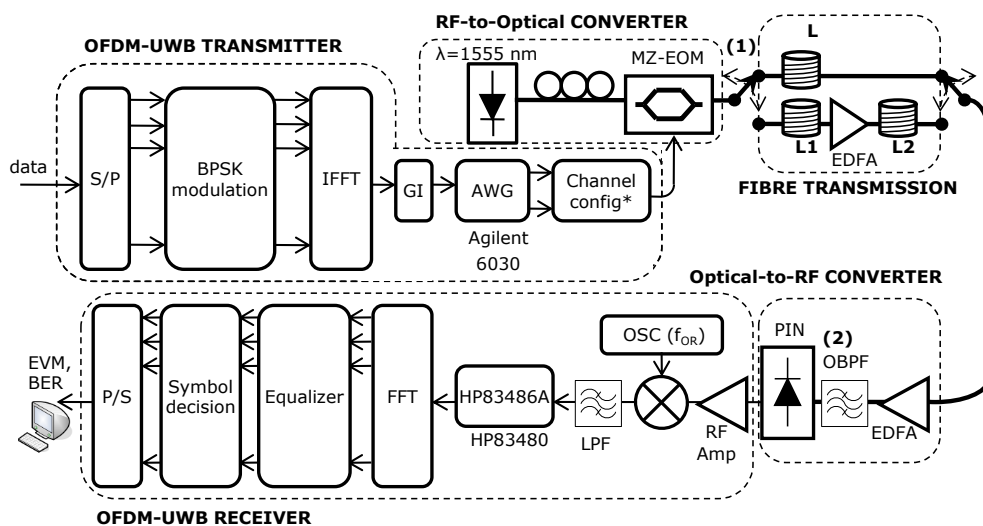


Figure 29. Experimental set-up used to evaluate the performance of OFDM-UWB signals with the number of pilots (S/P: serial-to-parallel; I)FFT: (inverse) fast Fourier transform; GI: guard interval insertion)

The amplification is done by a 23 dB gain, 4 dB noise figure EDFA (Keopsys KPS BT2C-13-LNFA). The receiver includes a 4.5 dB noise figure, 19 dBm saturation power EDFA (Exelite XLT-SFA-19).

After transmission, the signals are filtered by a 0.8 nm @ -0.5 dB optical filter and photodetected by a PIN photodiode (0.65 A/W responsivity, 50 GHz BW). In order to evaluate the performance of the UWB channel under study (CH2), the photodetected signal is down-converted to baseband with $f_{OR} = 6.5$ GHz and sampled by a digital communication analyser (DCA) HP83486A module (20 GHz BW). Once sampled, the channel under study is processed with Matlab for OFDM demodulation. The off-line processing involves: (i) removing cyclic-prefix and guard-time, (ii) fast Fourier transform to obtain the demodulated OFDM-UWB signal, (iii) equalization from pilot information, (iv) constellation construction for each carrier, and (v) EVM and BER computation.

The channel configuration block shown in Figure 29 supports three different configurations: Figure 30(a) shows the configuration for one BPSK OFDM-UWB channel transmission with a bitrate of 312.5 Mbit/s. This signal is upconverted with a mixer frequency of $f_{O2} = 6.5$ GHz. Figure 30(b) depicts the 3-BSPK OFDM-UWB configuration. Two BPSK OFDM-UWB channels are generated by the AWG and the third one is obtained from one of these ones after a delay line. The central channel is located as in one channel configuration at $f_{O2} = 6.5$ GHz. It is surrounded by two adjacent channels centred at frequencies $f_{O1} = 5$ GHz and $f_{O3} = 8$ GHz. The 3-channel configuration has an aggregated bit rate of 937.5 Mbit/s. Figure 30(c) shows the third configuration used for generating five BPSK OFDM-UWB channels. Neighbouring channels are centred at frequencies 4, 5.25, 7.75, and 9 GHz, using two up-conversion processes with initial mixer frequencies of $f_{O1} = 1.25$ GHz and $f_{O3} = 2.5$ GHz and then, the resulting signal up-converted to $f_{O2} = 6.5$ GHz. Configuration 5-BPSK OFDM-UWB has an accumulated bit-rate of 1.56 Gbit/s. The insets in Figure 30(b) and (c) show the corresponding transmitted spectrum of the 3- and 5-channel BPSK OFDM-UWB transmission respectively.

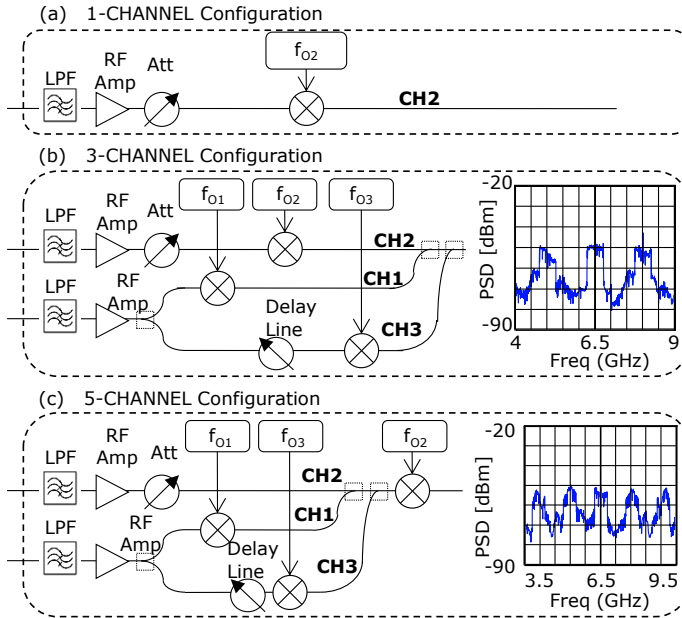


Figure 30. Channel configuration block implementation for: (a) one OFDM-UWB channel, (b) three OFDM-UWB channels, and (c) five OFDM-UWB channels, with electrical spectrum captures insets

All the OFDM-UWB up-converted signals meet the UWB mask [5]. De-correlation between the different UWB channels is guaranteed by using different DeBriujn sequences for the two channels available in the AWG6030. Configurations with 3 and 5 channels are de-correlated by electrical time delays.

The pilot-assisted equalization strategy employed in our OFDM-on-fibre experiments is based on the known BPSK modulated pilots subcarriers inserted over all the bandwidth in the OFDM signal generation. The received OFDM signal is equalized as the amplitude and phase distortion introduced by the FTTH link are predicted from pilots subcarriers.

Figure 31 shows the performed pilot-assisted equalization scheme, where $X_{\text{OFDM},i}(f_k)$ is the un-compensated k -th pilot subcarrier, $E_{\text{FTTH},i}(f_k)$ is the estimated distortion compensation transfer function of the k -th pilot subcarrier and $Y_{\text{OFDM},i}(f_k)$ is the k -th compensated pilot subcarrier, of the i -th received OFDM symbol.

$$X_{\text{OFDM},i}(f_k) \longrightarrow \boxed{E_{\text{FTTH},i}(f_k)} \longrightarrow Y_{\text{OFDM},i}(f_k)$$

Figure 31. Representation of the k -th pilot subcarrier equalization performed through the FTTH link transfer function estimation for the i -th OFDM symbol. $X_{\text{OFDM},i}(f_k)$ and $Y_{\text{OFDM},i}(f_k)$ are the k -th received and compensated pilot subcarrier, respectively, and $E_{\text{FTTH},i}(f_k)$ is the estimated distortion compensation transfer function of the k -th pilot subcarrier

Thus, the relation between $Y_{\text{OFDM},i}(f_k)$ and $X_{\text{OFDM},i}(f_k)$ is given by:

$$\begin{aligned} Y_{\text{OFDM},i} &= E_{\text{FTTH},i} X_{\text{OFDM},i} = \\ &= E_{\text{FTTH},i} X_{\text{OFDM},i} e^{j(\alpha_{\text{FTTH},i} + \theta_{\text{OFDM},i})} \end{aligned} \quad (6)$$

where $X_{\text{OFDM},i}$, $E_{\text{FTTH},i}$ and $\theta_{\text{OFDM},i}$ and $\alpha_{\text{FTTH},i}$ are the amplitude and phase response of $X_{\text{OFDM},i}$ and $E_{\text{FTTH},i}$, respectively. The dependence on the pilot subcarrier frequency was omitted to simplify the notation. Notice that $Y_{\text{OFDM},i}$ is known, as it should correspond to the known k -th transmitted BPSK pilot subcarrier. Therefore, the equalizer amplitude and phase response for the k -th pilot subcarrier can be obtained through:

$$E_{\text{FTTH},i} = \frac{Y_{\text{OFDM},i}}{X_{\text{OFDM},i}} ; \alpha_{\text{FTTH},i} = \phi_{\text{OFDM},i} - \theta_{\text{OFDM},i} \quad (7)$$

where $Y_{\text{OFDM},i}$ and $\phi_{\text{OFDM},i}$ are the amplitude and phase response of $Y_{\text{OFDM},i}$.

To obtain $E_{\text{FTTH},i}$ over all OFDM bandwidth, a linear regression of $E_{\text{FTTH},i}$ and $\alpha_{\text{FTTH},i}$ as a function of the OFDM bandwidth is performed based on least squares method. Thus, it is easily concluded that the accuracy on the channel distortion compensation can be dependent on the used pilot subcarriers number.

The performance of 1-, 3- and 5-channel OFDM transmission has been measured for the four FTTH links described in the previous section. The performance assessment is performed for the channel located at $f_{02} = 6.5$ GHz, and evaluated through the EVM of the received OFDM-UWB symbols after equalization. From EVM, the BER is obtained for the four paths described above and for different values of optical powers at PIN input (point 2 in Figure 29). These results are obtained considering different number of pilot-tones.

Figure 32 shows the BER as a function of the fibre length for the three configurations under study. This compares the results with 0 dBm received optical power for 6 and 26 pilot subcarriers. The results shown indicate that the influence of the number of pilot subcarriers is important at low BER values, as error due to un-perfect constellation rotation compensation is noticeable. Generally, including more subcarriers for pilot compensation leads to improved BER values. This improvement is more significant when only one channel is transmitted. In Figure 32 can be observed that for one channel case changing from 6 to 26 pilot equalization involves a great BER improvement.

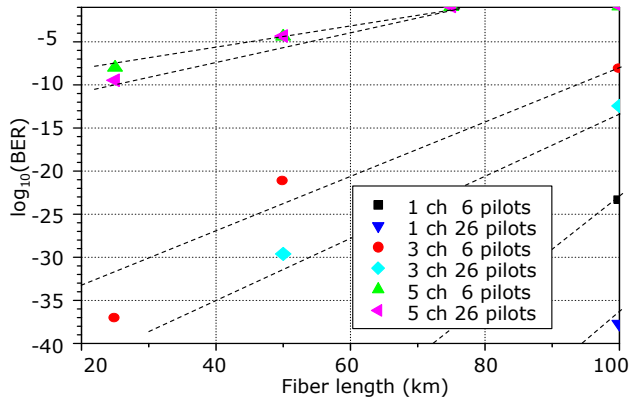


Figure 32. BER as a function of the fibre length for 1, 3 and 5 channels and different pilot compensation process for 0 dBm received optical power

This improvement decreases as the number of channels present in the system is bigger. We can conclude that if the number of channels increases, there is a point where increasing the number of pilot subcarriers does not lead to a significant BER improvement. This is due because multi-channel distortion prevails in this case.

Figure 33 shows the BER as a function of the number of pilots subcarriers used to estimate the equalizer transfer function for 5-channel BPSK OFDM-UWB configuration. The results are presented for different fibre lengths and optical received power levels. It can be concluded that the BER remains almost constant when more than 14 pilots are used to estimate the equalizer transfer function, independently of the optical fibre lengths and optical power levels. Further investigation has shown that this conclusion holds also for all received optical power levels analysed in the experimental work.

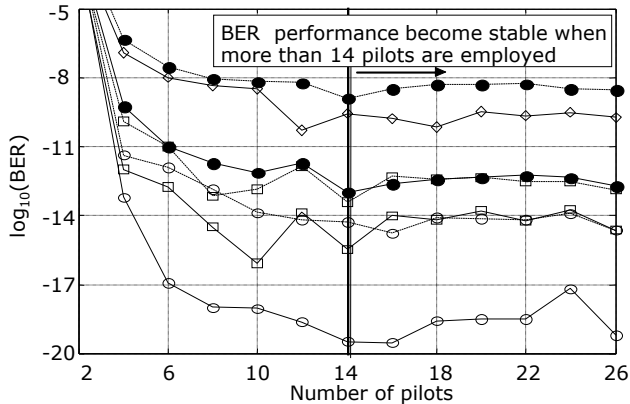


Figure 33. BER vs. number of pilots for 5 BPSK: (○)25 km, (□)50 km, (●)75 km, (◇)100 km of fibre. Continuous lines: $P_{opt}=10$ dBm, dashed 3 dBm

The experimental results show that BER values degrade when the number of pilot subcarriers is reduced. This behaviour is more important in single-channel OFDM transmission. When the multi-channel distortion increases no performance gain can be observed increasing the number of pilots transmitted. It was also shown that 14 pilot subcarriers are enough to obtain a BER of 10^{-9} for a five-channel BPSK OFDM-UWB configuration for 100 km fibre transmission.

Figure 34 shows BER as a function of the received optical power at point (2) in Figure 29 for the different configurations: (i) 1, 3 and 5 channel BPSK OFDM-UWB configurations; (ii) 25, 50, 75, and 100 km of SSMF. The results are presented considering the equalization transfer function estimated with: 6, 14 and 26 subcarriers assigned for pilot compensation. It can be observed that BER values improve as the number of pilots increases. This is due to the increased accuracy on the equalization transfer function estimation. Otherwise, BER decreases when the number of channels present in the system increases due to the inter-modulation distortion.

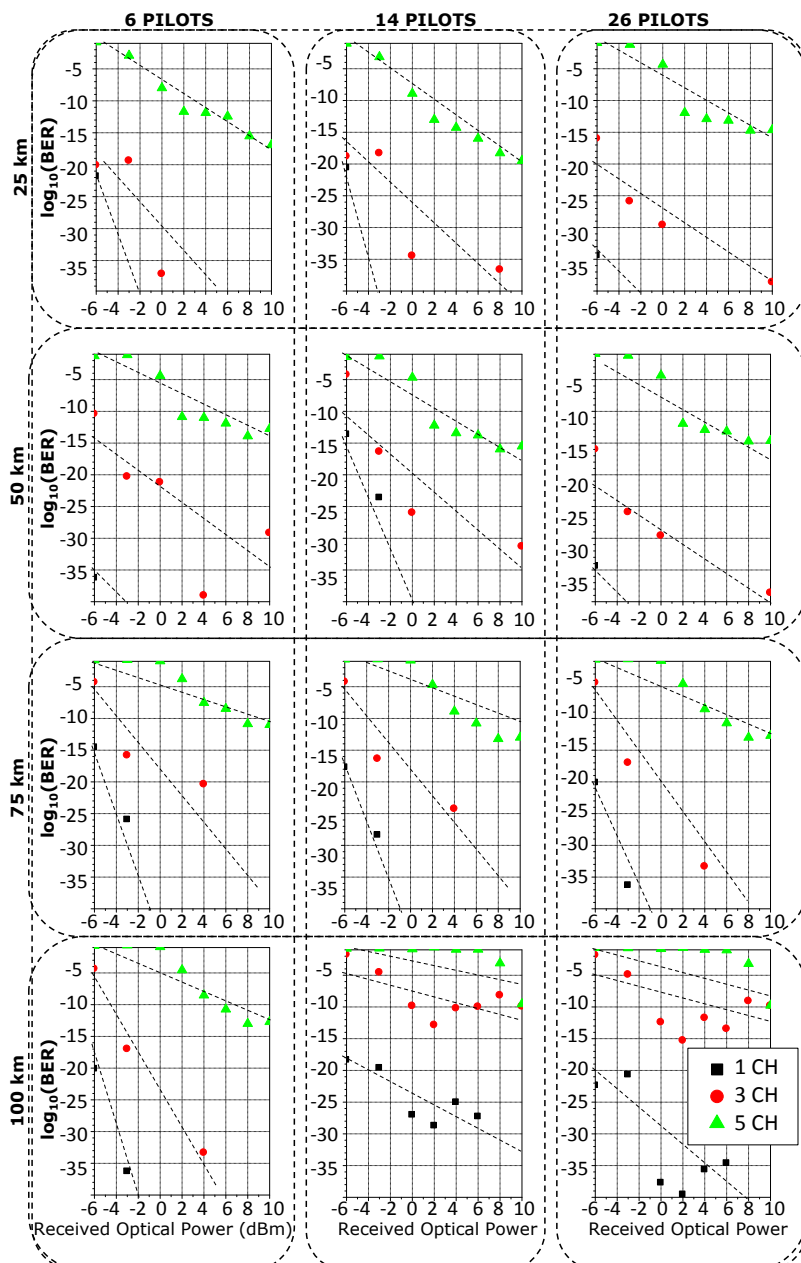


Figure 34. Experimental BER comparison using 6, 14, and 26 pilots for compensation process, for 1 channel (squares), 3 channels (circles) and 5 channels (triangles), transmitted through SSMF of 25, 50, 75 and 100 km

2.4.3. Hybrid wireless-optical access evaluation

The proposed hybrid wireless-optical access based on OFDM UWB signals is depicted in Figure 35. This figure shows an OLT located at the operator core network, typically in the central office (CO) that distributes the signal through a SSMF-based FTTH network to an optical network terminators (ONT) located at the customer premises. Depending on the transmission distance, optical amplifier sections are required in the FTTH links [65]. OFDM-UWB is especially well suited in this case as optical transmission impairments like chromatic dispersion, intra-channel nonlinear distortion and nonlinear phase noise can be compensated by electronic processing at the receiver side [66].

Two typical FTTH optical path architectures are considered: First, trunk fibre links without optical amplification with maximum reach of 25 km, and second Fibre links with inline optical amplification with maximum reach of 50 km [60].

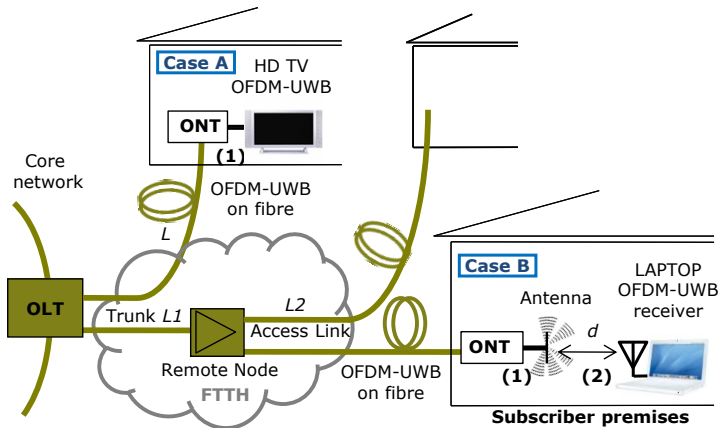


Figure 35. Proposed concept for UWB wireless-integration in FTTH networks. At subscriber premises the UWB signals are extracted and in Case A feed into an enabled receiver, and in Case B radiated to a user device

These distances exceed typical FTTH range (~ 10 km) and permit to investigate the operational limits [60]. As shown in Figure 35, after FTTH optical transmission, the OFDM-UWB signals can be photodetected at the ONT and demodulated (Case A) or, they can be photodetected, amplified, and radiated for its wireless transmission (Case B in Figure 35).

The transmission performance for Cases A and B in Figure 35 are analysed by the setup shown in Figure 36. This setup comprises two OFDM-UWB channels (named Ch 1 and Ch 2) generated with two Wisair DV9110 modules following ECMA-368 standard [6]. The bitrate of each OFDM-UWB channel is 200 Mbit/s giving an aggregated bitrate of 400 Mbit/s per user. The two OFDM-UWB channels are amplified and externally modulated by a Mach-Zehnder electro optical modulator (MZ-EOM) and transmitted through SSMF-based optical paths of $L=5, 10$ and 25 km without inline optical amplification, and $L1=L2=25$ km (total reach of 50 km) with inline optical amplification. The launched optical power is controlled by an erbium-doped fibre amplifier EDFA(CO) in Figure 36 typically located at the OLT [65]. The optical paths with 50 km reach also includes inline (IL) optical amplification EDFA(IL) in Figure 36. After optical transmission, the OFDM-UWB signal is photodetected (PIN), amplified and its error-vector-magnitude measured (Agilent DSA 80000B). The OFDM-UWB EIRP is adjusted at the ONT to -41.3 dBm/MHz, the maximum level allowed in current regulation [5]. Further wireless transmission is done by two omnidirectional patch antennas (In4Tel-omni, 0 dBi). After wireless transmission the OFDM-UWB signal is amplified and the EVM is measured again. Table 6 summarizes the main OFDM-UWB signal parameters and the device specification in the experimental work.

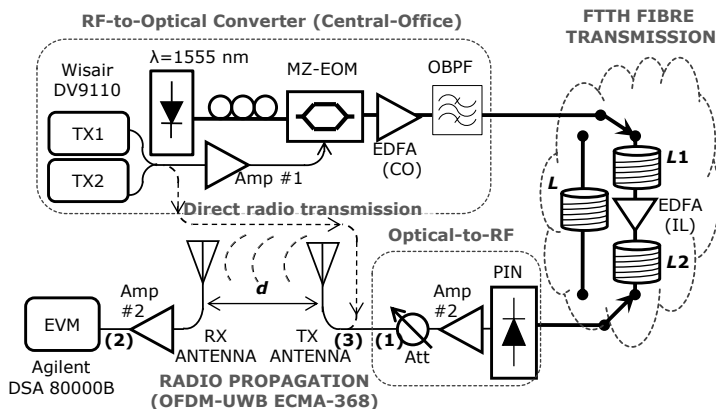


Figure 36. Experimental setup for OFDM-UWB combined performance evaluation of optical and wireless transmission in hybrid access networks

Table 6. OFDM-UWB parameters and device specifications

	Channel 1	Channel 2	Device	
Center frequency	3.432 GHz	3.96 GHz	Amp#1	G=21 dB
Bandwidth	528 MHz [6]		Amp#2	G=26 dB
Modulation	QPSK OFDM 128 carriers (6 null and 12 pilot tones)		EDFA(CO) EDFA(IL)	G=23 dB P _{sat} =13dBm
Bitrate	200 Mbit/s		Att	0-9 dB
EIRP	-41.3 dBm/MHz [5]		Antennas	G= 0 dBi

Two sets of measurements have been done to analyse Cases A and B in Figure 35: First, the EVM is measured after optical distribution before TX antenna, point (1) in Figure 36. Second, the EVM is measured after radio transmission -after RX antenna, point (2)-. The measurements consider radio distances (d) from 0 to 3 m for all optical transmission ranges.

The Case A in Figure 35 is analysed measuring the EVM of the received OFDM-UWB signal after optical transmission. The impact of the optical noise introduced by the EDFA(CO) is analysed varying the amplification level. Figure 37 shows the resulting EVM measured at point (1) in Figure 36 for both OFDM-UWB channels before radiation. Measurements have been done for four FTTH optical links (5, 10, 25 and 50 km reach) and in back-to-back (B2B) configuration (i.e. $L=0$ km) to evaluate the effect of fibre length in the system performance.

In Figure 37 it can be observed that the EVM variation at a given optical transmission distance range from -20.75 dB to -22 dB for channel 1 (Ch 1), and range from -21 dB to -23 dB for channel 2 (Ch 2). Adequate EVM values (below the -14.5 dB ECMA-368 threshold [6]) are obtained for all optical ranges measured. The results indicate that the EDFA amplification is not a limiting factor in the proposed approach for the SSMF ranges considered.

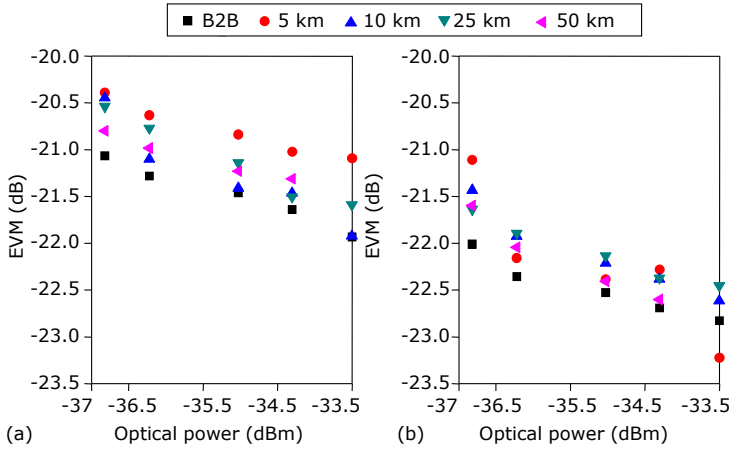


Figure 37. EVM vs. fibre vs. optical power before photodetection (a) Ch 1,(b) Ch 2

The Case B depicted in Figure 35 is analysed now. The EVM is measured after wireless radiation of the OFDM-UWB signal with and without optical transmission. The baseline performance is obtained when the signal is just radiated connected directly to point (3) as shown in Figure 36 (without using optical conversion). The EVM measured at point (2) in Figure 36 in this case is shown in Table 7 for different radio distances. Ch 2 performance is worse than Ch 1, due to the frequency response of the electrical amplifiers and antennas.

Table 7. Baseline EVM measured without optical transmission

	$d=0.5\text{ m}$	$d=1\text{ m}$	$d=1.5\text{ m}$	$d=2\text{ m}$
EVM Channel 1	-20.39 dB	-17.81 dB	-14.6 dB	-13.18 dB

It is important to note that the wireless radiated power is adjusted again in all the cases to the EIRP regulation limit of -41.3 dBm/MHz (shown in Figure 38 as a dashed line). This is done adjusting the electrical amplification by the variable attenuator shown in Figure 36. Figure 38(a) shows the power spectrum density (PSD) of the two OFDM-UWB channels under study after 25 km SSMF as an example. The corresponding spectrum (25 km optical transmission, $d=1.5\text{ m}$) is shown in Figure 38(b) for comparison. The constellations measured for each OFDM-UWB channel are shown in Figure 39. Ch 2 exhibits slightly higher distortion due to the frequency response of electrical and optical components.

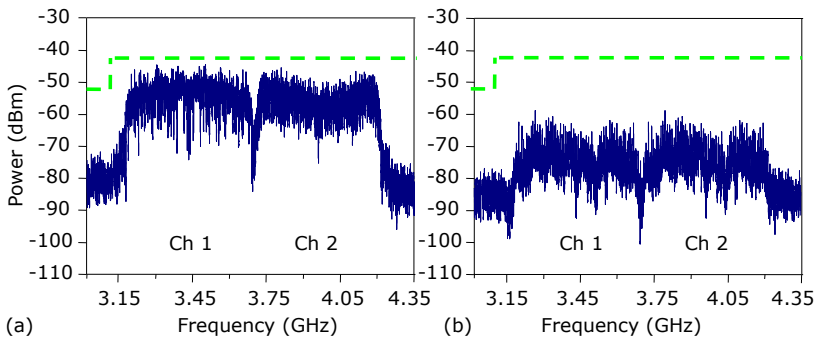


Figure 38. UWB spectrum measured (a) after 25 km SSMF transmission, photodetection and amplification –point (1) in Figure 36–; and (b) after $d=1.5\text{ m}$ radio propagation –point (2) in Figure 36– (RBW = 1 MHz)

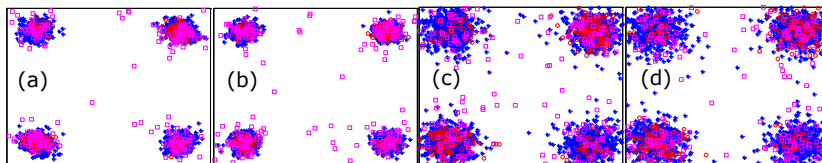


Figure 39. Received constellations for: (a) Ch 1, (b) Ch 2 after 25 km SSMF point (1) in Figure 36; (c) Ch 1, (d) Ch 2 after $d=1.5$ m radio propagation point (2) in Figure 36

Figure 40 shows the EVM measured at point (2) in Figure 36 after radio transmission from 0 to 3 meters for all optical distances considered, for a fixed optical power before photodetection of -34.3 dBm. Further study on the results demonstrated that this performance can be extended for the other optical powers employed taking into account the difference depicted in Figure 37. The EVM threshold is marked as a dashed line. In this case, the EVM remains almost constant for all the optical transmission distances. Therefore the optical path is not a limiting factor of the proposed approach in this case.

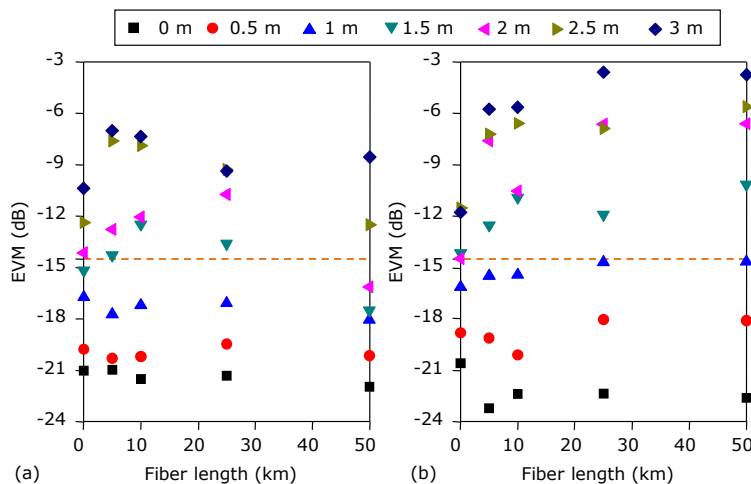


Figure 40. EVM vs. wireless distance vs. fibre length transmission with optical power before photodetection of -34.3 dBm for (a) Ch 1 and (b) Ch 2

Figure 41 shows the EVM measured for the same wireless radio distances. The EVM threshold is reflected in a wireless range for Ch 1 of 2 m (after 5 km of SSMF), 1.5 m (after 10 km SSMF), and 1 m in any other optical path configuration. For Ch 2 only B2B configuration reaches 1.5 m wireless distance and 1 m radio is achieved in any optical path configuration. Fibre propagation degrades the UWB signal to noise ratio (SNR) imposing a maximum wireless reach penalty of 1 m (from the limit of 2 m in B2B configuration to the reach of 1 m for 50 km SSMF).

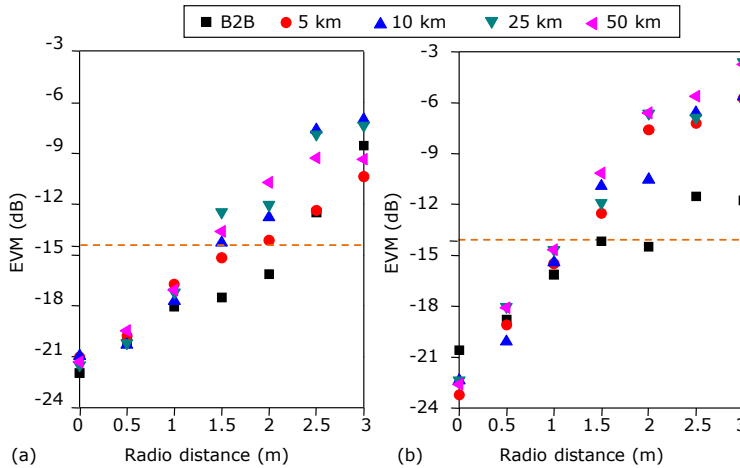


Figure 41. Measured EVM vs. radio distance from 0 to 3 meters with optical power of -34.3 dBm for different FTTH configurations (a) Ch 1 and (b) Ch 2

Comparing the results in Figure 41 with the baseline wireless transmission performance reported in Table 7, it can be observed that the worst-case EVM degradation introduced by optical transmission is 2.13 dB for Ch 1 (radio distance 1.5 m, 25 km SSMF) and 2.5 dB for Ch 2 (1.5 m radio distance, 50 km SSMF). The penalty results are summarized in Table 8. This EVM penalty comes from the optical noise, as in the extreme case of 50 km optical transmission, the optical amplification required is very high (about 18 dB).

Table 8. EVM penalty due to optical transmission

L (km)	CH1 $d=1.5$ m	Directly radio EVM= -14.6 dB	CH2 $d=1.50$ m	Directly radio EVM= -12.72 dB
5	-15.17 dB	-0.58 dB	-12.52 dB	0.19 dB
10	-14.2 dB	0.32 dB	-10.92 dB	1.80 dB
25	-12.47 dB	2.13 dB	-11.90 dB	0.81 dB
50	-13.61 dB	0.98 dB	-10.15 dB	2.57 dB

With this first experiment, it has been demonstrated the successful distribution of standard compliant (ECMA-368) dual-channel OFDM-UWB providing 400 Mbit/s bitrate per user with 0.38 Bit/s/Hz spectral efficiency over 5, 10, 25 and 50 km SSMF-based FTTH paths without dispersion compensation.

2.5. Polarization division multiplexing radio-over-fibre over PON

This Section analyses the distribution of polarization-multiplexed UWB (PM-UWB) signals as a suitable technique for the provision of wireless connectivity to a large number of users. This technique exhibits the following advantages: (i) It is capable of providing Gbit/s connectivity using a full standard UWB low-cost receiver. (ii) As UWB is a low cost technology, there is a reduction the overall network deployment costs. (iii) OFDM UWB is especially well suited to un-compensated and un-amplified passive optical access networks. (iv) A high spectral efficiency is feasible, and (v) user capacity is doubled compared with UWB on a single wavelength. The maximum transmission reach of the proposed PM-UWB technique is also investigated in this section.

In this experiment we investigate the expected transmission performance when PM is used in a sub-carrier multiplexed (SCM) optical transmission system with multi-user OFDM-based UWB signals. The experimental study herein presented addresses long-range passive optical access networks of more than 20 km reach in order to meet common PON requirements [68]. The evaluation of multi-user OFDM-based transmission in SCM is performed using polarization multiplexed systems. A multi-user UWB transmission is assessed considering up to three UWB channels per SCM.

The user data is generated following WiMedia standard by commercial low-cost transmitters using different multi-user configurations depicted in Figure 42 based on different time frequency codes (TFC) from the ones defined by ECMA-368 standard shown in Table 3. This experiment evaluates the first three UWB channels from 3.1 to 4.8 GHz used by the devices available in the market. For example, a three-user scenario employs UWB working with fixed frequency, each user with one channel of 200 Mbit/s with TFC5, 6 and 7 respectively as shown in Figure 42. Using PM we are able to double the capacity for each user and the spectral efficiency. In addition, we should point out that this sort of simultaneous TFC transmission could not be possible without using PM as the receiver would not be able to separate both transmissions. Nevertheless, perfect orthogonality is not feasible in PM systems employing commercial polarization splitters so the effect of cross-polarization in the transmission is analysed.

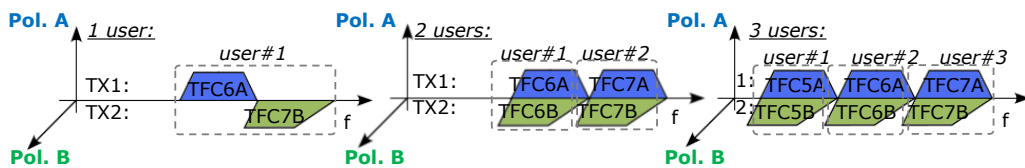


Figure 42. SCM-UWB multi-user configurations using two polarizations

Figure 43 shows the experimental setup where the central office transmitter generates a single wavelength at 1555 nm. The multi-user UWB signal is amplified (Picosecond 5865) and modulated at quadrature bias point on orthogonal polarizations by two MZ-EOM. The modulated signals at points (1) and (2) in Figure 43 are adjusted with polarization controllers (PC) to orthogonal states of polarization (SOP): horizontal and vertical (Pol. A and Pol. B, respectively). Both orthogonal lights are combined by a polarization beam combiner (PBC). The PM UWB signal is boosted by an EDFA (Amonics 30-B-FA) at the output of the central office and launched through a PON based on SSMF with different reach ($L=5, 10, 25$ and 50 km). These lengths correspond to distances expected in PON access [68].

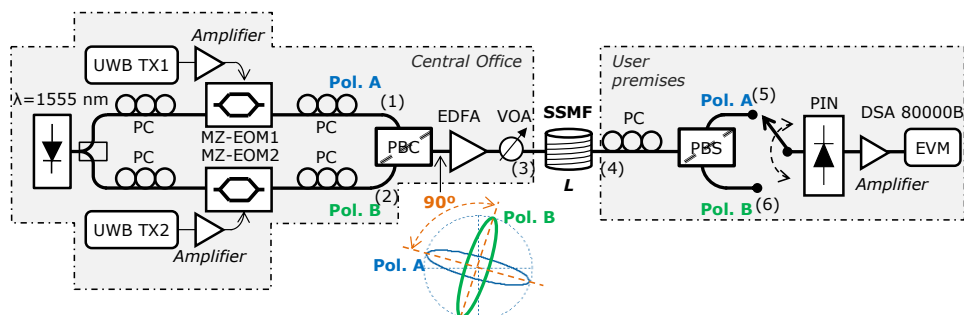


Figure 43. Experimental setup for SCM-UWB transmission with polarization multiplexing

The PM-UWB signal is received at point (4) in Figure 43, where the two polarizations are split, photo-detected, filtered, amplified and should be radiated to the final user. No demodulation or up-conversion stages are required with this technique.

The receiver at customer premises employs a polarization controller (that in an on-the-field deployment would be automatic) and a polarization beam splitter (PBS). Each PM-UWB polarization is detected with a PIN photo-detector (0.7 A/W responsivity), amplified and feed to a digital signal analyser (Agilent DSA80000B), to evaluate EVM in each OFDM UWB channel.

The polarization ellipses are shown in Figure 43 inset, measured with an optical polarization analyser (Optellios PS2300). The degree of polarization (DOP) parameter is 99.06% for Pol. A and 98.98% for Pol. B. The ellipticity of both polarizations is 0.22 with 90° difference in its orientation.

The residual polarization crosstalk has been measured for both polarization paths as shown in Figure 44. The cross-polarization crosstalk is obtained measuring the received electrical spectrum when the UWB signal is only travelling over each polarization. Figure 44(a) shows the corresponding spectrum at the receiver measured at point (5) in Figure 43 with $L=10$ km when a three users' UWB communications are being provided in Pol. A. The received spectrum in the same output of the PBS (point (5), $L=10$ km) but when the UWB signal is over Pol. B (Pol. A is off) is also measured. It can be observed that the cross-polarization discrimination is 30 dB for Pol. A. The crosstalk produced by Pol. A is measured in -78 dBm over a -82 dBm noise floor. This 4 dB crosstalk will interfere over the received signal and its effect is analysed in the next Section. The same is done in Figure 44 for Pol. B (point (6)) obtaining a higher polarization discrimination of 33 dB due to the characteristics of the PBS. The crosstalk produced by Pol. B is also of 4 dB over the noise floor.

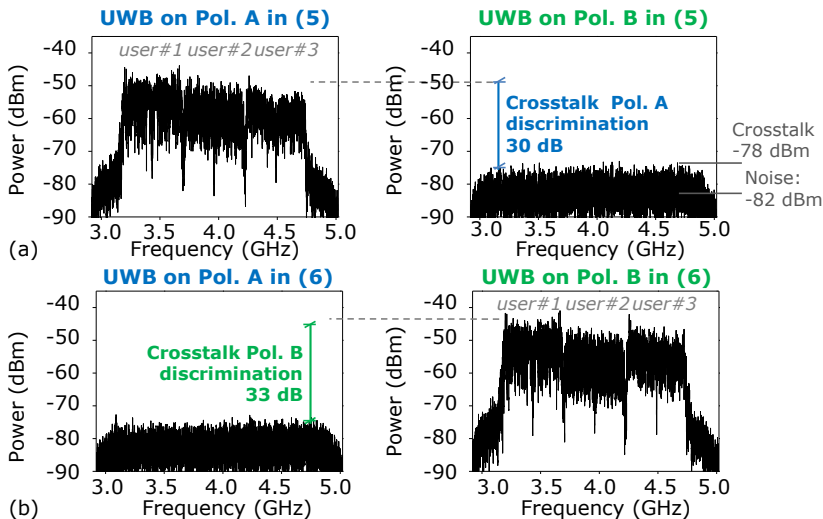


Figure 44. Cross-polarization residual measurements after 10 km of SSMF with RF-spectrum for both polarizations at: (a) point (5), (b) point (6) of Figure 43

2.5.1. Effect of multi-channel PM-UWB

Taking into account the cross-polarization over the received signal, the effect of channel aggregation and inter-channel distortion in multi-user operation is evaluated for PM systems. Figure 45 shows the EVM of the received PM UWB signal for each multi-user configuration at different fibre lengths L employing the experimental setup shown in Figure 43. The ECMA-368 EVM limit of -14.5 dB [6] is represented as a dashed line.

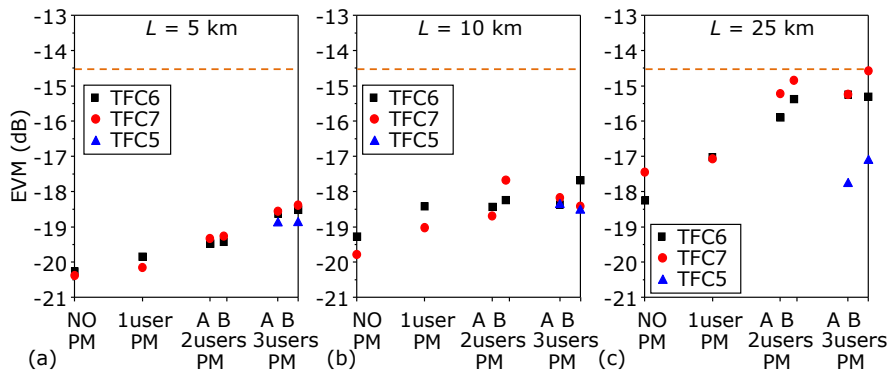


Figure 45. PM-UWB EVM performance of each UWB channel in different multi-user configurations (Figure 42) vs. L : (a) 5 km, (b) 10 km, (c) 25 km

In this case, the EDFA level is adjusted to maintain an optical power of 8 dBm at the output of the fibre for a fair comparison. For short distances ($L=5$ km) we can observe that when passing from no PM to one user PM the distortion is only 0.35 dB in TFC6. When adding a second user (co-channel interference) the EVM is 0.42 dB worse than a single user with different TFC per PM. Finally, transmitting the three-user channels the EVM in TFC6 is -18.52 dB (0.91 dB worse than two users PM).

For longer distances (25 km) the EVM penalty is of 1.2 dB from no polarization to single user PM and of 3 dB to three users PM. Symbol degradation can be seen in the QPSK constellations in Figure 46.

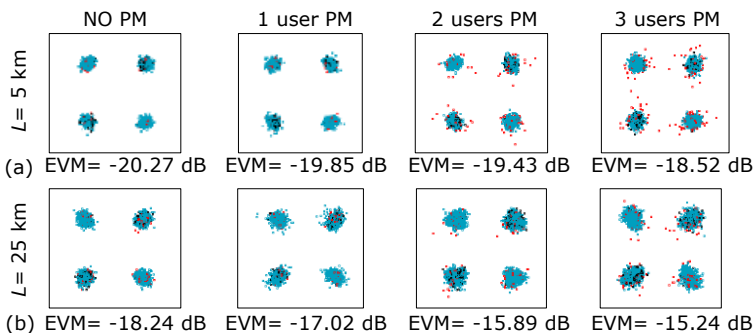


Figure 46. Constellations of the center channel TFC6 with different multi-user configurations using or not PM for L : (a) 5 km, (b) 25 km

2.5.2. Maximum reach evaluation for UWB signal transmission

Once evaluated the effect of multi-user transmission, the SCM-UWB performance after L km repeater-less optical transmission in PM networks is studied using different launch power levels. The experimental setup was shown in Figure 43, where a VOA at point (3) is used to change the launch optical power level (from -3 to 7 dBm) from the central office using a fixed EDFA pump level (keep the same noise conditions). The three first UWB channels are transmitted (3 users configuration in Figure 42) each one at 200 Mbit/s. In order to evaluate the penalty induced by using the proposed polarization multiplexing technique for UWB radio over fibre distribution, the UWB performance of the three-user configuration over the same setup using single polarization (only one path, for instance points (1) and (5)) is evaluated. This is shown in Figure 47 for $L=25$ and 50 km. The

opened blank symbols represent single polarization (No PM) to be compared with the EVM results obtained at both polarizations with a three-user transmission in PM.

The results indicate that the SCM-UWB multi-user signal transmitted on both polarizations achieve successful communication (EVM under -14.5 dB [6]) for each user/TFC over PON distances up to 25 km. But a reach of 50 km SSMF can not be achieved as seen in Figure 48. So, the reach of the proposed system is estimated in 25 km using a launch power level from the central office above 5 dBm. This reach is adequate for typical PON networks deployments [68] and it is obtained without impairments compensation techniques or inline regeneration stages between the central office and user premises achieving 0.76 bit/s/Hz spectral efficiency.

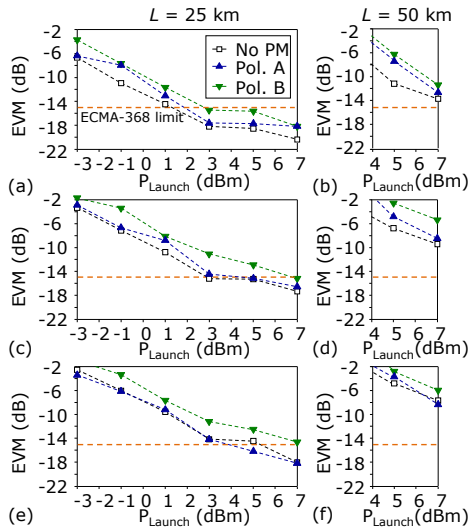


Figure 47. EVM performance using PM measured after 25 and 50 km SSMF for: (a-b) user#1 TFC5, (c-d) user#2 TFC6, (e-f) user#3 TFC7

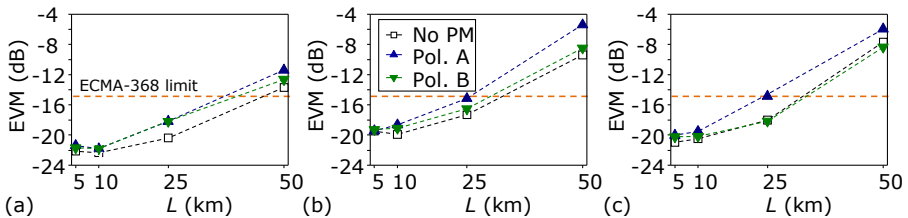


Figure 48. EVM performance using PM measured for different fibre lengths using 7 dBm optical launch power for: (a) user#1 TFC5, (b) user#2 TFC6, (c) user#3 TFC7

Comparing the results obtained with PM to the ones with single polarization (No PM), it can be observed that the interference between orthogonal polarizations induces a maximum penalty of 5.5 dB when the launch power level is below 0 dBm, and less than 2.4 dB if it is above 3 dBm.

Successful PM UWB transmission is feasible up to 25 km SSMF for launch power levels from the central office above 5 dBm, without loss or dispersion compensation, achieving a better EVM than -14.5 dB ECMA-368 threshold in all the UWB user's channels with 0.76 bit/s/Hz spectral efficiency.

2.5.3. Distribution of different OFDM-based services using polarization multiplexing

In this section the joint distribution of UWB and WiMAX radio over SSMF employing a polarization-multiplexing scheme is proposed and analysed [Per09a]. Different single- and orthogonal-polarization schemes are evaluated aiming to minimize the UWB and WiMAX mutual interference when distributed through SSMF and no amplification or transmission impairment compensation techniques are employed. Moreover, the impact of the optical transmission in the radio path for this PON distribution system is also investigated.

WiMAX is a wireless transmission technology targeting medium- to long-range data communications at bitrates up to 12 Mbit/s. WiMAX is expected to replace large wireless local-area network installations, e.g., University campus, commercial areas, etc. Comparing the bitrate and expected range, WiMAX and UWB are complementary radio technologies expected to coexist in a near future.

The transmission of UWB radio for audio/video distribution was first proposed for FTTH networks with optical amplifier sections in [Llo08a], where a single wavelength signal without polarization multiplexing is distributed per user. Since UWB can be regarded as a low cost technology, a reduction of the overall network deployment costs is expected. Another advantage arises from the use OFDM UWB as defined in WiMedia UWB, which is especially well-suited for un-compensated and un-amplified PONs. Nevertheless, OFDM-UWB and QAM-WiMAX modulation formats require higher linearity on the radio-over-fibre distribution system than less complex modulations, such as on-off keying (OOK) modulation [69]. UWB and WiMAX coexistence on low-cost multi-mode fibre (MMF) was reported in [49] for indoor applications. In this case, a single wavelength signal without any polarization multiplexing technique was employed.

The novelty of this work is the joint distribution of UWB and WiMAX radio-over-fibre using polarization-multiplexing. Two different orthogonal-polarization multiplexing schemes are studied targeting to reduce the mutual interference when UWB and WiMAX are distributed jointly through SSMF without transmission impairments compensation techniques and amplification. The proposed technique for joint UWB and WiMAX radio distribution in PON is depicted in Figure 49.

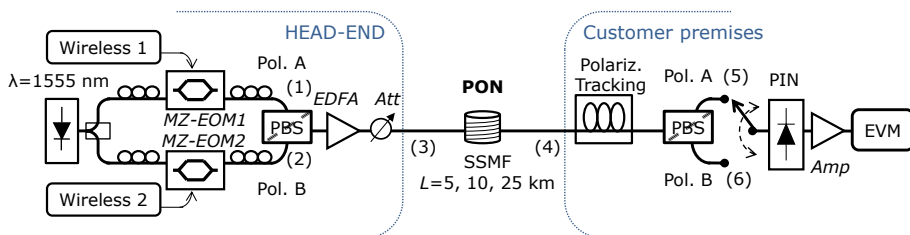


Figure 49. Evaluation setup for joint wireless services distribution by polarization multiplexing in hybrid radio-fibre on PON

Figure 49 shows a head-end node (central office), which can generate standard UWB and WiMAX wireless signals, indicated as generic Wireless-1 and Wireless-2 blocks in the figure. These radio signals are typically converted to the optical domain by external modulation. Both optical signals, after polarization adjustment, are combined by a polarization beam splitter/combiner (PBS) and distributed through a SSMF-based optical access network to a given number of subscribers. At the subscriber premises, the optical signal is adjusted in polarization to match the slow and fast axis of a reception PBS in order to separate the two orthogonal polarizations.

Once each polarization is split, the individual wireless signals are photodetected, filtered, amplified and directly radiated to the users present at the customer premises. This approach benefits from the high bitrate capabilities of UWB, supporting bitrates up to 1 Gbit/s at a few meters range, which can be extended to 30 m by multiple-input multiple-output (MIMO) processing [7].

The approach depicted in Figure 49 permits a high spectral efficiency. Two polarizations are distributed per user, each one carrying UWB or WiMAX radio. Multi-user operation can be implemented by WDM and/or SCM techniques [70]. In our system, simultaneous UWB and WiMAX transmission in a single channel is analysed for demonstration purposes. Both transmitted UWB and WiMAX signals are based on OFDM modulation with a spectral efficiency of 0.3788 bit/s/Hz and 0.634 bit/s/Hz, respectively. As shown in Section 2.5.2, this spectral efficiency is almost doubled when the polarization multiplexing technique is introduced.

Three different polarization strategies are analysed for the joint distribution of UWB and WiMAX radio in this section. These strategies are depicted in Figure 50(a): First a co-channel polarization multiplexing strategy where the UWB signal is allocated in the first and second UWB channels [6], marked as Ch 1 and Ch 2, and the WiMAX signal is distributed in the Pol. B at the centre frequency of 3.5 GHz [71]. This is the most restrictive situation from the optical transmission point of view since UWB and WiMAX overlap in frequency but are transmitted in different polarizations. Three WiMAX bandwidths are considered (5, 10 and 20 MHz) in this case. The second strategy comprises an adjacent-channel polarization multiplexing. This approach is based on transmitting the UWB signal in the second and third UWB channels (Ch 2 and Ch 3). In this way, WiMAX and UWB mutual interference is reduced.

Figure 49 showed the experimental setup employed for the polarization multiplexing transmission. Two different wireless services can be transmitted using the polarization diversity described in Figure 50(a). The two generated signals, UWB or WiMAX, are modulated by a MZ-EOM at QB point. The UWB- and WiMAX-modulated optical signal at points (1) and (2) in Figure 49, is adjusted with a polarization controller to linear-horizontal (LH, named Pol. A in Figure 50) and linear-vertical states (LV, named Pol. B in Figure 50), and combined by a PBS to generate the PM signal. The PM signal is boosted by an EDFA (Amonics 30-B-FA) at the CO output and launched through SSMF ($L=5, 10, \text{ and } 25 \text{ km}$). The EDFA output level remains constant to not improve the noise introduced by EDFA. However, the total optical power level in point (3) in Figure 49 (optical launch power over PON) is adjusted with a variable attenuator from -3 to 7 dBm, to investigate the PM performance from the customer point of view.

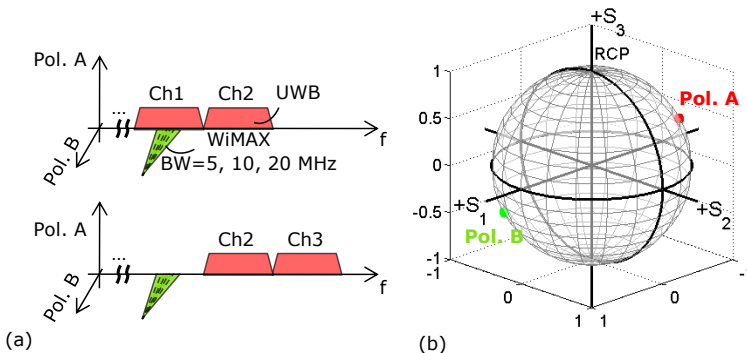


Figure 50. (a) Polarization multiplexing schemes for co-channel and adjacent-channel UWB and WiMAX transmission. (b) Polarization measurement in Poincaré sphere

The PM signal is received at point (4) in Figure 49, where the two polarizations are split, photodetected, filtered, amplified and should be radiated to the final user. No demodulation or up-conversion stages are required with this technique. At the receiver, the state of polarization is manually adjusted by a polarization controller (PC). This controller would be an automatic polarizer stabilizer in an on-the-field deployment [72]. After the PC, a PBS resolves polarization A and B (Pol.A, Pol. B) at points (5) and (6) respectively. Each PM polarization signal is detected with a PIN photodetector (0.7 A/W responsivity), amplified and analysed in order to evaluate the EVM of each signal.

In this section, UWB and WiMAX distribution over a PON fibre deployment has been studied. The first case under study is in-band coexistence, where WiMAX and UWB signals coexist on the PON fibre deployment but they are transmitted over an orthogonal polarization in order to minimize mutual interference between them. The two orthogonal polarizations shown in Figure 50 are employed in this case. The setup shown in Figure 49 is used to analyse the co-channel polarization multiplexing scheme. Wireless service 1 (in Figure 49) is a UWB signal that uses sub-band #1 and sub-band #2 (centre frequencies of 3.432 GHz (Ch 1) and 3.96 GHz (Ch 2), respectively) and service 2 is a WiMAX signal operating in the 3.5 GHz band.

The setup for wireless service 1 comprises UWB MB-OFDM signal generation by Wisair DV-9110 modules as described in the previous section. The UWB signal is generated following the WiMedia-defined UWB specification described in the ECMA-368 standard [6]. The wireless service 2 is a WiMAX signal that corresponds to a broadband wireless access (BWA) indoor terminal following IEEE 802.16e standard [11]. WiMAX utilizes scalable orthogonal frequency division multiple access (SOFDMA) QPSK modulation. The signal is centred at 3.5 GHz following the European regulation [71]. The main WiMAX signal parameters are summarized in Table 9.

Table 9. WiMAX signal parameters

Centre frequency	3.5 GHz		
Bandwidth	5 MHz	10 MHz	20 MHz
FFT-points	1024		
Subchannel spacing	5.46875 kHz	10.9375 kHz	21.875 kHz
Oversampling rate	24/28		
Guard period	1/8		
Symbol duration	182.86 μ s	102.85 μ s	57.14 μ s
Modulation	QPSK ($\frac{1}{2}$ CTC)		
Downlink Data rate	3.17 Mbit/s	6.34 Mbit/s	12.68 Mbit/s

The WiMAX signal is synthesized by software (Agilent N7615B signal studio) and generated by a vector signal generator (Agilent ESG 4483C). Three possible bandwidths (5, 10, and 20 MHz) are considered in the transmission performance measurements.

Figure 51 shows RF spectrum after 25 km SSMF transmission at point (5) and (6) of the setup depicted in Figure 49. It should be noticed that rejection ratio between pol. B and pol. A of the PBS is around 30 dB. Figure 9(a) is the RF spectrum with pol. A that comprises a 400 Mbit/s aggregated MB-OFDM UWB signal. Figure 51(b) shows the WiMAX 10 MHz bandwidth signal with pol. B.

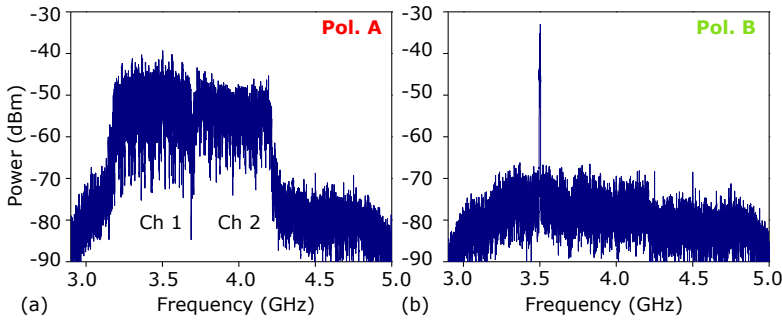


Figure 51. RF received spectrum after 25 km SSMF transmission measured with in-band coexistence in (a) point (5) pol. A, and (b) point (6) of Figure 49 pol. B (RBW = 1 MHz)

In Figure 52, the EVM measured for each wireless service (UWB, WiMAX) and for each polarization (Pol. A, Pol. B) in the co-channel polarization multiplexing configuration is depicted. EVM results for UWB signal shows that at 25 km PON transmission, the UWB EVM threshold of -14.5 dB is always accomplished [6]. Therefore, as optical launch power over fibre increases, the UWB transmission quality is improved. The EVM results shown in Figure 10(b) indicates that WiMAX distribution at 25 km PON distance is also feasible as the EVM limit recommended in the standards is always fulfilled in the experimental work.

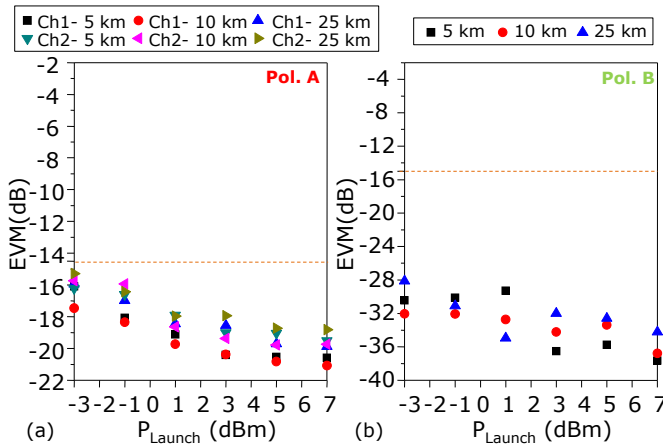


Figure 52. EVM vs. fibre length vs. optical launch power for (a) UWB Ch 1 and Ch 2 in pol. A, and (b) WiMAX (10 MHz BW) in pol. B

Next, the adjacent-channel polarization multiplexing configuration already described in Figure 50(a) is analysed. In the setup shown in Figure 49, the wireless service 1 is a UWB signal that uses sub-band #2 and sub-band #3 (centre frequencies of 3.96 GHz (Ch 2) and 4.448 GHz (Ch 3), respectively) and the wireless service 2 is the WiMAX 3.5 GHz signal described in Table 9. The two orthogonal polarizations shown in Figure 50(b) are employed in this case.

Figure 53 shows RF spectrum after 25 km fibre transmission at point (5) and (6) of the setup. Figure 53(a) shows the RF spectrum of the 400 Mbit/s MB-OFDM UWB transmission using pol. A. It should be noticed that orthogonal polarization-multiplexed WiMAX signal appears as a cross polarization residual crosstalk. Figure 53(b) is the 10 MHz bandwidth WiMAX signal in pol. B. In this case, rejection ratio between under-study signal and cross-polarization residual crosstalk is about 30 dB.

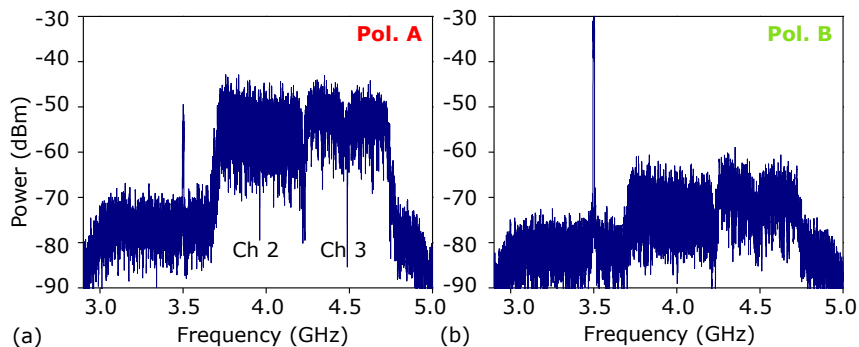


Figure 53. RF received spectrum after 25 km SSMF transmission measured with out-of-band coexistence at (a) point (5) pol. A, (b) point (6) of Figure 49 pol. B (RBW = 1 MHz)

Figure 54 shows the EVM measured for each wireless service for the adjacent-channel polarization multiplexing configuration. UWB (Pol. A) EVM results are presented in Figure 54(a) indicating that PON transmission at 25 km distance is feasible in all cases under study. However, for low optical power launch values, the EVM is close to -14.5 dB resulting in a poor transmission. On the other hand, WiMAX EVM results presented at Figure 54(b) are always under the -15 dB EVM threshold in WiMAX, demonstrating the successful transmission.

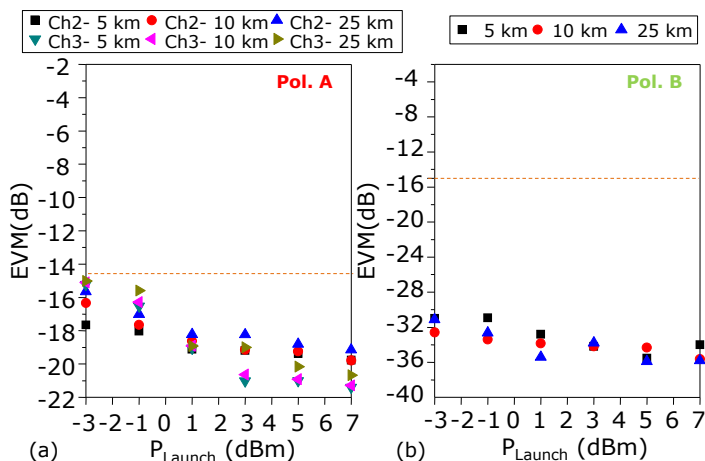


Figure 54. EVM vs. fibre length vs. optical launch power for (a) UWB Ch2 and Ch3 in pol. A, and (b) WiMAX (10 MHz BW) in pol. B

In Figure 55, the effect of different WiMAX BW on WiMAX EVM results is analysed. Figure 55(a) shows the co-channel configuration, and Figure 55(b) the adjacent channel WiMAX EVM measurements. These results confirm that adjacent-channel polarization multiplexing outperforms the co-channel polarization multiplexing scheme. This improvement is close to 2 dB EVM for each WiMAX BW. Otherwise, it should be noticed that EVM decreases with a larger WiMAX bandwidth. For example, the EVM value for WiMAX 5 MHz BW at -1 dBm optical power is close to -36 dB EVM, whereas for WiMAX 20 MHz BW at -1 dBm optical power is -29 dB EVM.

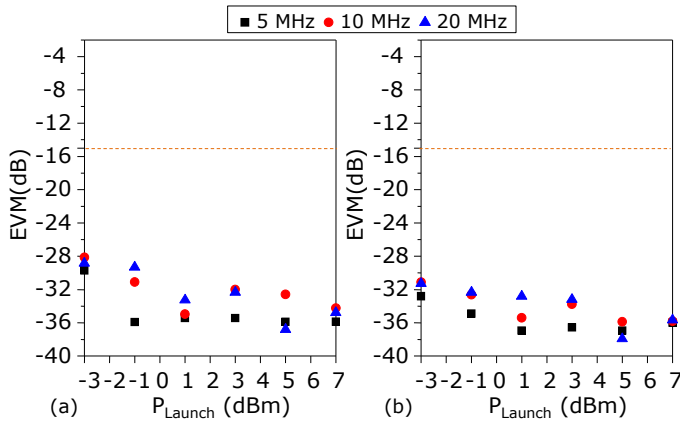


Figure 55. WiMAX EVM vs. WiMAX BW vs. optical launch power at 25 km for: (a) co-channel, and (b) adjacent channel interferer case

The study of the co-channel and adjacent channel polarization multiplexing configurations indicates that PON distances of 25 km fibre transmission are feasible and that EVM values depend on optical launch power at fibre in all the cases. However, the adjacent-channel configuration outperforms co-channel configuration in terms of EVM. This is due to the residual polarization crosstalk, which appears in band in the co-channel configuration. The same polarization crosstalk appears out-of-band in the adjacent-channel configuration, giving better performance. Comparing the EVM results with the single UWB distribution scheme presented Section 2.4.3, the co-channel and the adjacent-channel PM configurations introduce an EVM penalty lower than 2.5 dB and 1.5 dB, respectively.

2.6. Conclusion

In this Chapter the distribution of IR-UWB and OFDM-UWB signals in FTTH networks was proposed and experimentally demonstrated. The experimental results suggest that OFDM-UWB signals show better transmission performance than IR-UWB signals due to the stability with the setup components. For this reason OFDM-UWB technology was selected for further research in radio-over-fibre transmission.

Further investigation in OFDM-UWB signals was done for multi-channel transmission. Two system-level configurations have been compared from a system point of view in order to provide a given bit rate to UWB-on-fibre final user. First, a lower number (3 channels) of channels bearing a higher-order constellation (e.g. QPSK) and, second, a larger number (5 channels) bearing a lower-order constellation (e.g. BPSK). The results show better performance for the QPSK-OFDM configuration, which uses larger channel spacing and comprises a smaller number of channels occupying a smaller bandwidth.

The better performance of the 3 channel QPSK OFDM configuration compared with the 5 channel BPSK OFDM indicates that multi-channel effects can be very relevant in this technique. The optical transmission reach is limited by the chromatic dispersion to around one hundred kilometre. Dispersion compensation would be required to exceed this distance. From the experimental results, we can conclude that a feasible distribution of OFDM-UWB at $EVM_{RMS} < -17$ dB [6] achieves 100 km reach in a three-channels QPSK-OFDM UWB configuration, and with 25 km reach in a five-channels BPSK-OFDM UWB configuration.

Next, the hybrid wireless-optical transmission of OFDM-UWB signals was demonstrated in an integrated access network and further radio path. Two application cases are considered: In Case A the OFDM-UWB signal is distributed in optical domain. The OFDM-

UWB signal is photodetected, amplified and analysed. The measurements results indicate that optical transmission is not a limiting factor as the OFDM-UWB EVM threshold is always achieved. In Case B, the OFDM-UWB signal is optically transmitted and wirelessly radiated at distances up to 3 m. The experimental results indicate that 1.5 m wireless range is achieved after 10 km SSMF transmission. 1 m wireless range is achieved after 50 km SSMF. Optical transmission degrades OFDM-UWB SNR giving a maximum wireless reach penalty of 1 m (over B2B) measured after 50 km SSMF transmission. Comparing the OFDM-UWB performance with- and without optical transmission it can be observed a maximum signal degradation of 2.13 dB for Ch 1 and 2.5 dB for Ch 2 (1.5 m radio distance). This degradation is mainly due to the optical amplification (EDFA). Other factors as chromatic dispersion, reflected in the carrier suppression effect, gives 0.18 dB power attenuation after photodetection [63], not being a limiting factor for the optical transmission distances considered.

Finally, the feasibility of using polarization multiplexing in SCM multi-user OFDM-based radio-over-fibre transmission was investigated. This technique has been demonstrated with the transmission of multi-channel UWB signals over PON using polarization multiplexing. The impact of cross-polarization and co-channel crosstalk is evaluated experimentally in a three-user SCM configuration per polarization exceeding 25 km SSMF reach targeting fibre-to-the-home applications. Each SCM uses up to three UWB channels of 200 Mbit/s each in order to provide multi-user service. Employing polarization multiplexing we are able to double the data rate provided to each user.

Successful PM UWB transmission is feasible up to 25 km SSMF for launch power levels from the central office above 5 dBm, without loss or dispersion compensation, achieving a better EVM than -14.5 dB ECMA-368 threshold in all the UWB user's channels with 0.76 bit/s/Hz spectral efficiency.

CHAPTER 3. UWB RADIO-OVER-FIBRE IN IN-BUILDING OPTICAL PICO-CELL CLUSTER NETWORKS

3.1. Introduction

This chapter is dedicated to the investigation of optical distribution for pico-cell cluster network provision and also optical techniques for managing the UWB pico-cells such as high-bandwidth of analog-to-digital converters (necessary for sensing huge radio spectra such as UWB signals) and linearization techniques for maximizing the performance of a radio-over-fibre system.

FTTH technology, implemented as a passive optical network properly conditioned for UWB transmission, is expected to support other radio-over-fibre wireless technologies also employing OFDM modulation, allowing coexistence with other microwave access techniques (e.g. WiMAX). The use of a passive optical power splitting in PON is mostly preferred when large areas must be served with a larger number of users, being more economical than other point-to-point topologies. Also the easy repair of breaks in the PON reduces the network maintenance cost. A straight-forward PON implementation leads to limitations to the optical transmission reach as amplification, regeneration and impairment compensation stages are eliminated.

In Section 3.2, the in-building radio-over-fibre distribution of UWB signals for providing pico-cell cluster services in a home environment is proposed, analysed by simulation and demonstrated experimentally. Figure 56 shows the main application scenario for UWB range extension based on in building distribution. Figure 56 shows the fibre distribution inside a building connecting a distribution point to several UWB access nodes to provide service (e.g. audio and video contents) to several UWB personal area networks (PAN) pico-cells. This in-building fibre architecture aims to extend the broadband capacity offered by the access networks, i.e. FTTH networks [Llo08a].

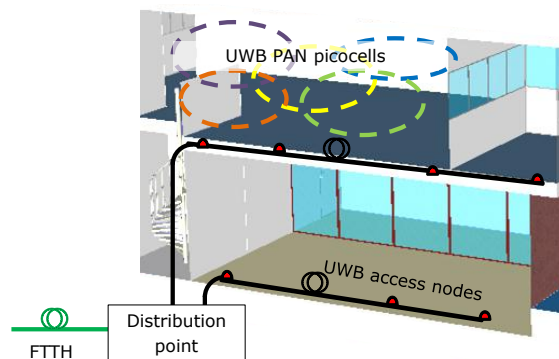


Figure 56. In-building distribution to several UWB access nodes

Once the pico-cell cluster network is active in a given area it is necessary to manage the pico-cells, which requires enhanced techniques for monitoring the huge UWB spectrum. In Section 3.3, an optical technique based on photonic analog-to-digital converters is proposed and demonstrated for sensing UWB pico-cells. As nowadays radio signal sensing technology is of special interest, the current research in wireless communications aims adaptive transmission systems where knowledge of the radio spectrum, or time signal, is required. This knowledge is used to maximize the user capacity and mitigating interference by adapting the transmitter parameters [50]. Radio sensing is also commonly used in security and public safety applications like people localisation in disaster areas. Radio sensing applications must deal with transmitters located far away, i.e. sensing extremely low power signals is of great interest.

Sensing radio signals is a challenging issue, especially when the frequency range to be covered is extremely large. This is the case of UWB radio communications, where the radio band from 3.1 until 10.6 GHz must be covered [5]. State-of-the-art electronic analog-to-digital converters (E-ADC) exhibit a bandwidth insufficient to the complete UWB band. Also UWB power levels range from -41 to -75 dBm sometimes called ultra-low power radio [75], further difficult the detection. Optical transmission techniques such as photonic analog-to-digital converters are the only technology capable of sensing ultra-low-power radio with enough bandwidth. The single-channel and multi-channel performance of photonic-ADC applied to the sensing of UWB signals is evaluated in Section 3.3.

Also, in order to be able to detect the UWB pico-cell signals in coexistence with other radio services, it is necessary to use electro-optical modulators with excellent dynamic range in a huge spectrum. For this reason, in Section 3.4, photonic techniques for linearization of electro-optical modulators are also investigated. The evaluation of different new modulators developed by Photline Technologies for high bandwidth signal transmission is studied and compared with conventional Mach-Zehnder architectures.

3.2. Optical media evaluation for in-building pico-cell provision of UWB radio-over-fibre signals

Figure 57 illustrates the fibre distribution in a home environment, where several UWB enabled devices such as laptops, televisions or telephones form different PAN pico-cells. These pico-cells obtain UWB content from the UWB access nodes located along the scenario and connected with optical fibre. This indoor distribution can be done using different media: SSMF is extensively used for long distance transmission and optical access networks, so its use for indoor distribution would be the step forward solution for all-optical interface between the access network and the in building network. MMF is commonly used for short distance communications as it is easier to install in in-building indoor environments, but efficient coupling to the access network has to be taken into account. Other types like plastic optical fibre (POF) or ultra-bendable single mode fibre (UB-SMF) [67] or multimode (UB-MMF) could be used.

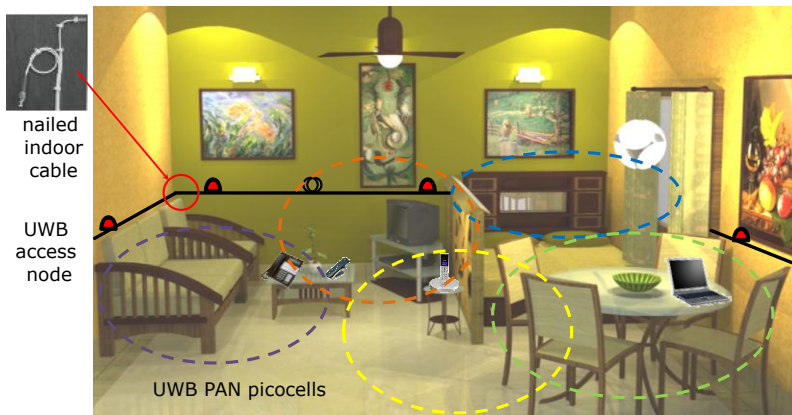


Figure 57. In-home distribution providing service to UWB PAN pico-cells

The OFDM-UWB transmission performance is evaluated by simulation and validated experimentally for short-range in building communications in Section 3.2.1. The analysis comprises the distribution of 3 MB-OFDM UWB channels (giving 0.378 bit/s/Hz spectral efficiency) over 300 m of different media: SSMF and 50 μm core MMF. In addition, in section 3.2.2 the comparison of OFDM-UWB with IR-UWB implementation is evaluated.

3.2.1. OFDM-UWB performance in in-building networks

First, a simulation study was performed to evaluate the effect of OFDM-UWB radio-over-fibre in short range networks for in-building applications comparing SSMF and MMF optical media. Figure 58 illustrates the simulation schematic used in Virtual Photonics VPI software [54] for the in building distribution approach validation. The device specifications of the modules correspond to the ones available at the laboratory. The power levels along the system are adjusted with the ones measured experimentally for a fair comparison.

The generated OFDM UWB signal shown in Figure 59 comprises 3 QPSK channels with 528 MHz bandwidth centred at frequencies 3.432 GHz, 3.96 GHz and 4.488 GHz respectively. Following ECMA-368 channelization, this signal conforms a non-frequency hopping scheme with three channels at time frequency codes TFC5, TFC6 and TFC7 respectively. This multi-channel signal is modulated on a continuous-wave optical carrier at 1555.75 nm wavelength with 13.9 dBm. External modulation is performed employing a MZ-EOM with $V_{\pi} = 1.46$ V_{DC} set in QB point. A variable optical attenuator (VOA) is used to study the link budgeted varying the launch power (P_{Launch}). Two types of media are considered: A SSMF module with 16 ps/km·nm dispersion and 0.2 dB/km losses, and a MMF module with 50 μ m core diameter and 1.45 refractive graded index. The inherent losses due to the connectors are considered in the simulation too.

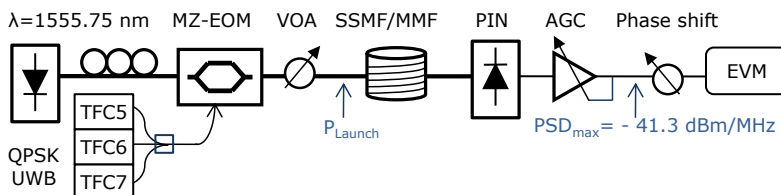


Figure 58. Simulation schematic for OFDM-UWB radio-over-fibre evaluation over SSMF and MMF

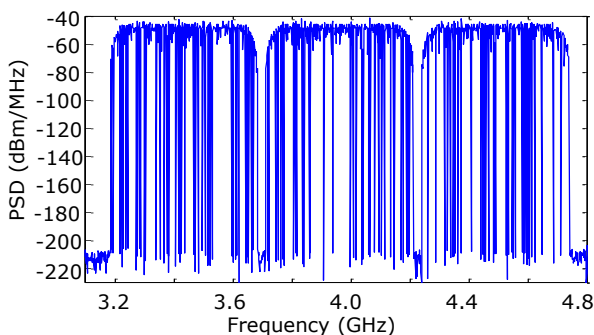


Figure 59. Simulated UWB electrical spectrum at the input of the system

After fibre transmission a PIN photodiode with 0.7 A/W responsivity is used. Once the signal is detected, the power spectral density (PSD) of the received signal is adjusted with an automatic gain control (AGC) amplifier to accomplish the UWB spectral mask set by FCC for indoor communications of -41.3 dBm/MHz [5]. The AGC amplifier takes into account the frequency response of the real amplifier used in the laboratory experiment.

MMF distribution is more sensitive to constellation rotation that is strongly dependent on the UWB channel frequency. This rotation can be solved using a phase shift. In the simulation process a phase shift module is included before demodulation to compensate the rotation of the constellation induced by MMF propagation and obtain the real EVM parameter.

Figure 60 and Figure 61 show the received electrical spectrum and demodulated constellations for each UWB channel after 300 m SSMF and MMF propagation respectively, considering a launch power of 2 dBm. It can be observed that the maximum PSD of -41.3 dBm/MHz is set for the first UWB channel in TFC5 as the other channels have lower power due to the frequency response of the electrical amplifier.

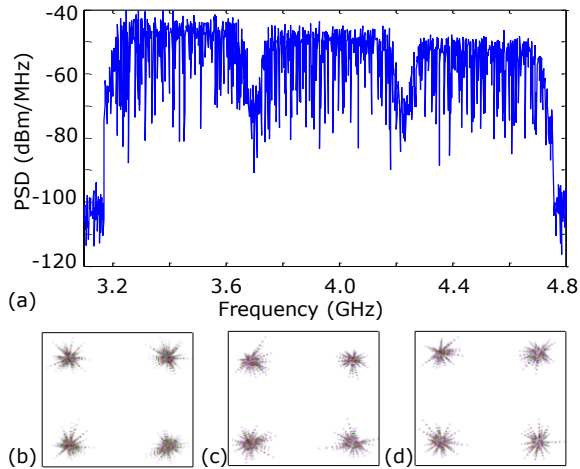


Figure 60. (a) Simulated electrical spectrum and demodulated constellations after 300 m SSMF at $P_{Launch}=2$ dBm for (b) TFC5, (c) TFC6, (d) TFC7

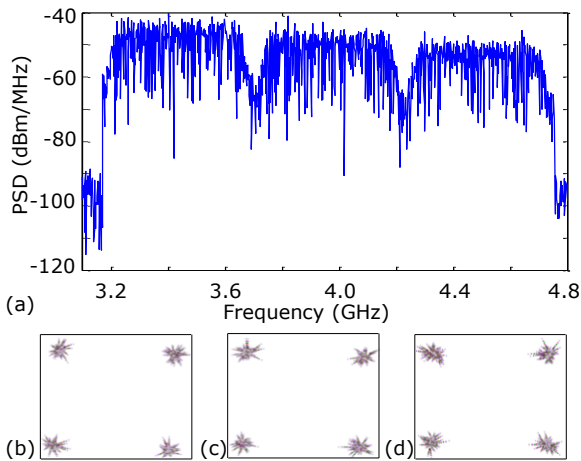


Figure 61. (a) Simulated electrical spectrum and demodulated constellations after 300 m MMF at $P_{Launch}=2$ dBm for (b) TFC5, (c) TFC6, (d) TFC7

Figure 62 describes the experimental setup used in the laboratory to validate the simulation results. The multi-channel MB-OFDM UWB signal shown in Figure 63 is generated combining the signals from 3 transmitters (Wisair DV9110) configured at 200 Mbit/s each with time frequency code TFC5, TFC6 and TFC7, as used in simulation.

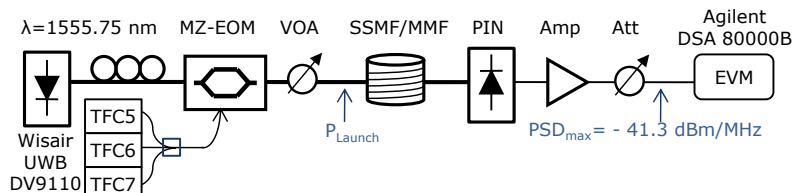


Figure 62. Experimental setup for OFDM-UWB radio-over-fibre evaluation

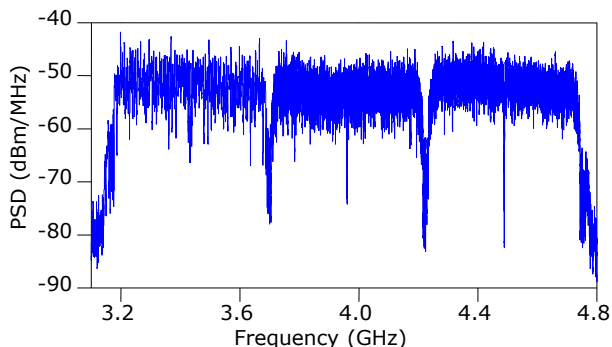


Figure 63. Experimental electrical spectrum at the input of the system (RBW= 1 MHz)

This signal is modulated with a MZ-EOM at QB. The link budget is analysed varying the launch power with a VOA from -5 to 2 dBm. After fibre transmission, the signal is photodetected properly depending on the optical media. In the case of SSMF a 40 GHz PIN photodiode with 0.7 A/W responsivity is used. On the other hand, for MMF transmission a PIN photodiode and an integrated transimpedance amplifier (TIA) are employed. Before demodulation the maximum PSD is adjusted to -41.3 dBm/MHz with an amplifier and variable attenuator as shown in Figure 62. The signal is demodulated and the EVM is measured with a digital signal analyser (DSA).

Figure 64 and Figure 65 show the experimental electrical spectrum and demodulated constellations for each channel after 300 m SSMF and MMF respectively. The considered launch power in these figures is $P_{\text{Launch}}=2$ dBm to be compared with the simulated results shown in Figure 34 and Figure 32.

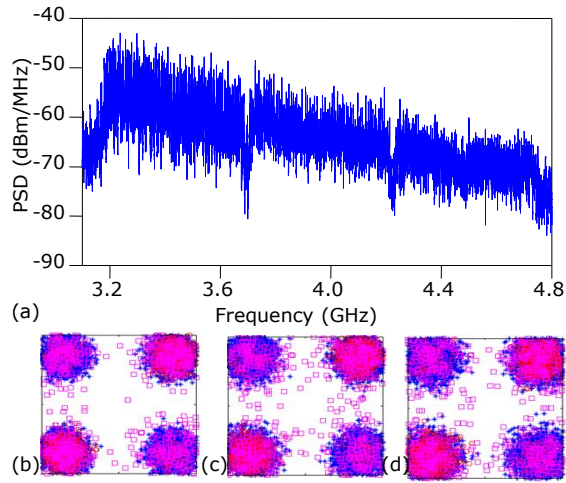


Figure 64. (a) Experimental electrical spectrum. Demodulated constellations after 300 m SSFM at $P_{Launch}=2$ dBm for (b) TFC5, (c) TFC6, (d) TFC7

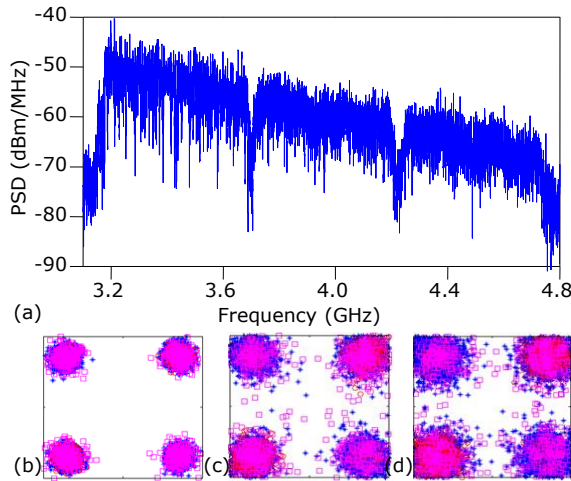


Figure 65. (a) Experimental electrical spectrum. Demodulated constellations after 300 m MMF at $P_{Launch}=2$ dBm for (b) TFC5, (c) TFC6, (d) TFC7

Figure 66 and Figure 67 show the comparison of EVM results obtained by simulation (dashed line with "sim" label) and experimentally ("exp" label) for each UWB channel and both considered media in back-to-back (B2B) configuration and after 300 m fibre.

The EVM threshold of -14.5 dB defined by ECMA-368 current regulation [6] is included as a horizontal line for reference. In both figures, the dependence of the EVM on the frequency of the UWB channel evaluated can be observed. This is due to the effect of fibre transmission and the response of the electrical devices with higher non linearities in the higher frequencies.

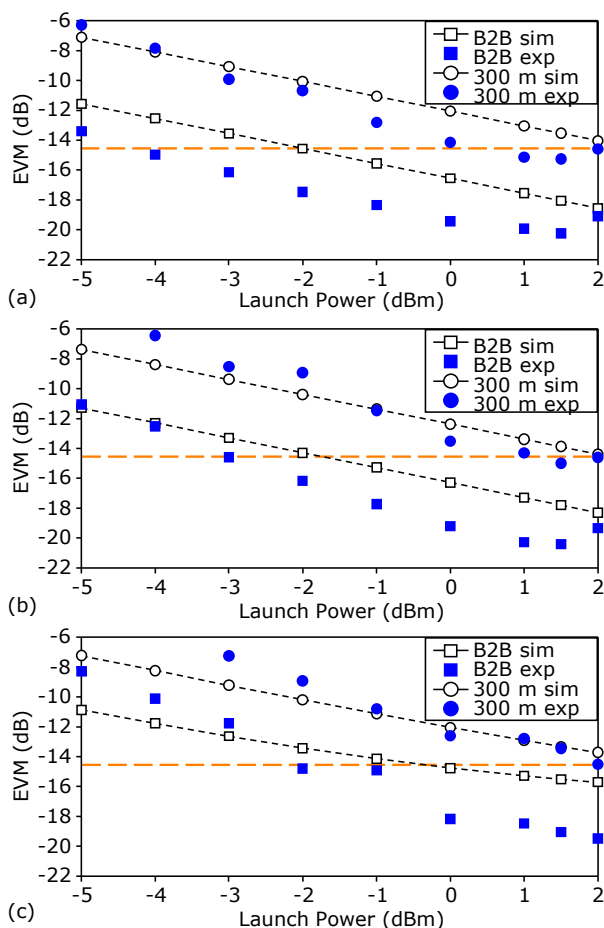


Figure 66. Experimental vs. simulated EVM results for indoor SSMF distribution as a function of the launch power: (a) TFC5, (b) TFC6, (c) TFC7

Simulated and experimental results are in very good agreement in the SSMF case as shown in Figure 66. For the MMF case, TFC6 (channel at 3.96 GHz) is the one that fits most the simulation results. For MMF propagation, simulation results (in dashed line in Figure 67) are worse than experimental, due to the phase lock used in simulation that does not correct the whole constellation rotation.

This phase error can be seen in Figure 61(b)-(d) where the constellation points are not scattered but a little rotated. The experimental data measured with DSA solve better this phase shift as can be observed in Figure 65(b).

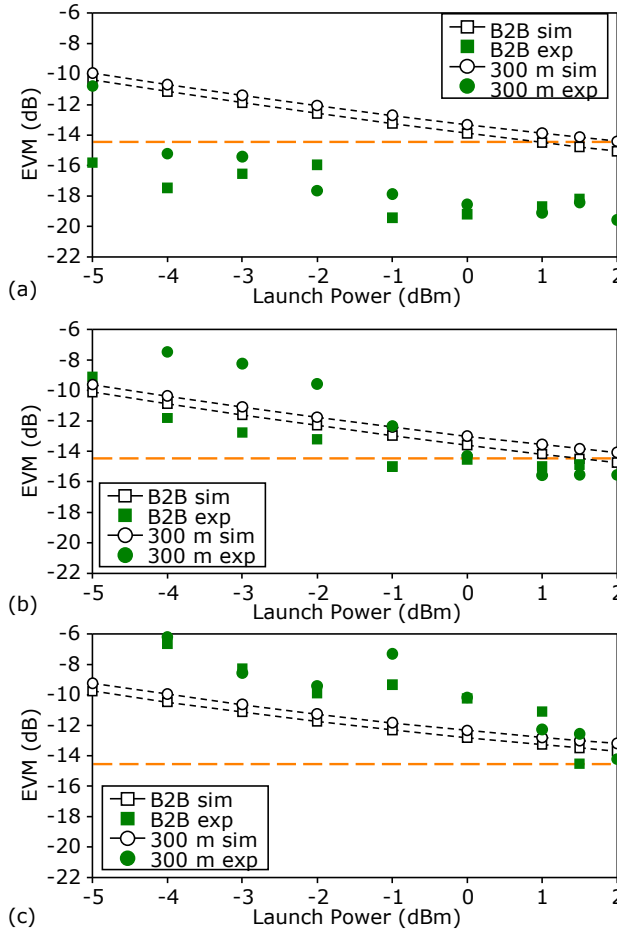


Figure 67. Experimental vs. simulated EVM results for indoor MMF distribution with different launch power for (a) TFC5, (b) TFC6, (c) TFC7

It can be observed in Figure 64 and Figure 65 that symbol mapped constellations present less dispersion in MMF than in SSMF. For this reason, in most of the cases the experimental EVM results are better in MMF than in SSMF. This is due higher power losses in the connectors of SSMF compared with the low-losses imposed by the transmission in 300 m SSMF. This effect can be seen in the difference in SSMF between B2B measurements and 300 m propagation results. This difference is much lower in the MMF case. If longer optical fibre distances were used (in the range of km), SSMF could lead to better results than MMF, but for short range communications MMF exhibits better performance.

Simulation and experimental results agree on that a typical range for in building distribution of 300 m can be reached using both SSMF and MMF media with launch power ranging from 1 to 2 dBm.

We can conclude that simulation and experimental results in good agreement point out that MMF distribution is more sensitive to constellation rotation that is very dependent on the frequency. This can be compensated using a phase shift. Once compensated, the symbol-mapped constellation presents more dispersion of the symbols in the case of SSMF, due mainly to the losses of the SSMF connectors compared with the low-losses imposed by 300 m SSMF. For higher distances, SSMF could lead to better results, but for short range communications MMF shows better performance. Both SSMF and MMF achieve ECMA-368 EVM limit of -14.5 dB at 300 m length.

Recent advances in photonic crystal and microstructure fibre suggest that tight light confinement (i.e. ultra bendable) may be possible. Transmission performance over other fibres such as plastic optical fibre (POF) or ultra-bendable SMF are evaluated in Section 4.4.

3.2.2. OFDM-UWB and IR-UWB performance in in-building networks

Following the results shown in Section 3.2.1, in this section we will compare the performance of OFDM-UWB and IR-UWB. The set-up implemented for the comparison is shown in Figure 68.

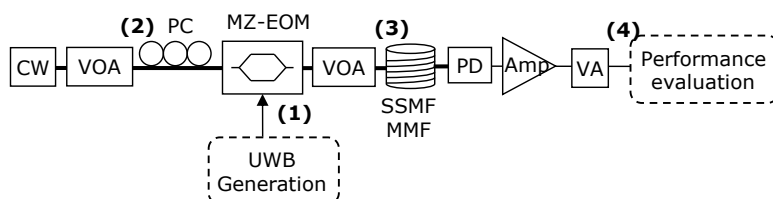


Figure 68. Experimental setup for performance evaluation of OFDM- and impulse-radio UWB distribution over fibre for indoor range

The UWB signal under study is externally modulated with a continuous-wave optical carrier at 1555.75 nm by a MZ-EOM ($V_n=1.46 V_{DC}$) working as a conventional double-sideband modulator. A VOA is employed before the MZ-EOM to adjust the power launched to the fibre by adjusting the power at point (2) in Figure 68 (from now referred as P2) emulating the launch power from the central office. The modulated signal is transmitted over fibre (SSMF or MMF) and the optical power launched to the fibre at point (3) in Figure 68 (from now referred as P3) is adjusted with a second attenuator in order to analyse the link budget. After fibre transmission, the signal is photodetected properly depending on the optical media: A 40 GHz PIN photodiode is employed for SSMF and a 7 GHz photoreceiver consisting in a PIN photodiode with 50 μm MMF pigtail and an integrated transimpedance amplifier is employed for MMF transmission. Subsequently, the power spectral density (PSD) of the photodetected signal is adjusted with an electrical amplifier (26 dB gain and 5 dB noise figure) followed by a variable electrical attenuator to accomplish, at point (4) in Figure 68, the UWB spectral mask defined in current regulation with a maximum PSD of -41.3 dBm/MHz [5].

Once the PSD is adjusted, the signal is demodulated and its performance is evaluated measuring quality parameters in each UWB implementation. Due to the different nature of the modulation of OFDM and impulse-radio signals, the measured quality parameters are different for each implementation. In the case of OFDM-UWB signals, the EVM of the received constellation is measured for each frequency channel. In order to compare with the IR-UWB signal performance, the BER is calculated from the EVM for a QPSK signal assuming Gaussian noise as [55]:

$$BER = \text{erfc}(\sqrt{2} / EVM) \quad (8)$$

The performance of OFDM-UWB signal in-building distribution is evaluated comparing with the ECMA-368 limit of 18.84% EVM [6], giving $3 \cdot 10^{-14}$ BER.

In the case of impulse-radio UWB signals, the signal-to-noise ratio (Q-factor) is measured in the eye diagrams of the demodulated pulses. BER is then calculated from the Q-factor according to equation (4). The performance of impulse-radio UWB signals in-building transmission is evaluated comparing with a typical system requirement for error-free transmission for BER of 10^{-9} . The BER limit is $2.2 \cdot 10^{-3}$ in case of incorporating forward error correction (FEC) codes.

In order to evaluate the performance of OFDM-UWB in optical fibre in-building distribution, the measurement setup shown in Figure 69 has been implemented according to Figure 68. A multi-channel MB-OFDM UWB signal is generated combining the UWB signals from three transmitters (Wisair DV9110). Each UWB transmitter is located at frequency band #1, #2 and #3 respectively from UWB band group #1, performing a non-hopping time frequency code (TFC5, TFC6 and TFC7), which enables a multi-channel MB-OFDM UWB transmission. The OFDM signal comprises 3 channels of 528 MHz bearing 200 Mbit/s each with QPSK modulation. This provides an aggregated bitrate of 600 Mbit/s and 0.378 bit/s/Hz spectral efficiency (10 dB frequency range of 3.168-4.752 GHz). The maximum PSD of the generated OFDM-UWB signal is -42 dBm/MHz. The input spectrum of the OFDM-UWB generated signal was shown in Figure 63.

The EVM of the OFDM-UWB signal transmitted through fibre is measured by the DSA after PSD adjustment to -41.3 dBm/MHz maximum at point (4) in Figure 69. EVM measurements are compared with the threshold imposed by ECMA-368 for MB-OFDM UWB successful communication [6]. BER is calculated in order to be able to compare with the impulse-radio performance.

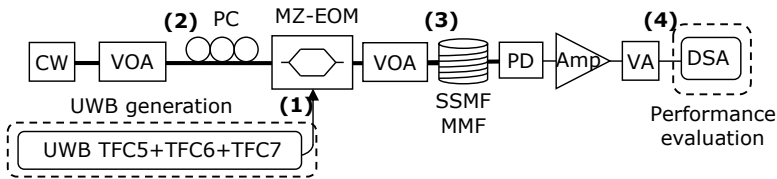


Figure 69. Experimental setup for OFDM-UWB distribution

In Figure 70, EVM results and BER calculation for OFDM over 300 m SSMF transmission are presented and compared with optical back-to-back (B2B) configuration for the SSMF photodetector at a P2 of 13.9 dBm. These results indicate that successful SSMF transmission for the three OFDM channels simultaneously is achieved at a punctual P3 of 2 dBm. However, successful communication for the first UWB channel, TFC5, is achieved at P3 from 0 to 2 dBm while for the second UWB channel, TFC6, is achieved at P3 from 1 to 2 dBm. Comparing with B2B configuration, impairments due to SSMF distribution are similar for the three UWB channels.

Figure 64 shows the MB-OFDM UWB spectrum and constellations for each channel received at DSA after 300 m SSMF fibre distribution. The frequency distortion is due to the frequency response of the attenuator employed to adjust the PSD at point (4) in Figure 69. This causes worse EVM at higher frequencies in both B2B and SSMF transmission configurations. The EVM difference among channels is higher at lower P3 because the dynamic range is lower.

In Figure 71, EVM results for OFDM-UWB over 300 m MMF 50 μ m transmission are presented and compared with B2B configuration for the MMF photoreceiver at a P2 of 13.9 dBm.

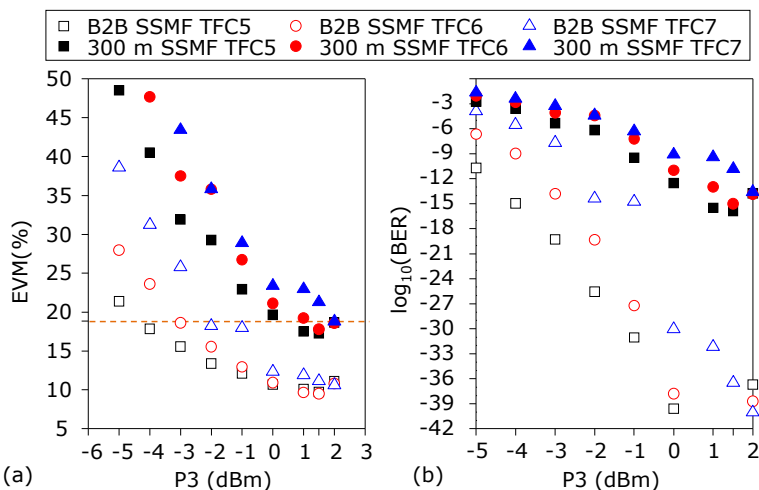


Figure 70. (a) Measured EVM and (b) calculated BER for OFDM-UWB performance after 300 m SSMF distribution. ECMA EVM threshold in dashed line

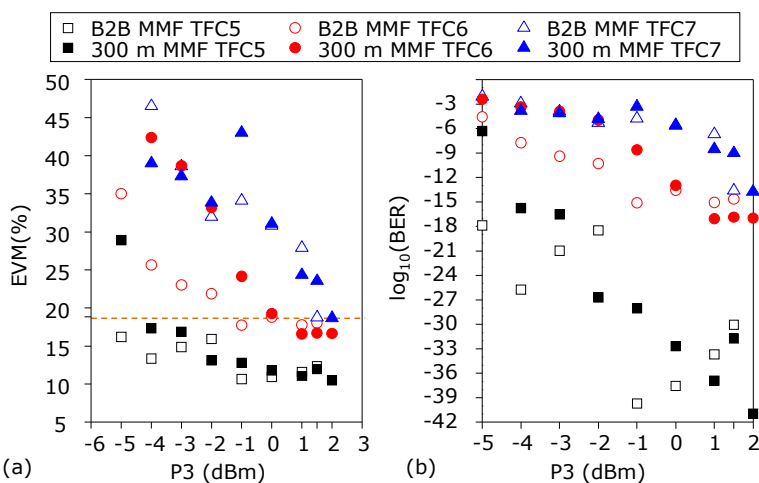


Figure 71. (a) Measured EVM and (b) calculated BER for OFDM-UWB performance after 300 m MMF distribution. ECMA EVM threshold in dashed line

The EVM results in Figure 71 indicate that successful MMF transmission is achieved at 2 dBm. However, EVM for TFC5 UWB channel enables the successful MMF transmission at P3 from -4 to 2 dBm. Successful transmission of TFC6 channel is achieved at P3 from 0 to 2 dBm. Comparing with B2B configuration, impairments due to MMF distribution are different for the three UWB channels. MMF well-known transfer function introduces attenuation and distortion increasing with frequency due to the intermodal dispersion, which is noticeable in OFDM-UWB MMF distribution where TFC7 UWB channel has worse EVM results after MMF transmission than TFC5 UWB channel.

Further measurements at P2 lower than 13.9 dBm led to worse EVM results. Also, EVM results are worse amplifying the generated OFDM-UWB signal at point (1) in Figure 69.

The experimental setup to evaluate the performance of impulse-radio UWB over fibre in-building distribution is shown in Figure 72, according to Figure 68.

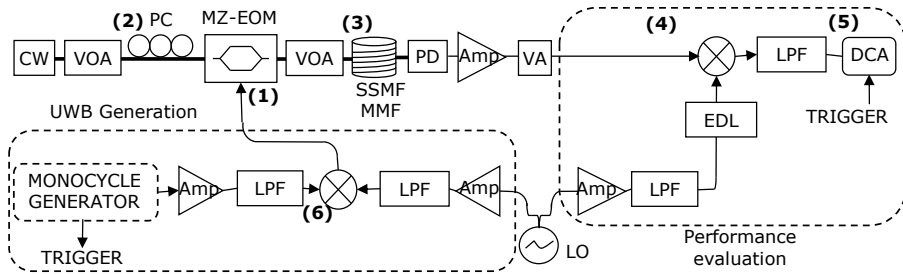


Figure 72. Experimental setup for impulse-radio UWB distribution

First, baseband monocycles are generated as shown in Figure 73 [57]. A return-to-zero data fixed sequence is generated at a bitrate of 622 Mbit/s. The modulation format employed is on-off keying (OOK) with ones and zeros equally frequent to emulate a random bit sequence. An actively mode-locked laser is employed to generate a high-quality optical pulse train at 1555.3 nm with 9.95 GHz repetition rate, 2 ps pulsewidth and 1.2 nm bandwidth (FWHM) which is intensity modulated with the data by a MZ-EOM. The data modulated optical pulses are time-stretched in 10 km of SSMF to adjust a suitable pulsewidth. Then, the stretched pulses are photodetected and amplified by a dual-output amplifier. The amplifier provides pulses of opposite polarity at the two outputs which are subsequently combined to shape monocycles. An electrical delay line is used at one amplifier output to adjust the relative delay between the two outputs. The photodetector and amplifier employed in the experiment are integrated in a dual photoreceiver with a limiting transimpedance amplifier (Teleoptix, DualPIN-DTLIA Rx). The pulsewidth, the pulse response of the photoreceiver, which is dependent on the threshold voltage controls of the limiting amplifier and the optical power applied to the photoreceiver, and the delay at the amplifier outputs are designed so that the generated monocycles exhibit approximately the same bandwidth as OFDM case, i.e. 1.584 GHz (3x528 MHz). The generated monocycles after amplification and low-pass filtering (3.3 GHz bandwidth) to remove noise are shown in Figure 73. This signal corresponds to that measured at point (6) in Figure 72.

Next, in order to meet the UWB mask in the same frequency range as OFDM case, the baseband monocycles are frequency up-converted by an electrical mixer. A local oscillator (LO) at 3.168 GHz with a power of 9 dBm (after amplification and 3.3 GHz low-pass filtering) is employed to perform the up-conversion. Thus, an impulse-radio UWB signal in approximately the same band as the three-channel OFDM signal employed before, as shown in Figure 74, is generated at point (1) in Figure 72. The impulse-radio UWB signal comprises a unique band in the 10 dB frequency range of approximately from 3.168 GHz to 4.752 GHz, bearing 622 Mbit/s and 0.392 bit/s/Hz spectral efficiency, similar to OFDM case for comparison purpose. The maximum PSD of the generated impulse-radio UWB signal is -23 dBm/MHz.

In practice, the impulse-radio UWB transmitted signal meeting the UWB mask, at point (4) in Figure 72, has to be filtered to remove the undesired frequencies before being radiated. In the experiment, at receiver, this signal is directly demodulated by down-conversion employing an electrical mixer.

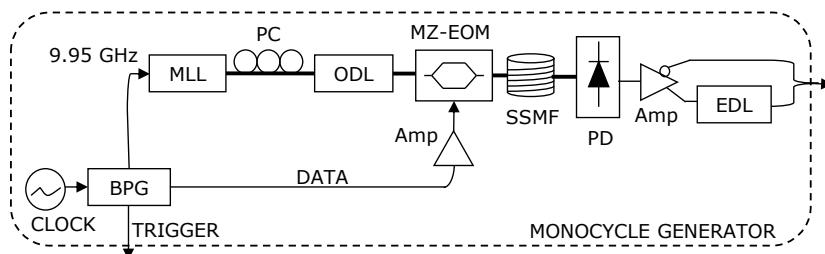


Figure 73. Baseband monocycle generator. BPG: bit pattern generator, MLL: Mode-locked laser, ODL: Optical delay line, TIA: Transimpedance amplifier, EDL: Electrical delay line

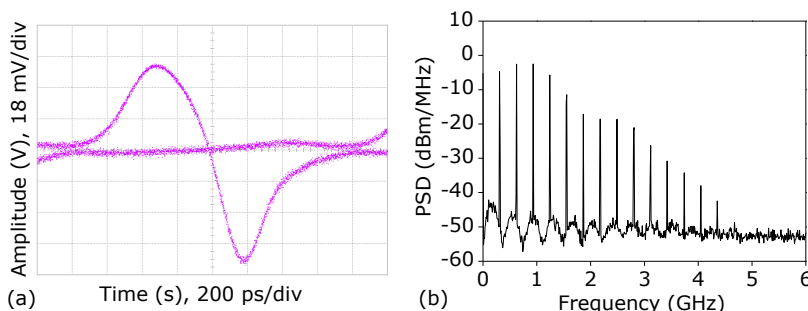


Figure 74. (a) Baseband monocycle eye diagram and (b) electrical spectrum at Figure 72 point (6)

The LO with a power of 7 dBm (after amplification and 3.3 GHz low-pass filtering) is employed to down-convert the impulse-radio UWB signal. An electrical delay line is used in the LO to fine tune the phase of the LO for accurate down-conversion. Afterwards, the down-converted signal is low-pass filtered (1.65 GHz bandwidth) and measured by a DCA (Agilent 86100C, HP83481A 12.4 GHz bandwidth). The Q-factor of the demodulated impulse-radio UWB signals is evaluated by the DCA in the measured eye diagrams.

Figure 75 shows BER results for impulse-radio UWB over 300 m SSMF transmission and for the corresponding optical B2B configuration as a function of P_2 . The results indicate that error-free transmission is achieved in the range of P_3 from -4 to 4.7 dBm; BER values maintain at P_3 in the range from -3 to 2 dBm while the higher P_3 the better BER at P_3 higher than 2 dBm and the lower P_3 the worse BER at P_3 lower than -3 dBm; BER is independent on P_2 . Comparing to B2B case, the performance with SSMF transmission improves with respect to B2B at P_3 in the range from -5 to 0 dBm. Note that at P_3 lower than -5 dBm the -41.3 dBm/MHz PSD limit is not reached and higher P_2 and/or PSD level at point (1) in Figure 72 is required to adjust P_3 higher than 4.7 dBm. Figure 76 shows the detected impulse-radio UWB pulses after 300 m SSMF distribution, measured at point (5) in Figure 72.

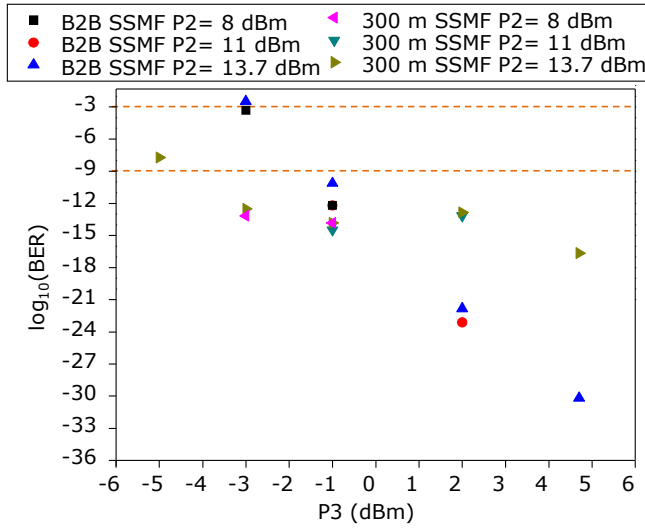


Figure 75. Impulse-radio UWB performance for SSMF distribution compared with optical back-to-back configuration. BER limits in dashed lines

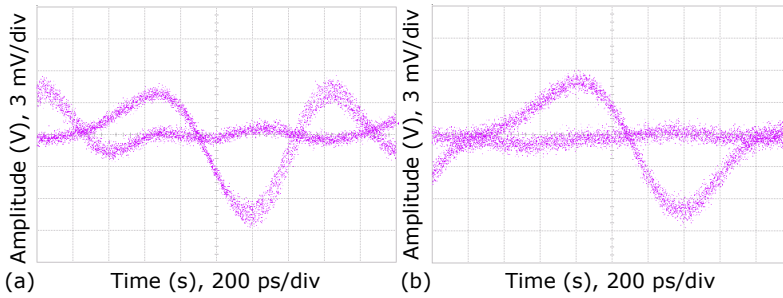


Figure 76. Eye diagrams of the down-converted impulse-radio UWB monocycles after 300 m SSMF distribution at point (5) in Figure 72. (a) P2= 13.7 dBm, P3= 4.7 dBm. (b) P2= 13.7 dBm, P3= -3 dBm

Figure 77 shows BER results for impulse-radio UWB over 300 m MMF 50 μ m transmission and for the corresponding B2B configuration as a function of P2. The results indicate that the best BER is achieved at P3 about 3 dBm for all P2 from 12 dBm to 13.7 dBm, but error-free transmission is only achieved at a P2 of 12 dBm. Comparing with B2B case, the performance with MMF transmission is always worse. Further observations are: No eye is measured in the range of P2 from 10.1 to 11.9 dBm and in the range of P3 from 2.5 to 2.9 dBm; There is an abrupt change in the eye at a P2 of 6.2 dBm and at P2 lower than 6.2 dBm the BER gets worse. From certain P3 between -1.8 dBm and 2.4 dBm there is an abrupt change in the eye at all P2 maintaining to lower values of P3, so that in the spectrum at point (4) in Figure 72 spurious frequencies appearing are more significant.

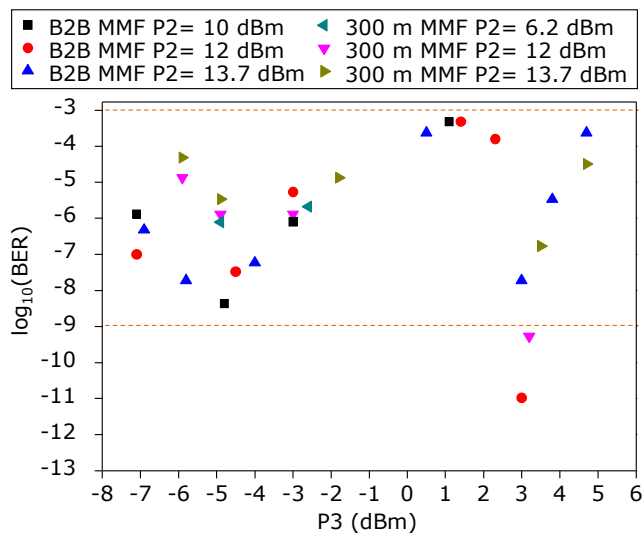


Figure 77. Impulse-radio UWB performance for MMF distribution compared with optical back-to-back configuration. BER limits in dashed lines

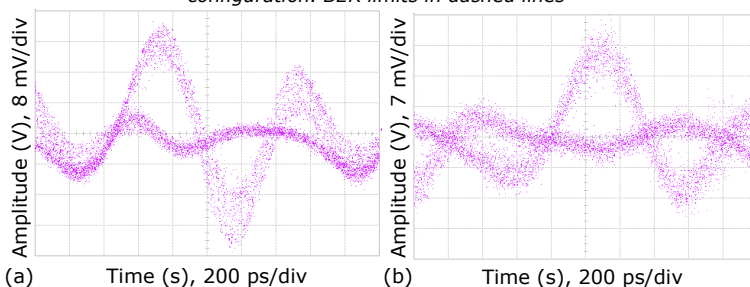


Figure 78. Eye diagrams of the down-converted IR-UWB monocycles at point (5) in Figure 72 after 300 m MMF: (a) $P_2=12$ dBm and $P_3=3.2$ dBm. (b) $P_2=12$ dBm and $P_3=-4.9$ dBm

Figure 78 shows the eye diagrams of the detected impulse-radio UWB pulses after 300 m MMF distribution, measured at point (5) in Figure 72. The BER behaviour as a function of P_2 and P_3 is ascribed mainly to the saturation of the amplifier in the photoreceiver.

Note that at other P_2 , P_3 and/or PSD level at point (1) in Figure 72, the BER behaviour is the same as that in a certain zone shown in Figure 75 but obtaining different BER values. Error-free transmission is not achieved at PSD lower than -23 dBm/MHz at point (1) in Figure 72.

3.3. Photonic-ADC architecture for sensing UWB radio signals

As it was commented in the motivation introduction of this Ph.D. thesis, another objective was the investigation of optical techniques for cognitive radio applications. Measurement of wide spectrum is typically performed using a spectrum analyser that has to be synchronized with a sampling digitizer in order to capture the entire spectrum when the signals are present.

That measurement technique requires filter sweeping and frequency down-conversion, which can be time-consuming when covering the whole frequency band. The real time spectrum monitoring proposed is based on the photonic analog-to-digital conversion and allows to achieve sampling rates larger than the Nyquist frequency and, depending on the

input signal amplitude, may achieve over 2 resolution bits compared to electronic ADC [73]. Several Ph-ADC architectures have been reported in the state-of-the-art enhancing electronic ADCs performance by using photonic techniques [74]. In Section 3.3, a time-stretching Ph-ADC architecture with engineered optical and electrical amplification is demonstrated sensing very low power signals, which is of special interest in cognitive radio applications.

Wide band real-time spectrum monitoring exhibits three key advantages over conventional narrow band monitoring: (i) instantaneous identification of potential outgoing interference, along the whole band spectrum used into the cell; (ii) due to the fast interference detection, the strict EIRP mask limits of the unlicensed services could be relaxed inside a time-slot and in the area under monitoring leading to: a increased radio path (coverage area) of the user terminals, higher throughput for high data rate services, and augment of the number of simultaneous users in the close area (cellular concept); and (iii) power-flow control techniques can be introduced for the next generation pico/microcell devices including cellular functionalities.

A pico-cell clustering technique has been proposed in the European project FP7-ICT-1-216785 UCELLS (www.ict-ucells.eu) for extending UWB radio range to provide indoor Gbit/s communications in medium distances, i.e. home or small office. In order to use pico-cell cluster architectures it is necessary to guarantee that there is no interference between pico-cells and maximize the spectrum usage. These aims can be achieved by implementing power-flow control techniques and spectrum monitoring inside each pico-cell area, allowing re-usability of the spectrum from cells located far one of each other and co-existence with narrowband interferers in the cluster operation.

Moreover, electronic ADC sensitivity is too limited for monitoring wide bands as UWB signals due to the low power levels compared to those with rather high radiated power from other licensed/unlicensed services.

Figure 79 shows an example of application of the proposed technique. A set of transceivers are arranged in different pico-cells. These transceivers are emitting at very low power levels, usually called ultra-low power radio [75], i.e. UWB signals that cover the band from 3.1 to 10.6 GHz with power levels in the range from -41 to -75 dBm. Peer-to-peer communications are established inside the cell or connect the transceiver to an access node for remote connectivity. The two key applications of the pico-cells cluster system are shown in this figure too: HD video streaming and high-speed data communications.

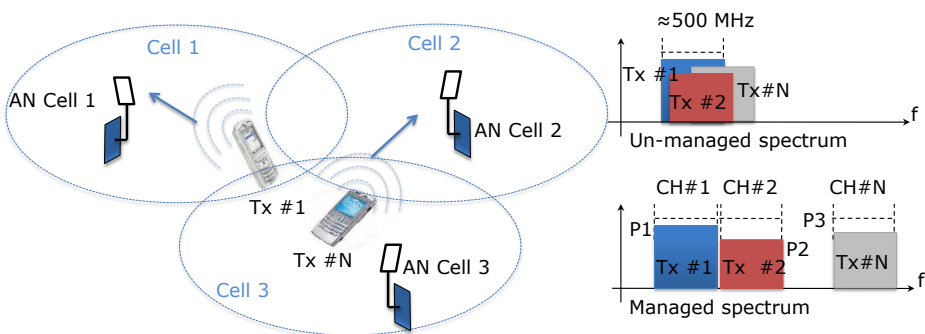


Figure 79. Spectral interference management in pico-cells cluster architectures

The management strategy works as follows: The access nodes capture the signal to monitor the used spectrum to centrally control the UWB channel employed and the maximum transmitted power of each transmitter shown in Figure 79. This management guarantees that pico-cells do not interfere each other, and that the radiated power is under regulation limits [5].

Figure 80 shows the application scenario of the photonic-ADC architecture. In this figure it is depicted the three-dimensional (3D) localization of UWB radio transmitters. 3D localization requires different sensors to be positioned at different locations as shown in Figure 80. Sensor placement should be done at different heights in order to enhance resolution in the z dimension as shown in the figure.

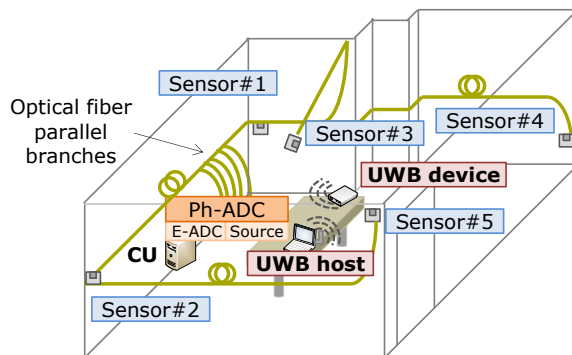


Figure 80. Radiometry of UWB signals in a home environment

The UWB localization coordinates are calculated based on a time difference of arrival (TDoA) algorithm. At least four relative delays are needed, which leads to a minimum of five sensors in the system, as shown in Figure 80. Each UWB sensor captures UWB activity on a pulsed optical signal. The sensors are connected with optical fibres forming a parallel photonic-ADC described in the next section.

Figure 80 also shows a pulsed optical source which feeds light to all sensors through a passive divider, and an E-ADC. Each sensor branch implements a specific optical time-stretch process to reduce the electrical and digital signal processing requirements. Time-multiplexing of the optical signal in each sensor branch is implemented permitting the use of a single E-ADC in the whole system. The E-ADC applies ad-hoc processing algorithms to analyse the optically-sampled data gathered simultaneously from all sensors, thus localizing the UWB transmitters in the area.

The photonic processing requires an EOM and fibres with specific chromatic dispersion values to achieve the desired time-stretching. In the optical receiver side, the optical signal is photo-detected, filtered, digitized (E-ADC) and processed (FFT) to evaluate its spectral components. The processing algorithms are applied to the time-stretched signal in order to manage the radio resources to accomplish cognitive functionalities and adapt radio operation to optimize the cellular performance.

The single-channel proposed Ph-ADC implementation is shown in Figure 81 for explaining the process: The pulsed laser source generates optical pulses with fs-range pulsewidth that are launched into the first spool of fibre where they are spread in time. The accumulated chromatic dispersion of this fibre (D_1) converts the spectral components of the wideband source to time domain (λ -to-t mapping). A segment of the electrical signal received from the antenna is modulated on the pulse intensity by the EOM. This signal is propagated in a second span of fibre with total dispersion D_2 . After photodetection the signal is stretched in time and its spectrum appears compressed. The stretching factor is imposed by the relation between the dispersion accumulated in the two spools of fibre.

The key parameters of the TS-PhADC are the aperture time T_A defined as the pulse duration at the EOM input, the capture time defined as $T_C = M \cdot T_A$, and the stretching factor M defined as:

$$M = 1 + D_2/D_1 \quad (9)$$

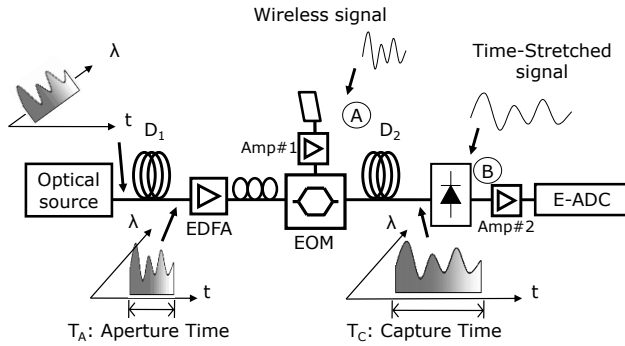


Figure 81. Time-stretch process in time and frequency domain in a single-channel Ph-ADC

The time-stretch process can be observed in Figure 82, where $x_A(t)$ stands for the RF UWB signal at the input of the EOM, in this case the signal detected by the UWB antenna and feed to the modulator, and $x_B(t) = x_A(t/M)$ stands for the RF signal captured by the E-ADC after photo detection.

With this signal processing the analog RF signal is slowed down and the requirements of the E-ADC are relaxed.

In Section 3.3.1 the single-channel Ph-ADC performance is analysed by simulation and experimentally. The Ph-ADC with engineered optical and electrical amplification [Llo09b] enables a commercial-off-the-shelf E-ADC to detect a radio carrier with peak amplitudes down to 24.975 μVp (-65 dBm).

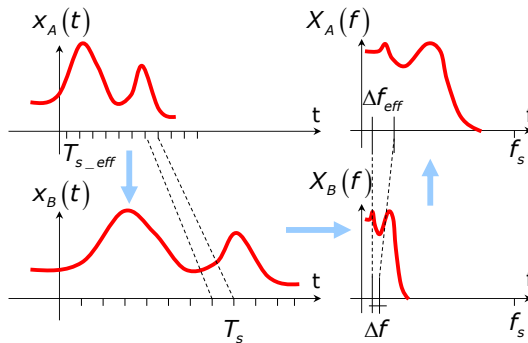


Figure 82. Time-stretch process in time and frequency domain

From this application scenario, a parallel multi-channel photonic-ADC architecture is evaluated in Section 3.3.2 targeting to provide an ultra-wide spectrum monitoring of existing radio standards allocated in the 3.1 to 10.6 GHz band with a conventional cheap E-ADC. This photonic-ADC architecture is tailored to generic original localization algorithms applied to multiband hopping signals. The parallel photonic-ADC includes multi-channel processing. Optical pulses bearing UWB radio activity, that in different branches form the optical channels, must be processed in parallel in order to localize the transmitters in the area. This architecture differs from other parallel photonic-ADC techniques, see by example [15], as in our proposed system time-simultaneous sampling is performed on all electro-optic sensors. This spatially-diverse time-simultaneous photonic sampling effectively enables the precise localization of radio transmitters in the area.

Finally, in Section 3.3.3 the simulations radio-over-fibre transmission of UWB signals through the dispersive element of the photonic-ADC is demonstrated.

3.3.1. Single-channel photonic-ADC performance

The multichannel photonic-ADC system herein proposed is based on the optical time-stretching technique reported in [76]. The basic principle can be summarized as follows: The radio signal under analysis is modulated on a pulsed laser light which is optically time-stretched prior to digitization with a conventional E-ADC. The time-stretch process introduces three key advantages: (i) The E-ADC sampling rate, and its analog bandwidth, is effectively multiplied by a factor exactly equal to the optical stretching factor M . (ii) The overall system jitter is dominated by the pulsed laser jitter, typically much lower than jitter in conventional E-ADCs [77]. (iii) The E-ADC dynamic range is maintained if the Ph-ADC is properly designed, i.e. optical distortion is limited. The time-stretching process implies that the temporal duration of the laser optical pulses is increased and a guard-time between pulses must be considered when designing the system. This implies that continuous operation would require parallel branches as described in [78]. In our case, this is not an important limitation as considerable computational efforts are required by the localization and fingerprinting algorithms, already constraining continuous operation. The time-stretching Ph-ADC approach is especially interesting for sensing ultra-low power radio as it permits the engineering of the required amplification between optical and electronic domains relaxing individual amplifier requirements.

Figure 83 shows a single channel Ph-ADC based on the time-stretching technique. This figure shows a radio signal detected by the antenna-amplifier-modulator chain, marked "radio sensor" in the figure, and a photonic part implementing the time-stretch process, marked as "optical processor". The radio sensor requires an EOM for the radio signal conversion to optical domain, and two DCF spools with accumulated chromatic dispersion D_1 and D_2 respectively. The resulting Ph-ADC time-stretching factor is then $M=1+D_2/D_1$.

The time-stretch Ph-ADC operation can be described as follows: The accumulated chromatic dispersion of the first fibre spool (D_1) converts the spectral components of the pulsed optical source to time domain (λ -to- t mapping) process as described in [76]. This process is based on the temporal analogy of the Fraunhofer spatial diffraction. This approach requires the propagation of the optical pulses through a highly dispersive element (chromatic dispersion) meeting the condition $|T^2/\Phi| \ll 1$ [79], where Φ [ps²/rad] stands for the chromatic dispersion in the dispersive element, and T stands for 1/e pulse width from pulsed optical source. In our implementation, dispersion compensating fibre (OFS LLMicroDK) is employed as dispersive element. After the λ -to- t mapping, the EOM modulates the radio signal under detection. The second fibre spool, DCF2, stretches the modulated optical pulses in time domain. At the receiver end the modulated and stretched pulses are photo-detected, amplified and digitized by a conventional E-ADC.

A simulation analysis employing Matlab™ targeting to evaluate the distortion added by the time-stretch process and the associated signal-to-noise ratio has been done. A radio-frequency (RF) sinusoid is considered as the radio signal under detection. The parameters characterizing the blocks in Figure 83 in are summarized in Table 10. Distortion is calculated comparing the simulation results with a-priori information (amplitude, frequency and phase) on the modulating RF signal at the E-ADC, point (1) in Figure 83. The simulation sampling frequency is 5 THz. Such sampling frequency is necessary to deal with the narrow optical pulses from the pulsed laser in Figure 83.

In these first experiments, the optical source generates pulses at 13.6 MHz repetition rate. These are hyperbolic secant shaped and are generated taking into account the superimposed amplitude noise, jitter of the pulses and time-width characteristics. The pulses are in accordance with the optical source employed in the experimental work in the next sections. Following the pulse laser source, DCF1 and DCF2 fibres in the analysis are characterized by the attenuation, chromatic dispersion (GVD, group velocity dispersion) and GVD slope measured by an optical network analyser (Advantest Q7760).

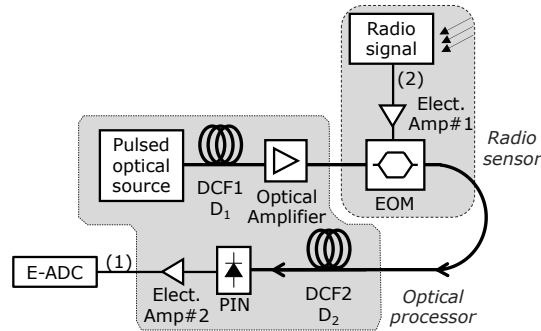


Figure 83. Block diagram of the single channel Ph-ADC evaluated by simulation

The DCF model does not take into account non-linear fibre behaviour as the average optical power in the laser source is kept limited to 3 dBm. The accumulated GVD in the first fibre spool is $D_1 = -1513.1$ ps/nm and relative dispersion slope is 3.29 %/nm. The second spool of fibre, DCF2, exhibits an accumulated dispersion of $D_2 = -3612.2$ ps/nm with 3.41 %/nm relative dispersion slope. The resulting stretching factor is $M = 1 + D_2/D_1 = 3.38$ with negligible distortion due to chromatic dispersion slope in the 3.1 - 10.6 GHz signal band. A Mach-Zehnder interferometer is employed for electrical-to-optical conversion. The RF input signal is amplified by 40 dB (3 dB noise figure) prior to the electrical-to-optical conversion. Finally, the optical signal is photodetected with a PIN photodiode taking into account thermal and shot noise, and amplified (Elect. Amp#2) with 62 dB gain (2.8 dB noise figure) in agreement with the amplifiers employed in the experimental work described in the next sections.

Table 10. Simulation parameters of the Ph-ADC

Parameter	Value	Parameter	Value
DCF1 accumulated dispersion (GVD)	-1513.1 ps/nm	Elect. Amp#1 Gain and Noise	G=40 dB NF=3 dB
DCF2 accumulated dispersion (GVD)	-3612.2 ps/nm	Elect. Amp#2 Gain and Noise	G=62 dB NF=2.8 dB
Vn modulator	1.5 V	PIN responsivity	0.7 A/W

In order to evaluate the Ph-ADC performance, a RF carrier at the first frequency of the UWB band ($f = 3.146$ GHz) is fed at point (2) in at different power levels ranging from -39 to -65 dBm. The resulting signals will be further compared with experimental measurements in the next section. Figure 84 shows the resulting Ph-ADC signals at point (1) in Figure 83 for the RF input tone at -59 and -65 dBm respectively. Looking at the spectrum in Figure 84(b) and (d) it can be observed that the tone signal at $f = 3.146$ GHz appears at $f/M = 0.928$ GHz. This confirms the time stretch with $M = 3.38$.

Proper operation of the single-channel photonic-ADC was demonstrated in the laboratory. The experimental setup is shown in Figure 85. A RF carrier at $f = 3.146$ GHz (first frequency of the lower UWB sub-band) is employed for test at different power levels (Agilent E4438). The optical source in the setup is a Pritel femtosecond fibre laser with 13.6 MHz repetition rate. The DCF are low loss dispersion slope compensating modules from OFS (LLMicroDK) with accumulated dispersion $D_1 = -1513.1$ ps/nm and $D_2 = -3612.2$ ps/nm. Optical amplification is introduced by a low-noise EDFA (Keopsys KPS-BT2-C-13-LN-FA). The saturation power is precisely set to 11 dBm to adequately match the optical intensity to the Mach-Zehnder dynamic range limiting intermodulation and harmonics.

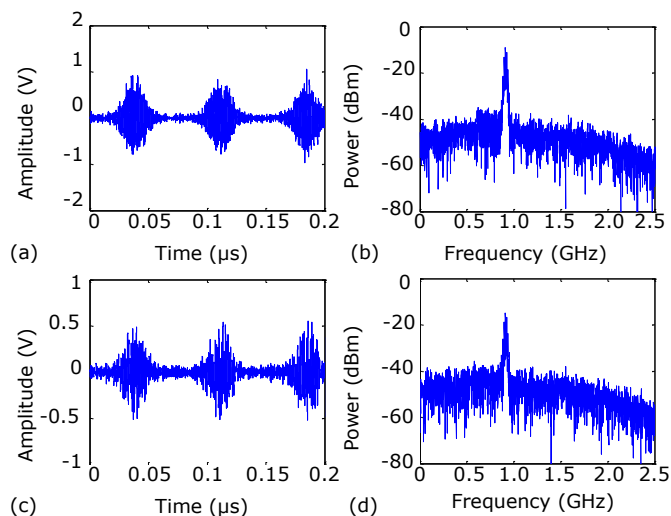


Figure 84. Simulated time signal and electrical spectrum results for the Ph-ADC with RF input carrier at 3.146 GHz and: (a-b) -59 dBm, (c-d) -65 dBm power respectively

The electro-optical modulator is a low V_n modulator. The antenna amplifier (Elect. Amp#1) has 40 dB gain (2.8 dB noise figure). The resulting signal is photodetected (PIN XPDV2020R, 0.7 A/W) and amplified with a tandem amplifier (62 dB gain). After photodetection, the signal is high-pass filtered (cut-off frequency 0.8 GHz) to eliminate the low frequency/high power spectrum from the optical pulse envelope. Upper cut-off frequency is 1650 MHz which is translated to 5.61 GHz equivalent frequency (with $M=3.38$).

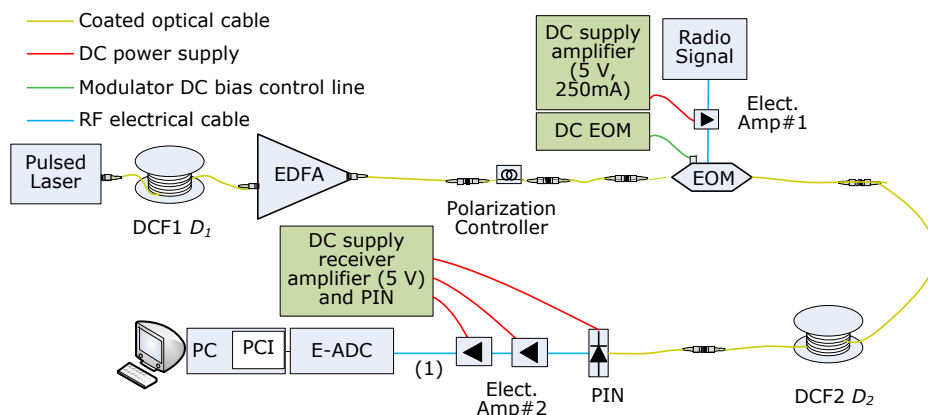


Figure 85. Experimental single channel photonic ADC setup

Figure 86 shows the measured electrical spectrum of the time-stretched signal at point (1) in Figure 85. The resulting signal was sampled with a real time oscilloscope of 6 GHz bandwidth (LeCroy SDA-760Zi) for different input power values ranging from -39 to -65 dBm as it is shown in Figure 87. The amplitude levels of the experiment are in good agreement with the simulation results shown in Figure 84.

Comparing the initial frequency of the sinusoidal signal with the measured spectrum shown in Figure 86, it is confirmed that the spectrum has been compressed by the factor $M = 1 + D_2/D_1 = 3.387$ as predicted. The sine peak appears at 925.48 MHz when theoretically should be at $f_t = f/M = 3146 \text{ MHz}/3.387 = 928.8 \text{ MHz}$, i.e. a 3.5 MHz shift can be observed in the experiment. This is a constant shift due to the residual dispersion of the optical fibres comprising the Ph-ADC architecture than can be corrected with calibration.

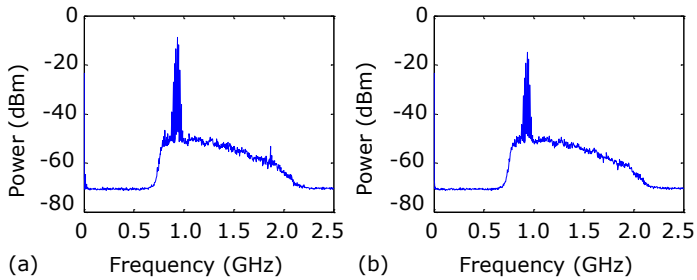


Figure 86. Measured electrical spectrum of the Ph-ADC system with RF input carrier at 3.146 GHz and: (a) -59 dBm, (b) -65 dBm power (RBW=1 MHz)

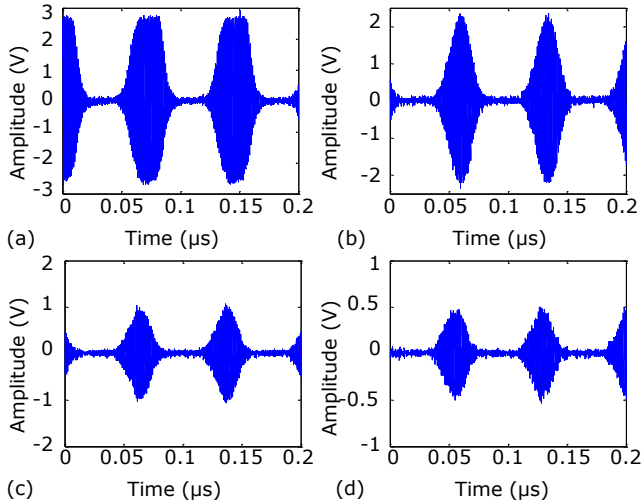


Figure 87. Captured time signal by the E ADC for an RF input power of: (a) -39 dBm, (b) -51 dBm, (c) -59 dBm, (d) -65 dBm

The sampled data is transferred to a PC and processed in Matlab to evaluate the signal to noise ratio (SNR). The cyclo-stationary period is evaluated and the carrier frequency, the phase and burst period are estimated. Afterwards, the burst envelope is estimated and the Ph-ADC SNR is computed.

Figure 88 shows an example of the sampled signal and the results after processing. Figure 89 shows the received signal power, the noise power and the computed SNR as a function of the burst period for the different input levels evaluated.

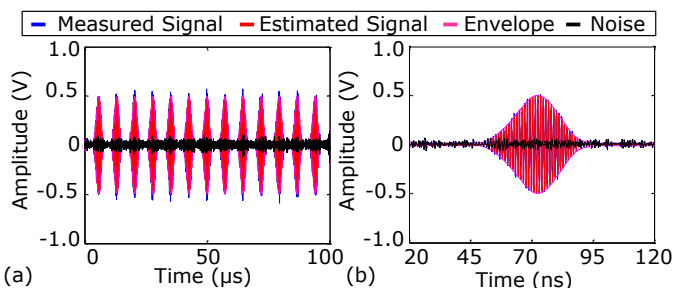


Figure 88. (a) Processed results and (b) zoom of estimated signal with RF input power of -65 dBm

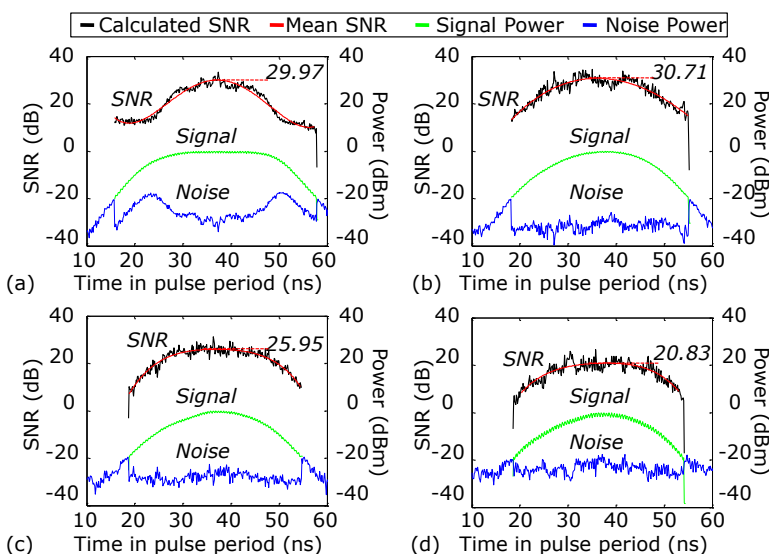


Figure 89. SNR inside the optical pulse period for an RF input power of: (a) -39 dBm, (b) -51 dBm, (c) -59 dBm, (d) -65 dBm

It can be observed that the SNR degrades significantly at the edges of the pulse period. This is due to the decrease of signal power induced by the shape of the optical source pulses. The maximum SNR obtained by simulation and experimentally are compared in Figure 90 with good agreement. In Figure 90, it can be observed that for higher input power levels there is some deviation on the SNR results due to the amplitude clipping in the electrical amplifiers observed in Figure 87(a), not considered in simulation. For lower power values, the simulated noise is bigger due to mismatches in the response of the filters used to remove the DC component coming from the optical source.

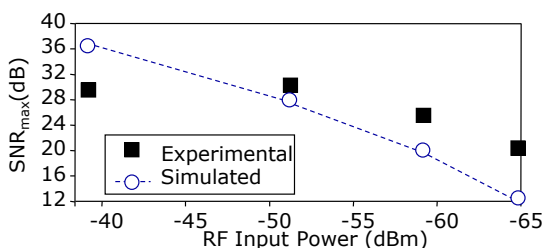


Figure 90. Maximum SNR values obtained by simulation and experimentally vs. RF input power

3.3.2. Multichannel photonic-ADC including localization and fingerprinting functionalities

The basic time-stretch Ph-ADC principle is further developed in this section proposing a novel time-multiplexed multichannel architecture where precise control of the time alignment in the optical signal permits the simultaneous detection of a given radio signal at different spatial locations. The proposed system required synchronization of the E-ADC with the optical source and proper processing of the optical pulses coming to the E-ADC to enable the localization and fingerprinting of the detected radio signal.

As it was commented before, the proposed photonic-ADC targets sensing the radio spectrum in a home or office environment where several sensors are located along the area to sense, and the information captured by each sensor is processed with ad-hoc fingerprinting and localization algorithms.

This architecture finds application in security, public-safety and disaster-recovery scenarios where it is necessary to detect and localize ultra-low power radio signals with high accuracy in a large frequency span. Also, localization of UWB or other radio signals is an enabling step for advanced cognitive radio and spectrum-sharing applications [50].

Figure 91 shows the experimental setup for demonstration of the proposed parallel photonic-ADC. Device specifications are summarized in Table 11. System operation depicted in Figure 91 can be described as: First, narrow optical pulses were generated with a femtosecond fibre laser (FFL) with repetition frequency f_{sample} . This frequency was selected to sample the whole OFDM-UWB symbol. In order to avoid overlapping of the different pulses before combining them together two aspects must be taken into account.

In first place, the repetition rate of the laser (f_{sample}) should be calculated as:

$$f_{sample} > \frac{1}{N \cdot T_{stretched}} \quad (10)$$

where N is the number of branches to combine ($N=5$), and $T_{stretched}$ is the duration of the optical pulses once stretched with $M=3.38$. In second place, this sampling frequency has been defined such that consecutive snapshots sweep perfectly the OFDM blocks according to:

$$f_{sample} = \frac{1}{T_{OFDM} + T_A} \quad (11)$$

where T_{OFDM} is the OFDM block period and T_A the aperture time of the optical pulse coming to the modulator. According to this, the repetition rate of the optical source is $f_{sample}=3.233$ MHz.

The optical pulses were stretched by a DCF with dispersion D_1 . The signal was afterwards amplified by an EDFA and divided in different branches. In this demonstration five sensors are used, hence the multi sensor parallel architecture comprises five branches or channels.

Each sensor includes an electro-optic modulator, amplifier and antenna in order to capture UWB activity on a pulsed optical signal. The electro-optic sensor is indicated by a dashed box in Figure 91.

The UWB sensor architecture comprises a MZ-EOM, a RF wideband amplifier and a patch omnidirectional antenna. Different heights were selected during sensor placement to achieve adequate resolution in the z-axis. Sensor locations are also summarized in Table 11. A fibre patchcord of $L=10$ m is used to deploy each sensor at different room allocations as depicted in Figure 80.

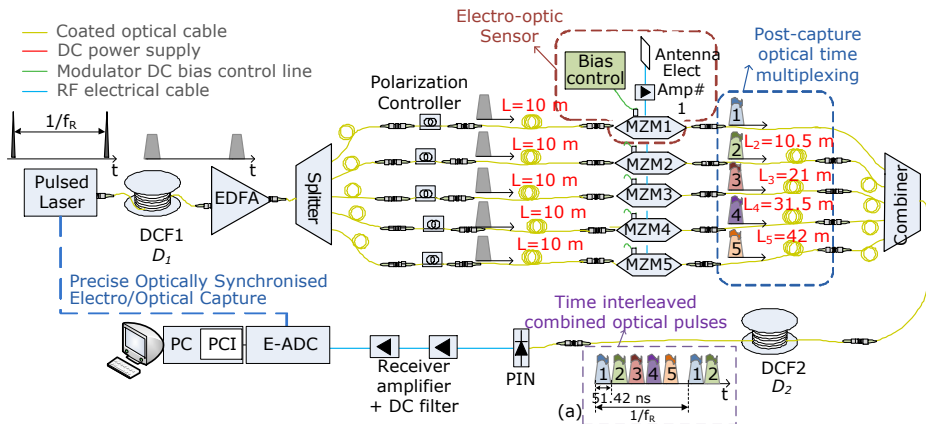


Figure 91. Multi-channel time-multiplexed photonic ADC experimental setup with optical pulse time-multiplexing scheme. Inset (a) Time interleaved optical pulses coming from the different branches combined before the E-ADC

Table 11. Device Specifications of multi-channel Ph-ADC

Device	Specification value
Source	$f_R=3.233$ MHz, 1.6 ps width pulse
DCF1	$D_1=-1513.1$ ps/nm
DCF2	$D_2=-3612.2$ ps/nm
Antenna amplifier	$G=44$ dB, $NF=2.2$ dB, $f=3-10.6$ GHz
MZ-EOM	$V_{\pi}=3.8$ V, $BW=15$ GHz
Optical amplifier	EDFA $P_{sat}=19$ dBm, $G=42$ dB
Splitter/Combiner	5x1 with losses < 7.9 dB
Optical delay (m)	$L_2=10.5$, $L_3=21$, $L_4=31.5$, $L_5=42$
Photodiode	PIN, $R=0.7$ A/W, $BW=50$ GHz
Receiver amplifier	$G=62$ dB, $NF=2.8$ dB, $BW=3$ GHz
Electrical ADC	2 GHz front-end, $f_s=8$ GS/s
Sensor position in m (x,y,z) measured from the corner	$S1=(0, 0, 1.8)$, $S2=(0, 4.75, 0.2)$, $S3=(5.26, 4.75, 1.8)$, $S4=(6.21, 0, 0.2)$ and $S5=(3, 3, 2.4)$

Each channel in the time-multiplexed photonic-ADC architecture is dedicated to optically process the UWB radio signal. The different branches are combined in parallel with time-multiplexing serialization achieved employing cleaved fibres with lengths $L_2=10.5$ m, $L_3=21$ m, $L_4=31.5$ m and $L_5=42$ m guaranteeing a 51.42 ns slot for each optical channel and that there is no overlapping between the optical pulses coming from the different branches. The combined time-interleaved optical pulses are shown in inset (a) of Figure 91. The maximum delay inaccuracy was measured during system set-up to be lower than 1 ps.

The five branches are combined together and stretched over a second spool of fibre with dispersion D_2 to complete the time stretching conversion factor with $M=1+D_2/D_1=3.38$. The global stretch operation allows to the upper frequency of the first UWB band to be translated from 4.752 GHz to 1.4 GHz as it can be seen in the electrical spectrum shown in Figure 92. This matches with the 2 GHz front-end bandwidth specification of the E-ADC.

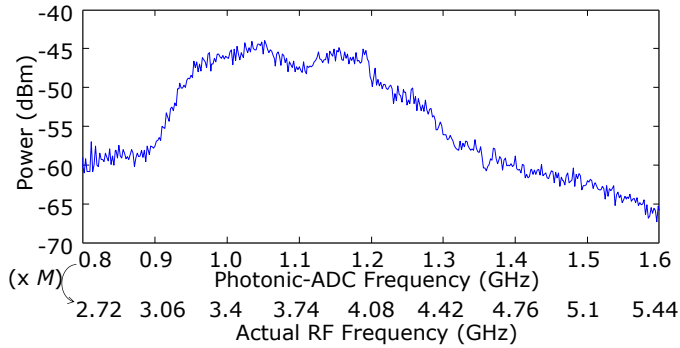


Figure 92. Spectrum of TFC1 UWB transmission at 0.5 m range the sensor (RBW=50 kHz). M stands for the Ph-ADC stretching factor

3.3.2.1 Fingerprinting and TDoA algorithm

Regarding the fingerprinting, the proposed algorithm is made of two sequential parts. First, the power spectral density is computed over the bands of interest. The integrated value over time and over each band is then put in perspective with the noise levels to give a first estimate about the presence or absence of a UWB transmission. Second, each band identified as potentially carrying an OFDM signal is then converted to baseband. The corresponding sequence should be long enough to incorporate multiple snapshots. With the selected repetition rate of the optical source, concatenating the snapshots will lead to virtual OFDM blocks exhibiting the zero-padding structure used for UWB. As proposed in [80], we then perform a power correlation on the sequence which, in case of UWB, will lead to easily identifiable trains of triangles. The period between the triangles is then estimated and compared to its theoretical value (the previously known OFDM block duration). A match will confirm the presence of a UWB signal [80].

Once the UWB transmitter is identified by the fingerprint algorithm, the proposed system estimates its position employing a specific time difference-of-arrival (TDoA) algorithm. The TDoA algorithm is a converging step, which uses the previous estimated difference of delays from each channel to compute the position. Classical differences of delays are obtained by using synchronization with the device being localized with at least two synchronized point in the infrastructure. Here is only exploited both a pure power sensing of the signal on the air and the knowledge of the used time frequency code sequence. Indeed, by matching the known hopping sequence to the sensed one, a delay is observable. Figure 93 shows an example of this method. By repeating on each channel, difference of delays is obtained.

The TDoA approach is enabled here by the precise time-alignment in the optical domain of the signals captured in all sensors in a novel manner enabled by the time frequency power pattern sampled by the photonic-ADC. Moreover, the optical time stretching ensures a larger integration time of the sensed power increasing the delay estimation accuracy.

To exploit TDoA, least-squares based estimation schemes are the easiest and cheapest solution to perform localization from TDoAs measurements [81], so the total least square TDoA has been used [82]. Five sensors are enough to retrieve the position of the transmitters without ambiguity. As shown in Figure 94, in the case of two dimensions (2D) positioning two hyperbola can be generated with 3 sensors using the TDoA algorithm which ensures to find unique intersection. But in the case of three dimension (3D) positioning, the intersection of the two generated paraboloids returns an ambiguous set of possible solution. The inaccuracy of this area will remain ambiguous with 4 sensors.

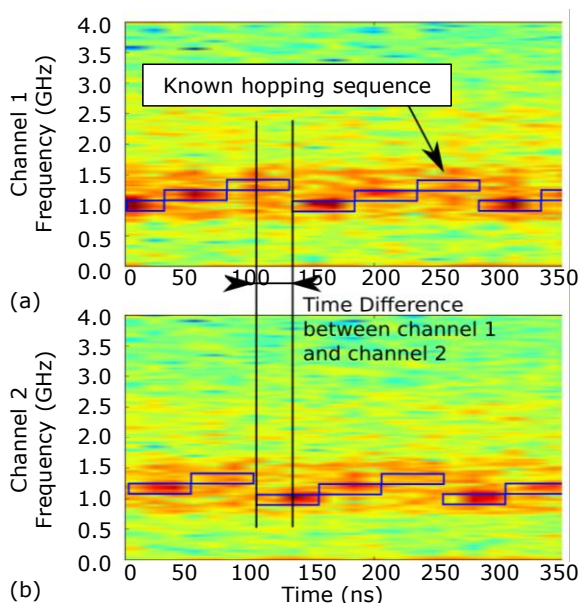


Figure 93. Spectrogram to the received signal from two optical channels to show the delay estimation based on matching measured power and the known hopping sequence: (a) channel 1 and (b) channel 2

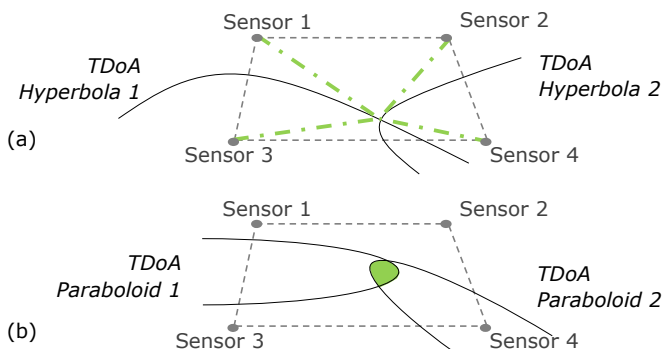


Figure 94. TDoA examples for: (a) 2D and (b) 3D positioning

For this reason, five sensors are the minimum number required to avoid this ambiguous case. However, the position of the sensors in the given area affects the positioning accuracy that can be achieved. Consequently, before performing experimental measurements, different sensor positions have been simulated to determine the best configuration to achieve the lowest error on the TDoA. This study is included in Annex B for reference.

An example of the resulting results with a UWB signal using time frequency code TFC3 [6] with frequency hopping in the first three channels $f_1, f_1, f_2, f_2, f_3, f_3$ is shown in Figure 95. The -100 dB labels indicate that no OFDM UWB symbols were detected in that time slot at that frequency band. If the number is different, then transmission presence was detected.

In the example of Figure 95, the frequency hopping pattern is clearly identifiable demonstrating the fingerprint of the UWB radio signal modulated in the optical pulses in the Ph-ADC.

Starting to analyze the data			
Time1:	8.718050e-002μs	70.7dB	-100dB
Time2:	3.964525e-001μs	66.5dB	-100dB
Time3:	7.057244e-001μs	-100dB	69.8dB
Time4:	1.014996e+000μs	-100dB	68dB
Time5:	1.324268e+000μs	-100dB	-100dB
Time6:	1.633540e+000μs	-100dB	-100dB
Time7:	1.942812e+000μs	72dB	-100dB
Time8:	2.252084e+000μs	65dB	-100dB
Time9:	2.561356e+000μs	-100dB	72.3dB
Time10:	2.870628e+000μs	-100dB	65.1dB
Time11:	3.179900e+000μs	-100dB	-100dB
Time12:	3.489172e+000μs	-100dB	-100dB

Figure 95. Example of fingerprinting processing result of a UWB signal using time frequency code 3 ($f_1, f_1, f_2, f_2, f_3, f_3$)

Real data from a UWB communication link at 480 Mbit/s (DCM modulation) has been sampled with the multi-channel parallel photonic-ADC architecture in Figure 91. The UWB transmitter was located at different positions inside a room at 1 m, 2 m, 2.5 m and 3 m from the origin corner marked in Figure 80 in order to check performance in different situations. Different positions lead to different delays and power levels on the sampled signal due to the different wireless paths.

The signal input to the E-ADC includes an optical intensity modulation on the optical pulses due to the to electrical voltage conversion at the photodetector. As explained, ad-hoc processing over the sampled data (by channels) is done to remove this effect.

Figure 96 shows an example of the processed signal results when the UWB host is at 2 m from sensor 1. The sampled time signal confirms the DCM-OFDM amplitude modulation over the optical pulses. The spectrogram shows the frequency components detected for a UWB transmission with time frequency hopping TFC1 (channel frequency band $f_1, f_2, f_3, f_1, f_2, f_3$). The maximum instantaneous value of the energy on each sub-band for each snapshot is provided to the weight estimation stage. Because this method is based on the maximum energy per snapshot, the state estimation can produce a decision on the dominating state in a snapshot even in low signal-to-noise ratio scenarios. The hopping sequence is directly observable on Figure 96.

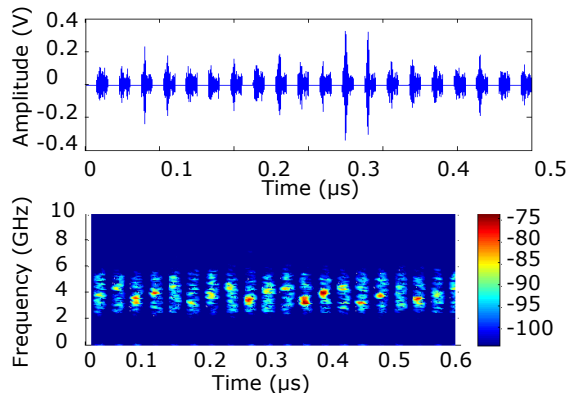


Figure 96. Example of optically sampled signal with the time-multiplexed photonic-ADC architecture and computed spectrogram

In order to obtain position estimation from the data measured, the PDE algorithm has been computed and the resulting delay estimations have been provided to the developed TDoA-TLS positioning algorithm. Some results obtained from the experimental dataset are provided in Table 12. The two first columns provide the coordinates of the real UWB device position. The estimated coordinates are presented in the two second columns.

Table 12. Position estimation from the experimental data

Real position		Estimated position		RMSE		Euclidean Distance (m)
X (m)	Y (m)	\hat{X} (m)	\hat{Y} (m)	ΔX (m)	ΔY (m)	
4.51	4.08	4.11	3.64	0.40	0.43	0.592
3.78	3.41	3.82	3.15	0.05	0.26	0.263
3.40	3.07	3.26	2.53	0.14	0.51	0.525
2.29	2.07	1.73	2.07	0.56	0.05	0.560
Mean value (m)				0.29	0.30	0.485

The RMSE is computed between each coordinates X and Y , considering their respective estimation \hat{X} and \hat{Y} . The Euclidean distance between the real position and its estimation is also evaluated. Finally, the last row of Table 12 provides the mean value for the computed RMSE of the coordinates and the Euclidean distance. Due to the sensors repartition in the room which is longer than wide in x-y, the mean value of the RMSE on the X coordinates is greater than Y . The positioning results can be observed graphically Figure 97 for different device positions.

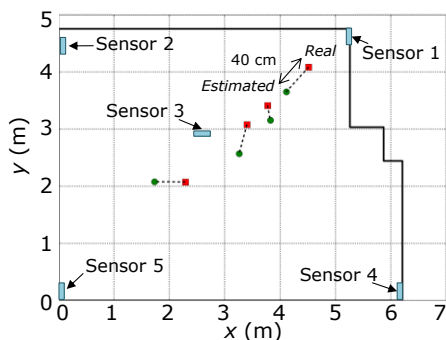


Figure 97. Localization accuracy from the experimental measurements. The red square represents the real position and the green dot the estimated

The real position of the UWB transmitter is represented by a red square and the green dot is the position estimated with the described algorithm. The difference between the real and the estimated positions is marked in a dashed line.

Observing Table 12 and Figure 97 we can confirm that in this dataset, a mean position error below 50 cm has been achieved. The mean error is 48.5 cm with standard deviation of 15 cm. The accuracy of these results could be improved for instance by choosing a RF antenna and amplifier combination with a better amplification for increasing the signal to noise ration and limiting the number of weight-estimation error or by increasing the number of used snapshots in the photonic-ADC.

3.3.3. UWB radio-over-fibre transmission and simultaneous sensing with photonic-ADC

In this Section we evaluate an optical access approach in which both UWB sensing and radio-over-fibre are provided by the same optical infrastructure. UWB sensing uses a photonic analog-to-digital converter [Llo09a] which comprises DCF, well suited for large bandwidth signals (3.1-10.6 GHz) with low power spectral density as studied in previous sections.

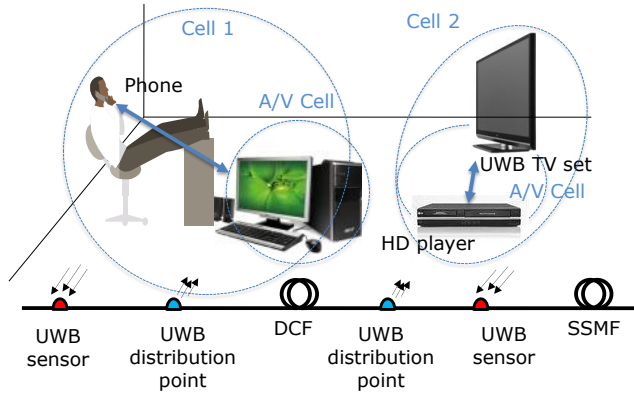


Figure 98. Sensing and UWB distribution concept

Figure 98 shows the proposed concept for sensing and providing UWB service. In this figure an optical infrastructure forming a time-stretch Ph-ADC [76] by DCF interconnects different UWB access nodes and sensors.

Two scenarios are considered in the experimental analysis: First, Figure 99 shows an in-building optical infrastructure where UWB radio-over-fibre provides point-to-point communication in different rooms. The communication is done through DCF fibres comprising the Ph-ADC sensing architecture.

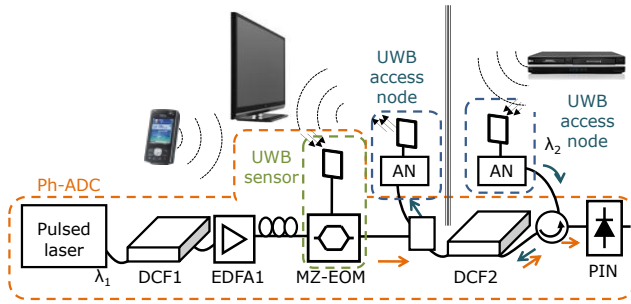


Figure 99. In-building UWB -over-fibre and sensing scenario

In the second scenario depicted in Figure 100, the UWB signals are distributed from a central office in radio-over-fibre through SSMF. On reaching the in-building optical network, the signal is distributed through the in-building DCF infrastructure.

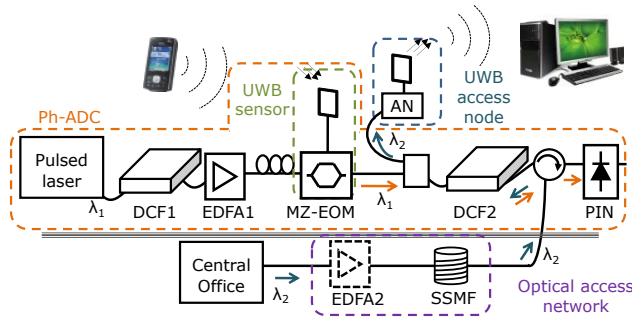


Figure 100. Optical access network UWB radio-over-fibre and sensing scenario

A proof-of-concept laboratory experiment was performed to demonstrate the feasibility of the sensing and UWB distribution concept in the two scenarios. The setup is shown in Figure 100 and comprises a time-stretch Ph-ADC [76] which performs the sensing operation and an UWB access node. UWB distribution from the CO is possible at distances from 10 to 75 km with EDFA amplification. Device specifications are shown in Table 13.

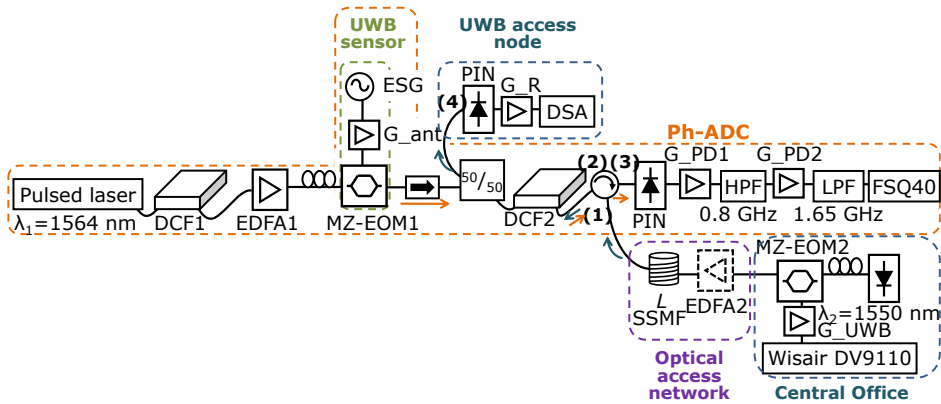


Figure 101. Laboratory setup for Ph-ADC and UWB distribution

Table 13. Device specifications of setup for Ph-ADC and UWB-over fibre

Ph-ADC parameters	Radio-over-fibre parameters
$G_{\text{ant}}=34$ dB	$G_{\text{UWB}}=34$ dB
$D1=-1513.1$ ps/nm	$D2=-2538.1$ ps/nm or $D2=-3612.2$ ps/nm
Covega 6538015	Photline MZ-LN-40-PD
Keopsys $P_{\text{sat}}=13$ dBm	Exelite $P_{\text{sat}}=19$ dBm
$G_{\text{PD1}}=36$ dB, $G_{\text{PD2}}=26$ dB	$G_{\text{R}}=40$ dB

The Ph-ADC comprises a Pritel femtosecond fibre laser source with 13.6 MHz repetition rate and the optical spectrum shown in Figure 102. A 1564 nm centre wavelength was used to avoid possible interference with the UWB radio-over-fibre signal travelling at 1550 nm. Spectral components are resolved in time through the DCF1 fibre.

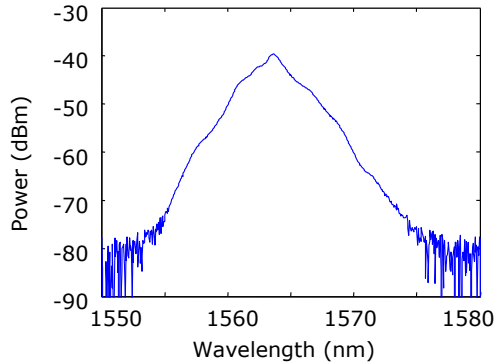


Figure 102. Pulsed laser optical spectrum employed

The signal sensing is emulated by a signal generator (ESG Agilent E4438) which is modulated the MZ-EOM1 in QB and is further dispersed through DCF2. An isolator and coupler are introduced after the optical modulation to combine Ph-ADC sensing and UWB radio-over-fibre optical distribution.

The key limiting factor in the propagation of UWB is the DCF2 fibre [69]. An UWB RoF carrier signal is generated by a CW laser at 1550 nm. A 200 Mbit/s UWB ECMA-368 compliant signal QPSK modulated (MZ-EOM2 in Figure 101) is then generated with Wisair DV9110 modules. Different SSMF paths with total length (L) of 10, 25, 50 and 75 km are evaluated. The accumulated dispersion values of the SSMF are shown in Table 14. At the central office, the EVM of the UWB signal is measured with an Agilent digital signal analyser DSA80000B. Current ECMA-368 regulation set a maximum EVM of -14.5 dB for UWB signals up to 200 Mbit/s [6]. The first spool of fibre (DCF1 in Figure 101) exhibits $D1 = -1513.1$ ps/nm dispersion. In the second module DCF2, dispersion can be $D2 = -2538.1$ ps/nm for $M=1+D2/D1=2.67$, or $D2 = -3612.2$ ps/nm for $M=3.38$.

Table 14. Accumulated Dispersion in SSMF Paths

Fibre length L	Accumulated dispersion
10 km	170 ps/nm
25 km	428.4 ps/nm
50 km	854.59 ps/nm
75 km	1281.9 ps/nm

Different time-stretched signals were measured at point (3) for both DCF2 values and shown in Figure 103. A -50 dBm sinusoid input signal, generated with an ESG with 3.146 GHz frequency is used for simplicity in the Ph-ADC evaluation. With $D2 \approx -2500$ ps/nm, the stretched peak appears at 1.21 GHz. In theory, with $M=2.67$ stretching factor: $f_t = f/M = 3.146/2.67 = 1.17$ GHz. When $D2 \approx -3600$ ps/nm is considered, it appears at 957.53 MHz. In the case with $M=3.38$: $f_t = f/M = 3.146/3.38 = 928.8$ MHz. This confirms that the Ph-ADC monitoring part keeps operating correctly (with 28 MHz offset) while UWB-over-fibre is transmitted in the opposite direction.

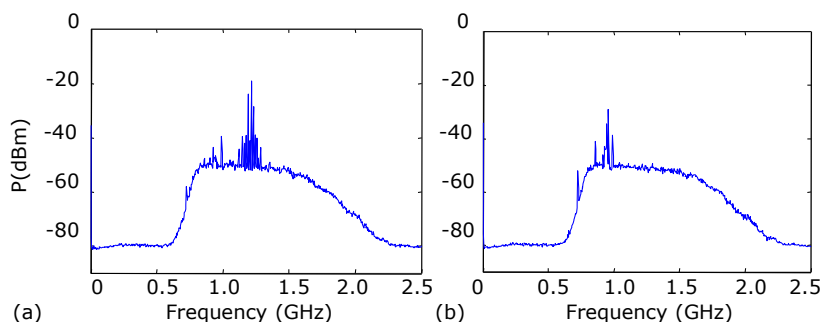


Figure 103. Time stretched signal for (a) $D2 \approx -2500$ ps/nm and (b) $D2 \approx -3600$ ps/nm

The UWB signal is measured at Figure 101 point (4) with and without SSMF propagation. The EVM and demodulated constellations are shown in Figure 104. When the second spool of DCF is $D2 \approx -3600$ ps/nm, the measured EVM is -8.17 dB without SSMF propagation ($L=0$ km), due to the low optical level received at the PIN input (4) of -16 dBm. With $D2 \approx -2500$ ps/nm the measured EVM is -16.16 dB when $L=0$ km, which is below ECMA-368 threshold of -14.5 dB, with an optical level received at the PIN input of -10.1 dBm. However, this signal cannot reach even 10 km SSMF due to the low optical power available. This was solved placing an optical amplifier before SSMF transmission (EDFA2). This corresponds to CO amplification. The output power of the EDFA2 is adjusted to 2 dBm.

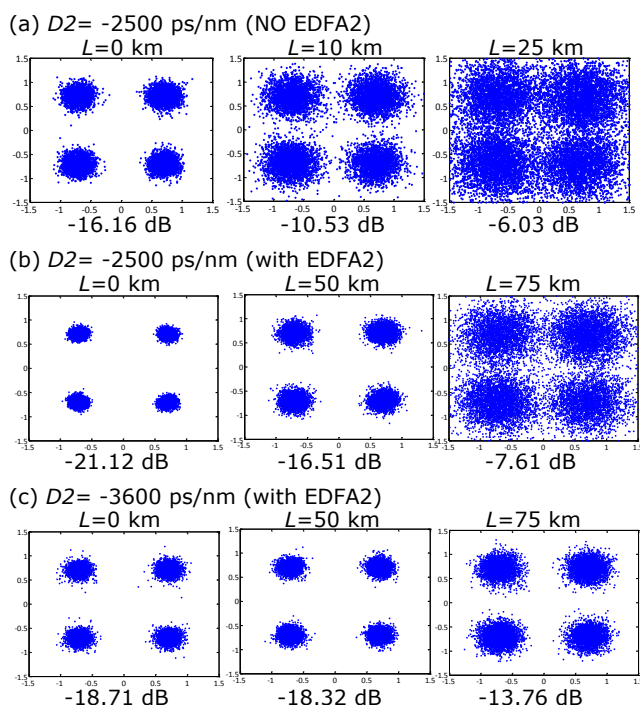


Figure 104. EVM and constellations measured for (a) $D2 \approx -2500$ ps/nm without second EDFA2, (b) $D2 \approx -2500$ ps/nm with EDFA2 at $P_{out} = 2$ dBm, (c) $D2 \approx -3600$ ps/nm with EDFA2 at $P_{out} = 2$ dBm

Figure 105 shows the EVM measured for different SSMF lengths (L). Including an optical amplifier improves the EVM and longer SSMF lengths can be used. Comparing the case without fibre propagation, the improvement is about 10.5 dB ($D2 \approx -3600$ ps/nm case). The improvement is 5 dB in the $D2 \approx -2500$ ps/nm case because the optical power gain is lower. However, in both cases SSMF transmission reach 50 km.

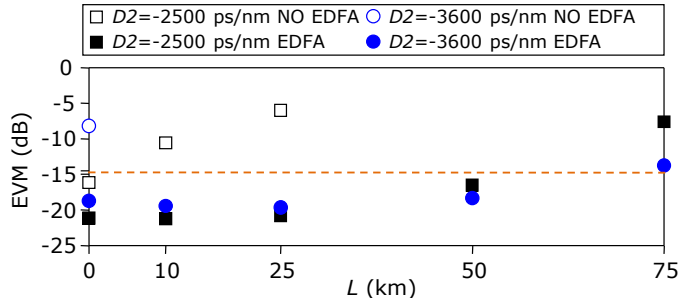


Figure 105. Measured EVM for different $D2$, length L and amplification

With this experiment the combined time-stretching Ph-ADC and UWB-over-fibre transmission in DCF has been experimentally demonstrated. This experiment confirms that the Ph-ADC fibres can be used for UWB signal distribution at DCF dispersion values $D2 \approx -2500$ ps/nm in in-building communications. Higher dispersion values distort severely UWB carrier constellation.

In the case of a signal distributed in an optical access network in SSMF, the positive optical access dispersion compensates to a limited extent the DCF2 negative dispersion enabling transmission at values $D2 \approx -2500$ ps/nm or $D2 \approx -3600$ ps/nm (50 km SSMF with EDFA amplification).

3.4. Linearized electro-optical modulators

As we commented in Chapter 2, radio-over-fibre technology is recently gaining interest mainly in the fields of analog optical transmission, i.e. transmission of wireless signals [Llo08a], or optical signal processing techniques like photonic-ADC sensing of ultra-low power radio [Llo09a]. Radio-over-fibre techniques require optical devices with high-linearity in order to reduce intermodulation and harmonics which are difficult to be compensated, at least to some extent. This is not the case of other transmission impairments as chromatic dispersion or polarization mode dispersion. Analog transmission is expected to gain further interest due to the research efforts targeting integrated wireless and baseband connectivity in fibre-to-the-home access networks [84]. Linearity is of special importance when the final application involves the photonic processing of several radio signals in coexistence, i.e. different wireless signals with different dynamic ranges are jointly processed. The most restrictive case, considering the wireless state-of-the-art, is the sensing and/or radio-over-fibre transmission of UWB radio [6], which exhibits a PSD lower than -41.3 dBm/MHz in the frequency band from 3.1 to 10.6 GHz, transmitted in coexistence with WiMAX radio [85] or cellular UMTS radio signals [86].

The key element in all the radio-over-fibre applications is the electro-optical modulator. It is of great interest the availability of electro-optic modulators with good dynamic range at a reasonable cost. This section proposes and analyses a linearized electro-optic modulator comprising Y-junction waveguides (Section 3.4.1) and also a dual-drive modulator (Section 3.4.2) developed by Photline Technologies during UCELLS Project. The linearized techniques for radio-over-fibre transmission using these modulators are reported in this section.

3.4.1. Dual-parallel Y-coupled Linearized Modulator

Lithium-Niobate Electro-optic modulation employing Y-junction waveguides exhibits several advantages over conventional Mach-Zehnder LiNbO₃ modulators. These can be summarized in: (i) Lower V_{π} polarization voltage, (ii) no interferometric architecture, i.e, a linear electro-optic response can be expected, and (iii) Broader electro-optic bandwidth. The main trade-off of the proposed architecture is the device sensitivity to deviations in the fabrication process, which implies that detailed process monitoring is required to achieve adequate performance.

A dual-parallel Y-coupled LiNbO₃ waveguide device is proposed for linearized high-dynamic range electro-optical modulation. The device is fabricated and characterized in different configurations. The Y-coupled LiNbO₃ waveguide fabrication is sensitive to process deviations which would be translated to a decreased linearity. The fabrication process requires the control of the local spreading of the ferroelectric domains while monitoring the entire wafer process. A detailed study is performed in advance to select a reliable design window. The fabricated device exhibits 15.2 dB spurious free dynamic range (SFDR) enhancement over a conventional LiNbO₃ Mach-Zehnder interferometer when characterized in different configurations: single linearized modulator, dual-parallel linearized modulator and compared with single Mach-Zehnder modulator and dual-parallel Mach-Zehnder modulator. The proposed device finds application in radio-over-fibre techniques like optical analog transmission or optical processing like photonic-ADC technology.

The linearized electro-optical modulator concept herein proposed comprises a dual architecture with two parallel active Y-branch directional couplers with phase reversal travelling-wave electrodes including ferroelectric domain inversion. This architecture targets electro-optical modulation with a low voltage π -shift voltage and broadband linearized electro-optical response.

State-of-the-art linearization techniques are based on the serial/parallel arrangement of several MZ interferometers [87]. In the MZ interferometer, the modulation of the energy at the output of the device derives from interference between the two waves propagating in each of the waveguide arm of the MZ-EOM. The resulting electro-optic characteristic (transmission versus the applied voltage) is a sinusoidal function. The half-wave voltage is the voltage required to switch from a minimum to a maximum of transmission. In a MZ-EOM, the range of linearity of the sinusoidal characteristic is strongly reduced to a short portion of the curve around the quadrature biasing point. We can consider approximately that if the modulation amplitude is greater than half of the half-wave voltage (only 50% of the possible range, so 50% of modulation depth), the third harmonic will be less than 40 dB below the first harmonic. A perfect modulator would ideally give more than 40 dB with near 100% of modulation, i.e. a fundamental harmonic with +6 dB of RF power improvement.

The herein proposed device is based on a Y-coupling junction driven by phase reversal electrodes. The proposed device architecture is derived from [88] and it is enhanced integrating two Y-junction waveguide couplers in parallel with $\pi/2$ electrical phase shift and e-wall isolation [89].

E-wall isolation is required to mitigate residual coupling between the parallel stacked Y-junctions, as residual coupling would cancel the linearization effect.

Figure 106 depicts the dual-parallel device structure for practical analysis. The principle of operation can be described as follows: The incoming light is optically split in two arms (E_1 and E_2) which are fed to two parallel Y-junctions. Each of the Y-branch directional couplers is comprised by an integrated Z-cut Lithium-Niobate crystal substrate.

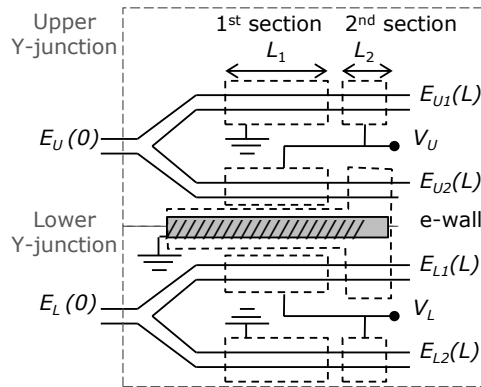


Figure 106. Proposed dual parallel Y-coupled device structure

Successful linearization of the electro-optic response of the overall architecture depends on two factors: First, the L_1 and L_2 parameters indicated in Figure 106, which stand for the length of the first and second section electrodes respectively. And second, the V_U and V_L voltages applied to the upper and lower Y-junctions respectively. Both voltages must be precisely set to produce a phase shift of $\pi/2$ in order to achieve adequate linearization. The most restrictive requirement is the precision achieved when implementing L_1 and L_2 section lengths as the actual length can be largely affected by deviations in the fabrication process.

In this section, the experimental results measured to evaluate the performance of the proposed dual-parallel Y-junction structure are shown and discussed. A complete study has been performed analysing different cases: in first place the performance results of the proposed dual-parallel linearized architecture are shown, to be compared afterwards with the new linearized modulator in a single configuration. The spurious free dynamic range (SFDR) is measured as:

$$SFDR = P_{1^{st} \text{ harmonic}} / \max(P_{\text{distortions}}, P_{\text{noise}}) \quad (12)$$

The experimental results of the proposed dual-parallel Y-junction structure are lately compared with SFDR results obtained using a single and dual-parallel architecture with conventional Mach-Zehnder modulators.

3.4.1.1 Single Linearized modulator results

Figure 107 shows the laboratory setup used to evaluate the performance on the linearized modulator in a single architecture (Photline UCCELLS21 chip in this case). The RF input is a 10 dBm tone at 3.1 GHz, which is the first frequency of the UWB band. This signal is amplified and modulated on a continuous wave (CW) light at 1550 nm wavelength of 7 dBm mean optical power. The modulator is set to quadrature bias point (2.88 V). The resulting optical signal is photodetected with a PIN photodiode of 0.7 A/W responsivity. Electrical amplification (with 21 dB gain and 5.8 dB noise figure) is used at the RF ports and after photodetection.

Figure 108 shows the electrical spectrum measured with the spectrum analyser after photodetection and amplification. In order to evaluate the performance of the proposed technique for UWB signals applications, the full UWB band covering from 3.1 to 10.6 GHz is shown with the resulting harmonics of the input signal at the first frequency 3.1 GHz.

The peak power of the harmonics present in the UWB band are labelled in the figure. In this case, according to (6), the SFDR of the linearized modulator in a single architecture is 26.3 dB.

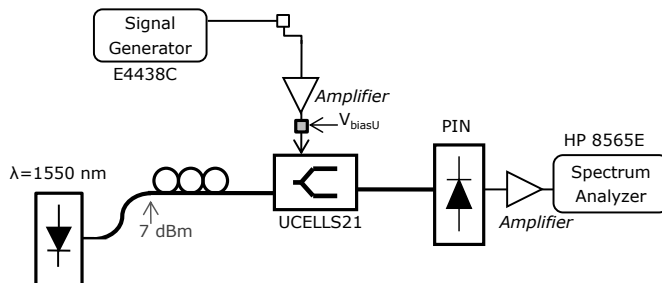


Figure 107. Laboratory setup with a single Y-coupled linearized modulator

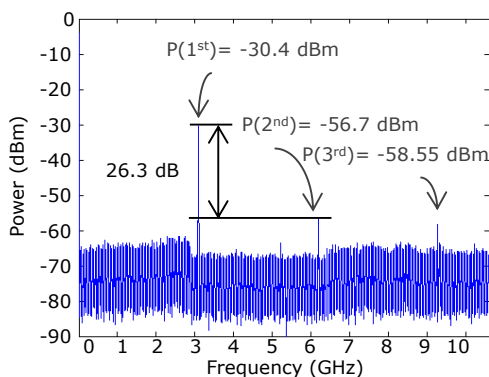


Figure 108. Measured electrical spectrum with single Y-coupled linearized modulation (RBW=50 kHz)

3.4.1.2 Experimental results with a single Mach-Zehnder

In order to compare with conventional architectures the SFDR was measured too using a single MZ-EOM (Photline MX-LN-10-PD) as shown in Figure 109.

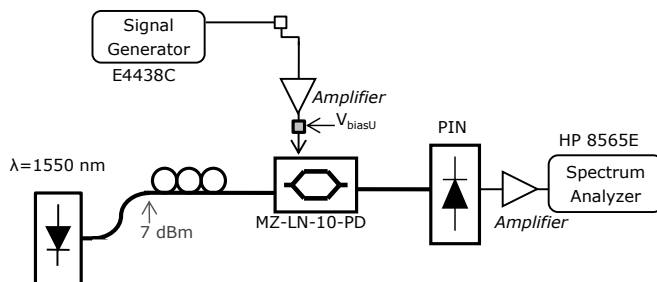


Figure 109. Laboratory setup with a single Mach-Zehnder modulator

In the case of single Mach-Zehnder modulation shown in Figure 110, the highest distortion is produced by third order harmonic, achieving a 19 dB SFDR. Comparing with the linearized modulator the new Y-coupled chip has a 7.3 dB SFDR gain over single conventional Mach-Zehnder.

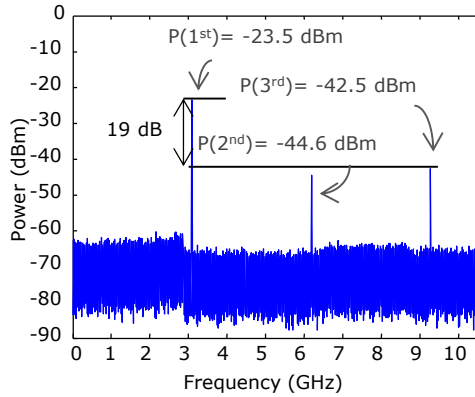


Figure 110. Measured electrical spectrum with a Mach-Zehnder modulator (RBW=50 kHz)

3.4.1.3 Dual-parallel Linearized modulator results

Figure 111 shows the experimental set-up to evaluate the performance of the proposed dual-parallel Y-junction structure. The set-up includes the dual parallel Y-junction architecture fed by a 3.1 GHz (10 dBm) RF tone. The applied V_U corresponds directly to the RF tone, and V_L includes a $\pi/2$ phase shift. The resulting input with this $\pi/2$ phase shift is included in Figure 111. The RF tone is modulated on a CW light (1550 nm, 11 dBm) divided in two branches (7 dBm, E_U and E_L) polarization controlled. Both Y-junctions are biased at quadrature (0.9 V UCELLS5, 2.88 V UCELLS21). The resulting optical signals are combined, photodetected and amplified as in the previous measurements.

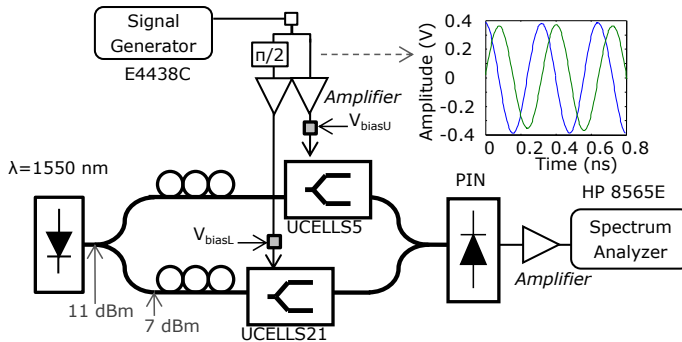


Figure 111. Laboratory setup for dual-parallel Y-coupled linearized modulation

In Figure 112, the first order harmonic has -20.4 dBm power, and the following harmonic with greater power is the second one with -54.6 dBm, achieving a SFDR of 34.2 dB. This means that the dual-parallel architecture improves 7.9 dB the SFDR over a single linearized modulator, and 15.2 dB SFDR over a single conventional Mach-Zehnder modulator.

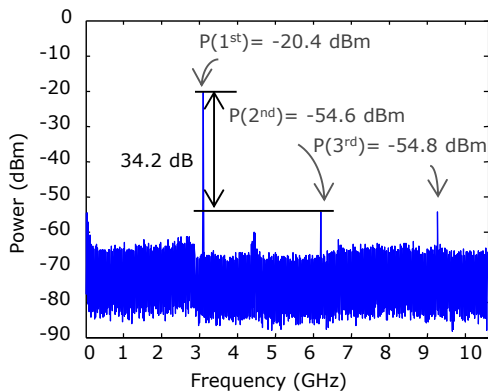


Figure 112. Measured electrical spectrum for dual-parallel Y-coupled linearized electro-optical modulation (RBW=50 kHz)

3.4.1.4 Dual-parallel Mach-Zehnder architecture results

In this case, the performance using a parallel Mach-Zehnder architecture is measured using the laboratory setup shown in Figure 113. In this case, two Photline MX-LN-10-PD modulators substitute the UCELLS5 and UCELLS21 Y-junctions of the proposed architecture. The resulting electrical spectrum is shown in Figure 114 which reveals a 24 dB SFDR, that compared with the dual-parallel linearized result is 10.2 dB lower.

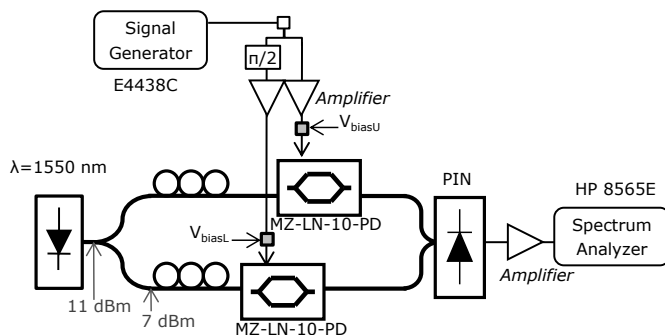


Figure 113. Laboratory setup for dual-parallel MZ-EOM evaluation

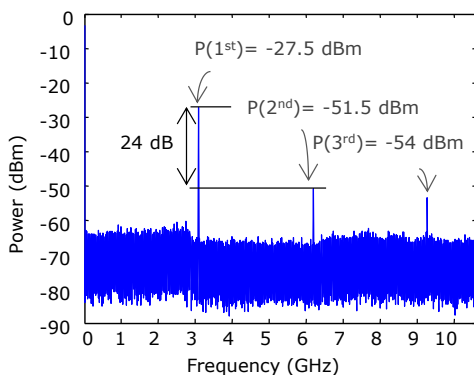


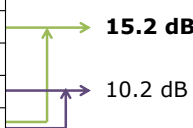
Figure 114. Measured electrical spectrum for dual-parallel MZ-EOM (RBW=50 kHz)

3.4.1.5 Results comparison

From the measurements, it can be observed that in the case of conventional optical links, the 3rd harmonic leads to the highest degradation, as can be seen in the case a single MZ (Figure 110, SFDR of 19 dB). In the case of the parallel architectures, the higher distortion component falling inside the UWB band is the 2nd order harmonic (SFDR of 34.2 dB for the proposed dual-parallel Y-junction, SFDR 24 dB for parallel MZ). As summarized in Table 15, the dual-parallel Y-coupled structure gives 15.2 dB SFDR gain compared with a single MZ, and 10.2 dB improvement compared with the parallel MZ arrangement.

Table 15. SFDR comparison of linearized modulator

	SFDR
Single Mach-Zehnder modulator	19.0 dB
Single Y-junction modulator	26.3 dB
Dual-parallel Mach-Zehnder modulator	24.0 dB
Dual-parallel Y-junction modulator	34.2 dB



3.4.1.6 Linearity after Optical Fibre Transmission

The proposed linearization architecture can be used for radio-over-fibre transmission and photonic-ADC sensing applications that demand high-linear electro-optical behaviour to be able to combine different wireless technologies which require a very high dynamic range. For this reason, the effect of the optical fibre in the proposed dual-parallel linearized architecture is analysed experimentally using the setups shown in Figure 115. In this case, the resulted signal is transmitted through SSMF and DCF.

The resulting spectrum after propagation over 25 km of SSMF is shown in Figure 116. In this case a SFDR of 20 dB is achieved using the dual-parallel linearized architecture. Figure 117 shows the results after propagation over DCF of accumulated dispersion of -1500 ps/nm. In this case, the obtained SFDR is 17.6 dB.

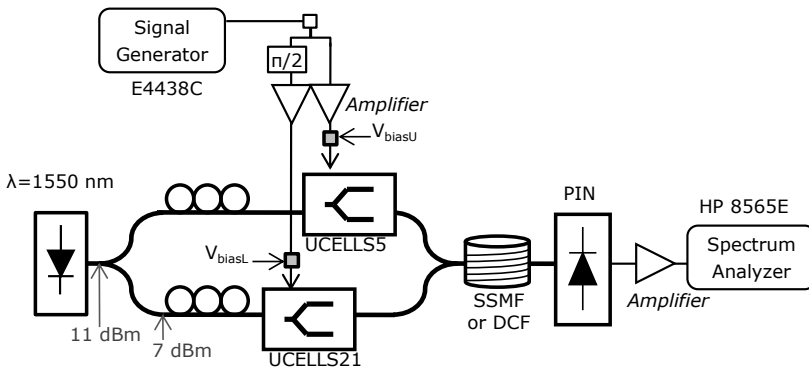


Figure 115. Laboratory setup for the evaluation of the effect of optical fibre transmission

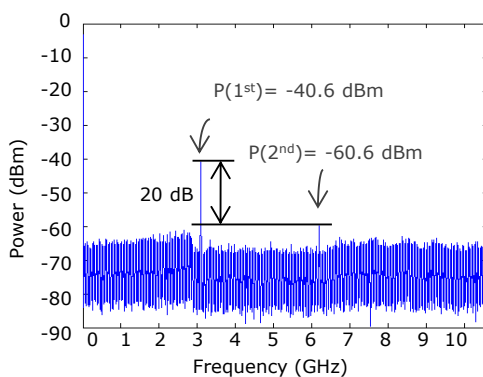


Figure 116. Measured electrical spectrum of dual-parallel linearized modulation after 25 km single-mode fibre (RBW=50 kHz)

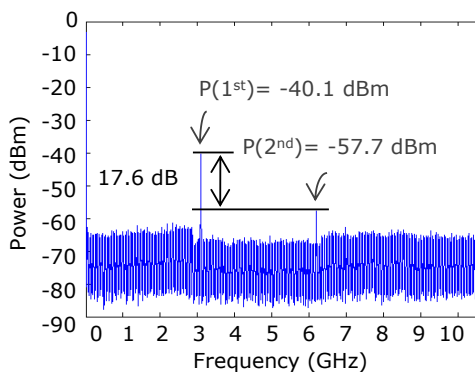


Figure 117. Measured electrical spectrum of dual-parallel linearized modulation after high dispersive fibre of -1500 ps/nm (RBW=50 kHz)

3.4.2. Dual-drive Mach-Zehnder linearized modulator

As it was commented before, radio-over-fibre transmission of several wireless services in coexistence through the same optical network requires EOM with excellent dynamic range and an extensive linear regime. Transmitter digital-to-analog converters for radio systems employing OFDM modulation such as UWB require a linearity of at least 25 dB [91]. Multi-carrier signals with large number of sub-channels like multi-band OFDM-UWB signals have large peak-to-average power ratio (PAPR) which joint with the high bandwidth of each UWB channel (528 MHz) is the main limitation of intensity-modulation systems [92]. In this section, a dual drive (DD) MZ architecture with enhanced linearity and chirp controlled modulation scheme was designed, characterized and applied to radio-over-fibre transmission of high PAPR signals.

Also, radio-over-fibre systems can take advantage of this chirp management as the produced chirp combined with the dispersion the transmission fibre in optical access networks can compensate the effects of the optical transmission and, as a result, improve the overall performance of the system [Alv11]. Chirp control measurements obtained with the developed dual-drive modulator are reported in Annex C. Here, the performance comparison with a conventional Mach-Zehnder modulator is examined. The developed DD-MZ was also assessed in a UWB-over-fibre transmission of high PAPR signals.

3.4.2.1 Modulator design and characterization

The dual-drive modulator architecture is described in Figure 118. It has one broadband RF-electrode per optical arm of the optical interferometer. This DD-MZ requires two electrical signals, each driving the modulator at half the voltage of a single-drive device. Normal operation consists of applying half of the required electrical amplitude on each RF port, RF+ and RF-, with a π phase shift between them: $+V/2$, $-V/2$. By design, both electrodes are synchronized so as to modulate the optical field at the same time and with the same group delays. In standard usage, both modulating signal voltages are equal so as to provide intensity modulation. Naturally, one can modify the amplitude (and phase) of the modulating signals for specific applications.

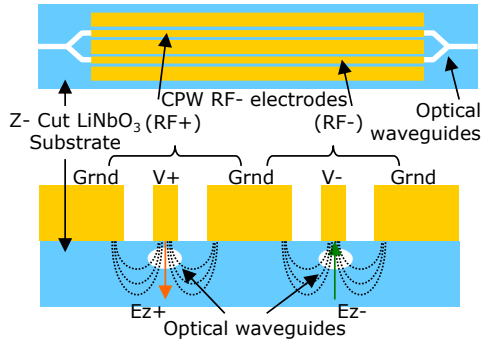


Figure 118. Scheme of the designed dual drive modulator

In this way, the electro-optical field overlap in each arm of the interferometer can be varied significantly if required, leading to the presence or the absence of residual phase modulation and hence frequency chirp control (sign and amplitude). This process can be adjusted so as to mitigate or enhance the effect of fibre dispersion. Moreover, when applying an appropriate phase-delay between input signals (typically $\pm\pi/2$) it is possible to suppress harmonics in the modulated optical spectrum (typically first order modulation harmonic) and a single-side band (SSB) modulation spectrum can be obtained.

3.4.2.2 Comparison of the developed Dual-Drive with conventional modulators

The two-tone performance of the DD-MZ-EOM was evaluated and compared with a conventional single MZ-EOM (Covega LN-058) by considering two sinusoidal signals with frequencies of 4 GHz and 4.7 GHz. The optical link under study is depicted in Figure 119(a) and comprised a continuous wave (CW) laser, the EOM under evaluation fed with the corresponding bias voltage and a PIN photodetector of 10 GHz bandwidth (Discovery DSC-R402AC). The optical power at the input of the EOM was $P_{IN} = 7$ dBm.

Figure 119(b) shows the SFDR performance and the variation of the output optical power of the modulator (in this setup is the power arriving to the photodiode, P_{PIN}), whilst changing the modulator bias voltage. It can be observed firstly that the maximum SFDR is 0.7 dB higher in the dual-drive modulator than in a conventional modulator, achieving 40.6 dB SFDR in the optimum bias point. In addition and which is more important, the linear regime of the modulator is greatly increased using the dual-drive modulation scheme. It can be seen in Figure 119(b) that the SFDR is in excess of 25 dB over 1.4 V range using the DD-MZ-EOM compared with a 0.5 V range in the single-MZ-EOM. This extended linear regime provides significantly more stability for radio-over-fibre systems.

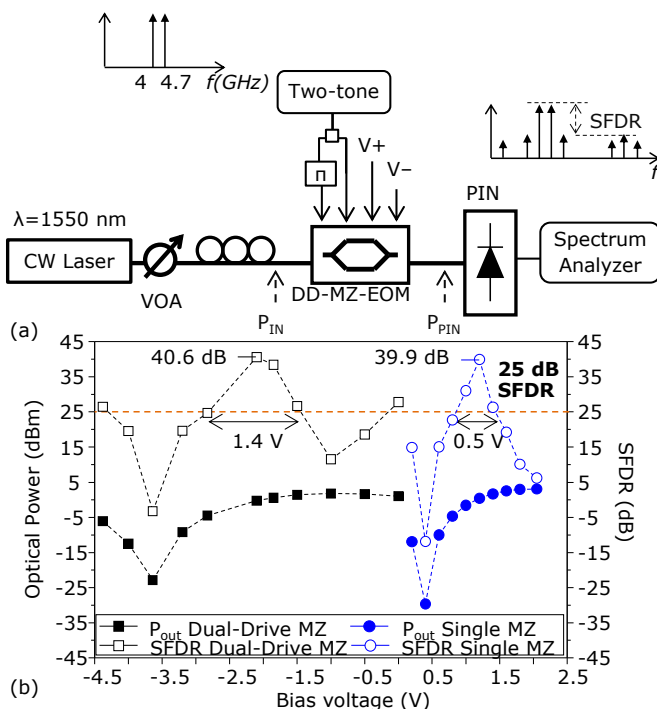


Figure 119. (a) Experimental setup for two-tone distortion evaluation of the dual-drive modulator. (b) Output optical power and SFDR experimental results of the DD-MZ compared with a conventional single MZ

3.4.2.3 Demonstration for High Peak-to-Average OFDM-based transmission

To evaluate the improvement of the DD-MZ in radio-over-fibre applications, an experiment was performed based on UWB radio transmission in passive optical networks as shown in Figure 120(a-b). An OFDM-UWB fully-compliant WiMedia channel centred on 4.488 GHz with 528 MHz bandwidth and using dual carrier modulation (DCM) at 480 Mbit/s [6] was transmitted through different fibre links. DCM MB-OFDM UWB systems have a high PAPR problem [92] which is reduced using the DD-MZ proposed scheme.

Figure 121 shows the EVM performance of both modulators using the OFDM-UWB signal. The EVM limit according to current standards is -17 dB for UWB signals using 480 Mbit/s [6]. In Figure 121, it can be observed that the dual-drive modulator performance is always better when the optical power at the photodiode is more than -10 dBm.

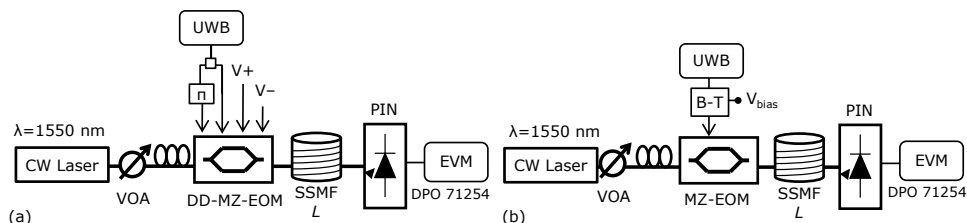


Figure 120. Experimental setup for UWB-over-fibre transmission using: (a) DD-MZ, (b) single MZ-EOM

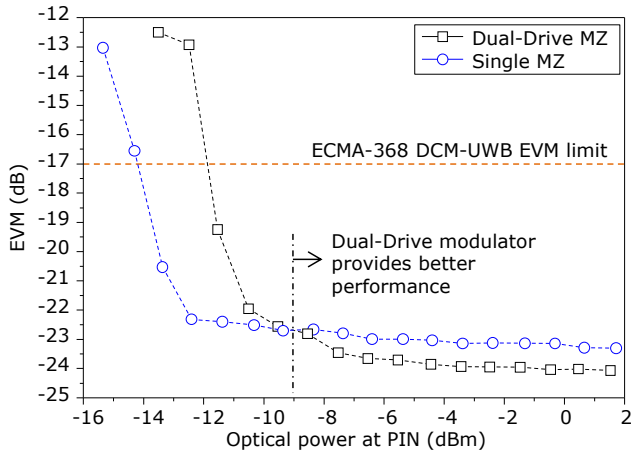


Figure 121. Measured EVM for both single and DD-MZ in back-to-back for different optical power arriving at the PIN photodiode

Figure 122 confirms that the chirp enhances the performance when combined with fibre transmission and this improves with distance. EVM improvements of 1.9 dB and 2.2 dB over 44 km and 57 km SSMF respectively were measured. The DCM OFDM-UWB constellations received after different lengths are compared in Figure 123.

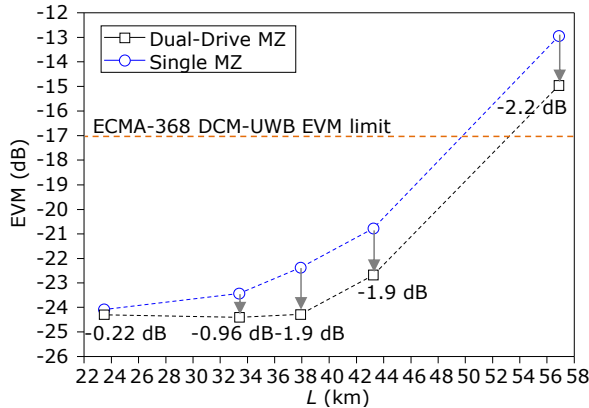


Figure 122. Measured EVM of Dual-Drive MZ compared with Single MZ after different fibre transmission lengths (L). EVM improvement of the DD-MZ labelled for reference

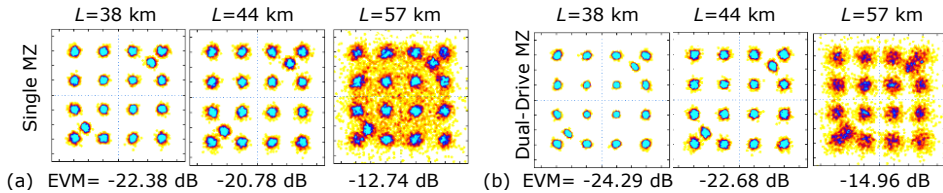


Figure 123. DCM OFDM-UWB constellations comparison

It can be observed that with DD-MZ the EVM limit is met without optical amplification even after 44 km SSMF and after 57 km the clear points of the constellation are still observable with an improvement of 2.2 dB over the performance with a single-MZ.

3.5. Conclusion

In this Chapter, different photonic techniques for UWB radio-over-fibre transmission in pico-cell cluster networks were evaluated. First, the simulation analysis and experimental demonstration of UWB-over-fibre transmission for pico-cell service provision in in-building networks considering SSMF and MMF was developed. From the experimental results we can conclude that impulse-radio UWB requires less optical launched power than its OFDM-UWB counterpart for successful SSMF transmission over a distance of 300 m. Although IR-UWB implementation is more sensitive to variations in the pulse generation and the OFDM-UWB option was more stable. In the case of MMF, the experimental results exhibit a large variance and successful transmission over 300 m can only be achieved at a launched power of 2 dBm for complete OFDM-UWB or 3 dBm for impulse-radio UWB. This behaviour is due to the saturation of the limiting amplifier integrated in the MMF photoreceiver and to the transfer function of the MMF.

Next, a time-stretched Ph-ADC architecture with engineered gain stages has been proposed for the sensing of ultra-low-power pico-cell signals. Radio sensing was demonstrated using a multiplexed multichannel time-stretch photonic-ADC with engineered optical and electrical amplification. Fingerprinting and localization algorithms were developed and tested on UWB signals detected by the Ph-ADC. Proper operation has been demonstrated sampling a radio carrier down to 24.975 μ Vp (-65 dBm) achieving a 20.83 dB SNR. The Ph-ADC uses specialty DCF with stretching factor $M \approx 3.4$. This factor has been confirmed by off-line signal processing.

The proposed multichannel Ph-ADC configuration enables time spectrum gathering from different spatial points simultaneously by precise time-shift optical control, facilitating UWB transmitters' localization. Five sensors are identified as the minimum to achieve 3D localization. The multi-sensor photonic-ADC comprises five branches with time-multiplexing. The full-multiplexed architecture permits capturing the radio signal simultaneously at the different sensors employing a single E-ADC. A full-multiplexed photonic-ADC is demonstrated in the laboratory with precise cleaving of fibres in order to use the same optical source to feed all the sensors in a parallel architecture, only a pair of DCFs to make the λ -to-t conversion and stretching, and a single E-ADC to sample the sensed data. Using different photonic-ADC branches in parallel, the overall cost of the system is reduced. Further processing over the captured data separated by channels is done by ad-hoc algorithms, enabling the detection and localization of UWB transmitters in the area.

A TDoA algorithm has been developed to process the optically sampled data. The target is to obtain the pseudo delay estimation for each branch in the photonic system comprising a single electro-optic sensor. The detailed mathematical process to obtain the position estimation was depicted and confirmed off-line processing on the photonic-ADC sampled data considering actual UWB transmissions.

Applying the developed algorithms on the optically sampled data over five sensors information, the time frequency hopping pattern of an UWB transmission link is correctly identified. The performance of the proposed system is evaluated sensing and UWB communication with the transmitter located at different points of a room. Device localization is achieved applying the ad-hoc TDoA processing algorithm obtaining a mean error of 48.5 cm.

Also in this Chapter, linearization techniques for electro-optical modulators have been investigated. The concept dual-parallel LiNbO₃ Y-Coupled linearized electro-optic modulation has been proposed and demonstrated experimentally. Two linearized Y-junctions have been fabricated, being the performance especially sensitive to the fabrication process. Fabricated devices have been characterized exhibiting 15.2 dB SFDR gain over a conventional LiNbO₃ Mach-Zehnder modulator and 10.2 dB SFDR gain over a parallel Mach-Zehnder architecture. This linearization concept finds application in highly-

linear applications like radio-over-fibre transmission described in Chapter 2 and photonic-ADC sensing like in Section 3.3. The effect of optical fibre has been evaluated achieving a 20 dB SFDR after 25 km SSMF propagation and 17.6 dB after high dispersive fibre with accumulated dispersion of -1500 ps/nm.

Finally, a dual-drive modulator with chirp management was proposed and evaluated for UWB-over-fibre applications. The experimental results show that a linear regime extension with SFDR > 25 dB over 1.4 V bias range is achieved compared with the 0.5 V range of a conventional MZ-EOM. This provides enhanced linearity for radio-over-fibre transmissions. UWB transmission over PON was successfully demonstrated using this dual-drive modulator over 44 km SSMF with EVM < -22 dB. Additionally, chirp and PAPR control improves the UWB EVM by 2.2 dB after 57 km transmission.

CHAPTER 4. COEXISTENCE IN MULTI-STANDARD OFDM-OVER-FIBRE TRANSMISSIONS

4.1. Introduction

Future consumer requirements including high-definition TV on demand, latest generation mobile communications and internet access will require the use of services such as UWB, WiMAX and LTE to be handled over a common system.

Figure 124 shows the proposed integrated approach as compared with a typical FTTH deployment. Figure 124(a) shows a typical access network consisting of an optical line termination (OLT) located at the central office, which multiplexes in wavelength (typically 1310/1490nm for audio and data, 1550 nm for video) the services provided by the FTTH network. After the CO, the optical signal is transmitted (through SSMF) to a fibre distribution hub (FDH) where different drop fibres access a user or a group of users. The FDH include adequate filtering and splicing in 1x16, 1x32, etc. configurations. After the drop fibre, the optical signal arrives to the ONT. ONTs are usually dedicated to an individual end user. ONT equipment is typically located in a basement or a roadside cabinet and may be shared by a group of users.

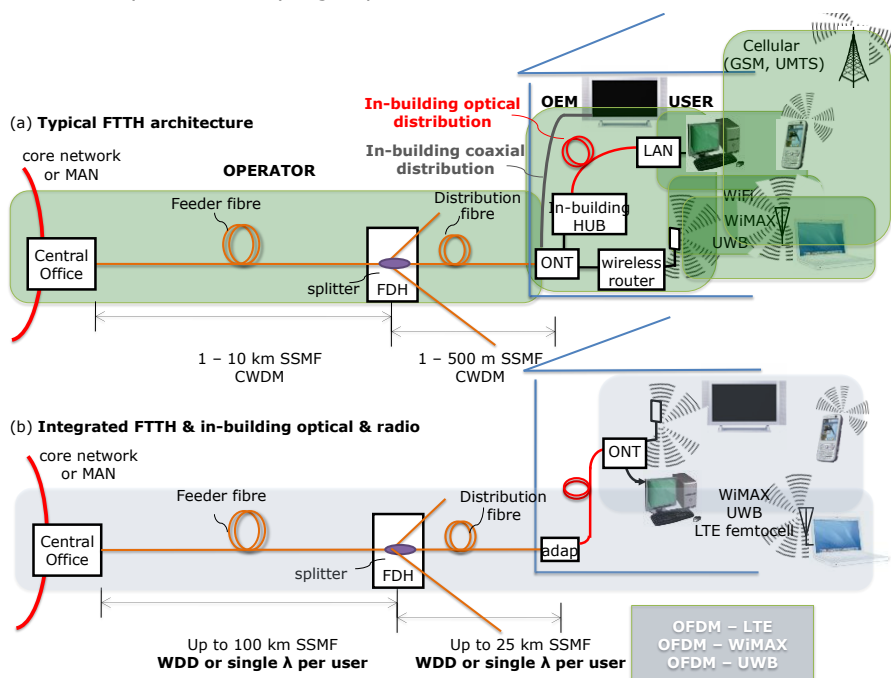


Figure 124. (a) Typical FTTH architecture, (b) proposed integrated FTTH, optical in-building and radio transmission

Focusing in a home user configuration, the most costly scenario from the operators point of view, the signal after the ONT is photodetected and then needs to be demodulated to provide the Internet, audio and video services. The network stops at the entrance of the building. After this point, the user is responsible for the wireless connectivity or the in-building distribution. The end user equipment provides the high bitrate connectivity desired at different locations. The proposed architecture shown in Figure 124(b) integrates the complete optical path (FTTH and the in-building distribution network) and also the user radio path for a converged service provision.

As depicted in Figure 124(b), the network provides different services. In this Chapter the radio-over-fibre distribution of triple-play services with full-standard wireless UWB, WiMAX and LTE signals is evaluated. HDTV is provided by UWB wireless signals in radio-over-fibre, LAN connectivity is provided by WiMAX and cellular phone connectivity is provided by LTE. This approach requires careful coexistence studies of the different signals in radio-over-fibre transmission.

This architecture permits a centralised network management strategy to be used in the WiMAX, UWB and LTE services in a given area, being able to use full-standard equipment at customer premises. In order to evaluate signal performance, current radio standards give a EVM limit of the signal quality at the transmitter antenna. This is set to EVM of -18 dB for GPP LTE signals using 16-level quadrature amplitude modulation (16QAM) modulation, to EVM of -24.43 dB for 802.16 WiMAX using 16QAM, and to EVM of -14.5 dB or -17 dB for ECMA-368 UWB using QPSK or DCM modulation, respectively.

The proposed all-OFDM approach gives clear benefits that can be summarised in:

1. The signals transmitted in the network include fully standard wireless (WiMAX, UWB and LTE) which can be received by low-cost fully standardised user equipment.
2. OFDM intrinsically permits a high degree of multi-path immunity, inherently corrected by the cyclic prefix and by ad-hoc signal processing, GVD and PMD optical impairments can be compensated.
3. Narrowband interference can be seamlessly compensated along the optical and radio paths.
4. Additionally, transmission impairments can be corrected in all baseband and wireless OFDM signals in the optical domain as long as the OFDM signals fall inside the bandwidth of the electro-optic converters.
5. Co-existence techniques can be included at network-level to mitigate channel spectral response issues. Techniques including notch filtering can be used to remove narrowband interference, enabling detection-and-avoid functionalities.

Several experimental studies have been done in the laboratory in order to evaluate different architectures for the distribution of different OFDM signals and are depicted in this chapter:

- The bi-directional optical distribution of simultaneous triple-format OFDM signals (LTE, WiMAX and UWB) in a reflective architecture using reflective electro-absorption transceivers (R-EAT) and in a conventional architecture using Mach-Zehnder modulation is studied. First, the analysis by simulation is performed in Section 4.2.1. In Section 4.2.2 the experimental demonstration of the bi-directional reflective architecture is depicted. Next, in Section 4.2.3, the radio distribution of the simultaneous triple-format OFDM signals (LTE, WiMAX and UWB) after a bi-directional access architecture using MZ-EOM is demonstrated.
- In the case of the bi-directional architecture using MZ-EOM, the wireless path was also evaluated after the access network in order to obtain the radio coverage at customer premises of the triple-format services. This is shown in Section 4.3 of this Chapter.
- Different optical media for in-building distribution after the access network were studied. The performance of ultra-bendable fibre, plastic optical fibre and special optical fibre on OFDM signals is evaluated in Section 4.4. In addition, a deeper study on the triple-format transmission over POF networks was done. This study includes the evaluation of radio-over-fibre transmission after 50 m POF, and also the demonstration of an integrated network including access, in-building and wireless paths.

The experimental work herein reported is part of the developments of the FP7-ICT-FIVER Project funded by the European Commission. FIVER is aimed at developing fully-converged quintuple-play integrated optical-wireless access architectures. The main results of the coexistence of radio-over-fibre signal transmission in access and in-home networks are described in this chapter.

4.2. Optical access architectures evaluation for multi-standard OFDM transmission

A block diagram of each proposed FTTH architecture is shown in Figure 125. Figure 125(a) shows a reflective deployment where both lasers at 1550 nm and 1300 nm are at the central office. The downstream information is modulated with a MZ-EOM and at the customer premises is the R-EAT that absorbs that wavelength λ_1 and the unmodulated light λ_2 is reflected and the upstream 3PLAY data is modulated and sent back to the central office where an optical circulator sends the signal to a PIN detector.

In Figure 125(b) is shown the conventional bi-directional architecture with MZ-EOM that uses two continuous wavelength lasers at 1550 nm and 1300 nm, one for each direction for upstream and downstream data transmission. Both wavelengths are combined and split using CWDM combiner/splitters the received signal then being detected with a PIN photodiode, amplified and demodulated.

In order to include the real behaviour of the electrical and optical components of the system, an experimental characterization has been measured in back-to-back configuration for the R-EAT and conventional system. This characterization has been modelled and included in VPI simulator to obtain the maximum SSMF reach for each architecture.

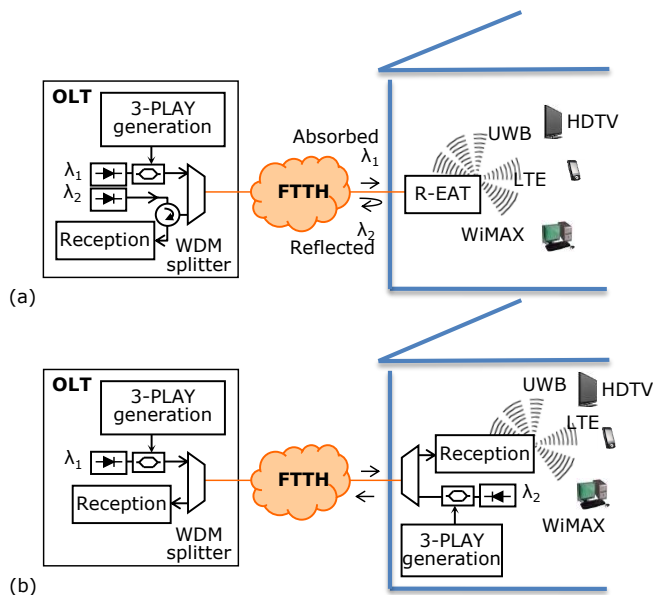


Figure 125. Schematic blocks for FTTH architectures (a) with R-EAT, and (b) with MZ-EOM

In the first stage of the simulation, the electrical power levels of each signal service are evaluated. In practice, generation of the 3PLAY signals is accomplished as follows: First, an advanced LTE signal was generated by a E4438C VSG using frequency division duplex at 2.6 GHz with 16QAM modulation in 20 MHz bandwidth [12]. Secondly, another VSG generated a fixed IEEE 802.16 WiMAX signal at 3.5 GHz using 16QAM $\frac{1}{2}$ (half-rate coding)

in 24 MHz bandwidth [11]. Both LTE and WiMAX signals were demodulated and analysed with an Agilent EXA N9010A signal analyser. And third, UWB signal generation was provided by fully-WiMedia compliant Wisair WUSB dongles using time frequency code TFC6 (centre frequency at 3.96 GHz with 528 MHz bandwidth), and DCM at 480 Mbit/s [6]. All three resulting signals are mixed together with a RF power combiner (MiniCircuits ZN4PD1-50). The received UWB signals after the FTTH back-to-back system were analysed by a Tektronix DPO 71254 oscilloscope.

4.2.1. Simulation studies of optical architectures

Evaluation of the two proposed architectures is based in a simulation study deployed using system-level tool Virtual Photonics VPI 8.3 for the distribution of triple-play services including LTE at 2.6 GHz, WiMAX at 3.5 GHz and a single UWB channel at centre frequency of 3.96 GHz. The schematic of each FTTH architecture is shown in Figure 126.

Included in the simulation approximation are the electrical power levels that can be achieved with conventional electrical amplification. The obtained electrical spectrums, both measured experimental and simulated, are shown in Figure 127.

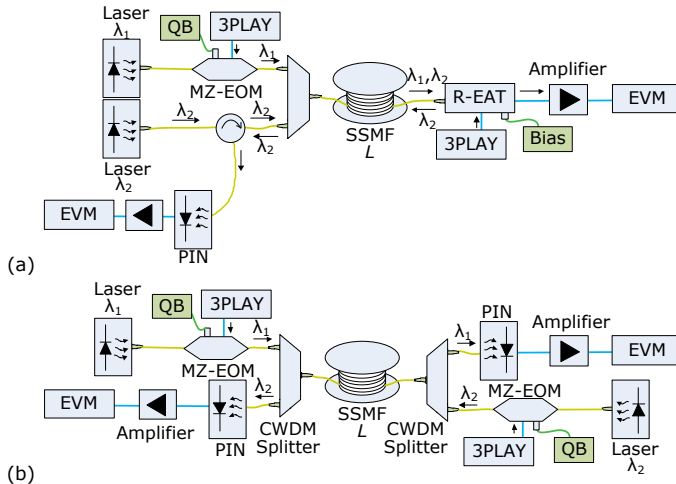


Figure 126. Simulation schematics for FTTH architectures analysis (a) with R-EAT, and (b) with MZ-EOM

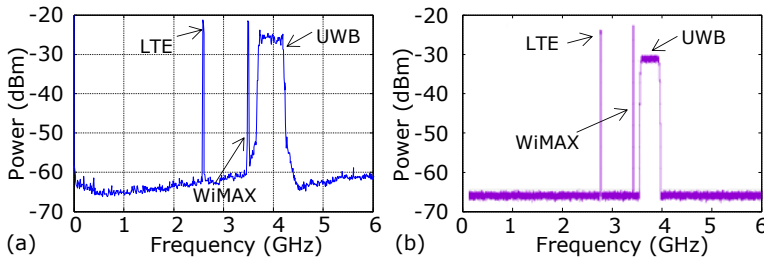


Figure 127. Combined 3PLAY electrical spectrum obtained (a) experimentally, and (b) by simulation

The simulation evaluation is done based on the parameters of the devices that will be used in the experimental demonstration. The main parameters of the components comprising the setups are summarized in Table 16.

Table 16. Simulation parameters according to experimental devices

Device parameter	Value	Device parameter	Value
Laser optical power	[-10 dBm, +15 dBm]	WDM splitter losses	0.5 dB
R-EAT bias	-1.4 V	MZ-EOM V_{π}	3.5 V
SSMF dispersion	17 ps·km/nm	PIN responsivity	0.8 A/W
SSMF length	[0, 100 km]	RF amplifier gain	56 dB

As stated previously, first the back-to-back performance is evaluated with $L=0$ km in Figure 126 for both architectures. The 3PLAY signal is received with the PIN photodiode and each OFDM signal is demodulated with the corresponding radio standard (LTE, WiMAX or UWB) and the EVM is measured. The resulting EVM values were then compared with the maximum limit stated in current standards of each OFDM radio signal. These thresholds are shown in the EVM plots as horizontal dashed lines for comparison.

Figure 128 shows the experimental results and the simulation approximation for B2B configuration for each signal transmitted simultaneously. The experimental results are shown with a filled symbol and the simulation approximation with a dashed line.

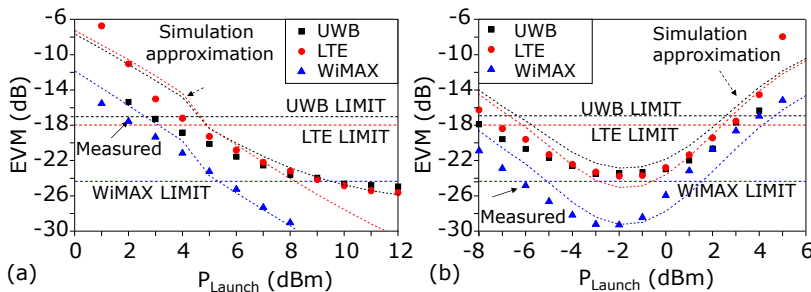


Figure 128. Experimental characterization in filled symbols and simulation approximation in dashed lines for 3PLAY transmission in back-to-back received: (a) absorbed with R-EAT, and (b) by a photodiode PIN

With this simulation modelling, the length of SSMF spools is changed in the architectures to evaluate the maximum reach of each configuration. For comparison the simulation results using this characterization are shown in the next subsections.

According to the reception performance depicted in Figure 128 for both the PIN photodiode and for the R-EAT in absorption configuration, the quality of the radio signals is affected by the device depending on the optical launch power level. This is the same as the received optical level arriving to the reception device. For this reason, the launch power was selected to be the optimum for the performance of the three radio services for each fibre length considered in the system. For example, for $L=0$ km according to Figure 128(a) the optimum optical power level at the central office is of -2 dBm when received with a PIN photodiode.

4.2.1.1 Reflective FTTH architecture with R-EAT simulation

Figure 129 shows the EVM simulation results for the reflective architecture using R-EAT according to the block diagram shown in Figure 126(a). In this case, the reflective architecture is affected by single-wavelength bi-directional distortion effects in the same optical fibre such as stimulated Brillouin scattering (SBS) and the SSMF reach is reduced. In this case the optical SSMF length is analysed from 0 to 40 km.

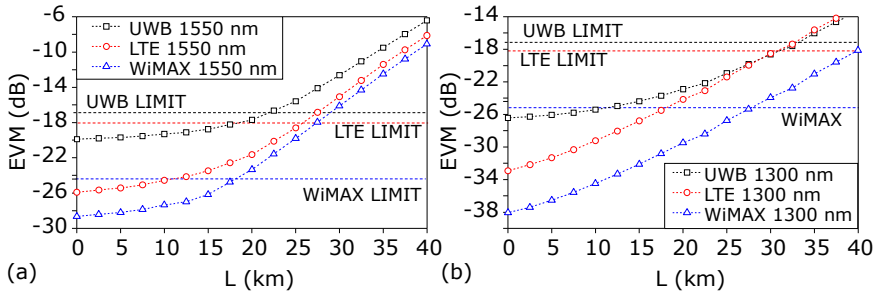


Figure 129. Simulation results for FTTH architecture using R-EAT for the (a) reflected 1550 nm path and (b) absorbed 1300 nm path

Looking at Figure 129(a) in the reflected path working at 1550 nm the maximum FTTH reach is 25.8 km for LTE, 18.1 km for WiMAX and 21.9 km for UWB. If we observe the behaviour of the absorbed path at 1300 nm, then the maximum reach is 31.1 km for LTE, 29.2 km for WiMAX and 33.4 km for UWB. For the overall architecture we can say the 3PLAY provision can be achieved up to 18.1 km in this case limited by the reflected path due to single-wavelength bi-directional distortion.

4.2.1.2 Bi-directional architecture with MZ-EOM simulation

Using the block diagrams of the FTTH architecture shown in Figure 126(b) the optical launch power and the SSMF length parameters have been evaluated to obtain the maximum reach of the FTTH architecture when using MZ-EOM and PIN for the modulation and reception respectively of the optical signals working in CWDM at 1550 nm and 1300 nm.

Figure 130 shows the EVM of each received radio signal when transmitted through a spool of SSMF with length L ranging from 0 to 100 km with the optimum optical launch power level for both wavelengths without dispersion compensation or intermediate optical amplification stages. The 3PLAY signals comprising LTE, WiMAX and UWB are transmitted simultaneously and after photodetection they are demodulated independently according to each radio standard.

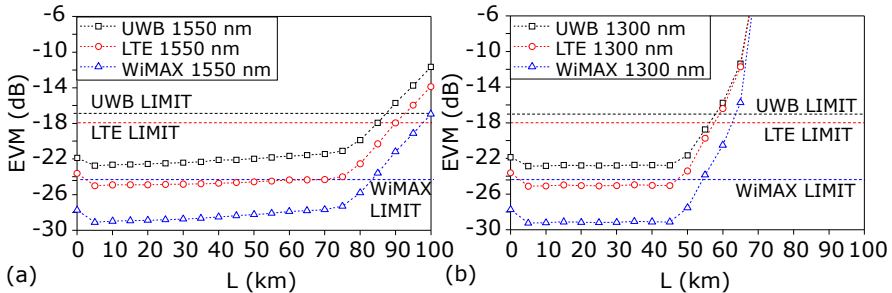


Figure 130. Simulation results for CWDM with MZ-EOM working at (a) 1550 nm and (b) 1300 nm

According to Figure 130(a), when using 1550 nm the maximum FTTH reach is 89.8 km for LTE, 83.3 km for WiMAX and 86.9 km for UWB comparing the received EVM with the corresponding thresholds. For the 1300 nm wavelength the maximum reach is 57.6 km for LTE, 54.6 km for WiMAX and 57.9 km for UWB. This set a maximum reach for the combined 3PLAY service distribution of 54.6 km limited by the performance of WiMAX in the 1300 nm path due to its restrictive EVM threshold of -24.43 dB for 16QAM signals.

Using this simulation modelling, the maximum SSMF reach of the distribution architecture is summarized in Table 17.

Table 17. Summary of simulation results obtained for 3PLAY distribution in FTTH

Service	Reflective FTTH using R-EAT		FTTH with MZ-EOM and PIN	
	1550 nm path	1300 nm path	1550 nm path	1300 nm path
LTE	25.8 km	31.1 km	89.8 km	57.6 km
WiMAX	18.1 km	29.2 km	83.3 km	54.6 km
UWB	21.9 km	33.4 km	86.9 km	57.9 km

From these results, it can be observed that the CWDM architecture with MZ-EOM achieves up to 54.6 km SSMF in bi-directional operation while the reflective architecture achieves 18.1 km without using intermediate optical amplification levels or chromatic dispersion compensation. The reflective path performance is affected by the distortion effects of single-wavelength bi-directional transmission in the same optical fibre. However, all the ranges fit with conventional passive optical network systems which usually have less than 20 km SSMF distribution.

4.2.2. Experimental demonstration of bi-directional reflective architecture using R-EAT

As it was commented before, this reflective architecture is based on a R-EAT. The R-EAT operates at two optical wavelengths, at 1300 nm in absorption mode where it acts as a photodiode and at 1500 nm it acts as a reflective modulator. Both functions share a common RF signal port, so in order to assess the device performance with our system, each path was considered separately.

For the purposes of continuity both the 1300 nm downstream (DS) and 1500 nm upstream (US) experimental systems were identical [Mor11b]. Each setup differs only in the positioning of the signal generation and signal analysis equipment, these being transposed for US and DS measurements. Shown in Figure 131 is a schematic diagram of the experimental system.

The initial task of the experimental proof-of-concept was to assemble a system capable of generating 3PLAY (LTE, WiMAX and UWB) wireless signals. Additionally this system must also be capable of the simultaneous transmission of all three formats with control over the relative power level of each signal. In order to accomplish this, two ESG Agilent E4438C were used to construct WiMAX and LTE signals and a Wisair WUSB dongle to generate the UWB waveform. The UWB signal was then amplified using an ERA Wideband WBA3-4-15G28Vp22RF amplifier with series 16 dB attenuator to the maximum level without the occurrence of spectral re-growth. This defined the maximum of the UWB signal. Relative levels of the LTE and WiMAX signals were then established empirically so as to obtain optimum EVM values for all three formats.

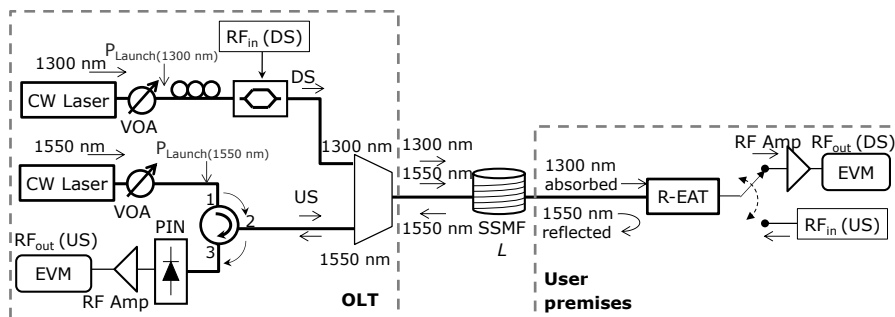


Figure 131. Experimental setup of reflective architecture

When performing the analysis of each individual format, care was taken to ensure that all three wireless signals were present at the same point in time. Due to the non-synchronised nature of the wireless bursts a time domain plot is difficult to interpret. To overcome this, spectral plots and spectrograms were used to establish simultaneous presence and guarantee accurate representation of any effects resulting from format coexistence. Figure 132 shows the resulting composite multi-standard wireless signal.

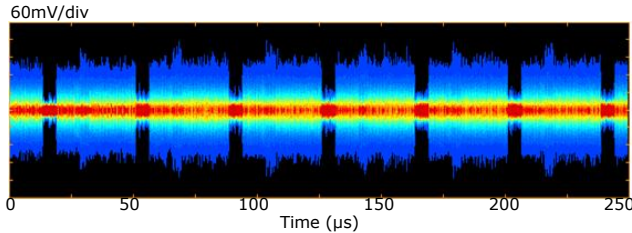


Figure 132. Time domain plot of the triple format signal

The 3PLAY signal is composed by: (i) an advanced LTE using FDD at 2.6 GHz with 16QAM in 20 MHz bandwidth [12], (ii) IEEE 802.16 WiMAX at 3.5 GHz using 16QAM in 24 MHz bandwidth [11], and (iii) WiMedia UWB carrier 2 centred at 3.96 GHz (time frequency code TFC6) with dual-carrier modulation DCM (480 Mbit/s) in 528 MHz bandwidth [6].

This procedure was adopted throughout the system evaluation using a Tektronix DPO 71254 oscilloscope running UWB analysis software. In conjunction with this an Agilent EXA N9010A spectrum analyser running VSA software was used to demodulate and analyse LTE and WiMAX. The resulting demodulated constellation diagrams are shown in Figure 133. It can be seen that at these chosen amplitude ratios all three formats exhibit EVM values that are well within that as laid down in their respective standards.

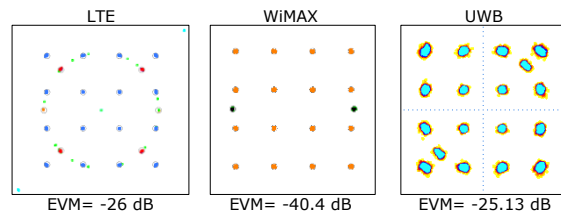


Figure 133. Constellation diagrams of triple format RF signal

With the wireless generation and analysis techniques established, it was then possible to examine the characteristics of the R-EAT and its influence on the system performance in both absorption and reflective modes.

4.2.2.1 Downstream path performance at 1300 nm

With the system set up as shown in Figure 131, it was first necessary to establish optimal conditions for the Covega LN-058 MZ-EOM. A DFB-1310-BF-31-CW-FC-537 1360nm Laser was biased at 100 mA to provide 14.5 dBm optical power to the input of an optical attenuator, this was then passed via a polarization controller to the MZ-EOM. The composite RF signal was then applied to the MZ-EOM which was biased to produce optimal EVM. The optical power was then varied in order to establish the suitability and performance of the MZ-EOM. Following the MZ-EOM, the transmission path is via the 1300 nm arm of a CWDM splitter to various lengths of SSMF and finally on to the R-EAT. The R-EAT was biased at the optimum point of -1.4 V and the resulting signals amplified by 56 dB preceding demodulation analysis.

Initially the R-EAT was directly connected to the MZ-EOM in order to evaluate the back to back performance of the device. Figure 134 indicates a trade off in optical launch power

and EVM performance, likely to be due to degradation in SNR as the optical power is decreased. Saturation effects are beginning to become apparent at the higher levels as indicated by the levelling off of plot gradient. The received signals for all three formats are compared with the acceptable EVM threshold levels stated in current standards.

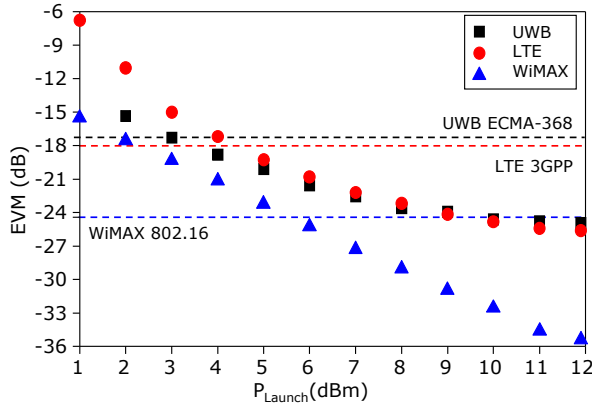


Figure 134. EVM performance of R-EAT for 1360 nm path at $L=0\text{km}$

The focus now moved to establishing the maximum useful reach of the system. To do this the technique employed was to introduce various lengths of SSMF as indicated in Figure 131 and adjust the optical launch power to compensate for system losses and so produce optimal EVM in the recovered signals.

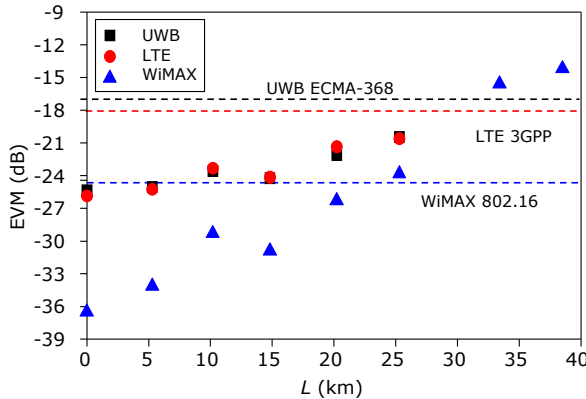


Figure 135. EVM vs fibre length 1360 nm path

As can be seen in Figure 135 the maximum reach for all formats is between 20 km to 25 km if standards compliance is to be maintained. Accompanying constellation diagrams are shown in Figure 136 indicating an upper range limit of 25.3 km.

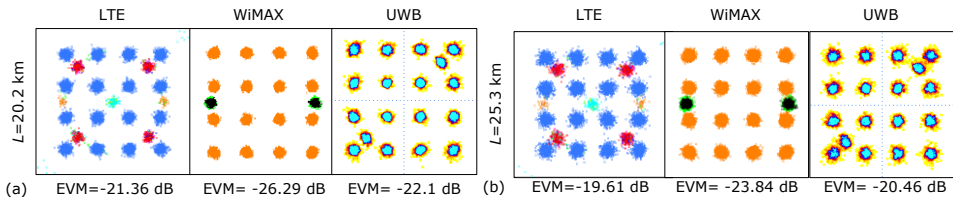


Figure 136. Constellations obtained at (a) 20.2 km and (b) 25.3 km

4.2.2.2 Upstream path performance at 1500 nm

The experimental system was now reconfigured for the upstream path from customer premises back to the OLT as shown in Figure 131, modulation now being achieved in reflection by the R-EAT itself. Optical power is now generated by a Fitel FOL15DCWD-A81-19270-B, 1557nm DFB laser producing a launch power of 14.5 dB; this is followed by an optical attenuator so that power may be optimised as before. From here the 1557 nm CW path leads to port 1 of an optical circulator, port 2 being connected to the 1500 nm arm of the CWDM coupler and fibre link to the R-EAT as before. In this mode the triple format RF signal is applied to the R-EAT and directly modulates the now reflected 1557 nm optical signal. After propagation through the optical fibre and returning through the CWDM coupler and port 2 of the circulator the modulated signal emerges at port 3 of the circulator and is applied to a Discovery DSC-R402AC photo receiver. It should be noted that this device contains approximately 20 dB of amplification. A further 36 dB of amplification were then applied to the now RF signal (56 dB total) before demodulation and analysis as previously described.

Using the same composite wireless signal as defined previously, this time applied directly to the RF input of the R-EAT the device was again characterised, this time in reflective mode. As before, with the device connected directly to the CWDM splitter EVM levels were recorded for differing optical power levels. Figure 137 indicates the optical operating power levels and the corresponding EVM's obtained, appropriate standards thresholds are indicated, above which each format does not comply with the required signal quality. As with absorption mode the WiMAX format exhibited the most sensitivity to power level variation, suggesting that this was due to close proximity to the UWB (Carrier 2) signal.

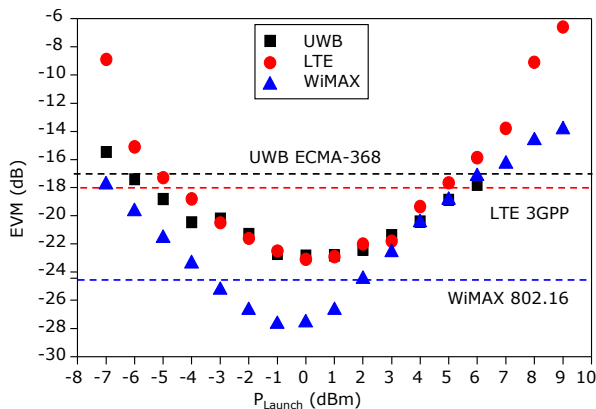


Figure 137. EVM performance of R-EAT for the upstream 1557 nm path in B2B ($L=0$ km)

In order to establish the maximum range of deployment of the R-EAT in reflective mode, the optical signal now travelling to the R-EAT and back again to the receiving photodiode.

Once again the optical power levels were optimised at each point and EVM values recorded. Shown in Figure 138 is the resulting plot, it can be seen that the WiMAX format fails to meet the required compliance level at a range of 15 km. This limits the overall operating distance of the device to this distance without the use of error correcting techniques.

Constellation plots of all three formats were also recorded at the 15 km and 20 km distances as shown in Figure 139. The upper section of the figure shows the constellations at 15 km and the lower at 20 km distances. As it can be seen in the constellations, at 20 km distance all three formats begin to degrade to the point where error correction will become necessary.

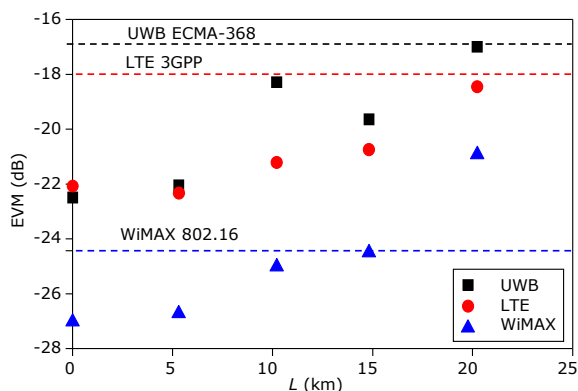


Figure 138. R-EAT system range capability

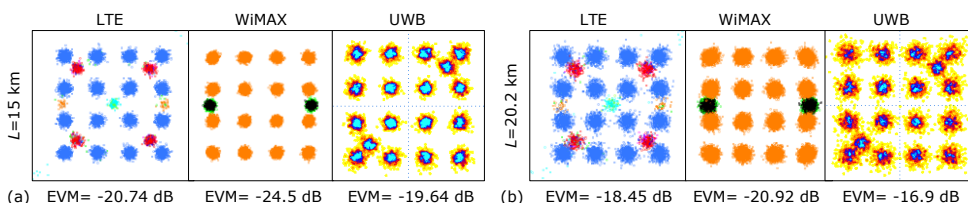


Figure 139. Constellations obtained at (a) 15 km and (b) 20 km

4.2.2.3 R-EAT cross-talk evaluation measurements

The R-EAT has a common upstream/downstream RF port so there will be inevitable collision/crosstalk of the two paths at this point that will require a switching arrangement. If crosstalk occurs in the optical domain this will necessitate optical splitting and the power sensing and switch arrangement to be extended. This would result in further loss in optical sensitivity and increased system complexity.

Using the previously established working power and signal levels, the downstream 1300nm signal (Figure 140(a)) was applied to R-EAT. A spectrum analyser was then deployed at the photoreceiver / RF amplifier output on the 1500 nm upstream path. The resulting trace is shown in Figure 140(b) (lower trace represented in red). To confirm that operating levels were appropriate the system was then operated in its 1500 nm upstream mode as shown in Figure 140(b). A comparison of these traces indicates that 1300 nm/1500 nm crosstalk is in the region of -40 dB.

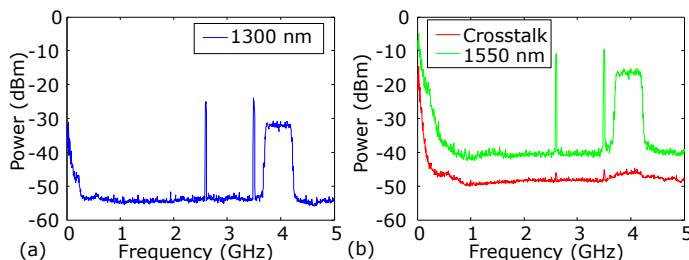
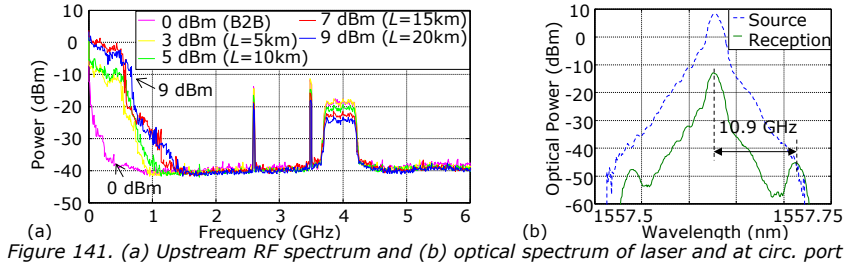


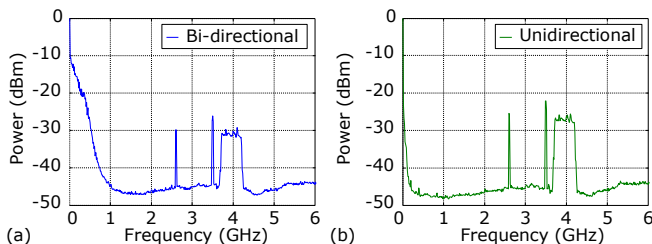
Figure 140. (a) Downstream 1300 nm signal (b) Upstream 1500 nm and crosstalk (lower)

Over the course of the above measurements, it was apparent that significant levels of RF noise were being experienced at the lower end of the spectrum, below 2 GHz, in the reflective 1500 nm upstream path. Both the amplitude and the bandwidth of this

phenomenon were seen to vary with the length of the fibre deployed and consequent laser power required. This is shown in Figure 141(a) where a comparison of the various RF spectra associated with range/launch power variation can be seen, compared with the back to back performance of the R-EAT working at 0 dBm launch power where this noise does not appear.



Signal generation amplitude levels far in excess to that of the wireless format levels can be seen, whilst out of band this will inhibit the use of the system for operation in this frequency region. On investigation of the optical system the cause of this was found to be stimulated Brillouin scattering (SBS). Shown in Figure 141(b) are the optical spectra obtained at the output of the laser (dotted line) and after reflective transmission through the system (solid line) with no modulation present. The generation of sidebands can be seen in this optical spectrum at a frequency spacing of 10.9 GHz, typical of those associated with SBS. This effect was strongly enhanced by single-wave, bi-directional transmission due to optical mixing of the reflected optical wavelength from the R-EAT combined with the forward transmission path within the fibre. This was confirmed by relocating the fibre to implement/remove bi-directional transmission. Figure 142 shows that the noise disappeared when there is no single-wavelength bi-directional transmission.



4.2.3. Experimental demonstration of bi-directional conventional Mach-Zehnder architecture

Bi-directional full-duplex transmission is achieved with coarse wavelength division multiplexing (CWDM) using two simultaneous paths in opposite directions at 1300 and 1550 nm. Opportunities for PON network spans up to 120 km without optical amplification or regeneration stages are considered in the experiment and the maximum reach whilst fulfilling current end user radio standard specifications is evaluated [Mor11c].

The full duplex optical transmission path is shown in Figure 143. The combination of the UWB, WiMAX and LTE signals was achieved using a RF power combiner (MiniCircuits ZN4PD1-50). These resulting composite signals were then applied to MZ-EOMs (Covega LN-058) working at quadrature bias point for each 1300 nm and 1550 nm path. As shown, polarisation and optical attenuation control was added prior to the MZ-EOMs to facilitate signal optimisation. CW lasers, each launching 14.5 dBm (Applied Optoelectronics Inc.

DFB-1310-BF-31-CW-FC-537 and Fitel FOL15DCWD -A81-19270-B), provided the 1300 nm and 1550 nm paths respectively.

The variable optical attenuators allow emulation of the optical launch power level used by operator defined as P_{Launch} . Both paths were then combined using CWDM splitters (LAS-10-086), providing 40 dB channel isolation. Standard single mode fibre was used as the transmission medium throughout the experiment. Signal detection was accomplished using 10 GHz bandwidth photodiodes (Discovery DSC-R402AC) in both directions followed by 52.5 dB RF amplification in both paths.

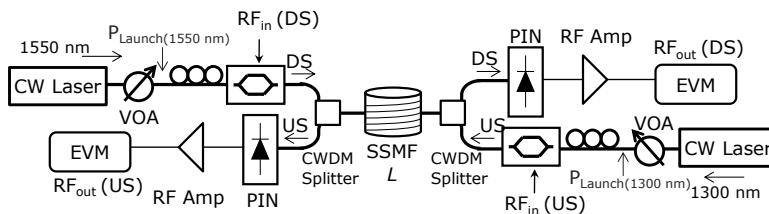


Figure 143. Experimental setup for 3PLAY distribution in CWDM architecture

UWB signal generation was provided by fully- WiMedia compliant Wisair WUSB dongles using time frequency code TFC6 (centre frequency at 3.96 GHz with 528 MHz bandwidth) and DCM working at 480 Mbit/s [6]. The UWB signals were analysed using a Tektronix DPO 71254 oscilloscope. An Agilent EXA N9010A signal analyser and two E4438C vector signal generators (VSG) provided signal analysis and generation for the LTE and WiMAX signals respectively. The first VSG generated a fixed IEEE 802.16 WiMAX signal at 3.5 GHz using 16QAM $\frac{1}{2}$ (half-rate coding) in 24 MHz bandwidth [11] (41.75 Mbit/s). An advanced LTE signal was generated by the second unit using frequency division duplex at 2.6 GHz with full-filled 16QAM in 20 MHz bandwidth [12] (67.2 Mbit/s). Figure 144(a) shows the electrical spectrum of the combined signals (RF_{in}).

As it was commented in Section 4.2.2, in a real life scenario all wireless formats may exist simultaneously. Due to the “burst nature” of these signals, all should be present during analysis. Figure 144(b) shows a typical spectrogram which, with signal capture, ensures that this “worst case” coexistence condition was present at the time of analysis; this technique being used for all experimental analysis. The performance of both directions of the system was then evaluated in a B2B configuration with no fibre present.

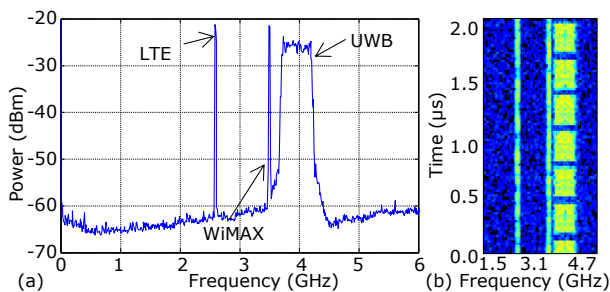


Figure 144. (a) Generated electrical spectrum (RF_{in}), (b) spectrogram of signals coexistence

In order to evaluate signal performance, each service (UWB, LTE and WiMAX) was demodulated and the EVM was calculated. The results were compared with the maximum EVM limit stated in the current standards of each radio signal, as depicted before. These current standard thresholds are drawn in the EVM plots for comparison.

Figure 145 shows the resulting EVM vs. optical launch power plots for both optical paths in a B2B configuration. It can be observed that the EVM performance curves for all wireless formats closely tracked each other indicating optimal modulation conditions. The best performance was obtained at optical power levels of -2 dBm at 1550 nm and -1 dBm at 1300 nm.

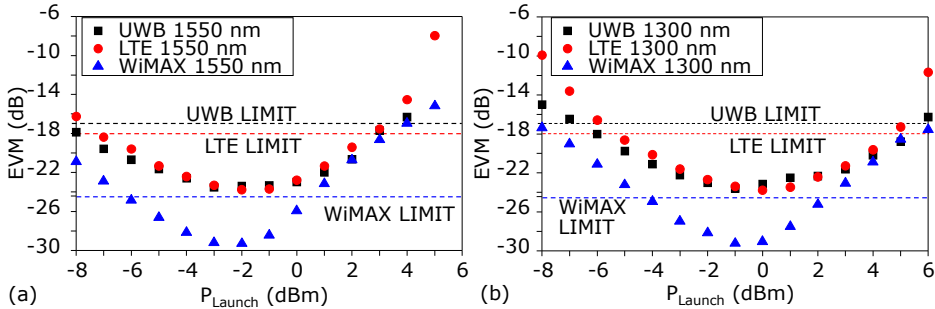


Figure 145. LTE, WiMAX and UWB EVM performance with launch power at (a) 1550 nm and (b) 1300 nm

Shown in Figure 146 are the resulting constellation diagrams of the simultaneously transmitted triple format radio over fibre signals.

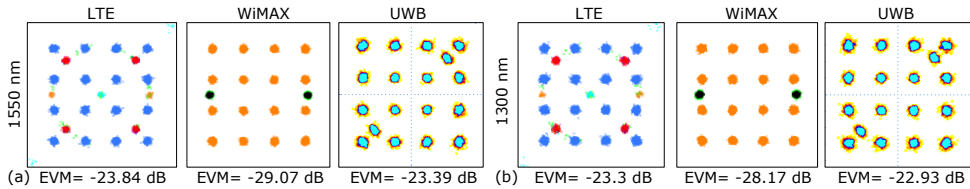


Figure 146. Constellations and EVM of the received LTE, WiMAX and UWB signals in B2B configuration: (a) $P_{Launch} = -2$ dBm at 1550 nm, and (b) $P_{Launch} = -1$ dBm at 1300 nm

These constellations indicate that channel performance always met and often exceeded the respective wireless standards specifications. With this base condition established, overall system performance was investigated by increasing fibre length whilst maintaining optimal power levels at the respective photodiodes. This procedure was repeated until the measured EVM performance of each format fell outside acceptable levels.

Figure 147 shows the measured EVM for each radio signal LTE, WiMAX and UWB in each CWDM path after propagation on different spools of SSMF.

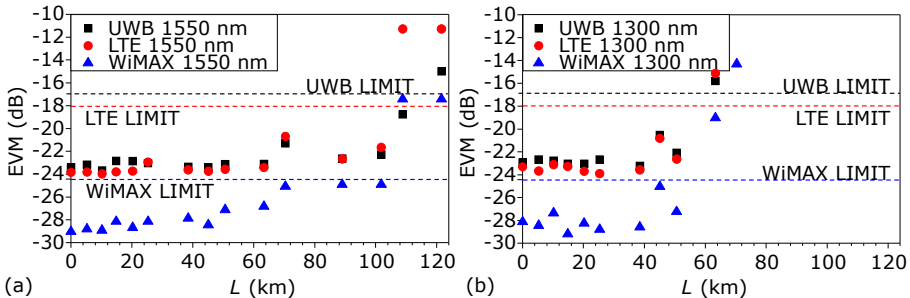


Figure 147. Measured EVM on LTE, WiMAX and UWB signals on the (a) 1550 nm and (b) 1300 nm path

It can be observed in Figure 147(a) that the 1550 nm path reaches up to 101.8 km SSMF with the three signals meeting the stipulated thresholds. The degradation of the constellations when using even more fibre is shown in Figure 148.

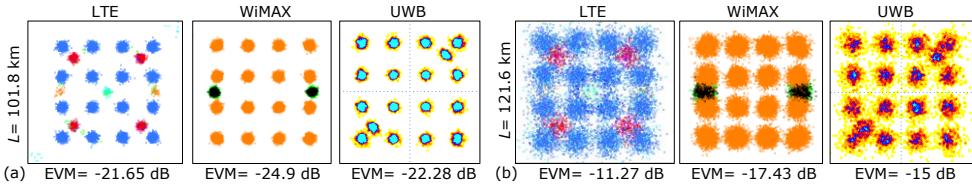


Figure 148. Constellations and EVM of the received LTE, WiMAX and UWB signals at 1550 nm with $P_{Launch}=14.5$ dBm after: (a) $L=101.8$ km, (b) $L=121$ km

However, the bidirectional reach of the architecture is limited by the 1300 nm path as shown in Figure 147(b). Here, the maximum distance over which 3PLAY signals comply with the radio standards at 1300 nm wavelength is 50.6 km.

The constellation degradation is shown in Figure 149, where Figure 149(b) shows that symbol mutilation begins at $L=63.3$ km for the 1300 nm path.

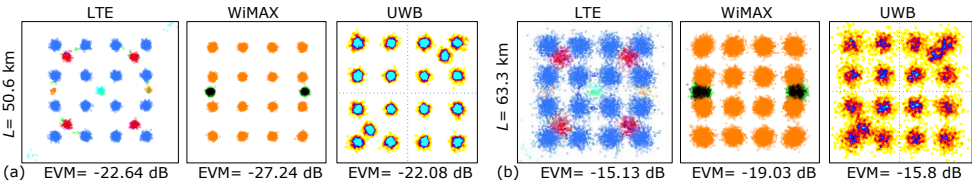


Figure 149. Constellations and EVM of the received LTE, WiMAX and UWB signals at 1300 nm with $P_{Launch}=14.5$ dBm after: (a) $L=50.6$ km, (b) $L=63.3$ km

As expected, the higher losses of the fibre at 1300 nm dictate that signal-to-noise ratio (SNR) is reduced more rapidly with increasing the fibre length than in the 1550 nm path. This effect can be seen in Figure 150, which shows the electrical spectrum of the received signal for both paths. It can be observed that, when the signals satisfy the required limits, the SNR is very similar in both directions: 24.2 dB in the 1550 nm path after 101.8 km, and 23.5 dB in the 1300 nm path after 50.6 km SSMF. This confirms that, for the same PON reach, the 1300 nm path needs more launch power than the 1550 nm path. It is clear that signals with <14 dB SNR do not fulfil the wireless channel specifications.

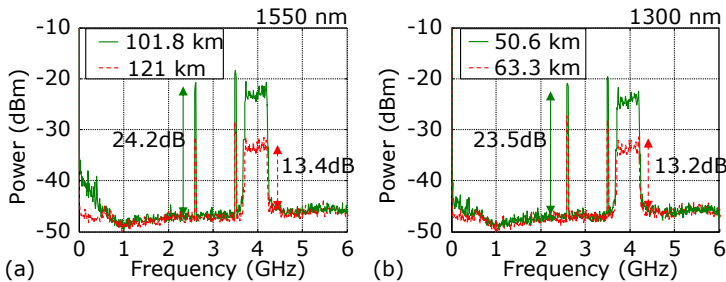


Figure 150. Electrical spectrum and signal-to-noise ratio received at (a) 1550 nm ($L=101.8$ and 121 km) and (b) 1300 nm ($L=50.6$ and 63.3 km)

4.3. Access and wireless transmission evaluation

Following the experiments depicted in Section 4.2.3, in this section the integration of the wireless path after radio-over-fibre transmission through the access FTTH network is demonstrated as shown in Figure 151(a). This aims to obtain the maximum radius coverage that we can achieve with the 3PLAY radio services with a wireless link as depicted in Figure 151(b).

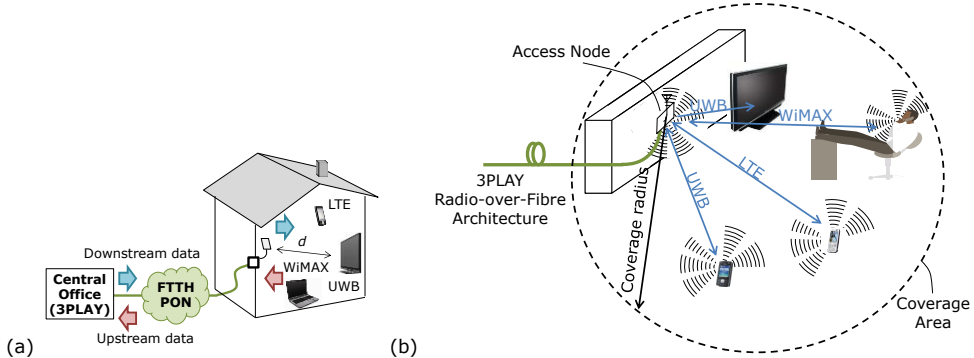


Figure 151. (a) Application scenario of 3PLAY bidirectional radio distribution after FTTH access networks, and (b) wireless coverage investigation

Figure 152 shows the experimental setup developed for evaluating the bi-directional radio-over-fibre communication system delivering triple-play services from a central office to the user premises using a PON in FTTH including the radio path [Mor11d]. At customer premises the signal is converted from optical to electrical and radiated wirelessly to the end user. The radio-to-optical interface is studied for radio distances d up to 4 m.

The OFDM radio signals used are the same standard signals as used in the previous experiments: (i) an advanced LTE signal using FDD at 2.6 GHz with full-filled 16QAM in 20 MHz bandwidth according to 3GPP standard, (ii) a fixed IEEE 802.16 WiMAX signal generated at 3.5 GHz using 16QAM $_{1/2}$ in 24 MHz bandwidth, and (iii) WiMedia-compliant UWB signal generated with Wisair WUSB dongles using time frequency code TFC6 at centre channel 3.96 GHz with 528 MHz bandwidth using QPSK modulation at 200 Mbit/s or DCM at 480 Mbit/s.

The spectrums of the RF signal at critical points in the system are shown in Figure 153. At the RF signal generated at the central office (point (1) in Figure 152), the SNR is around 40 dB. This was applied to a quadrature biased Mach-Zehnder modulator (MZ-EOM: Covega LN-058). From here the signal was passed to the 1550 nm arm of a CWDM splitter, providing better than 40 dB channel isolation, and then propagated through 20.2 km SSMF.

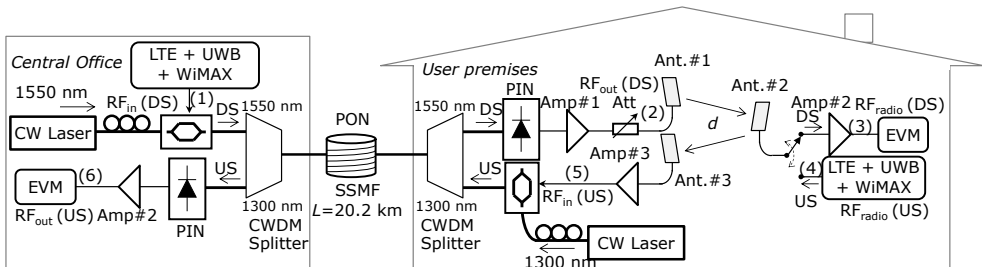


Figure 152. Experimental setup for bidirectional LTE, WiMAX and UWB distribution in FTTH networks and radio propagation at user premises

At user premises an identical CWDM splitter feeds a Discovery DSC-R402AC photodiode and an RF amplifier of 42 dB gain. The lasers for both downstream and upstream directions (1550 and 1300 nm respectively) were configured to have a -13 dBm optical power level at the input of the photodiode at both ends.

Before wireless transmission (point (2) in Figure 152) the SNR is in excess of 20 dB and all three formats were configured to be standards-compliant including UWB restrictive spectral mask of -41.3 dBm/MHz. RF attenuator situated before Ant#1 is used to ensure that the radiated power from the does not breach the standards. The antennas used are Omron WXA-N2SL wide-band monopole omni-directional antennas with a gain of 2 dBi approximately.

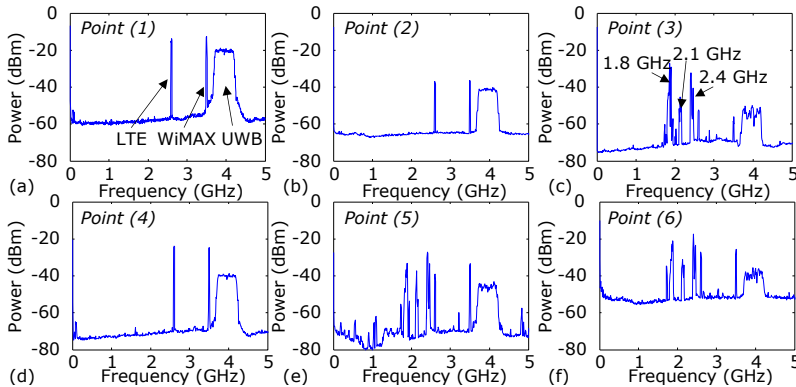


Figure 153. Electrical spectrums measured at different points of Figure 152. Downstream 1550 nm path (a) before MZ-EOM, (b) after 20.2 km SSMF before the antenna, and (c) after 3 m radio propagation. Upstream 1300 nm path (d) before the antenna, (e) before the MZ-EOM after 3 m radio propagation and (f) after 20.2 km SSMF

The available channel bandwidth was assessed using an Anritsu 37397D network analyser in Figure 154. It can be seen that coverage from 1 GHz to 6 GHz is possible allowing potential expansion for use with other wireless formats. A second antenna (Ant.#2) is located at the wireless client devices. At this point a Tektronix DPO 71254 scope was used to examine the UWB signal and an Agilent EXA N9010 signal analyser running Agilent VSA software demodulated and analysed LTE and WiMAX. Also at this point a RF switch and amplifier (40 dB) are incorporated to facilitate the analysis equipment used. Such switching is not normally needed as the wireless devices accommodate this as standard functionality. In the spectrum of the received signal at point (3) it can be seen that unwanted spectral components emanating from mobile phones (1.8 GHz and 2.1 GHz) and WiFi (2.4GHz) are present. As this system is designed to operate in "real world" conditions this is to be expected and correctly conditioned OFDM based signals are able to co-exist under these conditions.

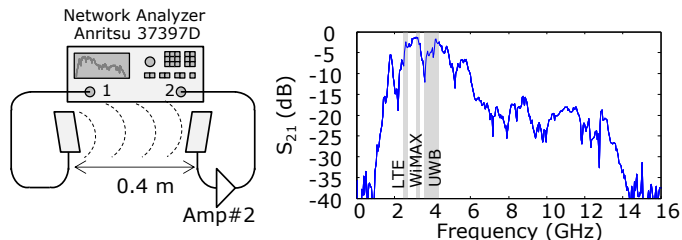


Figure 154. Radio channel response measured with the antennas used for the experiment

Figure 155 shows the resulting constellation diagrams and the measured EVM values for the upstream path.

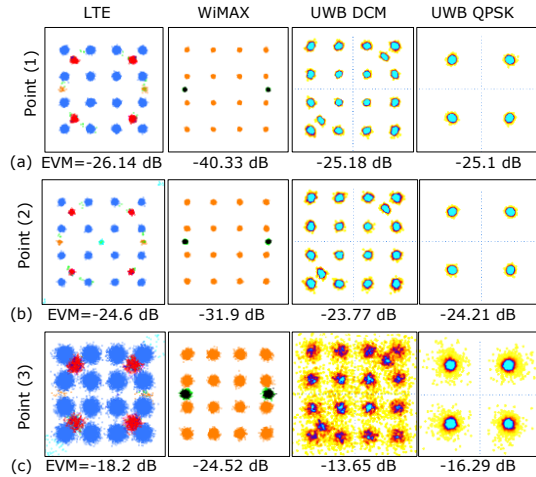


Figure 155. Constellations and EVM values for the downstream path at 1550 nm at: (a) input of the MZ-EOM [Point (1) in Figure 152], (b) after 20.2 km SSMF and before antenna [Point (2) in Figure 152], (c) after 3 m radio propagation [Point (3) in Figure 152]

Again, the EVM values are compared with the limits of each standard. Figure 156 indicate that at an antenna transmit/receive distance of 3 m all three formats are operational within acceptable levels without error correction, LTE and WiMAX in 16QAM and UWB in QPSK format.

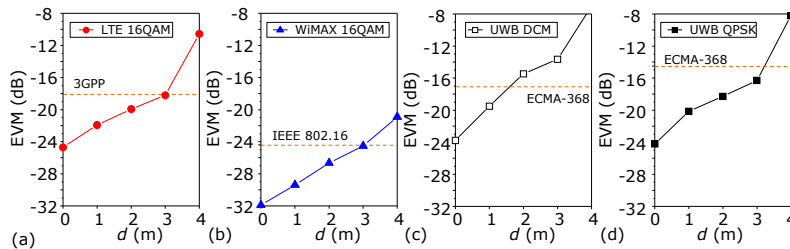


Figure 156. EVM vs. radio distance d for the downstream path at 1550 nm for (a) LTE, (b) WiMAX and UWB working at (c) DCM and (d) QPSK

In the upstream path, the signals to be transmitted at point (4) have level compliant with a SNR of 20 dB or better. There is another identical antenna (Ant.#3) which provides the modulating signal to the MZ-EOM responsible for providing the 1300 nm upstream signal. It was necessary to amplify the signal received from this antenna by 26.3 dB so as to provide sufficient depth of modulation to produce optimal SNR in the upstream optical path. Upon wireless reception before optical transfer (5) it can be seen that once again wireless interference is present but the LTE, WiMAX and UWB components are still clear and distinct. This signal is modulated and propagated through 20.2 km SSMF back to the central office. Reception is obtained via the 1300 nm arm of the splitter and the same equipment.

Figure 157 plots are now showing EVM vs. distance between upstream antennas. The performance evaluation is mirrored in Figure 158 for the upstream path.

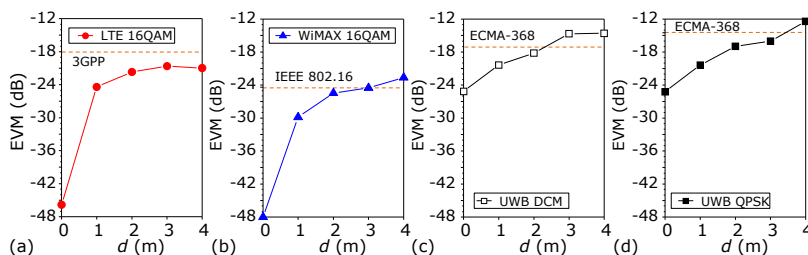


Figure 157. EVM vs. radio distance d for the upstream path at 1300 nm for (a) LTE, (b) WiMAX and UWB working at (c) DCM and (d) QPSK

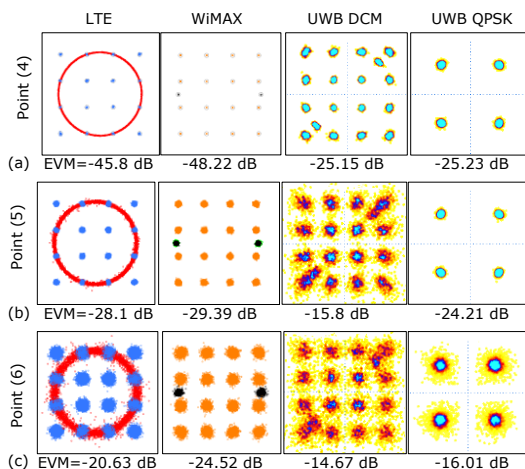


Figure 158. Constellations and EVM values for the upstream path at 1300 nm at (a) input of the antenna [Point (4) in Figure 152], (b) before the MZ-EOM after 3 m radio [Point (5) in Figure 152] and (c) after 3 m radio and 20.2 km SSMF [Point (6) in Figure 152]

It should be noted that upstream LTE has a different configuration as it can be observed in Figure 158 by the clearly visible red circle of the reference signal which are phase-modulated using an orthogonal Zadoff-Chu sequence.

Once again, the clearly defined constellations indicate a reliable opto-electronic link was established. The EVM values shown in Figure 157 also indicate adequate performance up to 3 m.

4.4. Access and in-home distribution evaluation

Due to the emitting power limitation, the coverage of UWB is limited to a few meters: maximum 4 m at the data rate of 480 Mbit/s or 10 m with the reduced data rate of 100 Mbit/s according to [94]. In order to extend the coverage, the in-home distribution and further radio transmission is a straight-forward step to reach the final user as shown in Figure 159. As nowadays the final user demands more bandwidth and more services it is not a solution to develop an in-home network providing a single service. So we propose to follow with the investigation of the provision of triple-play services including telephone, data connectivity and television (TV) in the same network.

In this Section we evaluate both in-building networks (up to 200 m reach) and in-home networks of shorter reach (<50 m fibre) providing 3PLAY comprising phone connectivity (provided by LTE) and LAN connectivity (by WiMAX) and HDTV (by UWB). The three of wireless services are full-standard compliant and used in commercial frequency bands.

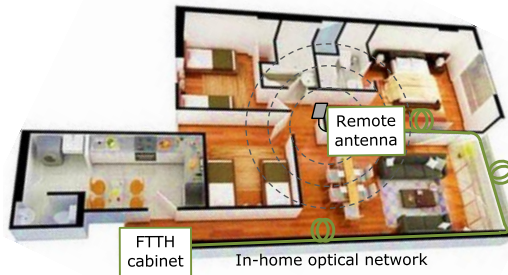


Figure 159. Radio services range extension using in-home optical networks

First in Section 4.4.1 different media are evaluated for in-building networks reaching 200 m fibre after access transmission. In Section 4.4.2 a low-cost network based on POF and eye-safe laser is evaluated for the 3PLAY transmission in in-home networks. In Section 4.4.3, the novelty of video broadcasting using UWB is demonstrated in presence of the other wireless services (LTE and WiMAX) being transmitted in coexistence through the in-home POF network and its further wireless transmission. Finally, in Section 4.4.4, the complete network comprising access, in-home POF based network and radio link is investigated.

4.4.1. In-building ultra-bendable and plastic optical fibre media comparison

Following the evaluation of multiple-format OFDM signals distribution in the CWDM network, different types of fibre for in-building distribution at customer premises have been evaluated. Three types of specialty fibres were evaluated [Mor11e] for in building distribution using a standard centre launch technique: (i) Corning ultra-bendable ClearCurve single-mode fibre, (ii) Fibercore single-mode specialty fibre SM980 of 125 μm and (iii) Chromis Fiberoptics multi-mode plastic fibre GigaPOF50SR.

Two possible CWDM architectures were examined. Firstly, single-mode fibre (SMF) with bi-directional transmission using different wavelengths for downstream and upstream information transmission as described in Figure 160(a). Secondly, the performance of a plastic MMF in a broadcast situation (Figure 160(b)) was assessed. Bi-directional communication with FTTH is problematic when deploying MMF within buildings. Without regeneration, the unacceptably high coupling losses and modal noise when converting to single-mode will reduce considerably the maximum distance over which the FTTH network (upstream) can operate.

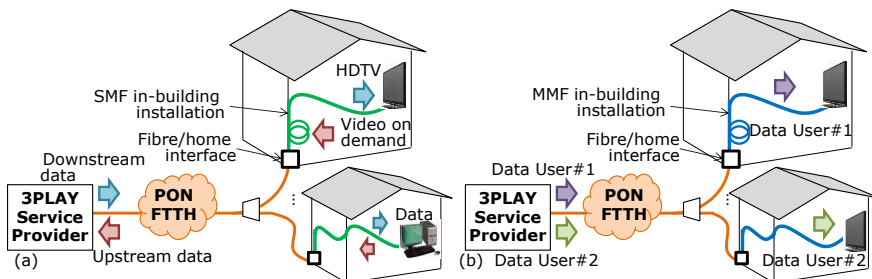


Figure 160. Application scenarios for FTTH access and in-building distribution using (a) bi-directional SMF and (b) unidirectional MMF

The three standard OFDM signals (LTE, WiMAX and UWB) are transmitted through 20.2 km of SSMF to the fibre/home interface. The 3PLAY standard signals are generated as previously: a 3GPP LTE signal using 16QAM at 2.6 GHz (20 MHz BW), IEEE 802.16 WiMAX

16QAM at 3.5 GHz (24 MHz) and WiMedia-compliant UWB signals in channel band 2 (3.96 GHz across 528 MHz) using DCM. These signals were combined using a RF power combiner (MiniCircuits ZN4PD1-50) to produce a composite signal whose spectrum and input constellations are shown in Figure 161. From here, the optical signal was transferred to the specialty fibre under test ($L_{in-home}$) and on to a CWDM coupler. It was then finally applied to a single-mode compatible photodiode (Discovery DSC-R402AC). After 52.5 dB amplification, the resulting RF signal constellations were analysed using a Tektronix DPO 71254 oscilloscope for the UWB signal and a spectrum analyser (Agilent EXA N9010A) running VSA software for the LTE and WiMAX signals. The 1300 nm upstream path was established with an Applied Optoelectronics DFB-1310-BF-31-CW-FC-537 laser operating at the optimum level for the same reach. From this point the 3PLAY signals follow a matching reverse path to another identical photodiode and the resulting constellations were once again analysed.

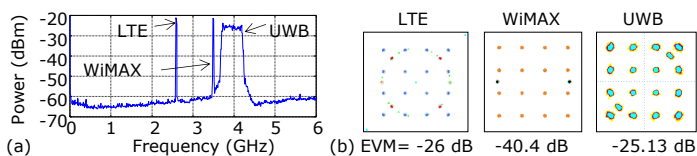


Figure 161. LTE, WiMAX and UWB 3PLAY (a) RF generated spectrum and (b) constellations

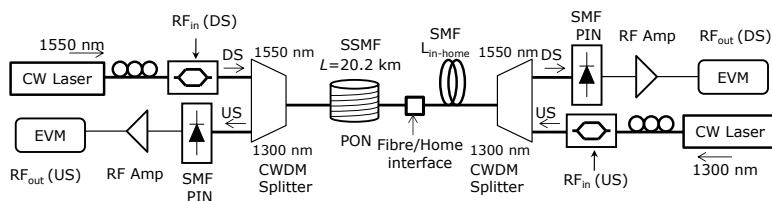


Figure 162. Experimental setup for SMF in-building distribution

For evaluation purposes, the experimental setup for MMF in-building evaluation was as shown in Figure 163. In this case, the fibre/home interface couples the signal from the SSMF coming from the FTTH access network to the MMF used for in-building distribution. As previously noted, this conversion inhibited the return path from user premises to the service provider because of the transformation from MMF to SMF. This in turn reduced the maximum FTTH reach considerably. In this instance, plastic MMF from Chromis Fiberoptics was evaluated. To accommodate the MMF, the receiver comprised a Kyosemi KPDX-10G multimode photodiode and amplification of 32 dB before demodulation and analysis of the 3PLAY signals as described before.

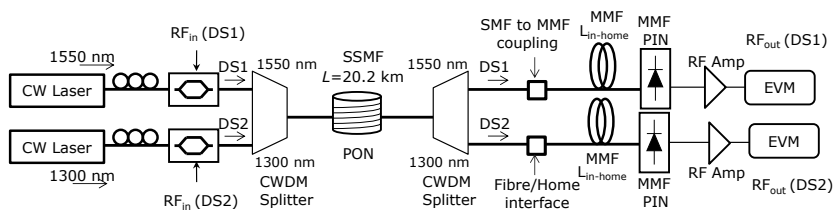


Figure 163. Experimental setup for MMF in-building distribution

Figure 164 shows the back-to-back performance of both SMF and MMF receivers in both wavelengths. The EVM threshold for each service is drawn as a dashed line for comparison: -18 dB for 3GPP LTE using 16QAM, -24.43 dB for 802.16 WiMAX using 16QAM, and -17 dB for ECMA-368 UWB using DCM.

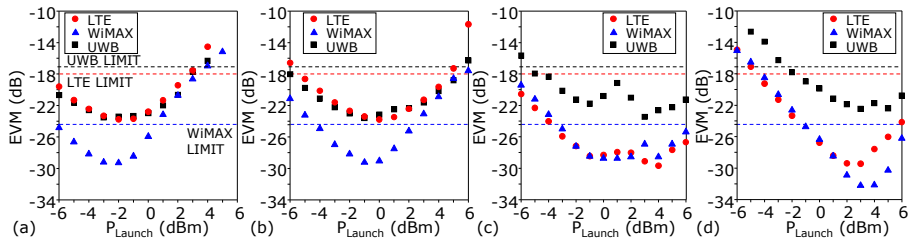


Figure 164. Back-to-back evaluation for receiver: (a) SMF at 1550 nm, (b) SMF at 1300 nm, (c) MMF at 1550 nm, (d) MMF at 1300 nm

Figure 165 shows the EVM results for each of the 3PLAY services in both evaluated architectures using SMF and MMF. It can be observed that in all cases the ultra-bendable SMF offers superior performance as the signal is not degraded even after propagation through 200 m. This is due to the low attenuation associated with this type of fibre.

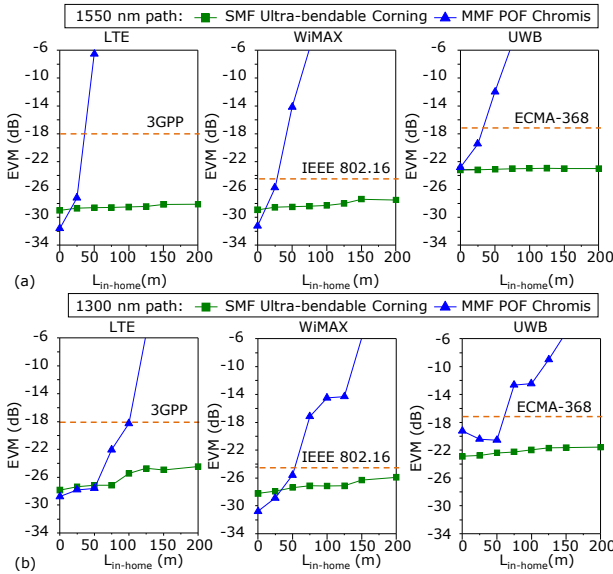


Figure 165. EVM vs. in-building distribution length for (a) 1550 nm and (b) 1300 nm

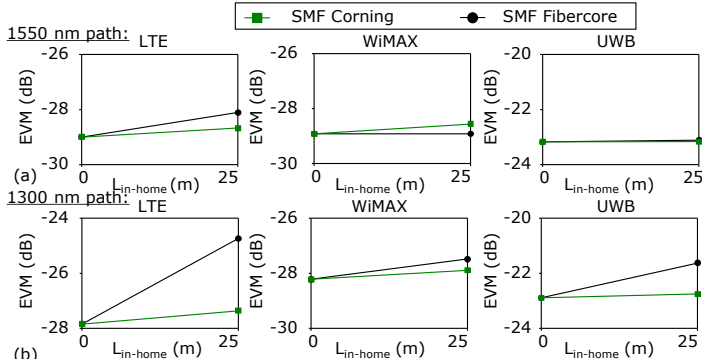


Figure 166. EVM for SMF in-building distribution length at (a) 1550 nm and (b) 1300 nm

Plastic SMF permits the distribution of the three OFDM services LTE, WiMAX and UWB after $L_{in-home}=25$ m. Comparing the constellations of plastic SMF and ultra-bendable SMF shown in Figure 167, it can be observed that plastic SMF has more impact at shorter wavelengths/lower frequencies, i.e. LTE working at 1300 nm. Plastic fibre is only 0.5 dB worse than ultra-bendable fibre at 1550 nm but it is 2.6 dB worse in 1300 nm. For higher frequencies WiMAX and UWB results are very similar for the same fibre distance.

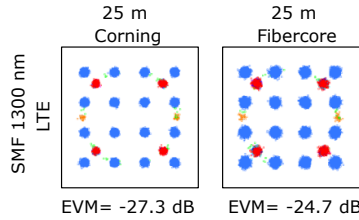


Figure 167. LTE received constellations for Corning and Fibercore fibres at 1300 nm

The received constellation degradation in SMF is shown in Figure 168 and Figure 169 for 1550 and 1300 nm, respectively. These figures compare the performance of Fibercore single-mode specialty fibre and Corning Clear-Curve fibre.

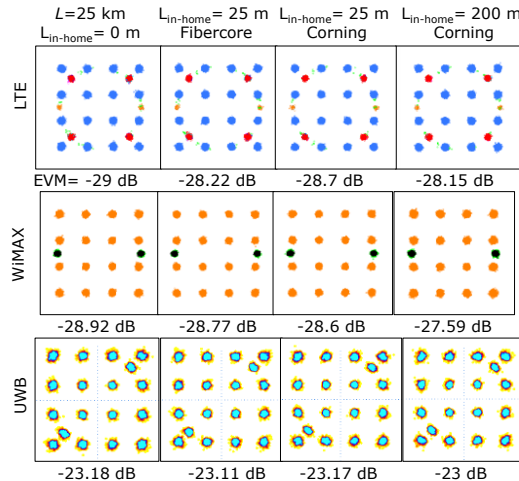


Figure 168. Constellations and EVM values for LTE, WiMAX and UWB for SMF at 1550 nm

We can observe that Clear-Curve fibre EVM performance at 200 m is very similar in terms of EVM to Fibercore at only 25 m in both wavelengths. This confirms that the performance of Clear-Curve fibre is much better for this application and achieves longer reach.

Figure 169 shows the constellations obtained in the 1300 nm path. Also Clear-Curve fibre exhibits the best performance.

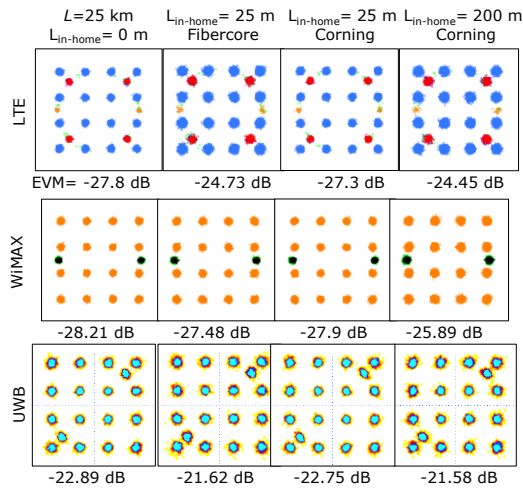


Figure 169. Constellations and EVM values for LTE, WiMAX and UWB for SMF at 1300 nm

The received constellation degradation in MMF is shown in Figure 170. This indicates that MMF achieves successful transmission of 3PLAY signals at 1550 nm up to 25 m as it can be observed that at 50 m the constellations of LTE, WiMAX and UWB show symbol collapse. At 1300 nm, the in-building reach is extended to 50 m.

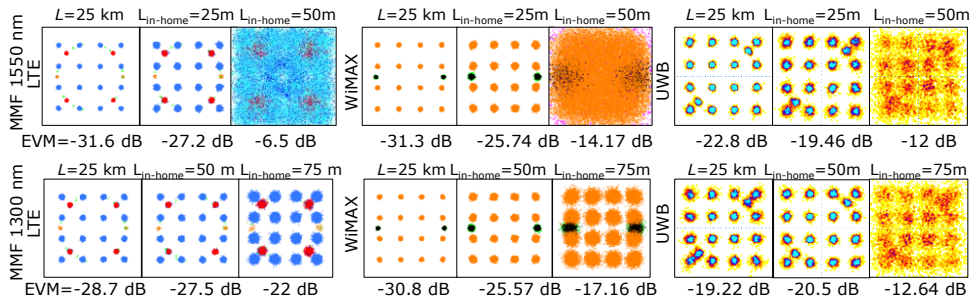


Figure 170. Constellations and EVM values for LTE, WiMAX and UWB for MMF

From the experimental results, we can conclude that ClearCurve ZBL single-mode bend-insensitive fibre achieves the best performance due to the low losses and high bandwidth of the fibre in both CWDM wavelengths 1300 and 1550 nm reaching 200 m radio-over-fibre transmission of the 3PLAY services suitable for in-building networks. Other fibres such as SMF Fibercore or MMF Chromis Fiberoptics could be used for in-home networks (with shorter reach than in-building networks) getting up to 25 m in both wavelengths.

4.4.2. In-home POF reach evaluation

Following the investigation of radio-over-fibre services at customer premises, it was also interesting to evaluate low-cost optical infrastructure for short-length transmission for applications such as in-home networks (<50 m fibre).

Graded-index plastic optical fibre (GI-POF) of 1 mm core diameter polymethyl-metacrylate (PMMA) has been shown as a cost-effective solution for in-home networks [95] due to its 'do-it-yourself' installation, easy maintenance, and smaller bending radius compared with silica single-mode and multi-mode fibres or other types POFs. Some studies on POF based infrastructure for in-home networks have been carried out [96][97].

The novelty of this investigation relies on the multi-service wireless signals transmission (3PLAY) and the usage of an eye-safe laser and low-cost ready-to-use optical transceiver.

The experimental setup is shown in Figure 171. A Wisair UWB transmitter (DVK-DV 9110M) is used to generate WiMedia-compliant UWB signal with DCM format working at 480 Mbit/s and two vector signal generators (Agilent E4438C) are used for the generation of standard WiMAX and LTE signals (OFDM with 16QAM format). Then, the generated UWB centred at 3.96 GHz (TFC6, 3.696 - 4.224 GHz) and WiMAX at 3.5 GHz are combined in the electrical domain and are down-converted to an intermediate frequency (IF) using a local oscillator at $f_{LO} = 2.93$ GHz. This down conversion was done due to the low-pass bandwidth profile of the POF and the optical transceiver (< 1.3 GHz as shown in Figure 172). The IF UWB (0.757 GHz - 1.285 GHz) and IF WiMAX (0.57 GHz) together with LTE (centred at 0.73 GHz) directly modulate a low-cost VCSEL (Firecomms RVM 665T) with wavelength at 667 nm. The modulated optical power is launched into an Optimedia PMMA GI-POF with optical loss of 0.3 dB/m. The optical signal after 50 m GI-POF link is detected by a silicon avalanche photodetector (Si-APD) with a photosensitive diameter of 230 μm equipped by a 2-stage electrical amplifier. Then the detected electrical signals are split to two paths. UWB and WiMAX are up-converted to their original frequency bands and filtered out separately. LTE signal is filtered by using a 900 MHz low-pass filter. To ensure that the emitting power spectral density complies with the standard we employed an electrical vector spectral analyser (R&S FSK40). For EVM evaluation, a digital signal analyser (Agilent DSA91304A) was used.

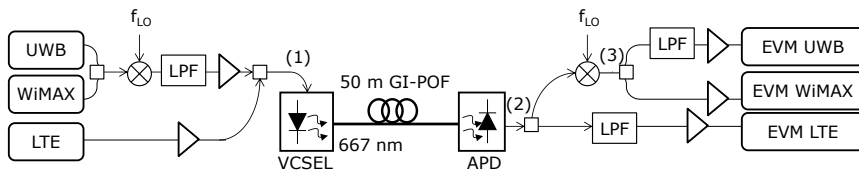


Figure 171. Experimental setup for radio-over-fibre transmission of UWB, WiMAX and LTE over 50 m GI-POF

Figure 172 shows the normalized POF system frequency response. The 3 dB bandwidth of the POF system is 1.3 GHz. The available bandwidth is largely limited by the optical photo detector which is 1.3 GHz. Therefore, all wireless signals should be spectrally located within this 1.3 GHz when converting them to the optical domain. For this purpose, intermediate radio frequencies for UWB and WiMAX are needed to be carefully considered when changing the frequency of the local oscillator.

The optimized frequency bands of UWB, WiMAX and LTE are represented in Figure 172 to show the usage of the available bandwidth of the RoPOF system.

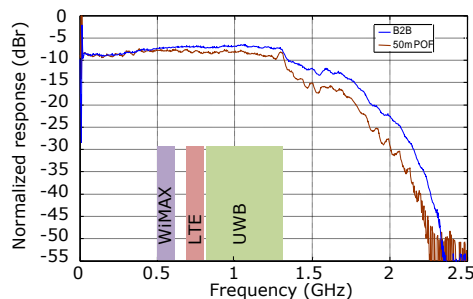


Figure 172. Normalized system response in B2B and after 50 m POF

The electrical spectrum of combined signals launching to the VCSEL (LTE with optimized IF UWB and IF WiMAX), is shown in Figure 173(a). Figure 173(b) and (c) show the signals which are directly detected by APD and the signals after up-conversion, respectively. The power spectrum density of UWB is ensured to be under the standard requirement of -41.3 dBm/MHz, as shown in Figure 173(c).

Due to the nature of the wireless standards employed, the radio signals are not continuous in time. In order to ensure the coexistence condition which happens in real world, our measurements are based on the three signals being present during analysis. The total launch electrical power of three signals is 2 dBm (point (1) in Figure 171).

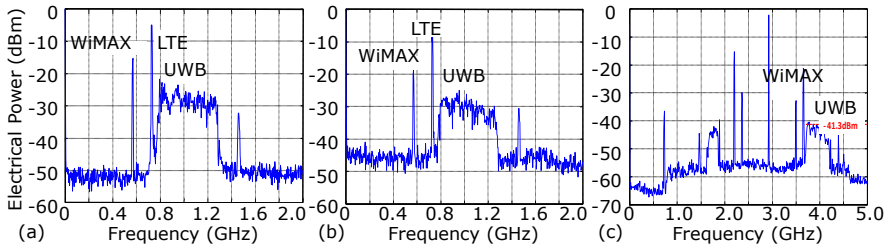


Figure 173. Electrical spectra of: (a) combined signals inserted into VCSEL at point (1) of Figure 171; (b) detected signals after APD at point (2) of Figure 171; and (c) up converted UWB and WiMAX at point (3)

A power balance budget is considered and optimized between three signals targeting all EVM performance compliant with the standards limits, shown as Table 18. The EVM performance for each format signal after transmission over 50m POF is summarized in Table 18 as well. In comparison with the standards requirement, we can observe that all EVM values, LTE of -18.84 dB, WiMAX of -25.52 dB and UWB of -17.07 dB, are well below the limit. The constellation diagram of each signal (LTE, WiMAX and UWB) comparing the generated signals with the received after 50 m GI-POF is shown in Figure 174 exhibiting clearly separated constellation points.

Table 18. EVM performance of 3PLAY after 50 m POF

	LTE	WiMAX	UWB
50 m POF transmission	-18.84 dB	-25.52 dB	-17.07 dB
Standard limits	-18 dB [12]	-24.43 dB [11]	-17 dB [6]

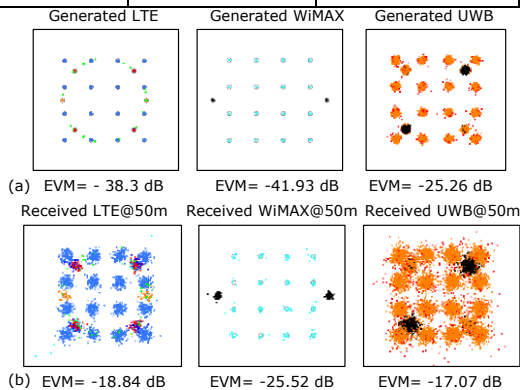


Figure 174. Constellation diagrams of LTE, WiMAX, and UWB signals: (a) generated and (b) received after 50 m POF transmission

Earlier works addressing POF transmission have only considered baseband or digital transmission due to the non-linearity issues of POF transceivers. In this work, we have demonstrated that POF can also be used to transmit and receive analog signals, meaning that one or more analog radio links on a single optical link can be realized by optimizing both transmission domains. The use of a single optical link is advantageous if we want to exploit the cost advantages of POF even further. This demonstration experiment shows us that even low-cost infrastructures (POF and its peripheral components) are able to provide digital (shown in earlier works) and analog signal transmission either separately or simultaneously. Recently, multi-core POFs are introduced for broadband transmission. This type of POF could be used to transmit each of different signals through each of its cores. However, for our work in this experiment, the launching condition would be complicated when coupling the signals in and out of the fibre. Optical alignment from each transmitter to its corresponding receiver becomes difficult to establish and maintain. A slight turning of POF will make the link out of operation. Therefore, we believe that the use of a single-core fibre, hence a single launching condition, is preferred for a simple and low-cost transmission of multi-standard wireless or wireline signals for in-home applications.

The results shown in this section make POFs as an alternative solution for realizing broadband in-home networks besides to the solutions offered by the glass fibre and it will be further investigated in the next sections including the wireless path and the behaviour after the access network.

4.4.3. In-home POF and wireless distribution

Streaming of audio and video has become one of the main applications of ultra-wide band (UWB) technology. The key market opportunity of UWB radio is the cable replacement in personal area networks using wireless universal serial bus (WUSB) technology [98]. Since UWB offers high capacity and can coexist with other wireless services, UWB is becoming a strong candidate for the connection of high-bitrate demanding devices (e.g. external hard disks) and high-definition (HD) video streaming for in-home networks.

The radio-over-fibre transmission of the triple-play signals in a hybrid optical-wireless network including the final radiation at customer premises is evaluated. The interference of the radio services in the simultaneous transmission is evaluated and the qualities of the broadcasting HD videos are analysed. From these results, the maximum wireless radius coverage that can be reached with this approach is investigated.

As we commented before, in order to exploit the in-home network capability, other radio signals are also transmitted through the same network in order to provide multi service applications including telephone, data and video. All the signals used are full-standard compliant in order to be able to use commercial devices at customer premises. Telephone and cell phone services can be provided employing 3GPP LTE in the 700 MHz used in USA and operative in most commercial-available devices. Internet wireless connectivity (e.g. Ethernet) is transmitted in this case using IEEE 802.16 WiMAX at the 3.5 GHz band which is commercially available in laptops. The HD video streaming application is provided by UWB. WiMedia standard used in WUSB devices is based on ECMA-368 which defines 12 bands of 528 MHz bandwidth each in the frequency range from 3.1 to 10.6 GHz [6]. WiMedia-based WUSB devices already available in the market use orthogonal frequency division multiplexing (OFDM) modulation and can provide a data rate up to 480 Mbit/s, which could be extended to 1024 Mbit/s with the latest regulation proposal. Another feature of UWB technology is that it has a very low transmission power level (maximum transmission PSD defined by the FCC of -41.3 dBm/MHz [5]) which enables UWB can operate in coexistence with other radio services without interfering. The low power consumption of UWB devices also provides better energy conservation for battery-powered mobile devices. Recently, the first HD video distribution over POF was presented in [100] with the dedicated transmission of the UWB signal. However, single UWB signal was considered without coexistence with other wireless services. In order to study the full

application scenario for in-home network with multi-wireless presenting the coexistence of UWB video broadcasting with LTE and WiMAX is evaluated for hybrid optical-wireless in-home distribution.

The experimental testbed to evaluate the quality of the video broadcasting using UWB in the wireless coexistence with LTE and WiMAX services is shown in Figure 175 including an in-home network of large core GI-POF of 25 m followed by a radio link ranging from 1 to 4 m. The normalized system frequency response is shown in Figure 176 for back-to-back and for 25 m POF transmission cases.

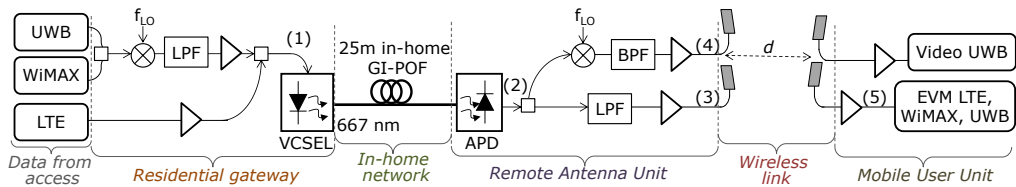


Figure 175. Experimental setup for in-home distribution of HD video using UWB in coexistence with LTE and WiMAX services in a POF network and radio path

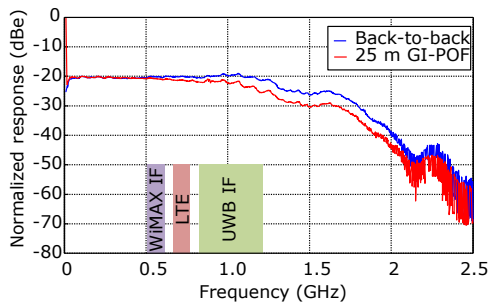


Figure 176. Normalized electrical response of the POF system in back-to-back and after 25 m POF. The IF WiMAX, LTE and IF UWB bands are included for reference

The 3 dB bandwidth of the system is 1.3 GHz, which is mainly attributed to the optical photodetector, as the bandwidth product of the POF is more than 3 GHz for 50 m. Therefore, all the radio signals should fit in this 1.3 GHz bandwidth. Due to this bandwidth limitation of the POF system, UWB and WiMAX are down-converted first and then combined with the LTE signal. The location of the triple-play services is depicted over Figure 176 for reference: (i) a LTE signal of 10 MHz bandwidth using 16QAM centred at 0.73 GHz is generated by an electrical signal generators (ESG Agilent E4438C). (ii) A 10 MHz WiMAX signals using 16QAM is generated at 3.5 GHz by another ESG and then down-converted (once combined with UWB) with a $f_{LO}=2.94$ GHz, resulting a WiMAX signal at an intermediate frequency (IF) of 0.57 GHz. And (iii) a UWB signal generated by a Wisair UWB transmitter (DVK-DV 9110M) using the time frequency code TFC6. The bandwidth of the UWB is 528 MHz ranging from 3.696 to 4.224 GHz. This signal is down-converted with WiMAX signal ($f_{LO}=2.94$ GHz), obtaining a UWB IF of 0.757 to 1.285 GHz as shown on Figure 177(a). A HD video using H.264 codification and 50 frames per second is encapsulated into UWB frames running at 200 Mb/s for video broadcasting.

The triple-play signal directly modulate an eye-safe broadband red VCSEL diode emitting at 667 nm (Firecomms RVM 665T) and transmitted through 25 m of Optimedia PMMA GI-POF with the optical loss of 0.3 dB/m at 667 nm.

The optical signal after the 25 m fibre link is detected by a Si-APD of 230 μm photosensitive diameter including a 2-stage electrical amplifier. The spectrum of the

electrical signal received after the APD is shown in Figure 177(b). The detected signals are split in two paths: The LTE signal is filtered by a 900 MHz LPF, amplified and radiated with a wide-band monopole omni-directional antenna of 2 dBi (Omron WXA-N2SL). The LTE radiated spectrum is shown in Figure 177(c). The UWB and WiMAX signals are up-converted to their original frequency bands, filtered and amplified. A patch omni-directional antenna of 0 dBi (In4Tel) is used for radiation of UWB and WiMAX signals. At this point it is ensured that the emitting PSD complies with the UWB FCC spectral mask [5] –as shown in Figure 177(d)– using an electrical spectral analyser (R&S FSQ40).

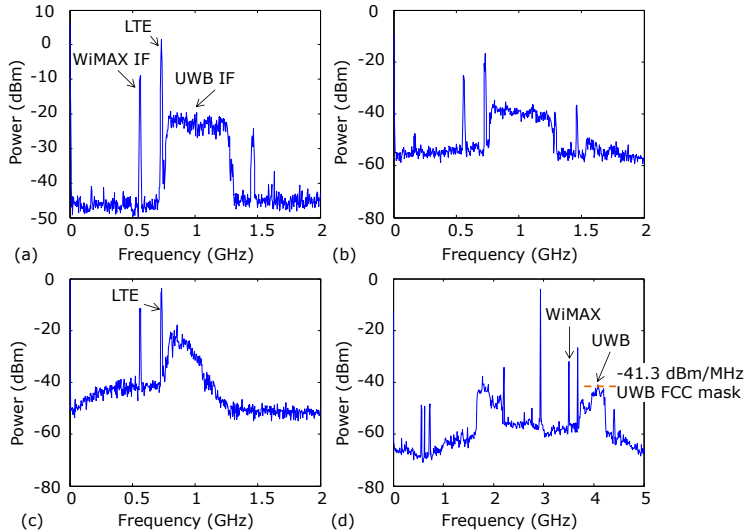


Figure 177. Measured electrical spectrum (RBW=1 MHz) at different point of Figure 175: (a) Combined signals before VCSEL (point (1)), (b) received signals after 25 m GI-POF at APD output (point (2)), (c) radiated LTE signal (point (3)), and (d) radiated WiMAX and UWB signals with UWB spectral mask (point (4))

After the radio link, the signals are received at the antenna, amplified and feed to a digital signal analyser (Agilent DSA91304A) for demodulation and EVM evaluation using VSA software for standard radio signals. Wireless paths of 1 to 4 m are evaluated, which could lead to a coverage area of 4 m radius.

In the case of the video transmission, the UWB signal is amplified and feed to the Wisair receiver connected to a laptop. A VLC media player configured with UDP mode is used to record the broadcasting video streams.

First, the performance of transmitted signals in terms of EVM of each signal is measured with the different lengths of the radio link at the transmitter antenna site –point (5) of Figure 175–. As all the signals are OFDM-based, we can demodulate the signal and obtain the EVM which shows the average constellation error. The standard wireless signals at the transmitter antenna site must be compliant with standard requirements specified in terms of EVM.

Figure 178 shows the measured EVM of each service after transmission over 25 m GI-POF and different length of the radio link. The system performance in single service transmission case and in coexistence with the other ones is compared in order to study the effect of interference. Note that the signal performances at the transmitter antenna both in coexistence and in standalone transmission are well compliant the requirement. The EVM performance of -18.2 dB in LTE, -26.2 dB in WiMAX, and -17.3 dB in UWB are observed when these triple-play services transmitted after 25 m POF link.

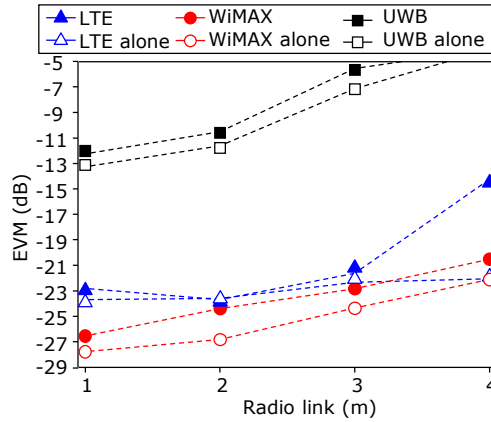


Figure 178. Measured EVM of each signal for different radio links being transmitted alone or in coexistence with the other radio services

Figure 179 shows the constellation diagrams of the wireless signals transmission over 25 m POF and 2 m radio link with and without the other services being presented simultaneously. It can be observed that the interference of the simultaneous transmission of the triple-play services led significant degradation to LTE service, as for 2 m radio link the 6.1 dB EVM increase can be noticed in the coexistence case than the single transmission. However, even with this impact the EVM value of LTE in coexistence remains -20.6 dB. The main reason of this impact on LTE is that the down-converted the UWB signal (UWB IF) is quite close to the LTE signal and the residual signal after up-conversion has not been completely removed by the electrical filter. This problem could be solved using a better filter. However, this impact is reduced with longer wireless distance, as the power level of the residual interference is reduced. Only 1.6 dB degradation in EVM for LTE signal can be observed from 2 m to 3 m radio link.

The impact of the coexistence in the other services is only of 1.6 dB on the WiMAX, and 1.2 dB on the UWB signal for 2 m wireless propagation. From Figure 178 and Figure 179, it can be concluded that the interference that occurs when the different services are transmitted simultaneously does not introduce a critical impact to the signal quality. The proposed in-home network architecture could support multi radio services simultaneous distribution to the end users.

Furthermore, if we compare the EVM values with the standard limits, we can observe that LTE complies with the requirements up to 3 m radio propagation, but WiMAX finds the EVM limit of -24.4 dB at 2 m radio link. We can conclude that we can provide 2-m radius coverage.

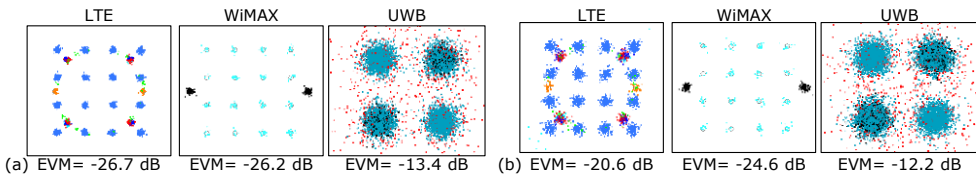


Figure 179. Measured constellations and EVM for LTE, WiMAX and UWB after 25 m POF and 2 m radio link transmission: (a) alone, (b) in coexistence with the other services

Next, a H.264 coded video with 50 fps is transmitted using UWB. The 2 minutes video is transmitted with more than 24000 UWB packets, which is enough for the quality assessment.

The measured packet loss after the different radio links ranging from 1 to 4 m is shown in Figure 180. It can be observed that for 1 and 2 m radio links there is no packet loss in the UWB transmission. For 3 m radio link, a 0.08% packet loss is observed (20 from 24249 packets transmitted). For 4 m radio link, 78 packets lost or were discarded at the UWB receiver which leads to a 0.32% packet loss.

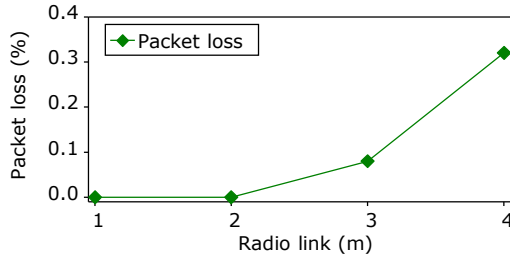


Figure 180. Measured packet loss in UWB video transmission in coexistence with LTE and WiMAX services for different radio links

The quality of the video received after the propagation through POF link and the radio path is assessed using a video quality analyser (VQA) provided by AccepTV [101]. This analyser is based on the prediction of the mean opinion score (MOS) obtained by the observer in a subjective method. The most representative quality value is the differential mean opinion score (DMOS) curve of a video, which is mainly the subtraction of the reference video (the video transmitted) and measured video (the video received). DMOS values ranges from 0 to 100. Values close to 0 mean that the measured video is the same as the reference one (the difference between them is almost 0). On the opposite, values near 100 indicate very bad video quality as most of the frames evaluated contain differences when comparing with the reference one. The DMOS values computed by the VQA algorithm are highly correlated with the ones that could be obtained with procedure obtained from human judgments.

Figure 181 shows the DMOS evaluation results for the received UWB video in coexistence with LTE and WiMAX services with different radio links. Since the VLC player took some frames to stabilize we decided to remove the first 299 frames before evaluate the quality of the videos. We applied the VQA to the video files running from frame 300 to 1200 and obtained the DMOS curve for each radio link.

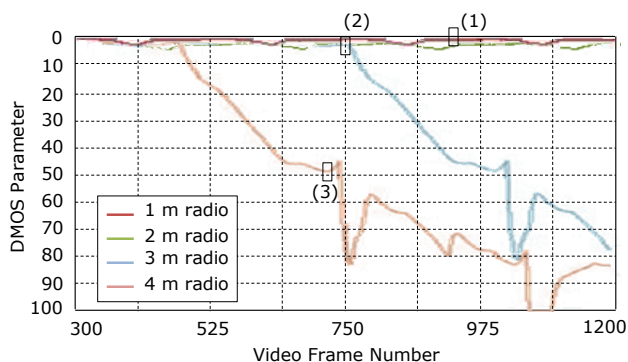


Figure 181. UWB received DMOS video quality in coexistence for different radio links

As shown in Figure 181, for radio links of 1 m and 2 m, the obtained DMOS is excellent at all the video frames (values around 0). Figure 182(a) shows an example of the difference between the received and transmitted video after 1 m radio link.

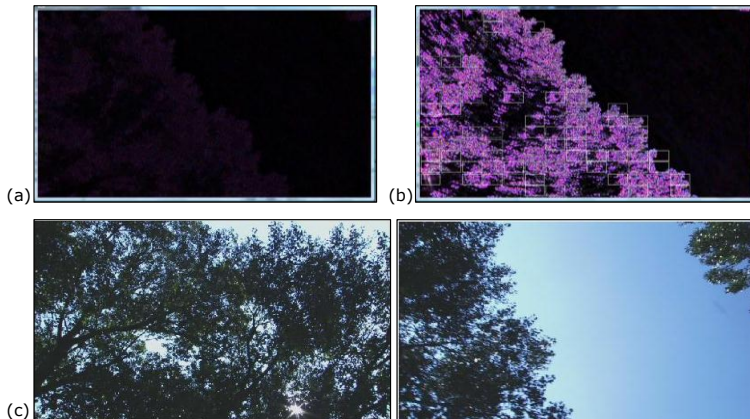


Figure 182. Quality analysis of the video at different points of Figure 181: (a) difference between received and transmitted video for 1 m radio (frame 927, point (1)), (b) difference for 3 m radio (frame 750, point (2)), and (c) delay between the received and transmitted video due to packet loss at 4 m radio (point (3))

As the video is received with very good quality the difference between the measured and the reference is 0 –black screen shown in Figure 182(a)–. With the wireless distance increases we can find that the DMOS gets worse. At 3 m radio, a significant drop of the quality of the received video can be observed from the frame 750 –point (2)–. In this case, an example of the degradation of the video is shown in Figure 182(b). Compared to the reference video, the received video introduced many distorted blocks in the image. This will be translated in pixels if we observe the received video.

Finally, observing the results of 4 m radio link we can see that the DMOS curve starts getting worse in the early frames (point (3) in Figure 181). This effect is largely due to the low UWB power level at the receiver antenna site. As some of the video packets were lost we can observe a delay between the received video and the reference video after some frames. It is like some of the frames in the middle were missing, so the algorithm is evaluating a received frame that is delayed in comparison with the one that has for reference. This effect can be better observed in Figure 182(c) where we can see that the video is clear (without much distortion or big pixels) but the frames that are being compared with the algorithm are different in time.

From this we can conclude that the packet loss affects the overall quality of the received video, and the HD video broadcasting using UWB can reach a 2 m radio link with excellent DMOS value and 0% packet loss. The discussion above confirms that the triple-play service distribution of LTE, WiMAX and UWB can be provided in hybrid optical-wireless networks at customer premises achieving a 25 m range extension of optical fibre and a 2 m wireless radius coverage.

4.4.4. Access, in-home POF and wireless distribution

The next step was to evaluate the end-to-end architecture comprising the access network, the in-home POF network and the wireless transmission. The experimental setup is shown in Figure 183. Two vector signal generators (Agilent E4438C) are used for the generation of standard WiMAX and LTE signals (OFDM with 16QAM format) as we did in the previous experiments of triple-play transmission. A Wisair UWB transmitter (DVK-DV 9110M) is used to generate WiMedia-compliant UWB signal with QPSK format. The generated UWB signal centred at 3.96 GHz (TFC6, from 3.696 to 4.224 GHz), WiMAX signal at 3.5 GHz and LTE signal at 0.73 GHz are combined in the electrical domain to feed a Mach-Zehnder modulator working at the quadrature bias point. A CW DFB laser (FOL15DCWD-A) at

1557 nm provides the access optical source with output power of 11 dBm. After transmission over 25 km of standard SMF, a PIN-diode (R2860E) detects the optical signal. Then the received signals are split into two paths using band-pass and low-pass filters. UWB and WiMAX are first down-converted to an IF using a local oscillator at $f_{LO}=2.94$ GHz because of the low-pass bandwidth profile of the POF and the optical transceivers. The resulting IF UWB (0.756 to 1.284 GHz) and IF WiMAX (0.56 GHz) combined with LTE (0.73 GHz) directly modulates a VCSEL (Firecomms RVM 665T) together with a bias DC voltage, emitting light at 667 nm with output power below 0 dBm. The modulated optical power is launched into an Optimedia PMMA GI-POF with optical loss of 0.3 dB/m. After transmission over 25 m POF link, the optical signal is detected by a Si-APD with a photosensitive diameter of 230 μm followed by a 2-stage electrical amplifier. The detected LTE signal is isolated for air transmission using a directional antenna (WXA-N2SL) with a gain of 2 dBi. On the other hand, UWB and WiMAX signals are up-converted to their original frequency bands before being radiated over the air.

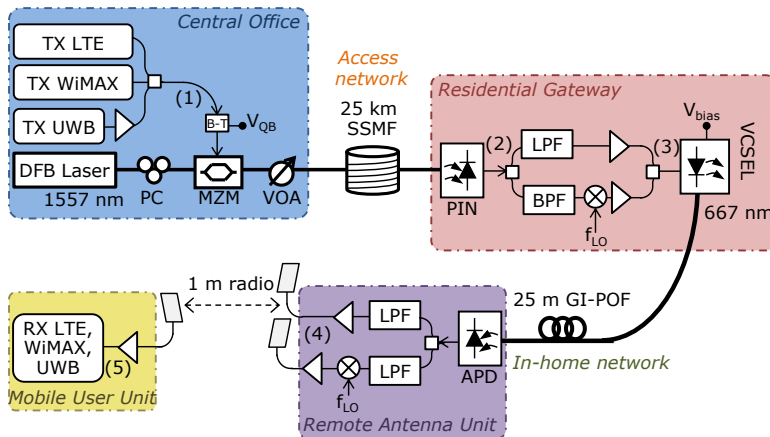


Figure 183. Experimental setup for radio-over-fibre end-to-end transmission with POF in-home distribution

The received signals after SMF transmission and the IF signals launched to the VCSEL are shown in Figure 184(a) and (b) respectively. Since we use different antennas for WiMAX/UWB and LTE, the electrical spectra at the transmitter antenna are shown in Figure 185 and the ones at the reception antenna after 1 m wireless transmission in Figure 186. The PSD of the UWB signal at the transmitter antenna is ensured to be below the required -41.3 dBm/MHz (Figure 185(b)).

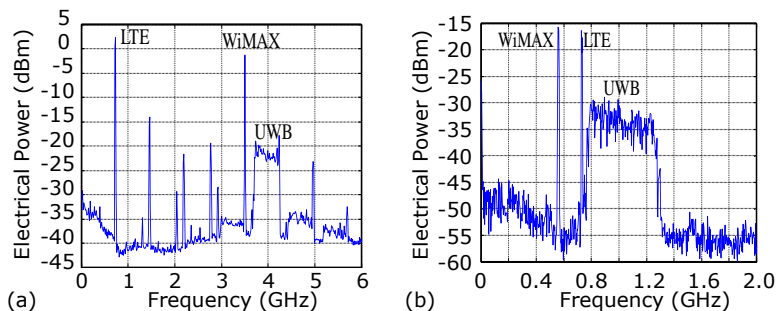


Figure 184. Electrical spectrum (RBW=1 MHz) measured at: (a) received signals after SMF link at point (2) of Figure 184; (b) signals inserted to VCSEL at point (3) of Figure 184

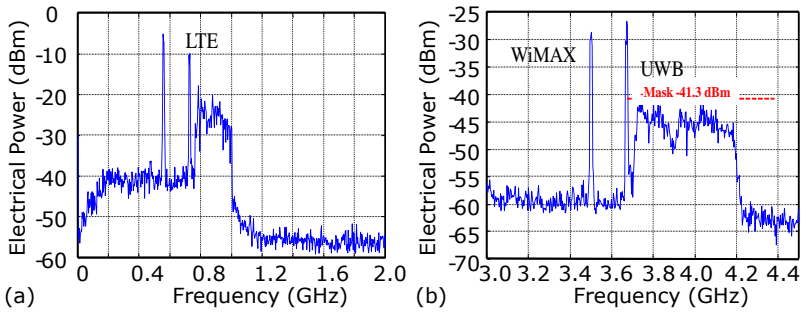


Figure 185. Electrical spectrum (RBW=1 MHz) measured at transmitting antenna site at point (4) of Figure 184 for: (a) LTE, and (b) WiMAX and UWB

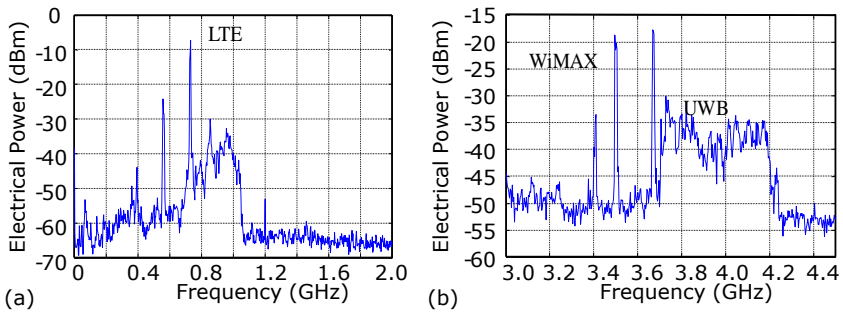


Figure 186. Electrical spectrum (RBW=1 MHz) measured at receiving antenna site at point (5) of Figure 184 for: (a) LTE, and (b) WiMAX and UWB

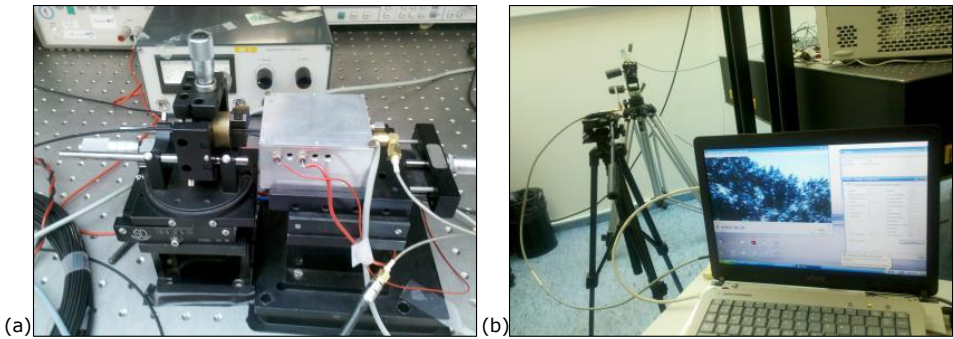


Figure 187. Photos of the experimental setup showing: (a) POF and receiver and (b) wireless link with UWB video transmission

Figure 187 shows some photos taken during the experiments, showing the VCSEL connected to the POF and the wireless link evaluation with the antennas.

Figure 188 shows the optimization of the received power going to the PIN diode after SMF transmission and the output power of the VCSEL.

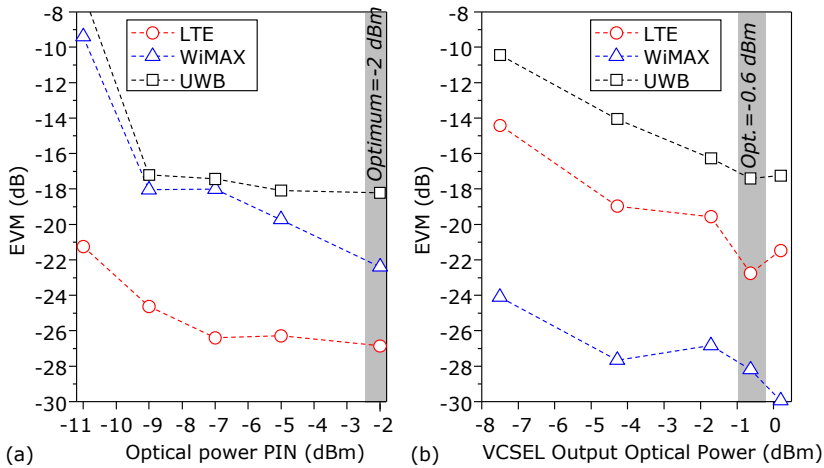


Figure 188. EVM measured at: (a) point (2) of Figure 183 with different optical power arriving at PIN. (b) point (4) with different VCSEL output power

Considering the EVM performance at point (2) of Figure 183, the optimized received optical power at the PIN is 2 dBm. When the optical power launched to the POF link is 0.63 dBm the best EVM performance can be achieved at the transmitting antenna sites (point (4) of Figure 183). We kept the optimized configuration for the optical power budget through all measurements which shown in the rest of the measurements.

As shown in Figure 190(a), the signal performance in terms of EVM is studied for different transmission points. The EVM values of LTE, WiMAX and UWB at point (1) in Figure 183 are -34.91, -39.45 and -24.73 dB respectively, which can be used as a reference for the penalty evaluation. A system penalty given by SMF link is 8, 13 and 6.87 dB respectively for these signals. For the POF link, the transmission penalty is of 1.09, 5.16 and 1.34 dB respectively. The signal degradation difference for the same optical channel is due to the robustness of the radio signals and the input power balance between LTE (5 dBm), WiMAX (5 dBm), and UWB (1.7 dBm). After optical and air transmission, the EVM performances are compliant with current standards for each signal. Figure 189 shows the constellation diagram of each signal at point (5) of Figure 183.

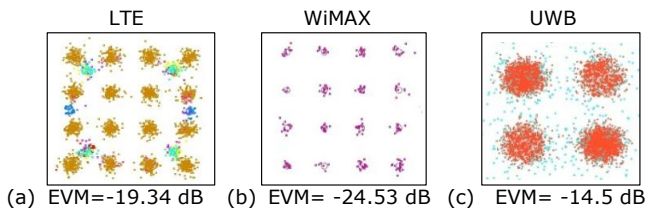


Figure 189. Constellation diagrams of the received signals at end user measured at point (5) in Figure 183 for: (a) LTE, (b) WiMAX, (c) UWB

In order to compare the signal performances in coexistence with each other and in single transmission case, Figure 190 shows the EVM values of each signal with and without the existence of the other two signals at the different transmission points. As proof of concept, we transmitted a HD 1080i (1920×1080 pixels) video encapsulated in UWB frames in the presence of the LTE and WiMAX signals.

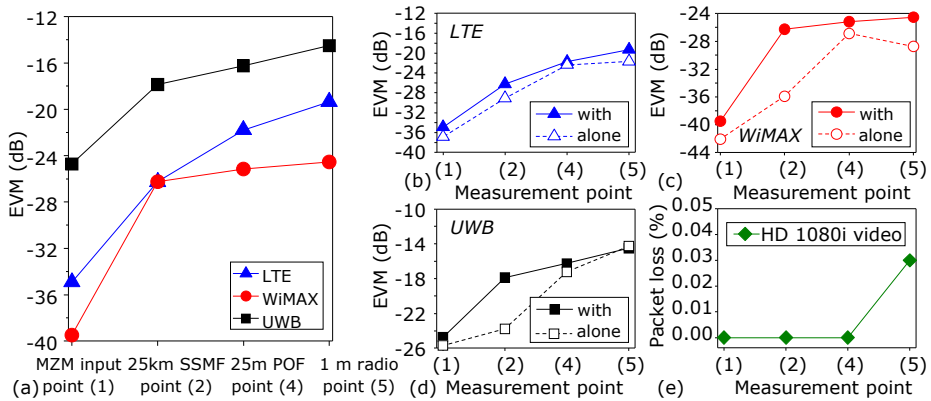


Figure 190. Measured EVM performance: (a) at various locations in Figure 183, (b) LTE alone and in coexistence, (c) WiMAX alone and in coexistence, (d) UWB alone and in coexistence. (e) HD 1080i video transmission packet loss measured in coexistence

Figure 190(e) shows the measured packet loss at various locations. It can be observed that the video is received correctly after 25 km SSMF and 25 m POF with no packet loss. After 1 m radio transmission only a few pixels were affected due to a 0.03% packet loss in the video file. The distorted area is marked in Figure 191.

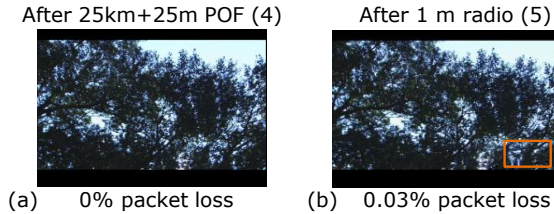


Figure 191. UWB video captured at: (a) point (4) and (b) point (5) in coexistence with LTE and WiMAX

4.5. Conclusion

In this Chapter, the coexistence of multi-standard OFDM signals providing triple-play services comprising LTE, WiMAX and UWB in radio-over-fibre transmission was evaluated for different access networks. Two network architectures are defined: a reflective based on a R-EAT devices, and a conventional CWDM bi-directional architecture.

In the reflective architecture based on R-EAT, the experimental results demonstrate successful communication of LTE, WiMAX and UWB after 15 km SSMF without optical amplification stages or error correction. Up to 20 km was achieved in the downstream path, but the upstream range was limited to 15 km by the SBS effect. This option permits offering 3PLAY services transmission at PON distances with only low-cost devices and no lasers at user’s homes using a R-EAT.

In the conventional CWDM architecture, up to 50.6 km SSMF bi-directional transmission in passive optical networks is possible without amplification or regeneration stages. The 1550 nm wavelength permits longer reach up to 101.8 km for the three formats simultaneously, whilst the 1300 nm path needs more launch power in order to achieve the same SNR. This points out that it should be better use a DWDM option in the 1550 nm window following the ITU grid.

Next, in section 4.3, the hybrid wireless-optical bi-directional transmission after 20.2 km FTTH network was confirmed experimentally up to 3 m wireless range for simultaneous LTE and WiMAX (both 16QAM), and UWB using QPSK. If DCM UWB were used, the maximum wireless range of the UWB devices would be 1.5 m radius, although LTE and WiMAX could work up to 3 m.

In Section 4.4 different in-home fibre media was evaluated. First several optical fibre options for deployment within the home environment were compared for distribution of triple-play services after a 20.2 km SSMF access network. Corning ClearCurve® ZBL single-mode bend-insensitive optical fibre permits installation over 200 m reach, compared to 50 m with plastic multi-mode fibre.

Also the first demonstration of 3PLAY distribution in plastic optical fibre was achieved up to 50 m POF employing an eye-safe vertical cavity surface emitting laser. This proves the feasibility of distribution of radio signals for in-home environment using large core plastic fibres. Further investigation was performed on this media with 25 m POF transmission and 4 m wireless link is evaluated including real HD video transmission in UWB signal. The quality of the received video which is encapsulated into UWB frames is also evaluated for wireless links ranging from 0 to 4 m. The differential mean opinion score (DMOS) of the received video after 25 m GI-POF transmission and further wireless link points out that a 2 m radius can be covered successfully in coexistence with LTE and WiMAX services after the optical transmission. Hence, WiMAX and LTE are EVM-compliant with current standards after 25 m GI-POF and 2 m radio propagation.

Finally, an end-to-end transmission from the central station to the final user personal area network was evaluated comprising a 25 km access network, followed by a 25 m POF in-home optical network and 1 m wireless transmission. The simultaneous transmission of LTE, WiMAX and UWB was achieved after this complete system with EVM compliant values. Also in this network a HD 1080i video was transmitted with minimal packet loss.

CHAPTER 5. IMPAIRMENT COMPENSATION TECHNIQUES FOR MULTI-STANDARD OFDM RADIO-OVER-FIBRE TRANSMISSIONS

5.1. Introduction

This chapter proposes using digital signal processing for the impairment compensation of the radio-over-fibre transmission of multi-standard OFDM signals in optical networks. We propose an impairment compensation subsystem that applies with the number of RF-pilots employed for obtaining the channel information and also the estimation method used for obtaining the transfer function of the optical channel from the RF-pilots information as shown in Figure 192.

For the impairment compensation, it is necessary to obtain information from the transmission channel so we propose a channel sounding technique based on the transmission of a set of extra RF-pilots next to the OFDM-based signals.

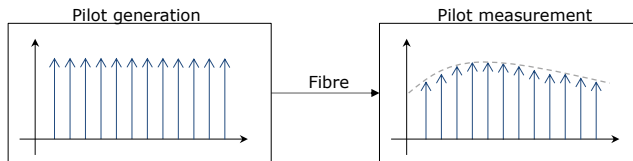


Figure 192. Proposed channel sounding scheme

An access optical network is a bi-directional system that uses different wavelengths for transmission of downstream and upstream information. So, to obtain a centralized management, the impairment compensation subsystem will use pre-compensation for the downstream path (going from the OLT to the ONT) and post-compensation in the upstream path (from the ONT back to the OLT).

Figure 193 shows an example of the access network approach with centralized management and compensation. At the OLT, the multiplexed OFDM-based signal comprises: GbE-OFDM (comprised by a custom I/Q OFDM modulator), LTE, WiMAX and UWB. In the downstream, the compensation is done with an FPGA that should affect the multiplexed OFDM-based signal by the inverse of the OLT-ONT channel transfer function obtained from the information extracted from the set of extra RF-pilots that are located in the free-spectrum of the OFDM-based signals. In order to keep the ONT as simple as possible, the upstream path compensation is done at the OLT with post-compensation.

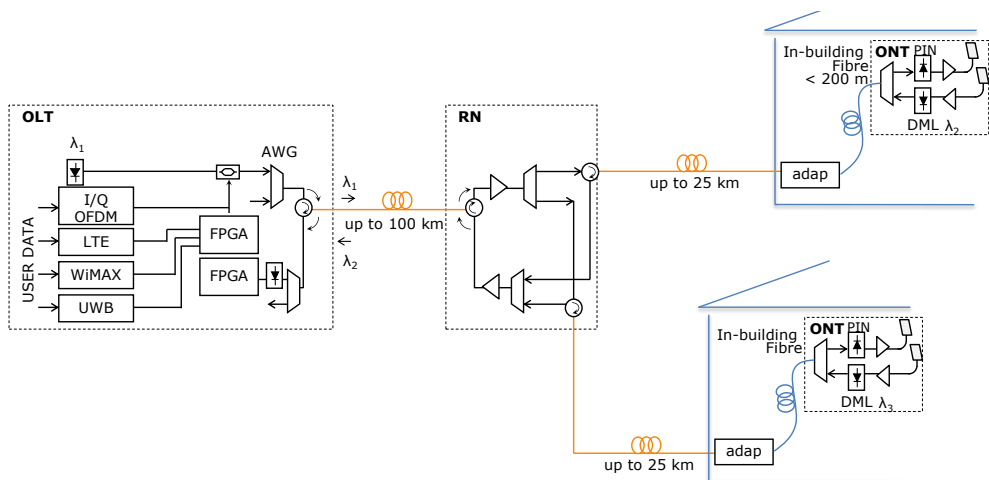


Figure 193. Access network architecture with centralized compensation

At receiver side, the transmitted pilots are detected and its amplitude is measured. The management block will be able to decide about the usage of each pilot, depending e.g. on the currently used services. Within the OLT, the measurement results can be given directly to the compensation algorithm, whereas the results from the ONT have to be transferred to the OLT by means of the management channel.

As it can be observed in Figure 194, at the ONT the pilot information is extracted and sent back to the OLT for processing using the upstream management channel. The extraction performed at the ONT side may be implemented using an ADC and a FPGA circuit. In order to relax the ADC requirements, an alternative approach using sub-sampling technique may be also possible.

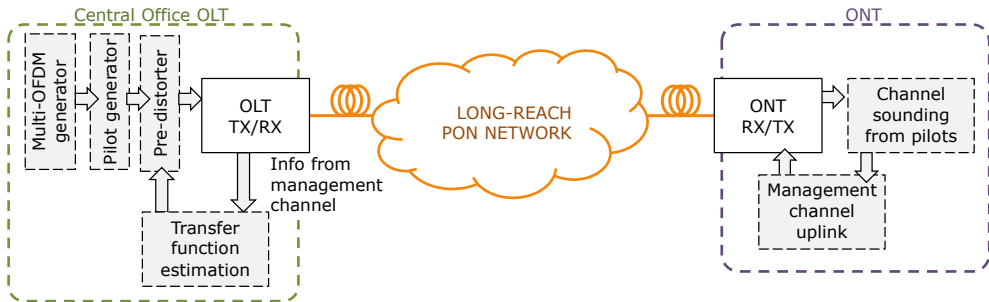


Figure 194. Channel sounding implementation scheme

When the pilots information arrives at the OLT, the channel response is evaluated and pre-distortion is applied by digital signal processing (DSP) to the multiplexed OFDM-based signal. Although phase and amplitude estimation may be obtained from the pilots information, only amplitude correction is applied as no significant phase distortion has been observed.

The amplitude estimation used for centralized compensation at the OLT is performed using the sounding of the amplitude response of the OLT-ONT channel provided by the pilots. Hence, the algorithm used to obtain the channel response can be described as:

$$A_c(f_k) = \frac{A_r(f_k)}{A_t(f_k)} \quad (13)$$

with $k=1, 2, 3, \dots, N_p$; where N_p is the number of pilots transmitted for channel sounding, $A_c(f_k)$ is the estimated amplitude used for centralized compensation at the OLT corresponding to the frequency, f_k , of the k -th pilot, and $A_t(f_k)$ and $A_r(f_k)$ are the transmitted and the measured received amplitudes, respectively, of the k -th pilot.

From the estimated amplitude at the frequency of the k -th pilot given by eq. (13), the amplitude response of the OLT-ONT channel at other frequency can be obtained using different DSP algorithms. In Section 5.3, the performance improvement provided by the centralized compensation algorithm is assessed considering two different DSP algorithms: i) amplitude frequency response of the OLT-ONT channel evaluated using linear interpolation and ii) amplitude frequency response of the OLT-ONT channel evaluated using a regression method (in a least-square sense). In addition, the impact of the order of the polynomials used by the regression method on the performance improvement provided by the compensation algorithm is also assessed in Section 5.3.2. Particularly, first order (linear regression), second order (parabolic regression) and third order (cubic regression) polynomials are used.

In addition, in Section 5.3.3 the impact of the extra RF-pilots over the UWB signal is analysed and no distortion was observed.

5.2. Evaluation procedure

The impairment compensation proof-of-concept is based on a quadruple-format OFDM signal (GbE, LTE, WiMAX and UWB) transmission in optical access network comprising:

- (i) A custom GbE-OFDM signal in 1 GHz bandwidth (from 1 to 2 GHz) with 128 subcarriers;
- (ii) An LTE signal of 20 MHz bandwidth and centred at 2.6 GHz with 2048 subcarriers;
- (iii) A WiMAX signal centred at 3.5 GHz with 20 MHz bandwidth and 256 subcarriers;
- (iv) Two UWB channels of 528 MHz bandwidth each, centred at 3.96 GHz and 4.49 GHz (channel band 2 and 3, respectively) with 128 subcarriers.

For comparison, all the signals use QPSK modulation.

As it was already commented, the channel sounding technique is based on the transmission of a set of extra RF-pilots next to the OFDM-based signals. These RF-pilots are generated in the free frequency range between the multi-format OFDM signals in order to not interfere with the real data transmission as it is shown in Figure 195.

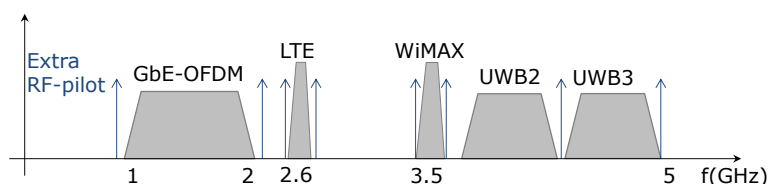


Figure 195. Extra RF-pilots insertion in the free spectrum of the multi-format OFDM-based signals

In the proof-of-concept, the multi-format OFDM signals are generated and the extra RF-pilots are added by Matlab® programming. The electrical signal is generated with a Tektronix 7122B AWG with 20 GSamples/s. The LR-PON comprises a feeder SSMF of 75 km.

At the remote node, an EDFA is used to compensate for the losses of the optical link and then the signal is sent to the corresponding ONT using a distribution SSMF fibre [102]. In these experiments, distribution fibre lengths ranging between 0 and 50 km are assessed. Hence, the maximum fibre reach analysed between the OLT and the ONT is 125 km of SSMF.

A 10 GHz PIN with integrated trans-impedance amplifier is used at the received side. Once photodetected, the signal is filtered and sampled by a real time Agilent oscilloscope DSO81204A at 10 GSamples/s and processed with Matlab® for EVM and BER calculation. In each case, the obtained EVM is compared with the limit stated in the corresponding radio standard for QPSK signals: GbE limit of -11 dB, LTE limit of -15.1 dB, WiMAX limit of -20 dB and UWB limit of -14.5 dB are considered.

The performance evaluation procedure is as follows:

1. Twenty different time signal waveforms (comprising all the quadruple play services) are generated and transmitted sequentially along the experimental setup using different binary sequences. This is accomplished in order to reduce the dependence of the performance accuracy on the binary sequences transmitted.
2. Each signal waveform comprises: 536 GbE symbols, 1 LTE symbol, 5 WiMAX symbols and 228 UWB symbols.
3. For each signal waveform transmitted, thirty un-correlated noise runs of the corresponding received signal are acquired by the DSO Agilent scope and saved through Matlab software for off-processing. The different noise runs are required

to describe the statistical properties of the noise process with an acceptable accuracy and, particularly, to evaluate the parameters required by the exhaustive Gaussian approach (EGA) [103] used to obtain the BER of each sequence.

4. The saving process required to obtain the files corresponding to the 600 signal waveforms (20×30) acquired at the output of the experimental setup requires 1 hour, approximately, using a core 2 duo PC with CPU operating at 2.66 GHz and with 4 GB of RAM. The high saving time required is mainly due to the size of the waveforms sampled by the scope (1 million samples for each waveform, approximately) and also due to the time required to transfer the data from the scope to the PC (the acquiring process performed by the scope is controlled by Matlab software developed by the partners) using Ethernet connection.
5. After saving, the OFDM signals of each one of the 4PLAY (GbE, LTE, WiMAX and UWB) are demodulated and the QPSK information is recovered. This is performed for the 600 signal waveforms acquired.
6. After demodulation, the BER and the EVM, corresponding to the 600 signal waveforms saved, of each one of the 4PLAY services are evaluated. The demodulation of the four OFDM-based services for the 600 signal waveforms and the corresponding performance evaluation process requires 2.5 hours in a Intel Core I7 950 with CPU operating at 3.06 GHz and with 8 GB of RAM.

Figure 196 shows an example of the Matlab workspace saving the received data.

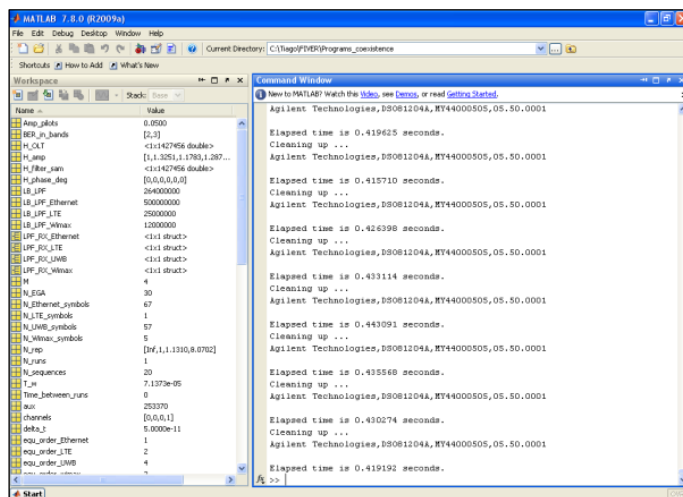


Figure 196. Capture of Matlab processing for digitizing the received signal at the DSO

5.3. Broadband impairment compensation performance

In first place, the number of pilots to be used for the channels sounding was evaluated experimentally. Also the order used for the channel response estimation was analysed.

The experimental setup follows the downstream path depicted in Figure 193. Figure 197 shows the experimental setup used for the evaluation of the performance of the impairment compensation system. The multi-format OFDM signals and the RF-pilots are obtained with Matlab® and generated with a Tektronix 7122B AWG with 20 GSamples/s.

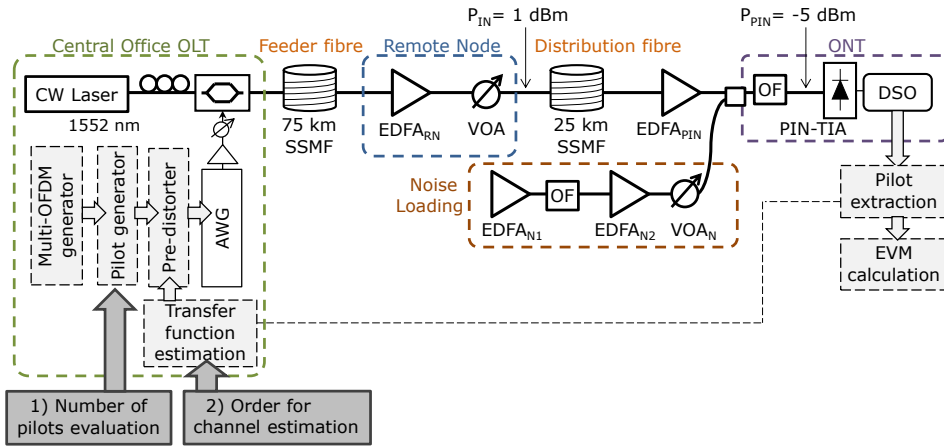


Figure 197. Experimental setup for impairment compensation subsystem performance evaluation

The access network in these experiments comprises a LR-PON with a total length of 100 km including a feeder of 75 km standard single mode fibre (SSMF) and a distribution fibre length of 25 km SSMF. External modulation is used, with the Mach-Zehnder working at quadrature point with an output power of 1.5 dBm. At the remote node (RN), an EDFA is used to compensate for the losses of the optical link. The optical power level at the input of the distribution fibre is set to 1 dBm (to avoid non-linearities in the fibre). A 10 GHz PIN with integrated trans-impedance amplifier is used at the receiver side. The pump current of the EDFA_{PIN} of the receiver side is adjusted to obtain an average optical power level of -5 dBm at the input of the photodiode. Also the noise loading block is configured to have a 30 dB optical signal-to-noise ratio (OSNR) in reference bandwidth of 0.1nm. Once photodetected, the signal is filtered and sampled by a real time Agilent oscilloscope DSO81204A at 10 GSamples/s and processed with Matlab® EVM calculation.

5.3.1. Performance vs. Number of pilots evaluation

The first evaluation experiment consists in analysing the dependence of the impairment compensation subsystem performance on the number of pilots used in the channel sounding for the estimation of the channel transfer function to be applied in the pre-distortion block.

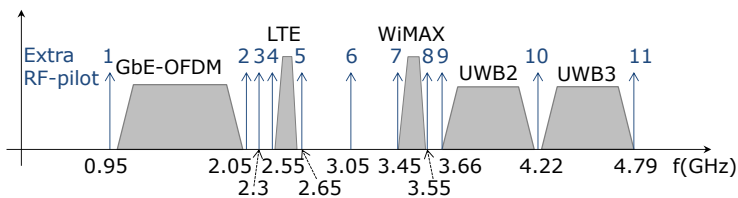


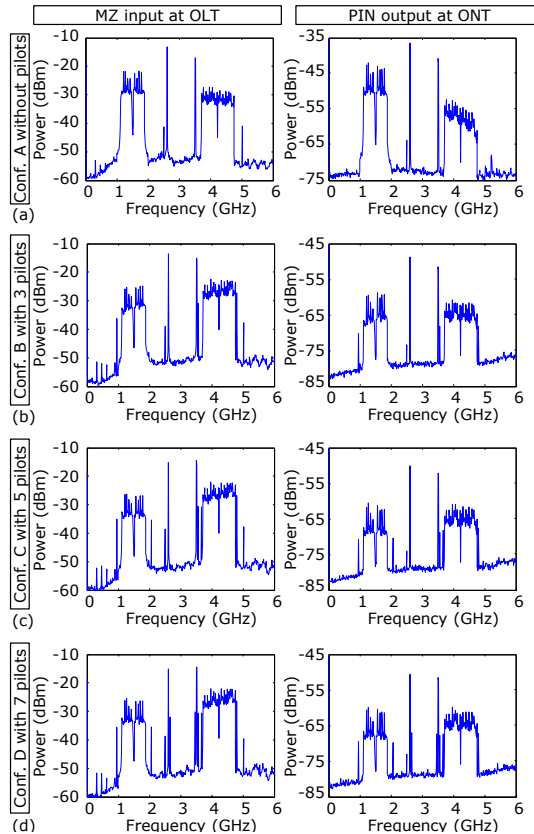
Figure 198. Frequency allocation of extra RF-pilots up to 11 pilots

Different configurations were evaluated considering from 3 to 11 pilots as shown in Figure 198. Table 19 shows the frequency of the extra RF-pilots inserted in the free-spectrum of the 4PLAY signals for the different configurations under study.

Table 19. RF-pilots frequency (GHz) used for evaluating the performance of the channel response estimation with different number of pilots

Conf.	#Pilots	0.95	2.05	2.3	2.55	2.65	3.05	3.45	3.55	3.66	4.22	4.79
A	0	X	X	X	X	X	ON	ON	ON	ON	ON	ON
B	3	ON	X	X	X	X	X	X	ON	X	X	ON
C	5	ON	ON	X	X	X	X	ON	ON	ON	X	ON
D	7	ON	ON	X	X	ON	X	ON	ON	ON	X	ON
E	9	ON	ON	X	ON	ON	X	ON	ON	ON	ON	ON
F	11	ON	ON	ON	ON	ON	ON	ON	ON	ON	ON	ON

The measurements for each configuration of Table 19 were done using the experimental setup shown in Figure 197 and the measurement procedure depicted in Section 5.2 for the downstream path considering Mach-Zehnder modulation. Figure 199 shows the measured electrical spectrum at the input of the modulator (once pre-compensation is applied) and at the output of the system (measured after the photodiode located at the ONT), for each of the pilot configurations depicted in Table 19.



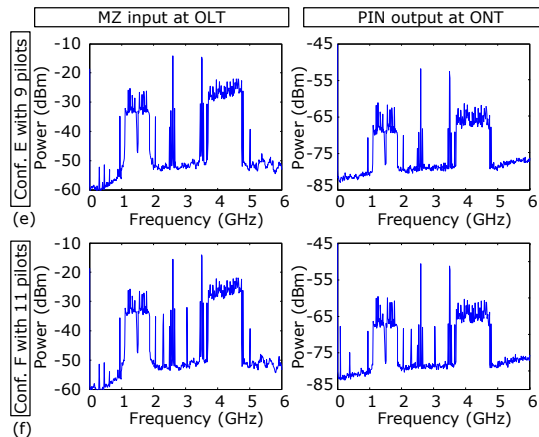


Figure 199. Electrical spectrum (RBW=1 MHz) measured at the input of the modulator and after the photodiode after a 100 km SSMF network for: (a) configuration A without pilot compensation, (b) configuration B with 3 pilots, (c) configuration C with 5 pilots, (d) configuration D with 7 pilots, (e) configuration E with 9 pilots and (f) configuration F with 11 pilots

In Figure 199 we can observe that the output spectrums are flatter when increasing the number of the RF-pilots for the channel sounding. Figure 200 shows the EVM results for each OFDM signal (GbE-OFDM, LTE, WiMAX and two UWB channels) obtained with different number of RF-pilots.

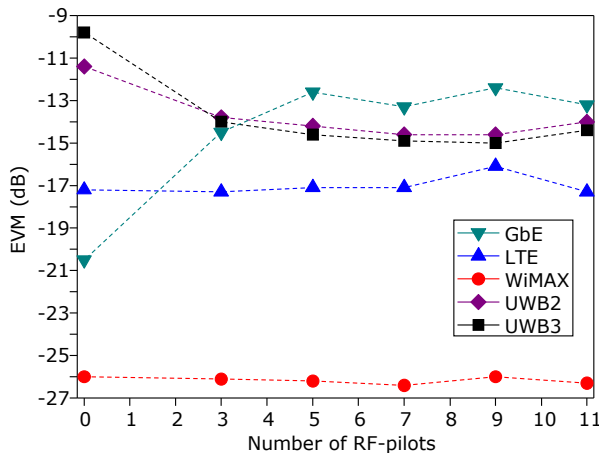


Figure 200. EVM results of GbE-OFDM, LTE, WiMAX and UWB using different number of pilots for the compensation approach

From the results shown in Figure 200 we can see that configuration E comprising 9 pilots gives the best improvement in received EVM after applying the pre-compensation. So, from the results of Figure 200, the configuration E is selected to be used in the proof-of-concept experiments reported in Section 5.4.

5.3.2. Performance vs. Transfer function order

In this section, the dependence of the amplitude frequency response on the DSP method used to estimate the channel response from the information provided by the sounding pilots is assessed. Particularly, the amplitude response estimated using the interpolation

and 1st order, 2nd order and 3rd order regression methods are studied. Additionally, the corresponding EVM obtained in each case is also presented and discussed.

The analysis is performed for a channel sounding realized by the nine pilots whose frequencies are presented in Table 19 for Configuration E. In addition, the study is performed for a feeder fibre between the OLT and the RN of 75 km and an ONT at 25 km far away from the RN (total OLT-ONT distance of 100 km).

Figure 201 depicts the amplitude frequency response used by the centralized compensation algorithm to mitigate the OLT-ONT channel impairments. The results are presented considering the amplitude response estimates evaluated from the two different approaches mentioned above. Figure 201 shows that very good fitting between the amplitude estimates evaluated and the amplitudes measured from the sounding pilots is achieved by the interpolation and the 3rd order regression methods. A worse fitting is obtained when the 1st and 2nd order regression methods are used.

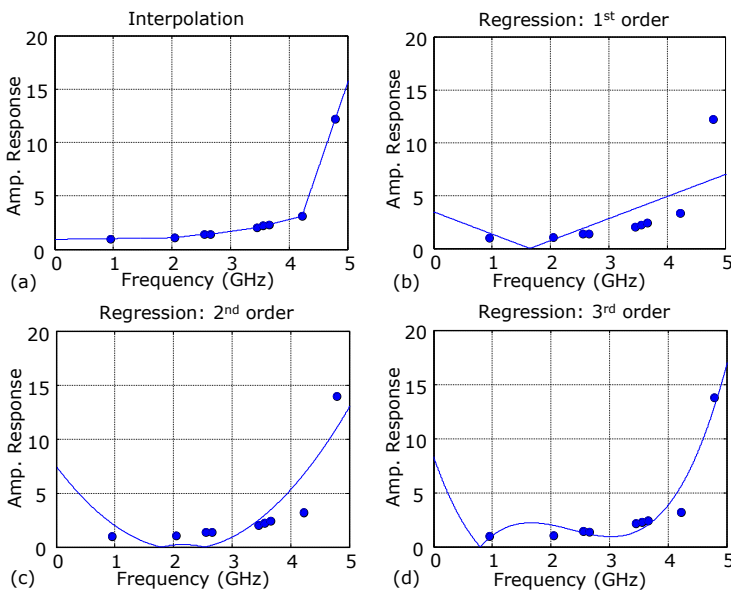
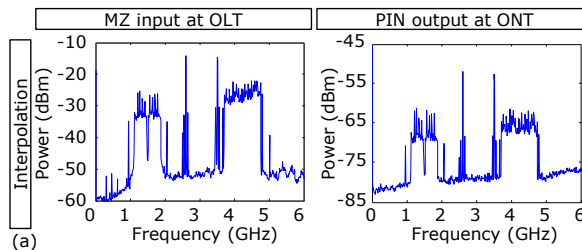


Figure 201. Amplitude frequency response estimated from DSP methods: (a) interpolation and (b) 1st order, (c) 2nd order and (d) 3rd order regression. Results obtained from: DSP method (line) and measured pilots amplitude (marks)

Figure 202 shows the input and output electrical spectra measured for each estimation method.



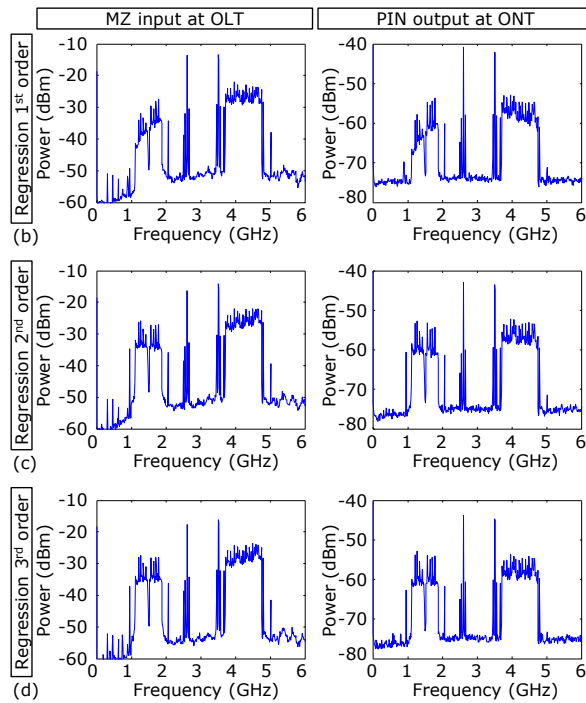


Figure 202. Electrical spectrum (RBW=1 MHz) measured at the input of the modulator and after the photodiode after a 100 km SSMF network for Configuration E with 9 pilots and: (a) interpolation, (b) 1st order, (c) 2nd order and (d) 3rd order regression methods

Finally, Figure 203 shows the EVM results for each estimation method considering 9 pilots and a 100 km fibre network without in-line chromatic dispersion compensation.

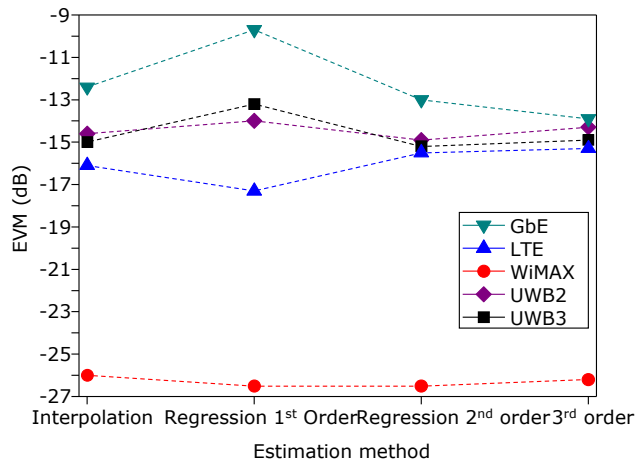


Figure 203. EVM results of GbE-OFDM, LTE, WiMAX and UWB using different estimation methods of the channel response

In order to conclude which DSP method should be implemented by the compensation algorithm at the OLT, the following two subjects must be also analysed in detail: i) which performance degradation of the quadruple play OFDM-based services is obtained when the different amplitude responses estimated by the DSP methods are employed and ii) which is the relative complexity required by each method when deployed in an actual network using a FPGA device.

Regarding the first aspect, as we observe in Figure 203, increasing the regression order for the estimation doesn't improve considerably the performance provided by the compensation block. Regarding the second aspect, we selected the interpolation method for the estimation as it is the simplest calculation approach and it will be easier to be implemented in a FPGA. This method will also be used in the impairment compensation proof-of-concept reported in Section 5.4.

5.3.3. Effect of extra RF-pilots on UWB signals

In addition, we wanted to test the performance of the extra RF-pilots over a transmission of real signals not generated with AWG. For these we generated the pilots according to configuration E of Table 19 with the same power levels as used in the performance experiments and we combined them with a real UWB signal generated with commercial-available devices. The performance in electrical back-to-back after the combination with the pilots was measured with the real time Agilent oscilloscope DSO81204A and the spectrum and EVM was analysed with VSA software for UWB channel 2 and channel 3. It was confirmed that the extra RF-pilots do not interfere with the real signals and no effect was observed in the received EVM. An example of UWB channel 2 results is shown in Figure 204.

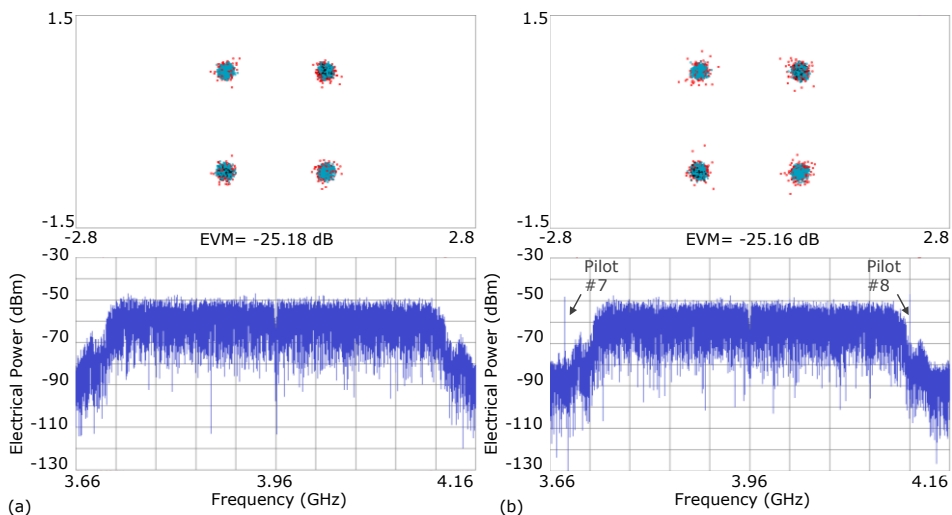


Figure 204. Measured EVM and electrical spectrum for UWB channel 2 when: (a) transmitted alone, (b) transmitted with the extra RF-pilots

5.4. Impairment compensation proof-of-concept

In the impairment compensation proof-of-concept, two RF-pilots next to each service are inserted at the OLT. In the case of UWB, a pilot is located also between the two channels as it is shown in Figure 205. Table 20 shows the frequency allocation of each RF-pilot. From the results obtained in Section 5.3.1, the total number of RF-pilots to be used in this proof-of-concept was selected to 9 pilots.

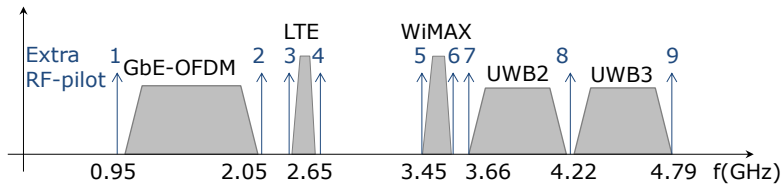


Figure 205. RF-pilots insertion in the free-spectrum of multi-OFDM services

Table 20. Frequency of the RF-pilots used for channel response estimation

RF-Pilot	1	2	3	4	5	6	7	8	9
Freq. [GHz]	0.95	2.05	2.55	2.65	3.45	3.55	3.66	4.22	4.79

5.4.1. Downstream path using external modulation and pre-compensation

For the downstream path, two different long-reach PONs architectures are considered: the first one without including in-line optical dispersion compensation, and the second one including it with a fibre Bragg grating (FBG). The block diagram of the downstream path is shown in Figure 204. The FBG block is marked in dashed line in Figure 204 as the network performance was evaluated with and without in-line chromatic dispersion compensation.

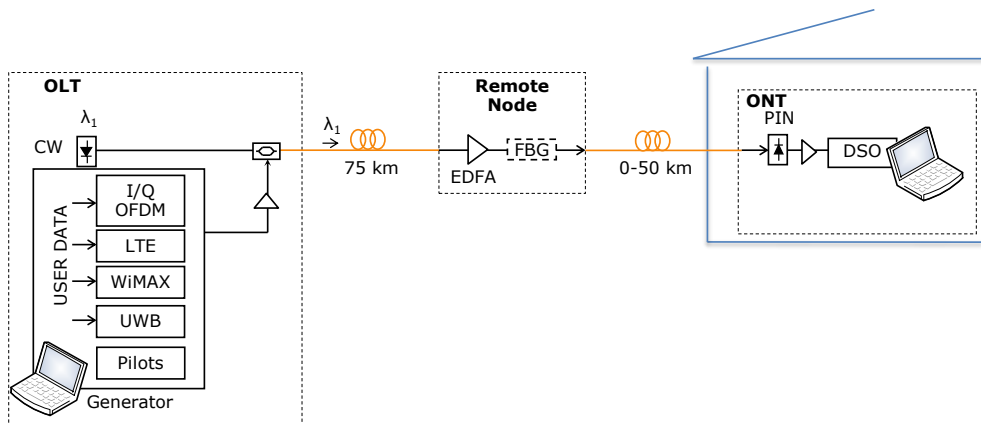


Figure 206. Downstream path evaluated in the proof-of-concept

5.4.1.1 Long-reach PON evaluation

Figure 197 shows the experimental setup used for the generation of multi-format OFDM signals and the transmission along the LR-PON using the proposed broadband channel sounding technique for impairment compensation. When no optical dispersion compensation device is included in the optical network, the signals suffer from fibre dispersion-induced power fading [69]. Nevertheless, the network should be able to overcome this impairment from the information provided by the RF-pilots.

The pump level of the amplifier at the remote node ($EDFA_{RN}$) is maintained constant and a VOA is used to ensure that the optical power at the input of the distribution fibre is 1 dBm to avoid nonlinear fibre effects.

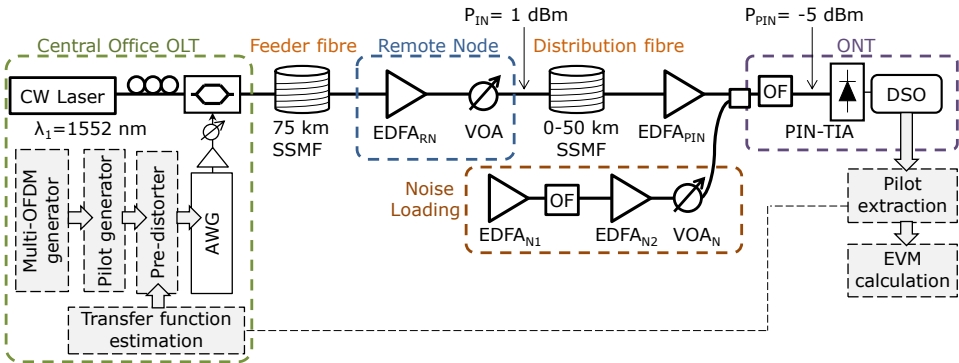


Figure 207. Experimental setup for multi-OFDM transmission along LR-PON applying pre-distortion at the OLT

Before the photodiode, amplified spontaneous emission noise is added through the noise loading circuit to obtain an OSNR of 30 dB (reference bandwidth of 0.1 nm). The optical power level arriving to the PIN is set to -5 dBm (using a receiver EDFA_{PIN}) to compare the performance under the same signal and noise power conditions.

Figure 208 shows some pictures of the experimental setup developed at IT premises.

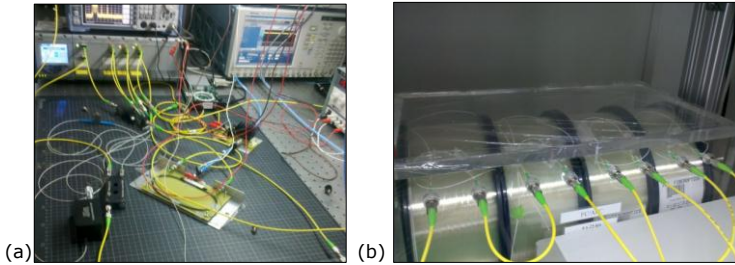


Figure 208. Pictures of (a) the experimental setup for downstream compensation proof-of-concept and (b) spools of fibre combination example for 100 km of SSMF network reach

First, the EVM of each signal was measured in back-to-back using the setup of Figure 209.

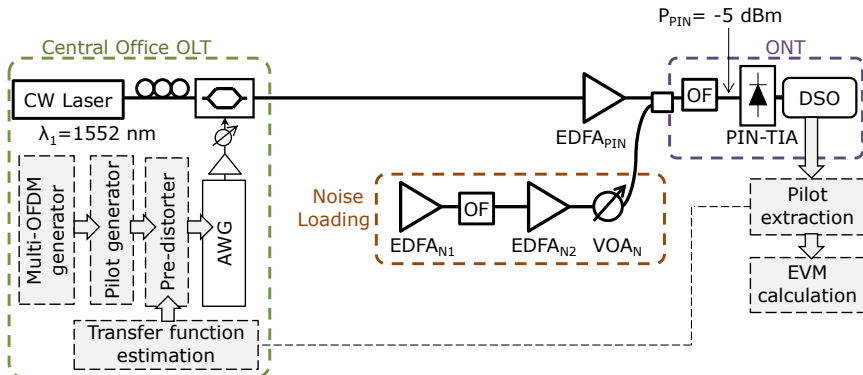


Figure 209. Experimental setup for back-to-back evaluation of multi-OFDM transmission along LR-PON applying pre-distortion at the OLT

These measurements compare a conventional system (without compensation) with the one applying the new compensation technique and are shown in Figure 210 for different modulation indexes (m). The modulation index is defined as the ratio between the RMS voltage of the electrical signal applied to the modulator and the modulator switching voltage according to (14).

$$m = \frac{V_{RMS}}{V_{\pi}} \quad (14)$$

From the results shown in Figure 210, a modulation index of 9% is selected, as it represents a good compromise between the EVM of the different services. Next, the evaluation over LR-PON was measured using the setup depicted in Figure 197 for different fibre lengths and using the selected modulation index.

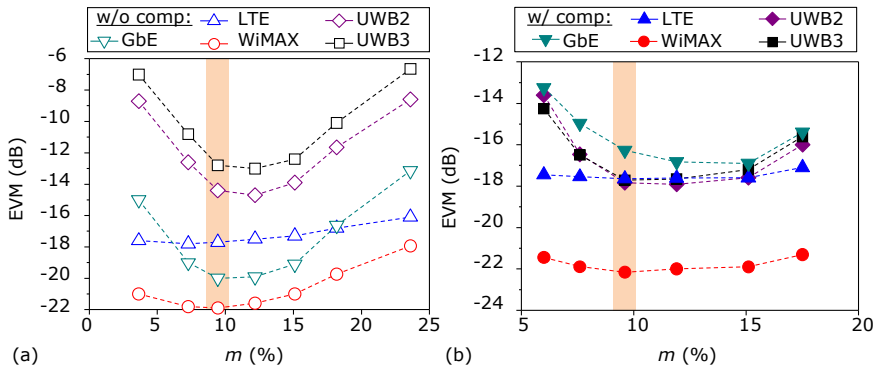


Figure 210. Measured EVM in back-to-back (a) without and (b) with pilot compensation (selected modulation index marked for reference)

Figure 211 show the spectrum of the combined multi-OFDM signal at the transmitter and receiver sides, respectively, considering a LR-PON with 125 km of length.

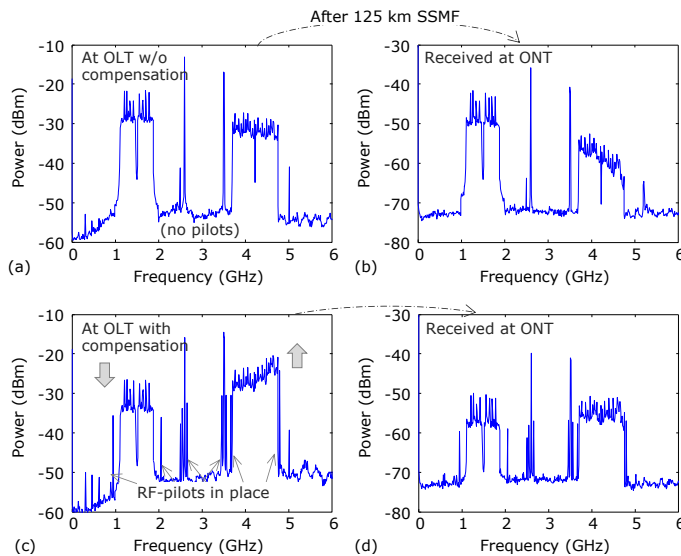


Figure 211. Electrical measured spectrums (RBW=1 MHz) of the signal at the OLT and ONT after 125 km SSMF: (a-b) without compensation and (c-d) with compensation for 125 km

When no compensation is used, the high frequency components of the received signal are distorted due to the frequency response of devices and the power fading induced by chromatic dispersion. If a pre-distorted signal is transmitted, the level of the higher signal frequencies is increased, as shown in Figure 211(c). In order to keep the same modulation index, the power increasing of the higher frequency signal components are obtained at the expense of decreasing the power level of the lower frequency signal. Nevertheless, transmitting the pre-distorted signal, a flat spectrum after 125 km SSMF is obtained (Figure 211(d)).

Figure 212 shows the optical spectrum measured in the long-reach network of 125 km SSMF reach, before the photodiode at the ONT.

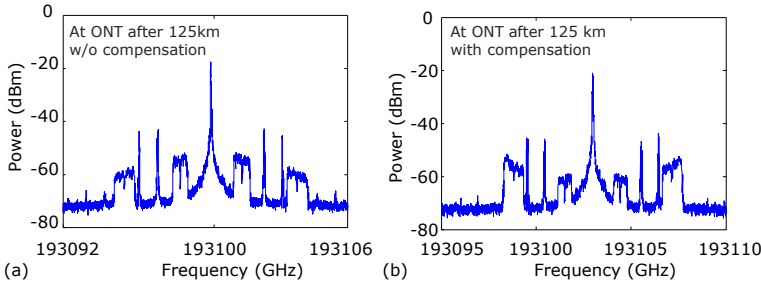


Figure 212. Optical spectrum measured before the photodiode at the ONT after 125 km: (a) without impairment compensation and (b) with applied compensation

The EVM of the different services at the ONT side were evaluated for different optical fibre reaches, and compared with the standard values as shown in Figure 213.

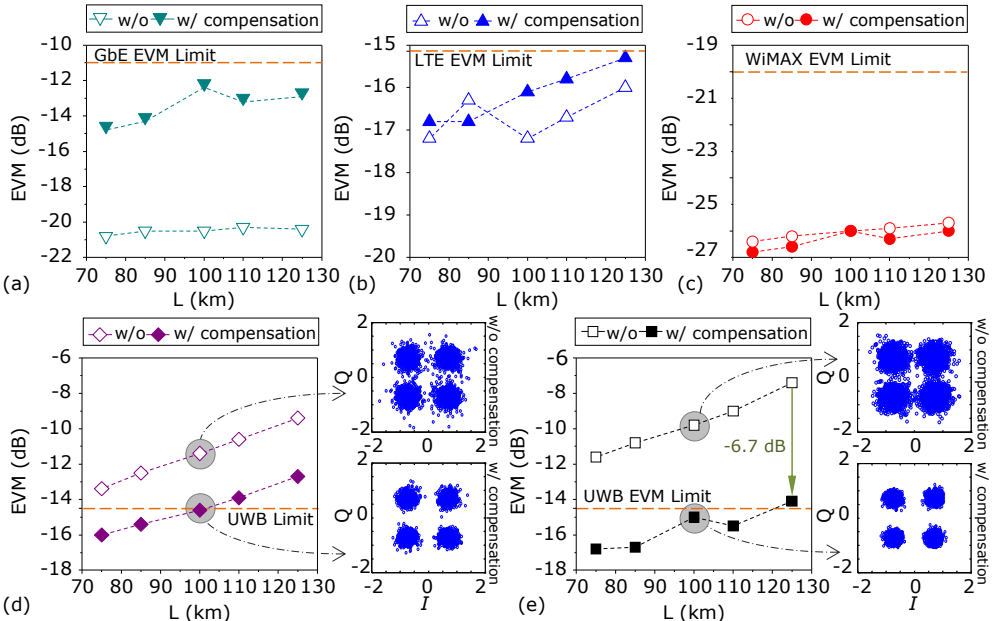


Figure 213. Experimental EVM vs. total fibre length between OLT and ONT obtained with and without pilot compensation for: (a) GbE-OFDM, (b) LTE, (c) WiMAX, (d) UWB channel 2 and (e) UWB channel 3 with constellations at 100 km of SSMF

As it can be observed in Figure 213, the proposed compensation technique allows reaching the transmission of the quadruple services along 100 km SSMF, while it could not be achieved in a conventional system due to the UWB signal degradation.

Figure 213(d)-(e) show the received constellations (with and without compensation) of UWB channel 2 and channel 3 after 100 km of SSMF (distribution fibre length of 25 km). When compensation is used, constellations show an EVM improvement of 3.2 dB and 5.2 dB, respectively, for UWB channel 2 and 3. This improvement still increases up to 6.7 dB in UWB channel 3 after 125 km. Figure 213 confirms also that the EVM of the GbE signal increases when the pre-distortion is used due to the decrease of the transmitted power of GbE signal. But its performance is always below the EVM threshold even at 125 km. Nevertheless, as the GbE-OFDM signal is generated with a custom I/Q OFDM modulator, the compensation could be applied directly to the I/Q generator. In this way it is foreseen that the performance of GbE could be better as the power of the signal will not be so deeply affected by the pre-compensation. This demonstration will be a further work after this Ph.D.

5.4.1.2 Dispersion-compensated long-reach PON evaluation

After the evaluation of the noise appearing in the long-reach PON experiments, it was evaluated a dispersion-compensated network. The experimental setup is identical to the one used for LR-PON adding a fibre Bragg grating (FBG) at the remote node (at the output of the EDFA_{RN}) as it is shown in Figure 214.

The FBG is adjusted to compensate an accumulated dispersion of 1700 ps/nm (corresponding to 100 km of SSMF). When the ONT is directly connected to the RN (75 km case), the accumulated dispersion of the link is -425 ps/nm approximately. On other hand, when the ONT is located at 50 km away from the RN (case of total network reach of 125 km SSMF), the accumulated dispersion of the link is 425 ps/nm, approximately. The full dispersion compensation case is achieved when the ONT is 25 km away from the RN (100 km case).

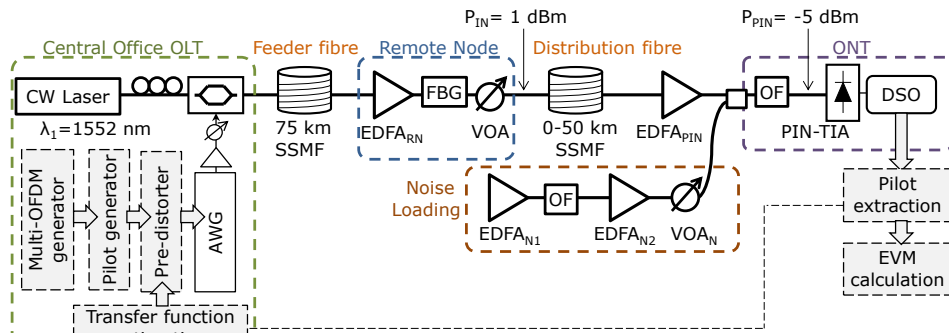


Figure 214. Experimental setup for multi-OFDM transmission along LR-PON applying pre-distortion at the OLT and optical dispersion compensation at the remote node

Figure 215 shows the spectrum of the combined multi-OFDM signal at the transmitter and receiver side, respectively, considering a dispersion-compensated LR-PON of 125 km. As it was observed before, in order to keep the same modulation index of the input signal at the modulator, the increasing of the higher frequency signals is obtained at the expense of decreasing the level of the low-frequency signal, although in this case we can see that the power increase of the high-frequency components in Figure 215(a) is not as big as the one applied for a network without in-line chromatic dispersion compensation as shown in Figure 211(c).

Compared with the spectrums without using FBG shown in Figure 211, we can observe that transmitting the pre-distorted signal, also a flat spectrum is obtained at the ONT after a 125 km SSMF network as shown in Figure 215(b).

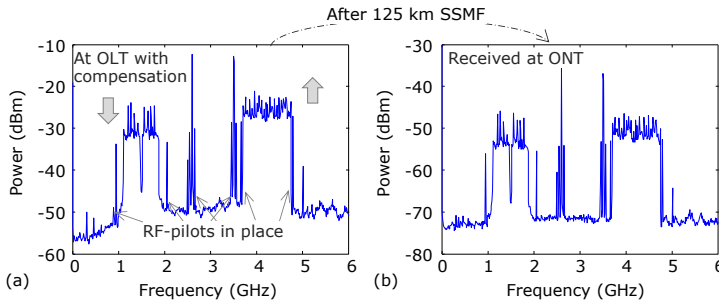


Figure 215. Electrical measured spectrums (RBW=1 MHz) for: (a) Signal at the OLT with compensation from RF-pilots for 125 km including FBG for compensating 100 km SSMF dispersion and (b) corresponding received signal at ONT after 125 km

The experimental measurements for the quadruple-play OFDM-based signals received after different network reaches are shown in Figure 216 including in-line dispersion compensation for 100 km SSMF. The measurements were done in the same conditions as the ones for long-reach PON without dispersion compensation reported in Section 5.4.1.1. The pump level of the amplifier at the remote node (EDFA_{RN}) is maintained constant and a VOA is used to ensure that the optical power at the input of the distribution fibre is 1 dBm to avoid nonlinear fibre effects, with a received OSNR of 30 dB in a reference bandwidth of 0.1 nm. The optical power level arriving to the PIN is also -5 dBm to compare the EVM performance under the same signal and noise power conditions.

In Figure 216 it can be observed the EVM performance of each OFDM signal when no compensation is applied with the information of the extra RF-pilots (blank symbols in the graphs of Figure 216) and when pre-compensation is used (filled symbols).

In this case we observe that the EVM behaviour of all the signals is always in a 1 dB range variation when changing the network fibre length. The EVM fluctuation when applying the proposed compensation technique is labelled in Figure 216 for reference, obtaining a maximum EVM variation of 0.9 dB in LTE and UWB, and only a 0.1 dB in WiMAX signal performance with accumulated chromatic dispersion changing from -425 ps/nm to +425 ps/nm. This means that the proposed algorithm is capable of compensating the residual chromatic dispersion.

From the results shown in Figure 216 it can be observed that including in-line dispersion compensation for 100 km, a network reach of 125 km can be achieved, and according to the behaviour of the graph even higher lengths could be reached. In addition, if we analyse the EVM improvement achieved for a 100 km network comparing the results with and without compensation we obtain: a 0.3 dB improvement in LTE, a 0.9 dB improvement in WiMAX, a 2.3 dB improvement in UWB channel 2, and 3.8 dB improvement in UWB channel 3.

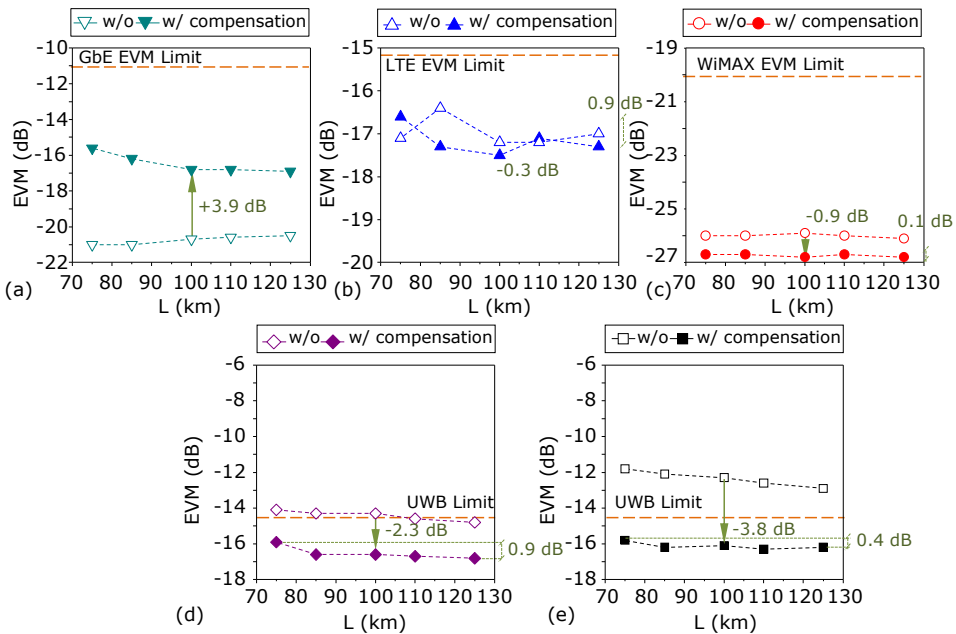


Figure 216. Experimental EVM vs. total fibre length between OLT and ONT using in-line dispersion compensation by FBG, obtained with and without pilot compensation for: (a) GbE, (b) LTE, (c) WiMAX, (d) UWB channel 2 and (e) UWB channel 3

As it happened in the non-compensated long-reach PON, the GbE signal has worse performance when applying the pre-compensation obtained with the extra RF-pilots. In this case the EVM is 3.9 dB worse if we use pre-compensation as the GbE power signal is decreased in order to be able to increase the power of the higher frequency signals and to keep the same modulation index. Nevertheless the GbE EVM meets the requirement even in a 125 km reach. However, as we commented before is it foreseen that in the GbE-OFDM performance will be better when applying the compensation directly to the I/Q OFDM modulator.

5.4.2. Upstream path using DML and post-compensation

Figure 217 shows the upstream path evaluated considering directly modulated lasers at the ONT at customer premises. In order to obtain a centralized network, all the management and compensation process should be developed at the OLT in order to keep the ONT as simple as possible at customer premises and reduce its cost. So, as pre-compensation was applied in the downstream data, in the case of upstream post-compensation will be applied at the received signal at the OLT. The same configuration of feeder fibre of 75 km SSMF and distribution fibres ranging from 0 to 50 km are considered to evaluate total network reaches from 75 to 125 km.

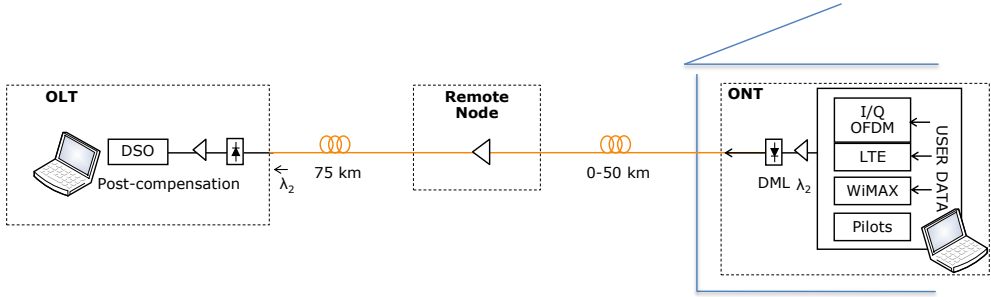


Figure 217. Upstream path evaluated in the proof-of-concept

In this experiment, as UWB is intended be used for video broadcasting, no upstream data is included in UWB, so a triple-format OFDM signal comprising GbE-OFDM, LTE and WiMAX is transmitted for the upstream performance evaluation. In the case also the pilots next to UWB service are also discarded and only 6 pilots are transmitted for channel sounding. The signal and pilots spectrum is represented in Figure 218 and the frequencies are detailed in Table 21.

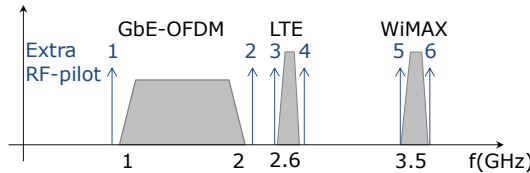


Figure 218. Triple-format OFDM signal and RF-pilots in the free-spectrum for upstream evaluation

Table 21. Frequency of the RF-pilots used for upstream channel response estimation

RF-Pilot	1	2	3	4	5	6
Freq. [GHz]	0.95	2.05	2.55	2.65	3.45	3.55

Figure 219 shows the experimental setup developed for the evaluation of triple-play signal transmission using directly modulated lasers and post-compensation with the information of the extra RF-pilots in the free spectrum of the multi-format OFDM signals. The setup starts from the right side to the left following the diagram direction depicted in Figure 217. At the OLT, the signals are sampled with a DSO and processed. The information of channel sounding is extracted from the extra RF-pilots and post-compensation is applied to the received signal. Finally, the quality of the signals in terms of EVM is calculated using the same procedure as in the previous Section.

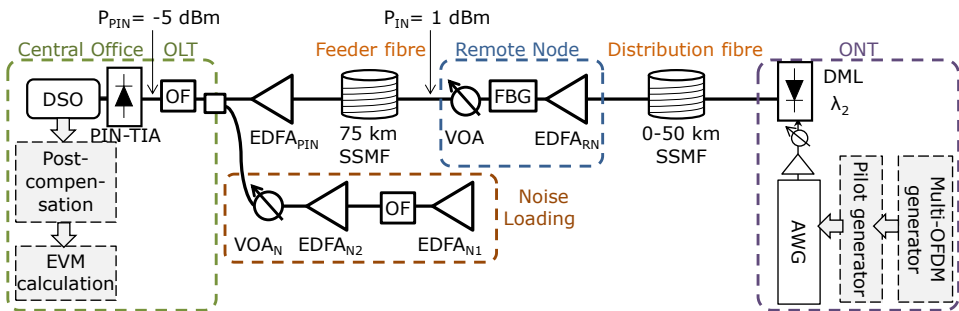


Figure 219. Experimental setup for upstream evaluation in LR-PON with post-compensation at the OLT

Figure 220(a) shows the experimental setup developed in IT premises in a joint activity between IT and UPVLC. Figure 220(b) shows a zoom of the DML with the RF-input connected for the triple-play OFDM signals modulation.

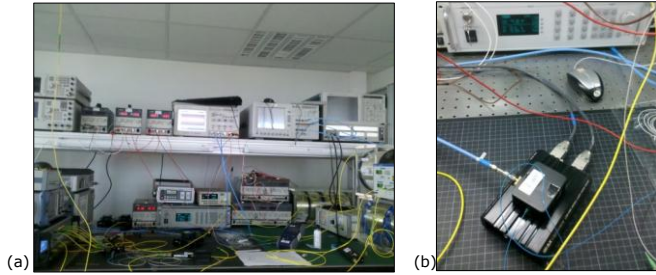


Figure 220. Pictures of (a) the experimental setup for upstream compensation proof-of-concept and (b) DML caption

Figure 221 shows the measured EVM for a network of 100 km reach (from the ONT with 25 km of distribution fibre to the remote node followed by 75 km SSMF to the OLT). In this case the EVM is calculated without applying the post-compensation with the information of the extra RF-pilots. Different modulation indexes were used at the DML in order to select the best one for the proof-of-concept. In a DML the modulation index (m) can be calculated as:

$$m = \frac{V_{RMS}}{(I_{bias} - I_{th}) \cdot R} \quad (15)$$

Where V_{RMS} is the root mean square voltage of the input signal applied to the DML, in this case the bias current applied to the laser is of $I_{bias}=30$ mA with a threshold of $I_{th}=8.1$ mA over a resistance of $R=50 \Omega$.

From the results shown in Figure 221 a modulation index of $m=14\%$ was selected for the experiments as it is the value for the best EVM performance of the triple-play services GbE-OFDM, LTE and WiMAX.

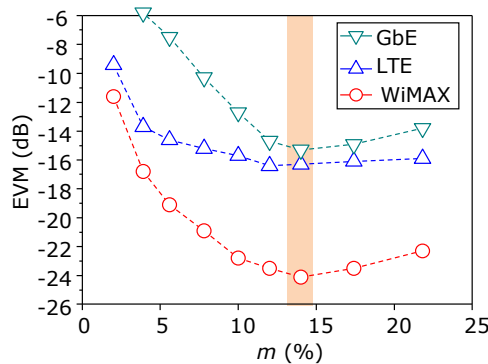


Figure 221. Measured EVM in a long-reach PON using DML of 100 km with different modulation indexes (selected modulation index marked for reference)

Figure 222 shows the received electrical spectrums at the photodiode located at the OLT after a total network length of 75 and 125 km respectively. The information obtained from the extra RF-pilots is used to post-compensate the signal level to get a flat spectrum.

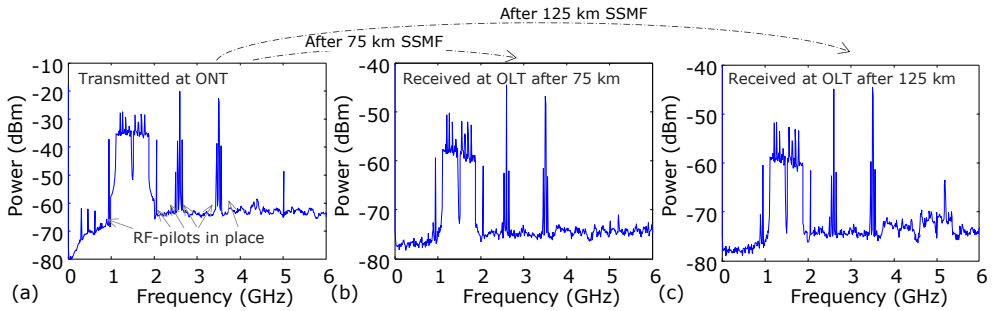


Figure 222. Electrical spectrum (RBW=1 MHz): (a) transmitted at the DML, and received at the OLT after (a) 75 km and (b) 125 km network

Figure 223 shows the measured EVM for each OFDM-based signal (a) GbE-OFDM, (b) LTE and (c) WiMAX. The results applying post-compensation are the same as without the post-compensation extracted from the pilots (the symbols are overlapped in the graphs). This comes from the fact that post-compensation is not able to improve the quality of the received signal because when the signal level is increased from the information of amplitude coming from the extra RF-pilots, also the noise and distortion effects are increased and no improvement is observed in EVM.

As it is observed in Figure 223, the performance of all the OFDM-based signals in coexistence in the upstream path are full-compliant with the EVM limits even for a long-reach PON of 125 km. These results point out that it would not be necessary to include extra-RF pilots for the upstream path which simplifies the ONT.

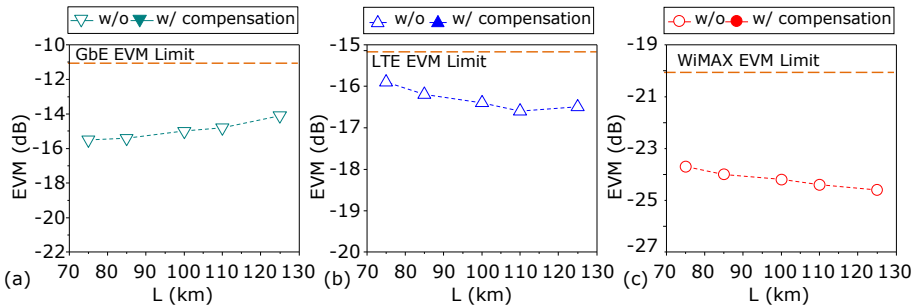


Figure 223. Experimental EVM vs. total fibre length between ONT and OLT obtained with and without pilot post-compensation for: (a) GbE, (b) LTE, and (c) WiMAX

However, further work will be done in the compensation of the upstream to see if we can achieve any improvement and also, the downstream path behaviour will be evaluated using DML to compare the performance with external Mach-Zehnder modulation.

5.5. Conclusion

In this chapter a broadband channel sounding technique based on RF-pilots insertion in the free spectrum of multi-format OFDM signals is used for the centralized impairment compensation in long-reach PONs. First, the compensation system was evaluated to obtain the optimum number of RF-pilots to use. Also the estimation order for the channel response was studied.

With this compensation technique, significant performance improvement in the simultaneous transmission of GbE-OFDM, LTE, WiMAX and two UWB channels along fibre

lengths indicated for LR-PONs has been demonstrated with the proposed technique. A 100 km LR-PON was reached without in-line dispersion compensation that could not be obtained without the impairment compensation technique due to the distortion of UWB signals. The signal pre-distorted with the information extracted from the pilots provides a maximum EVM improvement of 6.7 dB in the higher frequency signals (UWB) after 125 km SSMF transmission.

Also, a LR-PON including in-line chromatic dispersion compensation for 100 km was evaluated in the downstream. This confirms that the proposed algorithm is capable of compensating the residual chromatic dispersion as the EVM behaviour of all the signals are always in a 1 dB range variation within -425 ps/nm to $+425$ ps/nm residual dispersion. Using a FBG to compensate chromatic dispersion we can achieve more than 125 km network reach with all the quadruple-play OFDM-based signals in coexistence with a standard-compliant EVM.

Finally, the upstream path working with DML was evaluated using post-compensation over the received signal at the OLT with the information extracted from the extra RF-pilots for channel sounding. Experimental results point out that the post-compensation is not able to improve the quality of the received signal because when the signal level is increased, also the noise level increases and no improvement is observed in EVM. However, the performance of all the upstream OFDM-based signals in coexistence (GbE-OFDM, LTE and WiMAX) is full-compliant with the EVM limits even for a long-reach PON of 125 km.

CHAPTER 6. CONCLUSION AND FURTHER WORK

6.1. Main conclusions

This Thesis presents different architectures and functionalities for optical access networks based on OFDM signals.

Chapter 2 is dedicated of UWB-over-fibre transmission analysis and demonstration. First, a comparison of radio-over-fibre transmission of both UWB implementations (based on impulse-radio and OFDM) was evaluated. The OFDM-UWB experimental results showed better transmission performance than IR-UWB signals. So, following with OFDM-UWB investigations, the hybrid wireless-optical transmission of OFDM-UWB signals as defined in the ECMA-368 standard was experimentally demonstrated. An OFDM-UWB transmission providing 400 Mbit/s per user at optical distances from 5 to 50 km on SSMF is demonstrated. The analysis includes the wireless radiation from 0 to 3 m after optical transmission. The results indicate a maximum EVM degradation of 2.5 dB measured at 1.5 m radio after 50 km SSMF optical transmission for the first two UWB channels. This degradation translates to 1 m maximum wireless-reach penalty.

Also, the feasibility of using SCM multi-user OFDM-based transmission over polarization multiplexed systems was investigated. The experimental results for the polarization-multiplexed SCM configuration indicate that a 4 dB additional polarization crosstalk interference can be expected compared to a non-polarization multiplexed transmission system which translates to 2.4 dB EVM penalty in the UWB signals. This technique permits the multi-user UWB transmission in SCM over polarization-multiplexed networks with 25 km SSMF reach achieving 0.76 bit/s/Hz spectral efficiency.

In Chapter 3, the in-building optical distribution for UWB pico-cell provisioning was evaluated over SSMF and MMF media. Three UWB channels providing an accumulated bitrate of 600 Mbit/s are transmitted over 300 m SSMF and MMF employing external modulation. Simulation and experimental results in good agreement point out that MMF distribution is more sensitive to constellation rotation that is very dependent on the frequency. This can be compensated using a phase shift. Once compensated, the symbol-mapped constellation presents more scattering of the symbols in the case of SSMF, due mainly to the losses of the connectors compared with the low-losses imposed by 300 m SSMF. For longer distances, SSMF could lead to better results, but for short range communications MMF exhibits better performance. Both SSMF and MMF achieve ECMA-368 EVM limit of -14.5 dB at 300 m length.

Next, a time-stretched Ph-ADC architecture was proposed for the sensing of the pico-cell ultra-low-power signals. Radio sensing was demonstrated using a multiplexed multichannel time-stretch photonic-ADC with engineered optical and electrical amplification. Fingerprinting and localization algorithms were developed and tested on UWB signals detected by the Ph-ADC.

Also, linearization techniques for electro-optical modulators have been investigated. The concept dual-parallel LiNbO₃ Y-Coupled linearized electro-optic modulation has been proposed and demonstrated experimentally, exhibiting 15.2 dB SFDR gain over a conventional LiNbO₃ MZ-EOM. This linearization concept finds application in highly-linear applications like radio-over-fibre transmissions where multiple services coexist in a huge bandwidth. In addition, a dual-drive modulator with chirp management was evaluated for UWB-over-fibre applications observing a linear regime extension with SFDR > 25 dB over 1.4 V bias range is achieved compared with the 0.5 V range of a conventional MZ-EOM. This provides enhanced linearity for radio-over-fibre transmissions.

In chapter 4, coexistence studies for the 3PLAY transmission of simultaneous OFDM-based signals (LTE, WiMAX and UWB) in radio-over-fibre networks were performed. A reflective architecture using R-EAT achieved up to 15 km SSMF bidirectional communication of the

3PLAY services. The 3PLAY services distribution of simultaneous transmission of LTE, WiMAX and UWB is confirmed experimentally in bi-directional communication using CWDM (1550 nm and 1300 nm) in PON networks up to 50.6 km SSMF without optical amplification or regeneration stages. The bi-directional radio extension transmission of simultaneous provision of LTE, WiMAX and UWB achieved 3 m wireless communication after 20.2 km SSMF optical transmission.

In-home fibres have been tested and Corning ClearCurve single-mode fibre provided the best performance with 3PLAY transmission after 20.2 km SSMF and 200 m bend-insensitive fibre. Also, GI-POF media was evaluated in an end-to-end transmission comprising a 25 km access network, followed by a 25 m POF in-home optical network and 1 m wireless transmission. The simultaneous transmission of LTE, WiMAX and UWB was achieved after this complete system with EVM compliant values and also with a real high-definition video distribution on UWB signal.

Finally in Chapter 5, a broadband channel sounding technique based on using extra RF-pilots in the free spectrum of multi-format OFDM signals is proposed and demonstrated for the centralized impairment compensation in long-reach PONs. Significant performance improvement in the simultaneous transmission of GbE, LTE, WiMAX and two UWB channels was observed achieving a 100 km LR-PON without in-line dispersion compensation. This technique provides a maximum EVM improvement of 6.7 dB in the higher frequency signals (UWB) after 125 km SSMF transmission.

The techniques developed in this Ph.D. thesis provided solutions for increasing the reach of the wireless signals thanks to the optical network transmission and also improve the capacity of the network enabling the coexistence of different OFDM-based services. The usage of these techniques in the different levels of the network is necessary for the proper evolution of the Information Society, which was the main objective of this Ph.D thesis.

6.2. Further work

From the work done during this Ph.D. different topics will be further investigated. New ad-hoc modulation schemes based on OFDM will be developed for extend the reach and capacity of the optical access networks. The implementation of the new modulation schemes in FPGA devices is also an objective for the next research activities. Furthermore, the addition of DVB-T signals to the OFDM-based service bundle investigated in this Ph.D. thesis (GbE-OFDM, LTE, WiMAX and UWB) will be evaluated by simulation and tested at the laboratory during 2012.

Also, the investigation of MIMO transmission techniques using polarization multiplexing is an open field to explore after this Ph.D. And further investigation of OFDM-based signals radio-over-fibre distribution in new optical media will be performed as soon as the new fibres are available.

From the results of the impairment compensation subsystem, the evaluation of the performance on the GbE-OFDM signal when applied directly to the I/Q generator will be investigated. Also, from these results, further research will be done regarding the impairment compensation of the upstream path using DML to obtain better performance. New schemes for improving the impairment compensation will be proposed and investigated. In addition, the evaluation of the downstream path behaviour using DML to compare the performance with the results obtained with external Mach-Zehnder modulation will be done after this Ph.D. Thesis. Also the investigation of radio-over-fibre transmission in a WDM network in a 4λ configuration will be performed in the next months.

Furthermore, the investigation of Raman amplification in the access architecture for the uplink path will be performed in order to simplify the optical architecture and use a passive remote node. In addition, coherent detection will be considered a research topic in further investigations.

6.3. Acknowledgements

I want to thank all the people at Valencia Nanophotonics Technology Center who worked with me during these years and in particular to my Ph.D. supervisor Dr. Roberto Llorente for his help and guidance.

Also, I want to thank all the partners I worked with in European projects since the beginning of this research at 2008 in FP6-IST 26592 ISIS and FP6-IST-2005- 5-033615 UROOF Projects. The main work on this thesis was done under the framework of FP7-ICT-2009-4-249142 FIVER and FP7-ICT-2007-1-216785 UCELLS projects. Also, FP7-ICT-2007-1-216863 BONE, FP7-ICT-2007-2-224402 EUROFOS, Plan Nacional I+D+I TEC2009-14250 ULTRADEF projects are acknowledged. This Thesis was supported by the Spanish Government MEC grant *Formación de Profesorado Universitario* FPU AP2007-01413.

Finally, I would like to deeply thank my colleagues from the University of Essex (Terry Quinlan and Professor Stuart Walker) and from Instituto Superior Técnico de Lisboa (Tiago Alves and Professor Adolfo Cartaxo) for their support during the research stays and all the hours spent in the lab.

ANNEX A. PUBLICATIONS

A.1. Original publications

A.1.1. International peer-reviewed journals

[Alv11] T. Alves, M. Morant, A. Cartaxo, and R. Llorente, "Performance Comparison of OFDM-UWB Radio Signals Distribution in Long-Reach PONs Using Mach-Zehnder and Linearized Modulators", *IEEE Journal on Selected Areas in Communications (JSAC) special issue on Distributed Broadband Wireless Communications*, Vol. 29, No. 6, pp. 1311-1320, June 2011.

[Gom09] Nathan J. Gomes, Maria Morant, Arokiaswami Alphones, Béatrice Cabon, John E. Mitchell, Christophe Lethien, Mark Csörnyei, Andreas Stöhr, and Stavros Iezekiel, "Radio-over-fibre transport for the support of wireless broadband services [Invited]", *J. Opt. Netw.* 8, 156-178 (2009)

[Llo08a] R. Llorente, T. Alves, M. Morant, M. Beltran, J. Perez, A. Cartaxo, and J. Marti, "Ultra-Wideband Radio Signals Distribution in FTTH Networks", *IEEE Photonics Technology Letters*, Vol. 20, No. 11, June 1, pp. 945-947, 2008.

[Llo10a] Roberto Llorente, Maria Morant, José F. Puche, Jac Romme, Nicolas Amiot, Bernard Uguen, Jonathan Duplicy, "Localization and Fingerprint of Radio Signals Employing a Multichannel Photonic Analog-to-Digital Converter", *IEEE Transactions on Microwave Theory and Techniques*, Vol. 58, Issue: 11, Part: 2, pp. 3304 – 3311, 2010.

[Llo11a] Roberto Llorente, Maria Morant, Nicolas Amiot and Bernard Uguen, "Novel Photonic Analog-to-Digital Converter Architecture for Precise Localization of Ultra-Wide Band Radio Transmitters", *IEEE Journal on Selected Areas in Communications (JSAC) special issue on Distributed Broadband Wireless Communications*, Vol. 29, No. 6, pp. 1321-1327, June 2011.

[Mor09a] Maria Morant, Tiago Alves, Roberto Llorente, Adolfo Cartaxo, and Javier Marti, "Experimental Comparison of Transmission Performance of Multi-channel OFDM-UWB Signals on FTTH Networks", *IEEE Journal Lightwave Technology*, Vol. 27, Issue 10, May 15, 2009.

[Mor09b] Maria Morant, Joaquin Pérez, Roberto Llorente and Javier Marti, "Combined Analysis of OFDM-UWB Transmission in Hybrid Wireless-Optical Access Networks", *IEEE Photonics Technology Letters*, Vol. 21, Issue 19, pp. 1378-1380, Oct. 2009.

[Mor11a] Maria Morant, Roberto Llorente, Jerome Hauden, Terence Quinlan, Alexandre Mottet and Stuart Walker, "Dual-Drive LiNbO3 Interferometric Mach-Zehnder Architecture with Extended Linear Regime for High Peak-to-Average OFDM-based Communication Systems", *Optics Express*, Vol. 19, No. 26, December 2011

[Per09a] Joaquin Perez, Maria Morant, Roberto Llorente and Javier Marti, "Joint Distribution of Polarization-Multiplexed UWB and WiMAX Radio in PON", *IEEE Journal of Lightwave Technology Converged Optical Network Special Issue*, Vol. 27, Issue 12, pp. 1912-1919, June 2009.

[Qui11a] Terence Quinlan, Maria Morant, Sandra Dudley, Roberto Llorente and Stuart Walker, "480Mbps UWB Bi-Directional Radio over Fibre CWDM PON using Ultra-Low Cost and Power VCSELs", *Optics Express*, Vol. 19, No. 26, December 2011.

[Shi12] Y. Shi, M. Morant, C. Okonkwo, R. Llorente, E. Tangdiongga, and A.M.J. Koonen "Multi-Standard Wireless Transmission over SSMF and Large-Core POF for Access and In-Home Networks", *IEEE Photonics Technology Letters*, 2012.

A.1.2. International conferences

[Alv08] T. Alves, M. Morant, R. Llorente, A. Cartaxo and J. Marti, "Experimental demonstration of 1.56 Gbit/s OFDM-UWB distribution over 100 km of standard-fibre in FTTH networks", *OECC/ACOFT 2008 Conference*, Sydney, Australia, July 2008.

[Bel08] Marta Beltran, Maria Morant, Joaquin Perez, and Roberto Llorente, "UWB wireless coexistence by fibre-based photonic ADC interference monitoring" *FTTH, Wireless Communications, and their interaction 6th Workshop Network of Excellence ISIS*, Stockholm, Sweden, June 2008.

[Bel08a] Marta Beltran, Maria Morant, Joaquin Perez, Roberto Llorente and Javier Marti, "Photonic generation and frequency up-conversion of impulse-radio UWB signals", *The 21st Annual Meeting of The IEEE Lasers & Electro-Optics Society*, 2008 LEOS Annual Conference, Newport Beach, CA, 9-13 November 2008.

[Bel09] M. Beltran, M. Morant, J. Perez, and R. Llorente, "Performance Evaluation of OFDM and Impulse-Radio Ultra-Wideband over Fiber Distribution for In-Building Networks", *IEEE International Conference on Ultra-Wideband*, Vancouver, Canada, 9-11 September 2009.

- [Laz11] J. A. Lazaro, V. Polo, B. Schrenk, F. Bonada, I. Cano, E. T. Lopez, C. Kazmierski, G. de Valicourt, R. Brenot, J. Bauwelinck, X.-Z. Qiu, P. Ossieur, M. Forzati, P.-J. Rigole, I. T. Monroy, E. Tangdiongga, M. Morant, L. Nicolau, A. L. Teixeira, D. Erasme, D. Klonidis, I. Tomkos, J. Prat, C. Kouloumentas, H. Avramopoulos, "Optical Subsystems for Next Generation Access Networks", Invited paper in Access Networks and In-house Communications (ANIC2011), Toronto, Canada, June 12-14.
- [Llo08b] Roberto Llorente, Manoj P. Thakur, Maria Morant, Stuart D. Walker, Javier Marti, "Performance comparison of radio-over-fibre UWB distribution in SSMF and MMF optical media", ECOC 2008, 21-25 September 2008, Brussels, Belgium, Tu.3.E.2, Vol. 2, pp. 119-120.
- [Llo08c] Roberto Llorente, Joaquin Pérez, Marta Beltrán, Maria Morant and Javier Martí, "UWB picocell clusters: Real-time interference monitoring", ICT-MobileSummit 2008, Stockholm, Sweden, June 2008.
- [Llo09a] R. Llorente, T. Alves, M. Morant, M. Beltran, J. Perez, A. Cartaxo, J. Marti, "Optical Distribution of OFDM and Impulse-Radio UWB in FTTH networks", Conference on Optical Fibre communication/National Fibre Optic Engineers Conference, 2008. OFC/NFOEC 2008. JWA100, San Diego, CA, February 2008.
- [Llo09b] Roberto Llorente, Maria Morant and Marta Beltran, "Ultra-wideband Radio-over-Fibre in Transparent Optical Networks", Invited paper in International Conference on Transparent Optical Networks, ICTON2009, Azores, Portugal, 28 June 2009.
- [Llo09b] Roberto Llorente, Maria Morant, José Puche, Jac Romme and Tiago Alves, "Sensing Ultra-Low-Power Radio Signals by Photonic Analog-to-Digital Conversion", 35th European Conference on Optical Communication ECOC2009, Vienna, Austria, 20-24 September 2009.
- [Llo09c] Roberto Llorente, Maria Morant, José Puche, Tiago Alves and Jac Romme "Cognitive Radio by Photonic Analog-to-Digital Conversion Sensing", Second International Workshop on Cross-Layer Desing, IWCLD2009, Palma de Mallorca, Spain, 11-12 June, 2009.
- [Llo09c] Roberto Llorente, Maria Morant, Torger Togle, Terry Quinlan, Manoj Thakur and Stuart Walker, "UWB Radio-over-Fibre and Photonic Sensing for Cognitive Optical Access Networks", 22nd Annual Meeting of the IEEE Photonics Society, Turkey, 4 - 8 October 2009.
- [Llo10b] Roberto Llorente, Jerome Hauden, Maria Morant, Henri Porte and Nicolas Grossard, "Dual-Parallel Y-Coupled Lithium Niobate Electro-Optic Modulator with 15.2 dB SFDR gain", 15th European Conference on Integrated Optics (ECIO2010), Cambridge, 7- 9 April 2010.
- [Llo10c] Roberto Llorente, Maria Morant, Nicolas Amiot and Bernard Uguen, "Localisation of Ultra-Wide Band Radio Signals by Time-Multiplexed Photonic Analog-to-Digital Processing", ECOC 2010, P6.19, 19-23 September, 2010, Torino, Italy.
- [Llo10d] Roberto Llorente, Maria Morant, Jonathan Duplity, Toon Van Waterschoot, Vincent Le Nir, Marc Moonen, José Puche and Jac Romme, "Sensing and Fingerprinting of Ultra Wide Band Radio in UCELLS Project", Future Network and Mobile Summit 2010, Florence, Italy, 16 - 18 June 2010
- [Llo11b] R. Llorente, S. Walker, I. Tafur Monroy, M. Beltrán, M. Morant, T. Quinlan, and J.B. Jensen, "Triple-Play and 60-GHz Radio-over-Fibre Techniques for Next-Generation Optical Access Networks" Invited Paper in 16th European Conference on Networks and Optical Communications (NOC 2011), Newcastle upon Tyne, UK, 20-22 July 2011.
- [Llo11c] Roberto Llorente, Maria Morant, Terry Quinlan, Natán Medina and Stuart Walker, "Optical Architectures Evaluation for Triple-Play Distribution in FIVER Project", Future Network Mobile Summit 2011, Warsaw, Poland, June 2011.
- [Llo11d] Roberto Llorente, Natán Medina, Maria Morant, and Fernando Boronat, "Evaluation of UHDTV signal transmission in FTTH networks using Next Generation WiMedia UWB", Future Network Mobile Summit 2011, Warsaw, Poland, June 2011.
- [Llo11e] Roberto Llorente, Maria Morant, Jerome Hauden, Terence Quinlan, Alexandre Mottet and Stuart Walker, "Linear Regime Extension Technique in Parallel LiNbO3 Interferometric Architectures for UWB Applications", 37th European Conference and Exhibition on Optical Communication (ECOC2011), 18-22 September 2011.
- [Mor08a] Maria Morant, Tiago Alves, Roberto Llorente, Joaquin Pérez, Marta Beltran, Adolfo Cartaxo and Javier Marti, "Impact of Pilot Tone-assisted Equalization in Wimedia-defined OFDM-UWB signals Transmission in FTTH networks", International Topics Meeting on Microwave Photonics, 2008. Jointly held with the 2008 Asia-Pacific Microwave Photonics Conference. MWP/APMP 2008, Gold Coast, Australia, 30 Sept-3 Oct 2008, pp. 217 - 220.
- [Mor08b] Maria Morant, Marta Beltran, Joaquin Perez, and Roberto Llorente, "Impulse-Radio Ultra Wide-Band Signals Distribution in FTTH Networks", FTTH, Wireless Communications, and their interaction 6th Workshop Network of Excellence ISIS, Stockholm, Sweden, June 2008.

- [Mor08c] Maria Morant, Joaquin Pérez, Marta Beltran, Roberto Llorente and Javier Marti, "Integrated performance analysis of UWB wireless optical transmission in FTTH networks", The 21st Annual Meeting of The IEEE Lasers & Electro-Optics Society, 2008 LEOS Annual Conference, Newport Beach, CA, 9-13 November 2008, pp. 87 - 88.
- [Mor09c] Maria Morant, Joaquin Perez, Roberto Llorente, Javier Marti, "Transmission of 1.2 Gbit/s Polarization-Multiplexed UWB Signals in PON with 0.76 Bit/s/Hz Spectral Efficiency", Conference on Optical Fibre communication/National Fibre Optic Engineers Conference OFC/NFOEC 2009, paper OTuJ6, San Diego, CA, March 2009.
- [Mor09d] Maria Morant, Joaquin Pérez, Marta Beltrán and Roberto Llorente, "Performance Evaluation of In-Building Radio-over-Fibre Distribution of Multi-Band OFDM UWB Signals", 2009 IEEE International Topical Meeting on Microwave photonics, Valencia, Spain, 14-16 October 2009.
- [Mor10a] Maria Morant, Joaquin Pérez and Roberto Llorente, "Effect of multi-channel MB-OFDM UWB radio-over-fibre transmission using polarization multiplexed distribution in FTTH networks", Access Networks and In-house Communications (ANIC) of Optical Society of America, AThA6, Karlsruhe, Germany, 21-24 June 2010.
- [Mor11b] Maria Morant, Terence Quinlan, Stuart Walker, Roberto Llorente, "Complete Mitigation of Brillouin Scattering Effects in Reflective Passive Optical Networks using Triple-Format OFDM Radio Signals", Conference on Optical Fibre communication/National Fibre Optic Engineers Conference OFC/NFOEC 2011, paper JWA072, Los Angeles (EEUU), March 2011.
- [Mor11c] Maria Morant, Terence Quinlan, Roberto Llorente and Stuart Walker, "Full Standard Triple-Play Bi-Directional and Full-Duplex CWDM Transmission in Passive Optical Networks", Conference on Optical Fibre communication/National Fibre Optic Engineers Conference OFC/NFOEC 2011, paper OWB3, Los Angeles (EEUU), March 2011.
- [Mor11d] Maria Morant, Terence Quinlan, Stuart Walker and Roberto Llorente, "Real World" FTTH Optical-to-Radio Interface Performance for Bi-directional Multi-Format OFDM Wireless Signal Transmission", OFC/NFOEC 2011, paper NTuB6, Los Angeles (EEUU), March 2011.
- [Mor11e] Maria Morant, Terence Quinlan, Anthony Ng'oma, Sandra Dudley, Stuart Walker, Roberto Llorente, "Specialty Fibre Evaluation for In-building Distribution of Multiple-Format OFDM Radio Signals", Conference on Optical Fibre communication/National Fibre Optic Engineers Conference OFC/NFOEC 2011, paper JWA016, Los Angeles (EEUU), March 2011.
- [Mor12] Maria Morant, Tiago Alves, Adolfo Cartaxo, and Roberto Llorente, "Transmission Impairment Compensation Using Broadband Channel Sounding in Multi-Format OFDM-based Long-Reach PONs", Conference on Optical Fibre communication/National Fibre Optic Engineers Conference OFC/NFOEC 2012, paper OW3B.2, March 2012.
- [Per09b] Joaquin Pérez, Maria Morant, Marta Beltrán and Roberto Llorente, "Performance of MB-OFDM UWB and WiMAX IEEE 802.16e Converged Radio-over-Fibre in PON", 2009 IEEE International Topical Meeting on Microwave photonics, Valencia, Spain, 14-16 October 2009.
- [Per09c] J. Perez, M. Beltran, M. Morant, R. Llorente, A. Rahim Biswas, R. Piesiewicz, M. Cotton, D. Führer, B. Selva, I. Bucaille, S. Zeisberg, "Interference Analysis of WiMAX 802.16e Transmissions in the 3.5 GHz Band on WiMedia defined UWB wireless", 2009 IEEE 69th Vehicular Technology Conference VTC Spring, Barcelona, Spain, 26-29 April 2009.
- [Per09d] Joaquin Perez, Maria Morant, Libera Cavallin, Marta Beltran, Roberto Gaudino, Roberto Llorente, "Experimental Analysis of WiMedia-defined UWB and WiMAX 802.16e Coexistence in Personal Area Networks", ICT Mobile Summit 2009, Santander, Spain, 10-12 June, 2009.
- [Per09e] J. Perez, M. Beltran, M. Morant, L. Cavallin, R. Llorente, "Protection Margins for Joint Operation of WiMAX 802.16e and WiMedia-defined UWB Radio in Personal Area Networks", IEEE International Conference on Ultra-Wideband, Vancouver, Canada, 9-11 September 2009.
- [Qui11b] Terence Quinlan, Maria Morant, Roberto Llorente and Stuart Walker, "Ultra-Low Cost and Power VCSEL-Based 480Mbps UWB Radio over a Bi-Directional CWDM PON", 37th European Conference and Exhibition on Optical Communication (ECOC2011), 18-22 September 2011.
- [Qui12] Terence Quinlan, Sandra Dudley, Maria Morant, Roberto Llorente and Stuart Walker, "First Demonstration of Cooler-less, Bi-Directional, Format-Agnostic, Wireless and Gigabit Ethernet Network Provision using Off-The-Shelf VCSELs", Conference on Optical Fibre communication/National Fibre Optic Engineers Conference OFC/NFOEC 2012, paper OTh3G.1, March 2012.
- [Shi11] Y. Shi, M. Morant, E. Tangdiongga, R. Llorente, and A.M.J. Koonen, "Full Standard Triple Wireless Transmission over 50m Large Core Diameter Graded-Index POF", POF 2011 Conference Proceedings - Post Deadline Paper pp. 579-582, Bilbao, Spain, 14-16 September 2011.

A.1.3. Book chapters

[Llo09d] Roberto Llorente, Maria Morant and Javier Marti, "Chapter 13: Radio-over-Fibre Networks for 4G" in Book "Fourth-Generation Wireless Networks: Applications and Innovations", Ed. Information Science Reference, ISBN: 978-1-61520-674-2, December 2009.

[Llo11f] Roberto Llorente, Marta Beltrán and Maria Morant, "Chapter 16: UWB-over-Fibre in Next-generation Access Networks" in Book "Ultra Wideband Communications: Novel Trends - System, Architecture and Implementation", Ed. INTECH, 2011.

A.2. Technical Reports

FIVER Deliverable D2.1. "Scenarios identification and functional requirements", Roberto Llorente (UPVLC), Maria Morant (UPVLC), Natan Medina (UPVLC), António Gamelas (PTIN), Inês Oliveira (PTIN), Cláudio Rodrigues (PTIN), Vitor Mirones (PTIN), Joaquim Miguel Silva (PTIN), Michael Parker (UESSEX), Terrence Quinlan (UESSEX), Stuart Walker (UESSEX), Pierre Cluzeaud. FP7-ICT-2009-4-249142 FIVER Project, March 2010.

FIVER Deliverable D2.2. "State-of-the-art of quintuple-play services and femtocell networks", Roberto Llorente (UPVLC), Maria Morant (UPVLC), Natan Medina (UPVLC), Axel Schmidt (HTW), Pierre Cluzeaud (TCF), António Gamelas (PTIN), Inês Oliveira (PTIN), Cláudio Rodrigues (PTIN), Vitor Mirones (PTIN), Joaquim Miguel Silva (PTIN). FP7-ICT-2009-4-249142 FIVER Project, March 2010.

FIVER Deliverable D2.3. "State-of-the-art of FTTH, in-building optical distribution and integrated wireless radio", Anthony Ng'Oma (CORNING), Natan Medina (UPVLC), Maria Morant (UPVLC), Roberto Llorente (UPVLC), Pierre Cluzeaud (TFC), Axel Schmidt (HTW). FP7-ICT-2009-4-249142 FIVER Project, March 2010.

FIVER Deliverable D2.4. "State-of-the-art of OFDM optical/radio transmission impairment compensation", Radoslaw Piesiewicz (EIT+), Maciej Nawrocki (EIT+), Roberto Llorente (UPVLC), Maria Morant (UPVLC), Natan Medina (UPVLC), Filipe W. Carvalho (IT), Terry Quinlan (UESSEX), Michael Parker (UESSEX), Stuart Walker (UESSEX). FP7-ICT-2009-4-249142 FIVER Project, March 2010.

FIVER Deliverable D2.5. "Convergence of quintuple-play and femtocell services specification", Maria Morant (UPVLC), Roberto Llorente (UPVLC), Axel Schmidt (HTW), Pierre Cluzeaud (TFC). FP7-ICT-2009-4-249142 FIVER Project, September 2010.

FIVER Deliverable D2.6. "CWDD integrated network architecture specification", Maria Morant (UPVLC), Terry Quinlan (UESSEX), Roberto Llorente (UPVLC), Stuart Walker (UESSEX), Natán Medina (UPVLC), Marta Beltrán (UPVLC), Cláudio Rodrigues (PTIN), António Gamelas (PTIN), Vitor Mirones (PTIN), Joaquim Miguel Silva (PTIN), Inês Freitas Oliveira (PTIN), Axel Schmidt (HTW), Filipe W. Carvalho (IT), Daniel D. Fonseca (IT), José A. P. Morgado (IT), Adolfo V. T. Cartaxo (IT), Anthony Ng'Oma (CORNING). FP7-ICT-2009-4-249142 FIVER Project, December 2010.

FIVER Deliverable D2.7. "R-EAT-based (RWDD) integrated network architecture specification and management strategy", Michael Parker (UESSEX), Terrence Quinlan (UESSEX), Stuart Walker (UESSEX), Maria Morant (UPVLC), Natán Medina (UPVLC), Roberto Llorente (UPVLC), António Gamelas (PTIN), Inês Oliveira (PTIN), Cláudio Rodrigues (PTIN), Vitor Mirones (PTIN), Joaquim Miguel Silva (PTIN), Michael Sauer (CORNING), Axel Schmidt (HTW), Adolfo Cartaxo (IT), Filipe Wiener Carvalho (IT), Tiago Alves (IT). FP7-ICT-2009-4-249142 FIVER Project, December 2010.

FIVER Deliverable D2.8. "FIVER implementation and techno-economic analysis", Roberto Llorente (UPVLC), Maria Morant (UPVLC), José Sanchez (UPVLC), Javier Herrera (FIBRENOVA), António Gamelas (PTIN), Cláudio Rodrigues (PTIN), Vitor Mirones (PTIN), Michael Parker (UESSEX), Terrence Quinlan (UESSEX), Stuart Walker (UESSEX), Rakesh Sambaraju (CORNING), AnthonyNg'Oma (CORNING), Pierre Cluzeaud (TCF), Axel Schmidt (HTW), Adolfo Cartaxo (IT). FP7-ICT-2009-4-249142 FIVER Project, June 2011.

FIVER Deliverable D3.1. "Report on optical transmission coexistence requirements", Maria Morant (UPVLC), Natán Medina (UPVLC), Sandra Valentines (UPVLC), Roberto Llorente (UPVLC), Filipe W. Carvalho (IT), Adolfo V. T. Cartaxo (IT), José A. P. Morgado (IT), Daniel D. T. Fonseca (IT), Cláudio Rodrigues (PTIN), Joaquim M. Silva (PTIN), António Gamelas (PTIN), Mike Parker (UESSEX), Terry Quinlan (UESSEX), Stuart Walker (UESSEX), Axel Schmidt (HTW). FP7-ICT-2009-4-249142 FIVER Project, September 2010.

FIVER Deliverable D3.2. "Report on radio transmission coexistence requirements", Axel Schmidt (HTW), Dirk Burggraf (HTW), Thomas Bartzsch (HTW), Maria Morant (UPVLC), Marta Beltrán (UPVLC), Roberto Llorente (UPVLC), Terry Quinlan (UESSEX), Mike Parker (UESSEX), Stuart Walker (UESSEX), Pierre Cluzeaud (TFC), Filipe Carvalho (IT), Adolfo Cartaxo (IT). FP7-ICT-2009-4-249142 FIVER Project, September 2010.

FIVER Deliverable D3.3. "Optical and radio path OFDM transmission impairments compensation specification", Roberto Llorente (UPVLC), Maria Morant (UPVLC), José Sánchez (UPVLC), Sara Mas (UPVLC), Tiago Alves (IT), Adolfo Cartaxo (IT), Filipe Carvalho (IT), José A. P. Morgado (IT), Daniel D. Fonseca (IT), Lukasz Cywinski (EIT+), Radoslaw Piesiewicz (EIT+), Axel Schmidt (HTW), Terry Quinlan (UESSEX), Anthony Ng'Oma (CORNING). FP7-ICT-2009-4-249142 FIVER Project, December 2010.

FIVER Deliverable D3.4. "Report on baseband and radio-over-fibre OFDM transmission impairment compensation algorithms and expected performance", Łukasz Cywinski (EIT+), Axel Schmidt (HTW), Roberto Llorente (UPVLC), Maria Morant (UPVLC), Francisco Martínez (UPVLC), Joaquin Matres (UPVLC), Marta Beltrán (UPVLC), José Sánchez (UPVLC), Marcos Maestro (UPVLC), José A. P. Morgado (IT), Daniel D. Fonseca (IT), Adolfo Cartaxo (IT). FP7-ICT-2009-4-249142 FIVER Project, December 2010.

FIVER Deliverable D4.1. "Centralised management control architecture", Vitor Mirones (PTIN), Inês Oliveira (PTIN), Cláudio Rodrigues (PTIN), Joaquim Miguel Silva (PTIN), António Gamelas (PTIN), Ricardo Cadime (PTIN), Roberto Llorente (UPVLC), Maria Morant (UPVLC), Axel Schmidt (HTW), Michael Parker (UESSEX), Terry Quinlan (UESSEX), Stuart Walker (UESSEX), Pierre Cluzeaud (TCF). FP7-ICT-2009-4-249142 FIVER Project, December 2010.

FIVER Deliverable D4.2. "Multi-user OFDM GbE management protocol". Eloy Rico (DAS), Maria Morant (UPVLC), Roberto Llorente (UPVLC), Vitor Mirones (PTIN) and António Gamelas (PTIN). FP7-ICT-2009-4-249142 FIVER Project, March 2011.

FIVER Deliverable D4.3. "Multi-user UWB and WiMAX radio-over-fibre management protocol", Axel Schmidt (HTW), Markus Wehner (HTW), Pierre Cluzeaud (TFC), Maria Morant (UPVLC), Roberto Llorente (UPVLC), Vitor Mirones (PTIN), Antonio Gamelas (PTIN). FP7-ICT-2009-4-249142 FIVER Project, June 2011.

FIVER Deliverable D4.4. "Multi-user femtocell radio aggregation management protocol", Roberto Llorente (UPVLC), Maria Morant (UPVLC), Vitor Mirones (PTIN), Cláudio Rodrigues (PTIN), Antonio Gamelas (PTIN). FP7-ICT-2009-4-249142 FIVER Project, June 2011.

FIVER Deliverable D5.1. "OFDM-GbE signal generation", Eloy Rico (DAS), Elena García (DAS), Julián Blasco (DAS), Javier Herrera (DAS), Roberto Llorente (UPVLC), Maria Morant (UPVLC). FP7-ICT-2009-4-249142 FIVER Project, December 2010.

FIVER Deliverable D5.2. "Broadband OFDM impairment compensation subsystem". Maria Morant (UPVLC), Tiago Alves (IT), Roberto Llorente (UPVLC), Adolfo V. T. Cartaxo (IT), Javier Herrera (FIBRENOVA), Antonio Ramirez (FIBRENOVA). FP7-ICT-2009-4-249142 FIVER Project, June 2011.

FIVER Deliverable D5.4. "Report on off-the-shelf components and user equipment", Javier Herrera Llorente (FIB), Antonio Ramirez (FIB), José Correcher (FIB), Jacinto Portillo (FIB) José Sánchez (UPVLC), Maria Morant (UPVLC), Roberto Llorente (UPVLC), Axel Schmidt (HTW), Dirk Burggraf (HTW), Terry Quinlan (UESSEX), Mike Parker (UESSEX), Stuart Walker (UESSEX), Pierre Cluzeaud (TFC). FP7-ICT-2009-4-249142 FIVER Project, September 2011.

FIVER Deliverable D5.5. "Report on the baseband and radio-over-fibre ONT", Maria Morant (UPVLC), Roberto Llorente (UPVLC), António Gamelas (PTIN), Vitor Mirones (PTIN), Cláudio Rodrigues (PTIN), Mike Parker (UESSEX), Terry Quinlan (UESSEX), Stuart Walker (UESSEX), Eloy Rico (DAS). FP7-ICT-2009-4-249142 FIVER Project, September 2011.

FIVER Deliverable D6.1. "Laboratory platform architecture definition", Maria Morant (UPVLC), José Manuel Sánchez (UPVLC), Roberto Llorente (UPVLC), Pierre Cluzeaud (TFC), Isabelle Bucaille (TFC), Terry Quinlan (UESSEX), Michael Parker (UESSEX), Stuart Walker (UESSEX), Eloy Rico (DAS), Antonio Gamelas (PTIN), Vitor Mirones (PTIN), Tiago Alves (IT), Adolfo Cartaxo (IT), Axel Schmidt (HTW), Łukasz Cywinski (EIT+), Anthony Ng'Oma (CORNING). FP7-ICT-2009-4-249142 FIVER Project, December 2010.

FIVER Deliverable D6.2. "Converged OFDM optical transmission impairment compensation proof-of-concept", Maria Morant (UPVLC), Tiago Alves (IT), Roberto Llorente (UPVLC), Adolfo V. T. Cartaxo (IT), Terry Quinlan (UESSEX), Stuart Walker (UESSEX), José A. P. Morgado (IT), Daniel Fonseca (IT), Javier Herrera (FIBRENOVA), Antonio Ramirez (FIBRENOVA), Tomasz Wierzbowski (EIT+), Radoslaw Piesiewicz (EIT+), Axel Schmidt (HTW). FP7-ICT-2009-4-249142 FIVER Project, September 2011.

FIVER Deliverable D7.1. "Project presentation and web-site set-up", Maria Morant (UPVLC), Clara Calvo (UPVLC), Ingrid Juliana Niño (UPVLC), Carlos Gómez (UPVLC), Roberto Llorente (UPVLC). FP7-ICT-2009-4-249142 FIVER Project, March 2011.

FIVER Y1 Project Periodic Report. FP7-ICT-2009-4-249142 FIVER Project, 2011.

UCELLS Deliverable D2.1. "Report on Cellular-UWB functionalities, real-time UWB spectrum monitoring functionalities. Photonic-ADC and Radio-over-Fibre architecture, suitable scenarios and technology state-of-the-art", Roberto Llorente (UPVLC), Maria Morant (UPVLC), Joaquin Pérez (UPVLC), Marta

Beltrán (UPVLC), Tamar Danon (Wisair), Shimon Mantel (Wisair), David Schmertz (Wisair), Yossi Otiker (Wisair), Jonathan Duplicy (Agilent), José Puche (DAS Photonics), Toon van Waterschoot (KULEUVEN), Vincent Lenir (KULEUVEN), Tiago Alves (IST), Adolfo Cartaxo (IST), Jac Romme (IMST), Nicolas Amiot (UR1), Bernard Uguen (UR1), Yves Lostanlen (SIRADEL), Rafael Bañales (EUSKALTEL). FP7-2007-ICT-1-216785 UCELLS Project. September 2008.

UCELLS Deliverable D2.2. "UWB real-time monitoring and management strategies: system specification, target scenarios and functionalities", Roberto Llorente (UPVLC), Maria Morant (UPVLC), José Puche (DAS), Jac Romme (IMST), Tiago Alves (IST), Adolfo Cartaxo (IST), Jerome Hauden (PHOTLINE), Jonathan Duplicy (AGILENT), Amir Krause (WISAIR), Vincent

Le Nir (KULEUVEN), Bernard Uguen (UR1), Yves Lostanlen (SIRADEL), Rafael Bañales (EUSKALTEL). FP7-2007-ICT-1-216785 UCELLS Project. March 2009.

UCELLS Deliverable D2.3. "Cellular-UWB demonstrator specification", Roberto Llorente (UPVLC), Maria Morant (UPVLC), Javier Martí (UPVLC), José Puche (DAS), Jac Romme (IMST), Bernard Ugen (UR1) Nicolas Amiot (UR1), Jerome Hauden (PHOTLINE), Henri Porte (PHOTLINE), Jonathan Duplicy (AGILENT), Ton van Waterschoot (KULEUVEN), Vincent Le Nir (KULEUVEN), Adolfo Cartaxo (IST), Amir Krause (Wisair). FP7-2007-ICT-1-216785 UCELLS Project. March 2009.

UCELLS Deliverable D3.2. "Spectrum power monitoring software algorithms and hardware implementation", Vincent Lenir (KULEUVEN), Toon van Waterschoot (KULEUVEN), Jonathan Duplicy (Agilent), Roberto Llorente (UPVLC), Maria Morant (UPVLC). FP7-2007-ICT-1-216785 UCELLS Project. July 2009.

UCELLS Deliverable D3.3. "Dedicated heterogeneous radio simulator for UWB devices location", Grégory Gougeon (SIRADEL), Yves Lostanlen (SIRADEL), Roxana Burghilea (UR1), Stéphane Avrillon (UR1), Bernard Uguen (UR1), Roberto Llorente (UPVLC), Maria Morant (UPVLC). FP7-2007-ICT-1-216785 UCELLS Project. March 2009.

UCELLS Deliverable D3.4. "3D UWB incoming and outgoing interference estimation", Nicolas Amiot (UR1), Bernard Uguen (UR1), Mohamed Laaraiedh (UR1), Stéphane Avrillon (UR1), Roxana Burghilea (UR1), Gregory Gougeon (SIRADEL), Yves Lostanlen (SIRADEL), Maria Morant (UPVLC), Roberto Llorente (UPVLC), Jonathan Duplicy (AGILENT). FP7-2007-ICT-1-216785 UCELLS Project. October 2009.

UCELLS Deliverable D3.5. "Power-flow and channel management algorithms report", David Meshulam (WISAIR), Erez Weinberger (WISAIR), Amir Krause (WISAIR), Maria Morant (UPVLC), Roberto Llorente (UPVLC). FP7-2007-ICT-1-216785 UCELLS Project. October 2009.

UCELLS Deliverable D4.1. "RF and photonic subsystem specification", Roberto Llorente (UPVLC), Maria Morant (UPVLC), Marta Beltran (UPVLC), Joaquin Perez (UPVLC), Javier Marti (UPVLC), Yossi Otiker (Wisair), Tamar Danon (Wisair), Shimon Mantel (Wisair), David Schmertz (Wisair), Ronen Korman (Wisair), Tiago Alves (IST), Adolfo Cartaxo (IST), Jac Romme (IMST), Jerome Hauden (PHOTLINE), Henri Porte (PHOTLINE). FP7-2007-ICT-1-216785 UCELLS Project. September 2008.

UCELLS Deliverable D4.2. "Intermediate report on the RF, photonic subsystems, multichannel ADC and enhanced UWB terminals", Roberto Llorente (UPVLC), Marta Beltrán (UPVLC), Maria Morant (UPVLC), Joaquin Pérez (UPVLC), Javier Martí (UPVLC), David Meshulam (Wisair), Adolfo Cartaxo (IST), Jac Romme (IMST), Henri Porte (PHOTLINE), José Puche (DAS), Jonathan Duplicy (AGILENT), Ton van Waterschoot (KULEUVEN), Vincent Le Nir (KULEUVEN), Nicolas Amiot (UR1). FP7-2007-ICT-1-216785 UCELLS Project. December 2008.

UCELLS Deliverable D4.3. "Electro-optical subsystems final report", Jerome Hauden (PHOT), Henri Porte (PHOT), Tiago Alves (IST), Adolfo Cartaxo (IST), Maria Morant (UPVLC) and Roberto Llorente (UPVLC). FP7-2007-ICT-1-216785 UCELLS Project. August 2009.

UCELLS Deliverable D4.4. "Multi-channel electrical ADC", Jac Romme (IMST), Birgit Kull (IMST), Thorsten Kempka (IMST), Norbert Schmidt (IMST), Maria Morant (UPVLC), Roberto Llorente (UPVLC). FP7-2007-ICT-1-216785 UCELLS Project. March 2010.

UCELLS Deliverable D4.5. "Enhanced UWB terminals report", Amir Krause (WISAIR), David Meshulam (WISAIR), Denis Merakhovich (WISAIR), Maria Morant (UPVLC), Roberto Llorente (UPVLC). FP7-2007-ICT-1-216785 UCELLS Project. June 2010.

UCELLS Deliverable D4.6. "Optimised complete Ph-ADC architecture", Tiago Alves (IST), Adolfo Cartaxo (IST), Roberto Llorente (UPVLC) and Maria Morant (UPVLC). FP7-2007-ICT-1-216785 UCELLS Project. June 2010.

UCELLS Deliverable D5.1. "Intermediate reported on the Cellular-UWB laboratory platform", Roberto Llorente (UPVLC), Maria Morant (UPVLC), Joaquin Pérez (UPVLC), Marta Beltrán (UPVLC), José Puche (DAS), Jac Romme (IMST), Tiago Alves (IST), Adolfo Cartaxo (IST), Jerome Hauden (PHOTLINE),

Jonathan Duplicy (AGILENT), Rafael Bañales (EUSKALTEL), Vincent Le Nir (KULEUVEN), Bernard Uguen (UR1), Yves Lostanlen (SIRADEL), Yossi Kolkovich (WISAIR). FP7-2007-ICT-1-216785 UCELLS Project. December 2008.

UCELLS Deliverable D5.2. "Proof of concept laboratory set-up", José Puche (DAS), Maria Morant (UPVLC), Roberto Llorente (UPVLC), Jac Romme (IMST), Nicolas Amiot (UR1), Jurgen Vandermot (AGILENT). FP7-2007-ICT-1-216785 UCELLS Project. October 2009.

UCELLS Deliverable D5.3. "Cellular-UWB laboratory platform report", Eloy Rico (DAS), Maria Morant (UPVLC), Roberto Llorente (UPVLC), Amir Krause (WISAIR), Nicolas Amiot (UR1), Bernard Uguen (UR1), Jurgen Vandermot (AGILENT), Jonathan Duplicy (AGILENT), Gregory Gougeon (SIRADEL). FP7-2007-ICT-1-216785 UCELLS Project. April 2010.

UCELLS Deliverable D5.4. "Demonstration trial and Cellular-UWB strategies assessment", Maria Morant (UPVLC), Marcos Maestro (UPVLC), Roberto Llorente (UPVLC), José Puche (DAS), Eloy Rico (DAS), Nicolas Amiot (UR1), Bernard Uguen (UR1), Amir Krause (WISAIR), Jurgen Vandermot (AGILENT), Jonathan Duplicy (AGILENT). FP7-2007-ICT-1-216785 UCELLS Project. December 2010.

UCELLS Deliverable D6.1. "Exploitation and Business plan for Cellular-UWB technology", Rafael Bañales (EUSKALTEL), Maria Morant (UPVLC), Roberto Llorente (UPVLC), Amir Krause (WISAIR). FP7-2007-ICT-1-216785 UCELLS Project. December 2010.

UCELLS Deliverable D6.2. "Exploitation strategy and business plan for UWB T&M", Michael Dieudonne (AGILENT), Jonathan Duplicy (AGILENT), Jurgen Vandermot (AGILENT), Gery Verhaegen (AGILENT), Maria Morant (UPVLC), Roberto Llorente (UPVLC). FP7-2007-ICT-1-216785 UCELLS Project. December 2010.

UCELLS Deliverable D6.3. "Exploitation and Business plan for incoming/outgoing wireless interference monitoring in security environments", Eloy Rico (DAS), Miguel Ángel Piqueras (DAS), Maria Morant (UPVLC), José Manuel Sánchez (UPVLC), Marcos Maestro (UPVLC), Roberto Llorente (UPVLC). FP7-2007-ICT-1-216785 UCELLS Project. December 2010.

UCELLS Deliverable D7.2. "First report on the UWB technology evolution", Roberto Llorente (UPVLC), Joaquin Perez (UPVLC), Marta Beltran (UPVLC), Maria Morant (UPVLC), Jonathan Duplicy (AGILENT), David Meshulam (WISAIR). FP7-2007-ICT-1-216785 UCELLS Project. December 2008.

UCELLS Deliverable D7.3. "Intermediate report on the UWB technology and market evolution", Roberto Llorente (UPVLC), Maria Morant (UPVLC), Nathan Medina (UPVLC), Jonathan Duplicy (AGILENT), Amir Krause (WISAIR). FP7-2007-ICT-1-216785 UCELLS Project. December 2009.

UCELLS Deliverable D7.4. "Users forum report", Rafael Bañales (EUSKALTEL), Roberto Llorente (UPVLC), Maria Morant (UPVLC), Natán Medina (UPVLC), Marcos Maestro (UPVLC), José Sánchez (UPVLC). FP7-2007-ICT-1-216785 UCELLS Project. December 2010.

UCELLS Deliverable D7.5. "Y2 Workshop proceedings/report", Maria Morant (UPVLC), Roberto Llorente (UPVLC), Rafael Bañales (EUSKALTEL), Izaskun Pellejero (EUSKALTEL). FP7-2007-ICT-1-216785 UCELLS Project. December 2009.

UCELLS Deliverable D7.6- "Y3 Workshop proceedings/report", Marcos Maestro (UPVLC), Maria Morant (UPVLC), José Sánchez (UPVLC), Roberto Llorente (UPVLC), Rafael Bañales (EUSKALTEL). FP7-2007-ICT-1-216785 UCELLS Project. December 2010.

UCELLS Deliverable D7.7. "Report on Dissemination of Knowledge", Caterina Calatayud (UPVLC), Maria Morant (UPVLC), Roberto Llorente (UPVLC). FP7-2007-ICT-1-216785 UCELLS Project. December 2010.

UCELLS Deliverable D7.8- "Report on regulation activities", Roberto Llorente (UPVLC), Maria Morant (UPVLC), Natán Medina (UPVLC), Marcos Maestro (UPVLC), José Sánchez (UPVLC), Amir Krause (WISAIR), Gadi Shor (WISAIR). FP7-2007-ICT-1-216785 UCELLS Project. December 2010.

UCELLS D1.1. Final Project Report. FP7-2007-ICT-1-216785 UCELLS Project. December 2010.

UCELLS Y1 Project Periodic Report. FP7-2007-ICT-1-216785 UCELLS Project, 2008.

UCELLS Y2 Project Periodic Report. FP7-2007-ICT-1-216785 UCELLS Project, 2009.

UCELLS Y3 Project Periodic Report. FP7-2007-ICT-1-216785 UCELLS Project, 2010.

ULTRADEF Informe de Seguimiento Inicial. Proyecto I+D+i Plan Nacional TEC2009-14250 ULTRADEF, Febrero 2010.

ULTRADEF Informe de Seguimiento Annual. Proyecto I+D+i Plan Nacional TEC2009-14250 ULTRADEF, Diciembre 2010.

BONE Deliverable D13.2. "Report on Y2 activities and new integration strategy". FP7-ICT-2007-1 216863 BONE Project, November 2009.

BONE Deliverable D23.2. "Report on year 1 and updated plan for activities". FP7-ICT-2007-1 216863 BONE Project, November 2009

UROOF Deliverable D2.2 "UROOF sytem scenarios: Topology and architecture Part (a): identification of target scenarios", Roberto Llorente(UPVLC), Maria Morant(UPVLC), Javier Marti (UPVLC), Manoj P. Thakur (UoE), Stuart Walker(UoE), Arnaud Tonnerre(TCF), David Smith (CIP), Amir Krause (WI), Ghislaine Maury (INEPG), Moshe Ran (HIT), Henrique Salgado (INESC), Francisco Pereira (INESC). FP6-2005-IST-5-033615 UROOF Project.

UROOF Deliverable D2.3 "Guidelines for selection the most suitable UWB technology for UROOF", Ronen Korman (WI), Roberto Llorente (UPVLC), Maria Morant (UPVLC), Moshe Ran (HIT), Arnaud Tonnerre (TCF). FP6-2005-IST-5-033615 UROOF Project, June 2007.

UROOF Deliverable D4.4. "Report on Analysis of coverage and capacity for UROOF based systems", Maria Morant (UPVLC), Alberto Babiera (UPVLC), Libera Cavallin (UPVLC), Roberto Llorente (UPVLC), Javier Marti (UPVLC), Moshe Ran (HIT), Manoj Thakur (UoE), FP6-2005-IST-5-033615 UROOF Project, June 2007.

ISIS Deliverable D1.12 "Initial experimental results for flexible wireless systems using radio over fibre technology and optical networking techniques", Beatrice Cabon (CNRS-IMEP), Yannis Le GUENNEC (CNRS-IMEP), Christophe Lethien (CNRS-IEMN), Christophe Loyez (CNRS-IEMN), Jean-Pierre Vilcot (CNRS-IEMN), Philippe Lombard (INPG), Anne Vilcot (INPG), Anthony Nkansah (UNIKENT), Nathan Gomes (UNIKENT), Stavros Iezekiel (UNILEEDS), Márk Csörnyei (BUTE), Tibor Berceli (BUTE), Marek Chacinski, (KPRC), Pierre-Yves Fonjallaz (KPRC), Eva Rojas Alonson (TU/e), Ton Koonen (TU/e), María Morant Pérez (UPVLC), Sheila Galt (CHALMERS), John Mitchell, B Kalantari-Sabet, Thomas Ennouchy, Joseph Attard (UCL). FP6-IST 26592 ISIS Project, June 2008.

ISIS Deliverable D1.14. "Report on Verification of upgraded RoF experimental demonstrations compliance with wireless standards requirements", Maria Morant, Ruben Alemany, Joaquin Pérez, Javier Marti (UPVLC), John Mitchell, Chin-Pang Liu (UCL), Anthony Nkansah, Nathan Gomes (UNIKENT), Béatrice Cabon, Davide Bucci, Armin Schimpf, Yannis Le Guennec (CNRS-IMEP), Philippe Lombard (INPG), Christophe Lethien, Cathy Sion, Jean-Pierre Vilcot (CNRS-IEMN). FP6-IST 26592 ISIS Project, June 2008.

ISIS Deliverable D1.15. "Low-cost radio over fibre for current and next generation wireless systems", Anthony Nkansah (UNIKENT), Nathan Gomes (UNIKENT), P. Shen (UNIKENT), Jeanne James (UNIKENT), Majlinda Mjeku (UNIKENT), David Wake UNIKENT), C. Lethien (IEMN), C. Sion (IEMN), J.-P. Vilcot (IEMN), Stavros Iezekiel (UNILEEDS), Hejie Yang (TU/e), Eduward Tangdiongga (TU/e), Eva Rojas Alonso (TU/e), Bas Huiszoon (TU/e), Johan van Zantvoort (TU/e), Ton Koonen (TU/e), Gábor Kovács(BUTE), Tibor Berceli (BUTE), Márk Csörnyei (BUTE), Maria Morant (UPVLC), Manuel Alberto Violas (IT-Av), Javier Marti (UPVLC), Richard Schatz (KPRC), Marek Chacinski (KPRC), Pierre-Yves (KPRC), John Mitchell (UCL), Tabassam Ismail (UCL), Chin-Pang Liu, Alwyn Seeds (UCL), Manuel Alberto Violas (), Sheila Galt (CHALMERS). FP6-IST 26592 ISIS Project, December 2008.

ANNEX B. LOCALIZATION ALGORITHMS AND PERFORMANCE

As it was commented in Section 3.3.2, five sensors are the minimum number required to avoid ambiguity in the 3D localization. Obviously, the position of the sensors in the given area affects the positioning accuracy that can be achieved. Consequently, before performing experimental measurements reported in this Ph.D., different sensor positions were simulated to determine the best configuration to achieve the lowest error on the TDoA.

B.1. Localization of UWB signals approach

The localization algorithm is based on the laser pulse frequency repetition rate and the multiband DCM-OFDM UWB signal structure, which are perfectly known. When capturing the radio spectrum on optical pulses the resulting modulated signal generates a unique time-frequency code directly related to a unique predictable delay. Due to the non-contiguous observation of the radio electric spectrum, classical delay estimation based on correlation should not be employed.

The choice of f_R influence the predicted delay as it should be adequate to the DCM-OFDM signal structure, i.e. in order to sample the whole UWB symbol. The stretching factor M which only modifies the frequencies of the monitored band has no impact on the hopping sequence structure and therefore on the delay estimation algorithm, unless the stretching is so intense that optical overlap is produced between optical channels depicted in Inset (a) of Figure 91.

Once a set of delays are obtained for each channel with this method, a time difference of arrival (TDoA) algorithm is applied to obtain the position. The accuracy of such TDoA algorithm is linked to the accuracy of the delay estimation from the optically sampled signal, which strongly benefits from the simultaneous optical sampling of UWB radio in all the sensors at the same time. The goal of the delay estimation is to calculate a pseudo delay $\hat{\tau}_k$ on each k channel. The so-called pseudo delays are not the absolute delays of channels, but delays which refer to a common unknown delay reference. Because the TDoA total least square algorithm (TDoA-TLS) [81]-[82] is based on the difference of delays, this common delay reference disappears, and it remains the only parameter of interest: the pseudo delay $\hat{\tau}_k$.

The proposed delay estimation algorithm depicted in Figure 224 is based on two steps to obtain the pseudo delay estimation for a single k channel.

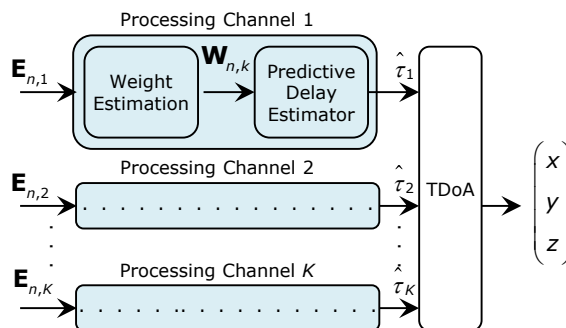


Figure 224. Delay estimation algorithm block diagram

First, the weight estimation is estimated. This stage uses the measured energy vector from the fingerprinting $\mathbf{E}_{n,k}$ to provide a vector $\mathbf{W}_{n,k}$, which can be interpreted as a confidence value on the measured energy.

Then, the weights sequence $W_{n,k}$ is processed by the predictive delay estimation (PDE) block, which provides estimation on the pseudo delay $\hat{\tau}_k$. Once the estimated pseudo delay $\hat{\tau}_k$ has been sequentially computed for the k channels, the TDoA-TLS algorithm provides the position of the UWB device.

The detailed process to obtain the position estimation is described mathematically now:

B.1.1. Building the weight vector

For each k channel, the output of the energy detection of the received signal is a vector \mathbf{E}_k built as following:

$$\mathbf{E}_k = [E_{n,k}^1, \dots, E_{n,k}^B] \quad (16)$$

where $E_{n,k}^b$ is the maximum value of the instantaneous measured energy in the b subband, the k^{th} channel for the n^{th} snapshot. We refer to snapshot as the information coming at the same time from all the sensors modulated on the optical pulses as was shown in Figure 91 in Section 3.3.2.

Rather than keeping this information of energy unchanged, it is convenient to convert the energy vector into a data type closer to the UWB signal which kept some information about the energy level. To fit with the UWB subband hopping mechanism, the B hopping subbands and the zero padding are assimilated to states. Thus a TFC with a hopping sequence in B subbands corresponds to L states with $L=B+1$. Thereby, the weight vector $\mathbf{W}_{n,k}$ is built as following:

$$\mathbf{W}_{n,k} = [w_{n,k}^0, \dots, w_{n,k}^B] \quad (17)$$

The weights $w_{n,k}^b$ are related to the state of confidence between two situations: no signal (zero state) or a significant activity in a given subband (state 1 to B). The weight computation method needs to distinguish between a situation where there is a strong amount of energy in only one subband from a situation where this energy is equally distributed over all subbands. The first situation can be associated with high confidence to a non-ambiguous subband state whereas the last situation is most likely associated with a noise only situation and then associated with the zero state. In that purpose, the weights which need to add up to 1 are built from the maximum absolute value of energy difference ΔE taken for all combinations of two subbands among B . It could be written:

$$\Delta E = \max_{(i,j)} |E_{n,k}^{b_i} - E_{n,k}^{b_j}| \quad (18)$$

Finally, the weights can be computed as follows:

$$\begin{aligned} w_{n,k}^0 &= 1 - \frac{\Delta E}{E_{tot}} \\ &\quad \vdots \\ w_{n,k}^b &= \frac{E_{n,k}^b \Delta E}{E_{tot}^2} \end{aligned} \quad (19)$$

with:

$$E_{tot} = \sum_{b=1}^B E_{n,k}^b \quad (20)$$

By using that procedure, the zero state weight increases when ΔE get smaller, which is the seek behavior. In practice, the value of ΔE is prevented to reach zero in order to maintain

a non zero probability for each state which appears to be important for the implementation of the $\hat{\tau}_k$ delay estimation Bayesian algorithm.

Figure 225 shows the weight estimation output which provides for each snapshot the confidence of being in one of the four possible states of a TFC1 sequence (including zeros padding states).

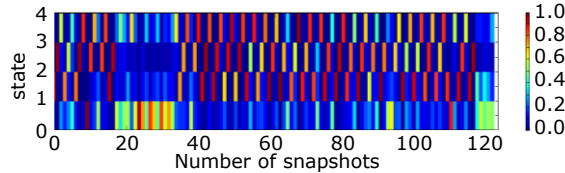


Figure 225. Example of weight estimation output for 120 snapshots. The confident of the measured state is evaluated. The redder the state is the more confident in the measure

B.1.2. Predictive delay estimator

The predictive delay estimator (PDE) is based on Bayesian scheme. An example operation is illustrated in Figure 226. The observations are used to update the probability a hypothesis. In other words, each snapshot will bring information on the interval where could be localized the estimated pseudo delay $\hat{\tau}_k$. By combining the knowledge on the most probable previous intervals and the actual one, it is possible to have a very accurate estimation on $\hat{\tau}_k$.

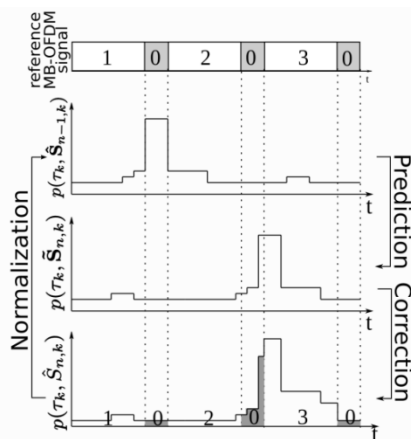


Figure 226. Example of operation of the two steps PDE algorithm: The prediction steps by applying a modulus on the PDF at rank $n-1$, and the update of this PDF thanks to the weight vector and normalization before iterate the process at rank n

Thus, the predictive delay estimation algorithm could be summed up in two major steps:

- 1) A prediction step, which estimates thanks to the whole previous sequence information until rank $n-1$, the most probable state at rank n . At step n the algorithm has got an estimation of the conditional probability density function (PDF) $p(\tau_k | \hat{\mathbf{S}}_{n-1,k})$ of the pseudo delay $\hat{\tau}_k$ knowing the past of the estimated state sequence $\hat{\mathbf{S}}_{n-1,k}$. The prediction step is based on the knowledge of the repetition rate T_s of the optical pulse and the length T_{symp} of an OFDM symbol.

Due to the knowledge of the repetitive scheme of the OFDM-UWB symbols for a given TFC, a modular arithmetic notation is used to build the next prediction of the PDF. Thus, the

PDF prediction a rank n is build thanks to the estimation of this PDF $p(\tau_k, \hat{\mathbf{S}}_{n-1,k})$ at rank $n-1$:

$$p(\tau_k, \hat{\mathbf{S}}_{n-1,k}) = p((\tau_k - nT_s) [T_{\text{symp}}], \hat{\mathbf{S}}_{n-1,k}) \quad (21)$$

The value between brackets stands for the modulus value.

2) A correction step, which takes advantage of the calculated weights and can be once confront to the prediction and exploit to update the next prediction step after normalization. Due to the weight information previously computed by the weight estimator, it is possible to update the PDF following:

$$p(\hat{\mathbf{S}}_{n,k}) = \sum_{b=0}^B w_{n,k}^b p(\tau_k, \hat{\mathbf{S}}_{n,k}) \quad (22)$$

When the innovation $\hat{\mathbf{S}}_{n,k}$ has been estimated it can be exploited to for normalization:

$$p(\tau_k, \hat{\mathbf{S}}_{n-1,k}, \hat{\mathbf{S}}_{n,k}) = \frac{p(\tau_k, \hat{\mathbf{S}}_{n,k})}{\int_0^{T_{\text{symp}}} p(\tau_k, \hat{\mathbf{S}}_{n-1,k}) d\tau_k} \quad (23)$$

This could be also written as:

$$p(\tau_k, \hat{\mathbf{S}}_{n-1,k}, \hat{\mathbf{S}}_{n,k}) = p(\tau_k, \hat{\mathbf{S}}_{n,k}) \quad (24)$$

Thus the pseudo $\hat{\tau}_k$ interval estimation at rank n is obtained. The exact pseudo $\hat{\tau}_k$ value is chosen as the center of the most probable pseudo $\hat{\tau}_k$ interval.

B.2. Simulations for position computation

In this part the performance of the proposed PDE algorithm is evaluated for different cases. The Root Mean Square Error (RMSE) is evaluated as:

$$RMSE = \sqrt{(\hat{\tau} - \tau)^2} \quad (25)$$

In these simulations three percentages of errors (0%, 10%, and 20%) are considered. These percentages refer to the number of false weight introduced in the weight vector. For instance, with 80 snapshots, a 10% of error means than 8 of the maximum weights are randomly set to a wrong state. In the simulations 5000 uniformly random values of τ were computed for each of these three different percentages.

Figure 227 presents a decreasing RMSE with a growing number of snapshots for any percentage of the evaluation errors. Obviously, the knowledge of previous estimation ensures a better precision on the further estimations but it is noticeable that around 70 snapshots it appears a slope modification. After 70 snapshots, RMSE decrease slower. This could be explained by the very nature of the algorithm. Indeed, a rough estimation could be performed in a very low number of snapshots, allowing determining a delay in the range of a state duration. For instance, with a TFC1, if the first estimated state is a "1", the final pseudo delay $\hat{\tau}$ value will stand between 0 ns and 242.42 ns. While no new information is able to split this interval, no better accuracy can be reached. As a consequence, the more accurate is the estimation, the more difficult it is to improve it.

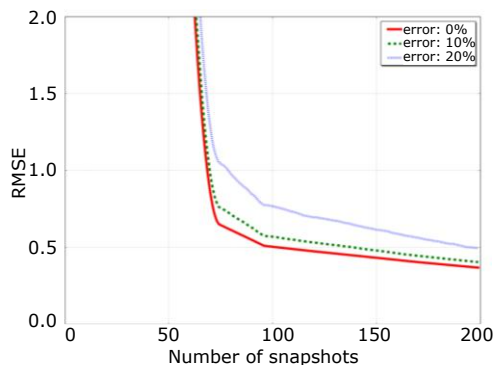


Figure 227. Root Mean Square Error as a function of number of snapshot for 5000 uniformly distributed random τ values

In order to deal with the accuracy and a fast computation, a number of 80 snapshots has been chosen to perform the delay estimation. Figure 228 presents the cumulative density probability function of the PDE algorithm for three percentage of code error for 80 snapshots.

By assuming a 1.3 ns error, 80% of the delays are correctly estimated even for 20% of error. Then when inserted into the TDoA-TLS positioning algorithm, the algorithm gives a positioning accuracy better than 50 cm.

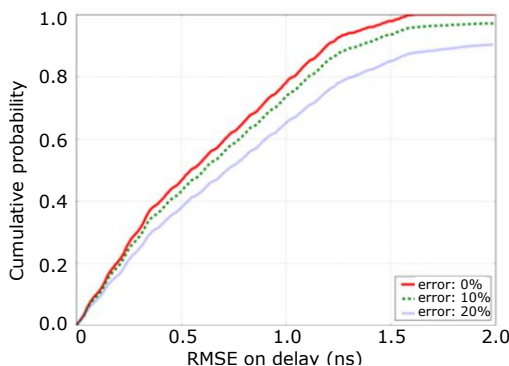


Figure 228. Cumulative density function for 80 snapshots and 5000 uniformly distributed random τ values for different percentages of error

The performance of the proposed algorithm is evaluated experimentally using the multi-sensor photonic-ADC with UWB signals in next Section 3.3.2.1.

B.3. Position of the sensors evaluation

The configurations evaluated for different positioning of the 5 sensors in the room are summarized in Table 22.

Prior simulation analysis has been done considering the experimental demonstration room which shape is drawn in the Figure 229 and Figure 230 along the sensor position (white circles). The demonstration room is 4.65×6.21 m. For each sensor configuration, a simulated UWB source has been moved in and around the room (with a 0.1 m step), to easily detect the parabolic sector with high errors which is an intrinsic limitation of TDoA computation. For each position, the resulting difference of range has been computed 100 times using different random Gaussian error by assuming an achieved standard deviation of 0.1 m.

Table 22. Sensors position (x, y, z meters) for each configuration

Conf.	Sensor 1	Sensor 2	Sensor 3	Sensor 4	Sensor 5
A	(3.15, 0, 1.2)	(0, 2.38, 1.2)	(3.15,4.75,1.2)	(5.26, 4, 1.2)	(6.21,1.2, 1.2)
B	(3.15, 0, 1.2)	(0, 2.38, 1.2)	(3.15,4.75,1.2)	(5.26, 4, 1.2)	(3.3, 2.4, 2.4)
C	(0, 0, 1.2)	(0, 4.75, 1.2)	(5.26,4.75,1.2)	(5.87,3.03,1.2)	(6.21, 0, 1.2)
D	(0, 0, 1.2)	(0, 4.75, 1.2)	(5.26,4.75,1.2)	(3.3, 2.4, 1.2)	(3.3, 2.4, 1.2)
E	(0, 0, 1.8)	(0, 4.75, 0.2)	(5.26,4.75,1.8)	(6.21, 0, 0.2)	(3, 3, 2.4)
F	(0, 0, 0.2)	(0, 4.75, 1.8)	(5.26,4.75,0.2)	(6.21, 0, 1.8)	(3, 3, 2.4)

The RMS error is evaluated. In first instance, 2D positioning is evaluated for different sensors position defined with 3D coordinates (x,y,z). Firstly, the TDoA algorithm is applied for 2 dimensions (x,y), in order to only take advantage of redundancy to increase the estimated position. In the first simulations (configuration A to D) the device was set at the same height at $z=1.2$ m. In configuration A, the five sensors are located at the middle width of each wall of the room at the same height ($z=1.2$ m). In configuration B, there are 4 sensors at the middle of each wall at the same height and one on the ceiling in the center of the room. In configuration C the five sensors are at the corners and in configuration D one is on the ceiling in the middle of the room and four at the corners.

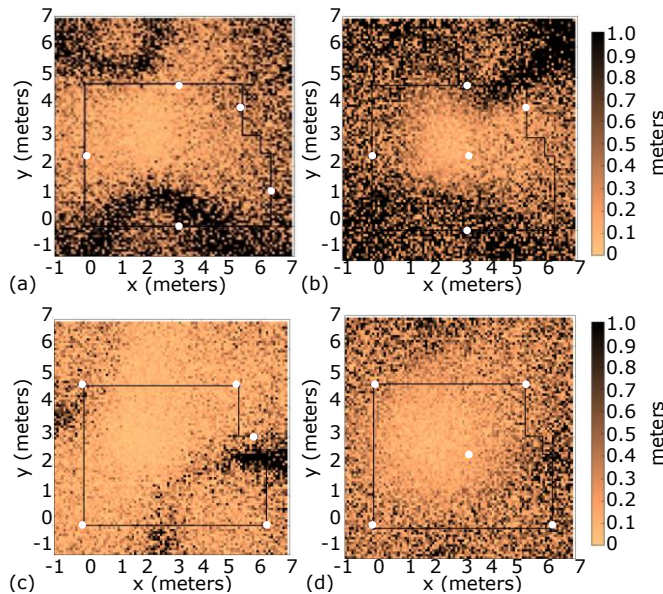


Figure 229. Root mean square error of positioning for 5 sensors located in different configuration: (a-b) the middle of the walls, (c-d) the edges of the room

Using configuration A, a hyperbolic undetermined area can be observed in Figure 229(a) due to the TDoA method. Using configuration B, the coverage area is reduced due to the closeness of the sensors. In the corner configuration (conf. C) the positioning error is reduced, and adding a fifth sensor on the ceiling increases the coverage area (conf. D). To achieve 3D localization, it is recommended to choose different heights for each sensor. This is evaluated in configurations E and F.

Locating the sensors at the same height provides a correct (x,y) 2D positioning, but will not be accurate along z -dimension [15]. Even for 2D positioning, using different sensor heights (conf. E and F) ensures an increase in the accuracy as shown in Figure 230.

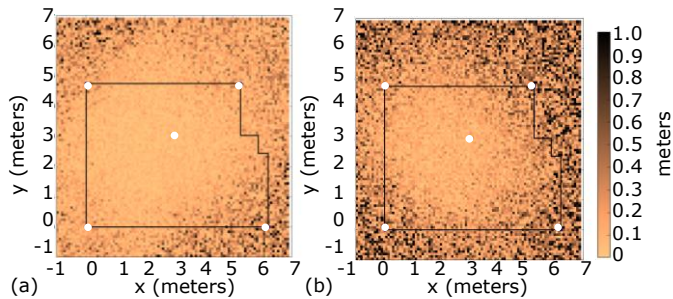


Figure 230. Root mean square error of 2D positioning for 5 sensors located at different heights: (a) configuration E, and (b) configuration F

The obtained mean, median and maximum positioning errors are summarized in Table 23. The performance is improved considerably by allocating the sensors at different heights. The best configuration (conf. F) achieves localization with 0.33 m mean and 0.23 m median error. Configuration F was selected and implemented in the demonstration experiment for comparison.

Table 23. Positioning absolute error (calculated)

Conf.	Mean Error	Median Error	Maximum Error
A	0.65 m	0.36 m	52.15 m
B	1.05 m	0.52 m	69.25 m
C	0.52 m	0.31 m	89.52 m
D	0.38 m	0.28 m	3.48 m
E	0.33 m	0.23 m	3.67 m
F	0.33 m	0.23 m	2.82 m

3D positioning simulations are shown in Figure 231. These results are not as good as in Figure 230 due to the absence of redundancy of information in the 3D case as well as less diversity in the repartition of sensors in the vertical plan. In the 2D case, the fifth sensor adds extra information which increases the robustness of the TDoA algorithm, but in 3D case the five sensors are useful to compute positioning. Simultaneous data captured from these five sensors in the multichannel photonic-ADC being an enabling step for the fingerprint and TDoA techniques described.

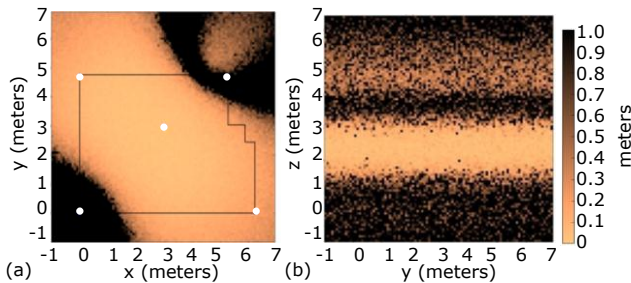


Figure 231. Root mean square error of 3D positioning for 5 sensors located using configuration F: (a) on position depth y as a function of width x , and (b) on position height, z , as a function of depth y

ANNEX C. ELECTRO-OPTIC MODULATOR DESIGN AND CHARACTERIZATION

This Annex includes the description and characterization measurements of the electro-optical modulators developed by Photline Technologies in the framework of UCELLS Project and that have been used for the linearization techniques studied in Section 3.4. Two types of EOM have been used: in first place a Y-coupled modulator, and in second place a dual-drive modulator.

C.1. Y-coupled electro-optical modulator

Figure 232(a) shows the structure of a single Y-junction couple modulator chips and the principle of operation. The linearized EOM proposed is an active Y-branch directional coupler with phase reversal traveling wave electrodes and ferroelectric domain inversion as shown in Figure 232(b). The input wave is split by the first Y-junction. The gap between the two parallel waveguide is sufficiently small to allow an optical coupling via the evanescent field. One waveguide has a positive ferroelectric orientation while the other has a negative one. Thus the central RF electrode which applies an electric field into the waveguide generates a positive phase variation in one arm while it is negative in the other arm. The Y-fed coupler is in a push-pull configuration. During a second section length, the ferroelectric domain inversion has been applied to the opposite waveguide, resulting in an inverted situation. The full configuration of the Y-fed coupler is of $\Delta\beta$ reversal type.

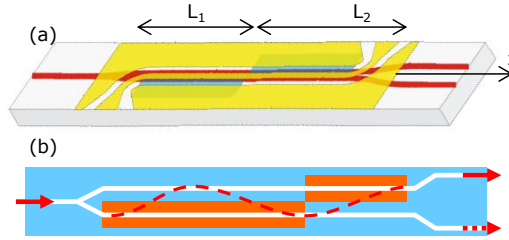


Figure 232. (a) Structure of a single linearized Y-fed coupler modulator chip and (b) principle of operation

The electrodes apply an electric field changing differentially the extraordinary refractive index via E_3 electric field and r_{33} electro-optic coefficient. As pointed out previously, adequate operation requires isolation by a metallic e-wall between the two junctions. The linearized electro-optic modulator is based on a two section Y-fed directional coupler as described in [88]:

$$\begin{bmatrix} E_{x1}(L) \\ E_{x2}(L) \end{bmatrix} = [M_2] [M_1] \begin{bmatrix} \sqrt{\rho_1} & \sqrt{1-\rho_1} \\ \sqrt{1-\rho_1} & \sqrt{\rho_1} \end{bmatrix} \begin{bmatrix} E_x(0) \\ 0 \end{bmatrix} \quad (26)$$

where $E_x(0)$ is the field at the linearized -EOM input and sub-index X represents the U for the upper Y-junction or L for the lower Y-junction in Figure 232, and the matrix M_i represents the field transmission in each section of the coupler:

$$[M_i] = \begin{bmatrix} m_{11} & m_{12} \\ m_{12} & \text{conj}(m_{11}) \end{bmatrix} \quad (27)$$

The elements m_{ij} of the matrix can be written as:

$$m_{11} = \cos\left(\frac{\pi}{2} S_i \sqrt{1+x_i^2}\right) - j \frac{x_i}{\sqrt{1+x_i^2}} \sin\left(\frac{\pi}{2} S_i \sqrt{1+x_i^2}\right) \quad (28)$$

$$m_{12} = -j \frac{1}{\sqrt{1+x_i^2}} \sin\left(\frac{\pi}{2} s_i \sqrt{1+x_i^2}\right) \quad (29)$$

where x_i is the normalized voltage applied to the modulator arms ($x_2 = -x_1$), s_i is the normalized length ($s_i = L_i / L_c$) with L_i the interaction length of the i -th coupler section and L_c the coupling length. The normalized voltage can be expressed as a function of the actual voltage V_x applied to each directional coupler section (sub-index X is U for the upper or L for the lower Y-junction respectively) as:

$$x = \frac{l n^3 r_{33}^3 \eta}{\lambda d} V_x \quad (30)$$

with n the refraction index obtained without voltage applied, r_{33} the electro-optic coefficient, λ the wavelength, d the inter-electrode distance and η the overlap coefficient.

Both upper and lower Y-junctions shown in Figure 232 are formed by two parallel waveguide in $\Delta\beta$ reversal configuration [90]. The gap between the waveguides is calculated allowing optical coupling via evanescent field. One waveguide in each Y-junction has a positive ferroelectric orientation while the other has a negative one, i.e. each arm include a central RF electrode (L_1) which applies electric field into the waveguide generating a positive phase variation in one arm and negative in the other. This is actually a push-pull configuration as in the second section (L_2) the ferroelectric domain inversion is applied to the opposite waveguide, resulting in an inverted situation when the light propagates through the waveguides.

C.1.1. Fabrication process

Fabrication of Y-branch integrated directional couplers is sensitive to process deviations. The sensitivity was studied by simulation in order to select the most tolerant design window simultaneously optimizing a factor of merit which determines linearity, i.e. the dynamic range is maximized and third harmonic generation is minimized. Figure 233 shows the region selected for device fabrication where optimized linearity is expected alongside a relatively low dependence on fabrication conditions with low dependence on wavelength.

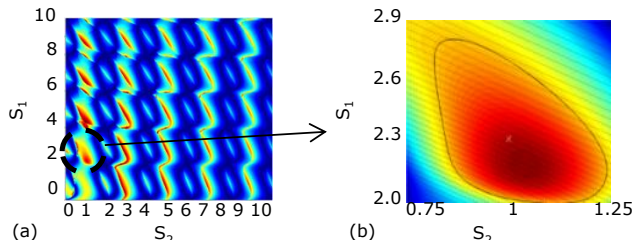


Figure 233. (a) Factor of merit depending on the active coupling length of first and second section normalized by the coupling length (by simulation). Red color corresponds to the highest linearity. (b) Zoom of the fabrication-target parameters

After further simulations, the target parameters selected for fabrication are: $L_1=27.88$ mm, $L_2=12.12$ mm, $L_c=12.12$ mm, and gap of $15.35 \mu\text{m}$ (total length 40 mm). The Y-junctions fabricated were named UCELLS5 and UCELLS21. Their basic characteristics measured after fabrication are summarized in Table 24. The fabricated gold electroplated RF electrodes are shown in Figure 234. Figure 234(b) shows the device packaged and ready to be characterized. Due to manufacturing process restrictions a two-port package was employed per each Y-junction. The two ports were connected being the same ground plane for both packages in accordance with the device structure shown in Section 3.4.1-Figure 106 as both Y-junctions are electrically isolated. Figure 235 shows the transfer function of the upper and lower Y-junctions respectively.

Table 24. Fabricated Y-junction specifications

	UCELLS5	UCELLS21
<i>Low Frequencies:</i>		
Optical losses @ 1542 nm (*)	4.1 dB	4.2 dB
Extinction Ratio @ DC (1542 nm)	35 dB	24 dB
V _n on DC port @ 1550 nm	5.5 V	7 V
<i>High frequencies:</i>		
Electro-optical bandwidth @ -3 dB	8-10 GHz	8-10 GHz
S ₁₁ at RF input	< -10 dB	< -10 dB
V _n on RF port @ 1550 nm	5.5 V	7 V

(*) including splicing and optical connectors

It can be observed that sensitivity to process deviation is high, and yield is low compared to standard MZI-modulators as was shown in Table 24. Further numerical analysis of the process deviation from the fabrication-targeted values for the UCCELLS5 and UCCELLS21 devices was carried out. The analysis results indicate that the E/O response measured shown in Figure 235 can be explained by coupling length being 10% shorter than predicted, while the poling section can be considered to be 10% greater and 10% smaller than the targeted values respectively for the first and second section at a given Y-junction. Nevertheless, numerical analysis confirms that the Y splitting ratio is 50%-50% and the mean overlap between optical and electric field are equal to 0.5. The shortening of the coupling length can be easily explained by an increase of the optical modes and/or the inter-waveguide gaps: small lithographic defects during the fabrication make the waveguide width imperceptibly increased will lead to deviation on the coupling lengths.

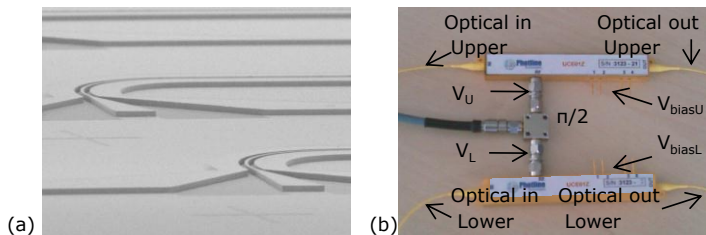


Figure 234. (a) Fabricated gold electroplated RF electrodes, and (b) packaged device

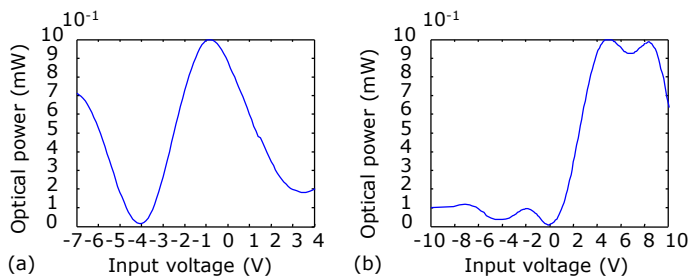


Figure 235. E/O response characterization for: (a) Y-junction UCCELLS5 and (b) Y-junction UCCELLS21 fabricated devices

A difficult aspect in the poling process is the control of the local spreading of the domain while monitoring the entire wafer process. Imperfect control may induce a spread of the reverted region into the second waveguide for few hundreds of microns. This is reflected in new propagated optical modes that make appear the two poled sections effectively (virtually) longer and shorter than expected.

C.2. Dual-drive electro-optical modulator with chirp management

In Section 3.4.2 a dual-drive EOM with chirp control was proposed for radio-over-fibre applications. The architecture of these dual-drive devices is recalled in Figure 236(a). Figure 236(b) show the eye diagrams measured at data rates of 10 and 20 Gbps when the DD-MZ modulator is driven by two amplifiers delivering half of the voltages ($V_n/2$) in opposite of phase. The low RMS time jitters (1.37 ps @ 20Gbps) show the very good synchronization of all the RF-lines. The packaged device was characterized in back-back configuration (detection just after the modulator). Figure 237 (a) shows the electrical back-reflection in S_{11} and S_{21} and the bandwidths that arrive up to 10 GHz @ -3 dB. Figure 237(b) shows the third order intersection point (IP3), indicating the spurious free dynamic range (SFDR) was characterized for each RF-port. The IP3 related to the input was measured to be at least of 36 dBm @ 5 GHz. For a noise floor of -120 dBm, the resulting SFDR is in the range of 60 dB.

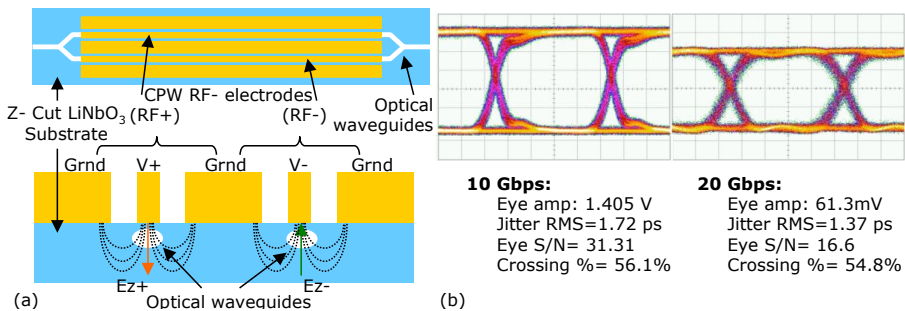


Figure 236. (a) Scheme of the designed dual drive modulator chip in top view and cross section. (b) NRZ output eye diagrams for measured for 10 Gbps and 20 Gbps

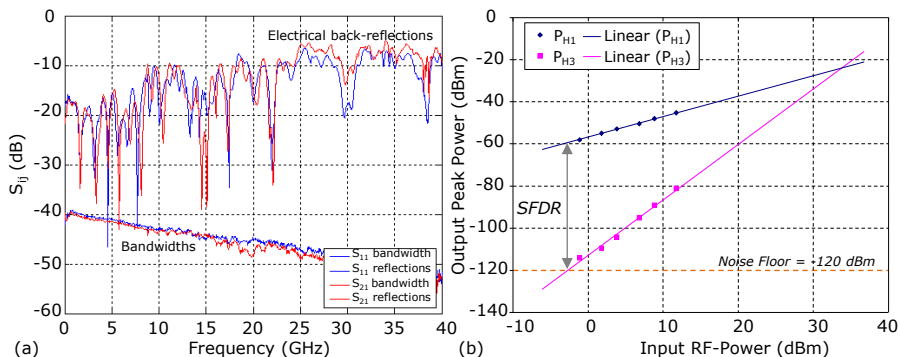


Figure 237. (a) Bandwidths (lower traces) and electric back-reflections at the inputs for both RF-lines measured with the packaged DD-MZ modulators; (b) IP3 measurements on DD-MZ RF+ at 5 GHz

C2.1. Chirp measurement

Among different available techniques, the chirp produced by the EO-modulation was measured here by frequency discrimination [93] using the experimental setup shown in Figure 238.

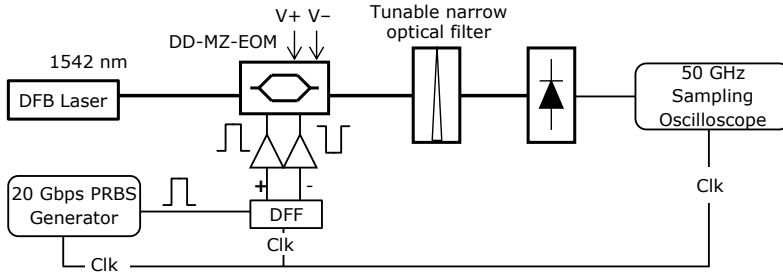


Figure 238. Experimental set up for frequency chirp control and measurement

The instantaneous pulsation in the presence of chirp, i.e phase modulation, is given at the output of a Mach-Zehnder Interferometer modulator by:

$$\omega(t) = \omega - \beta\kappa \frac{\partial V(t)}{\partial t} \quad \text{with} \quad \kappa = \frac{\pi}{2\eta_0 V_n} \quad (31)$$

where V_n is the half-wave voltage of the modulator; η_0 the mean EO overlap in both arm of the interferometer; and β the overlap discrepancy between them, source of the frequency chirp.

Considering a modulation Gaussian-like pulse $V(t)$ as:

$$V(t) = V_0 \exp\left(-\frac{t^2}{\tau^2}\right) \quad (32)$$

The first derivative in function of time can be expressed as:

$$\frac{\partial V(t)}{\partial t} = -\frac{2t}{\tau^2} V_0 \exp\left(-\frac{t^2}{\tau^2}\right) \quad (33)$$

According to (1), the instantaneous pulsation becomes:

$$\omega(t) = \omega + \beta\kappa \frac{2t}{\tau^2} V_0 \exp\left(-\frac{t^2}{\tau^2}\right) \quad (34)$$

When applying a pulse voltage of amplitude V_n , the instantaneous frequency turns into:

$$f(t) = \frac{\alpha}{4} \frac{2t}{\tau^2} \exp\left(-\frac{t^2}{\tau^2}\right) \quad (35)$$

with α the chirp parameter. Cancelling the first derivative of $f(t)$ we obtain the maximum frequency excursion occurs at $t_0 = \tau/\sqrt{2}$ and can be expressed as:

$$f_0 = \frac{\alpha}{2\sqrt{2}\tau} e^{-1/2} \quad (36)$$

At the output of the modulator, the narrow tunable optical filter is used as a frequency discrimination demodulator. It converts the residual phase modulation produced by the modulator (chirp) into intensity modulation, and adds it to the regular intensity modulation. Assuming it exhibits a symmetric transmission spectrum with a width ΔF , by recording two consecutive intensity modulations, one carried out on the positive slope (P^+) and the other on negative slope of the filter (P^-) one can deduce the frequency deviation as:

$$f - f_0 = \frac{P^+ - P^-}{2P_0 e^{-1/2}} \frac{\Delta F}{\sqrt{2}} \quad (37)$$

where f_0 and P_0 are the central frequency and the maximum transmission optical power detected after the filter, respectively. From equations (36) and (37) the chirp parameter α can be deduced.

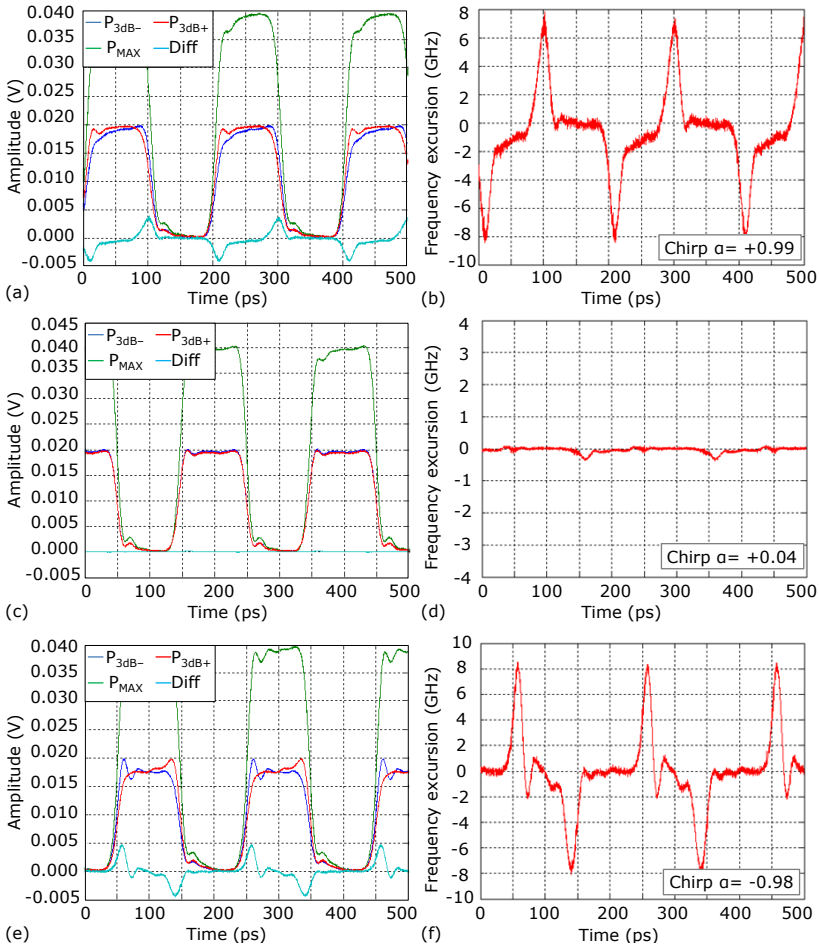


Figure 239. 20 Gbps output temporally responses with three positions of the optical filter (left) and corresponding frequency excursion (right) for: (a-b) $V+=Vn, V-=0$, (c-d) $V+=Vn/2, V=-Vn/2$, and (e-f) $V+=0, V=- Vn$

In practice, as can be observed in Figure 238, the DD-MZ is driven by two identical RF-amplifiers fed with a D-flip flop (DFF). Basically, the DFF makes a logic "AND" between the signal (square) from a PRBS generator and a clock signal. Both complementary outputs (+ and -) are connected to the amplifiers so as to get two amplified signals with a n -phase shift in between them. The modulator was fed with a series of short pulses, generating a relatively large spectrum. Due to non-infinite EO-bandwidths, we consider that the front and end edges of the pulses exhibit a Gaussian shape where the rising and falling times are equivalent to the τ parameter defined before.

Initially, the filter was centered on the optical carrier and then on the 3 dB left and right part of the optical spectrum. The output temporal signals were recorded as shown in Figure 239(left) for signals at 20 Gbps. Numerically, the time responses are subtracted

giving access to the frequency excursion, thus to the residual phase modulation, and then to the chirp parameter. Knowing the shape and the width of the optical filter one can isolate the resulting phase modulation. The sign is discriminated looking at the sign of the frequency amplitude.

First, the DD-modulator is excited at both RF-inputs with $V_+=V_n$ and $V_-=0$. In Figure 239(a) we can note the spikes at the beginning and the end of each pulse due to non-zero frequency chirp. In Figure 239(b) the chirp is estimated to be $\alpha=+0.99$, very close to 100%.

In the second case, the modulator is fed with two properly adjusted electric signals in phase opposition: $V_+=V_n/2$ $V_-=-V_n/2$. In Figure 239(c-d) it can be observed that the difference is almost null even at the front and the end of the pulses. The frequency excursion illustrates an almost-zero chirp operation ($4 \cdot 10^{-2}$).

Finally, the third configuration is symmetric to the first case, $V_+=0$ and $V_- = V_n$ which temporal traces and obtained frequency excursion are shown in Figure 239(e-f).

As in the first case, spikes at the edge of the pulses are typical from frequency chirp. Note that in that case the spikes are in the opposite way compared to the first case: positive at the beginning, negative at the end. The chirp is negative and measured to be $\alpha=-0.98$.

From these results we can confirm that using the DD-MZ the frequency chirp induced by the modulator can be tuned to any value between $\pm 100\%$ by adjusting the balancing of the input voltages.

REFERENCES

- [1] T. Lunttila, S. Iraji, H. Berg, "Advanced coding schemes for a multiband OFDM ultrawideband system towards 1 Gbps", IEEE 3rd Consumer Comm. and Networking Conf. 2006, pp. 553-557, January 2006.
- [2] A. Paier, J. Karedal, N. Czink, H. Hofstetter, C. Dumard, T. Zemen, F. Tufvesson, C.F. Mecklenbräuker, A.F. Molisch, "First results from car-to-car and car-to-infrastructure radio channel measurements at 5.2GHz", IEEE Personal, Indoor and Mobile Radio Communications, 2007.
- [3] K.M. Strohm, R. Schneider, and J. Wenger, "KOKON: A joint project for the development of 79 GHz automotive radar sensors", Int. Radar Symp., 2005.
- [4] R. Kohno, "State of Arts in Ultra Wideband (UWB) Wireless Technology and Global Harmonization", 34th European Microwave Conf. 2004, vol.2, pp. 1093-1099, October 2004.
- [5] FCC 02-48, "Revision of Part 15 of the Commission's Rules regarding ultra-wideband transmission systems", April 2002.
- [6] ECMA 368 International Standard: "High rate ultra wideband PHY and MAC Standard", 2007.
- [7] "ECC/DEC/(06)04: On the harmonised conditions for devices using ultra-wideband (UWB) technology in bands below 10.6 GHz", European Commission, March 2006.
- [8] J. del Prado Pavón, S. Shankar, N. Vasanth Gaddam, K. Challapali, and C-T. Chou, "The MBOA-WiMedia specification for ultra wideband distributed networks", IEEE Comm. Magazine, vol.44 n.6, pp.128 - 134, June 2006.
- [9] Wisair "Wisair Wireless USB products" info available at: <http://www.wisair.com/products/wireless-usb-solutions/wusb-dongle-set/>
- [10] Gemtek "UWB/Wireless USB Dongle WUWBD-101 WiMedia-based Ultra Wideband Product" info available at: http://www.gemtek.com.tw/pro_wuwbd101.html
- [11] Institute of Electrical and Electronics Engineers, Inc., IEEE Std 802.16-2004; IEEE Standard for Local and metropolitan area networks; Part 16: Air Interface for Fixed Broadband Wireless Access, October 2004.
- [12] 3GPP TS 36.101v8.8.0 "3rd Generation Partnership Project; Technical Specification Group Radio Access Network; Evolved Universal Terrestrial Radio Access (E-UTRA), User Equipment (UE) radio transmission and reception (Release 8)", Dec. 2009.
- [13] D. Jager and A. Stohr, "Microwave Photonics", in Proceedings of European Microwave Conference 2001.
- [14] T.E. Darcie, and G.E. Bodeep, "Lightwave subcarrier CATV transmission systems", IEEE Transactions Microwave Theory Technology, Vol. 38(5), pp. 524-533, 1990.
- [15] B. Wilson, Z. Ghassemlooy, I. Darwazeh, "Analogue optical fibre communications", Institution of Engineering and Technology, 1995.
- [16] S.V. Kartalopoulos, "DWDM: Networks, Devices, and Technology", Ed. Wiley, 2002.
- [17] H. Heidrich, D. Hoffmann, and R.I. Macdonald, "Polarization and wavelength multiplexed bidirectional single fiber subscriber loop", Journal of optical communications, Vol. 7(4), pp. 136-138, 1986.
- [18] A. Hirata, M. Harada, and T. Nagatsuma, "120-GHz wireless link using photonic techniques for generation, modulation, and emission of millimeter-wave signals", IEEE Journal Lightwave Technology, Vol. 21(10), pp. 2145-2153, 2003.
- [19] H. Ogawa, D. Polifko, S. Banba, "Millimetre-wave fibre optic systems for personal radio communication", IEEE Trans.Microwave Theory Techn.,vol. 40, pp. 2285-2292,1992.
- [20] K-A. Persson, C. Carlsson, A. Alping, A. Haglund, J.S. Gustavsson, P. Modh, and A. Larsson, "WCDMA radio-over-fibre transmission experiment using singlemode VCSEL and multimode fibre", Electronics Letters, Vol. 42, pp. 372-374, 2006.
- [21] M.Y.W.C hia, B. Luo, M.L. Yee and E.J.Z. Hao, "Radio over multimode fibre transmission for wireless LAN using VCSELs", Electronic Lett, vol.39, pp. 1143-1144, 2003.
- [22] T. Niiho, M. Nakaso, K. Masuda, H. Sasai, K. Utsumi, and M. Fuse, "Multi-channel wireless LAN distributed antenna system based on radio-over-fibre techniques", Proceedings of IEEE LEOS Annual Meeting, pp. 57-58, 2004.

- [23] A. Nkansah, A. Das, C. Lethien, J-P. Vilcot, N.J. Gomes, I.J. Garcia, J.C. Batchelor, and D. Wake, "Simultaneous dual band transmission over multimode fibre-fed indoor wireless network", *IEEE Microwave and Wireless Components Letters*, Vol. 16(11), pp. 627-629, 2006.
- [24] H. Pfrommer, M.A. Piqueras, V. Polo, J. Herrera, A. Martinez, and J. Marti, "Radio-over-fibre architecture for simultaneous feeding of 5.5 and 41 GHz WiFi or WiMAX access networks", *IEEE MTT-S International Microwave Symposium Digest*, pp. 301-303, 2006.
- [25] N. Anscombe, "Demand for indoor coverage drives radio-over-fibre", *Wireless Europe*, retrieved from <http://www.nadya-anscombe.com/pdfs/radio%20over%20fibre.pdf>
- [26] M. Kunigonis, "FTTH Explained: Delivering efficient customer bandwidth and enhanced services", Corning Cable Systems, 2009.
- [27] L. Hutcheson, "FTTx: Current status and the future", *IEEE Communications Magazine*, Vol. 46 (7), pp. 90-95, July 2008.
- [28] J. Capmany, and D. Novak, "Microwave photonics combines two worlds", *Nature Photonics*, Vol. 1, pp. 319-330, 2007.
- [29] N. Dagli, "Wide-bandwidth lasers and modulators for RF photonics", *IEEE Transactions on Microwave Theory and Techniques*, Vol. 47(7), pp. 1151-1171, 1999.
- [30] R.H. Blumenthal, "Design of a microwave frequency light modulator", *Proceedings of Institute of Radio Engineers IRE*, Vol. 50, pp. 452-456, 1962.
- [31] T. Ikegami, and Y. Suematsu, "Resonance-like characteristics of the direct modulation of a junction laser", *Proceedings of the IEEE*, Vol. 55, pp. 122-123, 1967.
- [32] D. Wake, D. Johansson and D.G. Moodie, "Passive picocell A new concept in wireless network infrastructure", *Electronic Letters*, Vol. 33(5), pp. 404-406, 1997.
- [33] C. Liu, A. Seeds, J. Chadha, P. Stavruniy, G. Parry, M. Whitehead, A.Krysa, J. Roberts, "Bi-directional transmission of broadband 5.2 GHz wireless signals over fibre using a multiple-quantum-well asymmetric Fabry-Pérot modulator/photodetector", *Proceedings of IEEE/OSA OFC 2003*, pp. 738-740, 2003.
- [34] C.P. Liu, V. Polo, F. Van Dijk, H. Pfrommer, M.A. Piqueras, J. Herrera, A. Martinez, S. Karlsson, O. Kjebon, R. Schatz, A. Enard, Y.C. Yu, T. Tsegaye, C.H. Chuang, A.J. Seeds, J. Marti, "Full-duplex DOCSIS/wireless DOCSIS fibre-radio network employing packaged AFPMs as optical/electrical transducers", *Journal Lightwave Technology*, Vol. 25(3), pp. 673-684, 2007.
- [35] X. Qian, P. Hartmann, J. D. Ingham, R. V. Penty and I. H. White, "Directly-modulated photonic devices for microwave applications", *Proceedings of IEEE MTT-S Intl Microwave Symposium*, 2005.
- [36] J. Ingham, M. Webster, A. Wonfor, and R. Penty, "Wide-frequency-range operation of a high linearity uncooled DFB laser for next-generation radio-over-fibre", *Proceedings of IEEE/OSA OFC 2003*, pp. 754-756, 2003.
- [37] P. Hartmann, M. Webster, A. Wonfor, J. D. Ingham, R. V. Penty, I. H. White, D. Wake, and A. J. Seeds, "Low-cost multimode fibre-based wireless LAN distribution system using uncooled directly modulated DFB laser diodes", *Proceedings of ECOC 2003*, pp. 804-805, 2003.
- [38] Q. Chang, H. Fu, and Y. Su, "Simultaneous generation and transmission of downstream multiband signals and upstream data in a bidirectional radio-over-fibre system", *IEEE Photonic Technology Letters*, vol. 20, pp. 181-183, 2008.
- [39] Corning, "ClearCurve single-mode optical fibre" info available at: http://www.corning.com/opticalfibre/products/clearcurve_single_mode_fibre.aspx
- [40] OFS Optics, "Bending the rules: ofs to demonstrate ez-bend™ optical technology", at: http://www.ofsoptics.com/press_room/view_press_release.php?txtID=247
- [41] Draka, "Enhanced low macrobending sensitive Single Mode Fibre: BendBrightXS", at: http://www.drakafibre.com/draka/DrakaComteq/Drakafibre/Languages/English/Navigation/Markets%26Products/Single_mode/BendBright-XS/index.html
- [42] Corning, "ClearCurve® OM3/OM4 multimode optical fibre", available at: http://www.corning.com/opticalfibre/products/clearcurve_multimode_fibre.aspx
- [43] G. P. Agrawal, "Fibre-optic communication systems", Ed. John Wiley & Sons, 1997
- [44] H. Ito, T. Furata, S. Kodama, and T. Ishibashi, "InP/InGaAs uni-traveling-carrier photodiode with 310 GHz bandwidth", *Electronics Letters*, Vol. 36, pp 1809-1819, 2000.
- [45] A. Rahim, S. Zeisberg, and A. Finger, "Coexistence Study between UWB and WiMAX at 3.5 GHz Band", *Proceedings of ICUWB 2007 Conference*, pp. 915-920, 2007.

- [46] D. Cassioli, S. Persia, V. Bernasconi, A. Valent, "Measurements of the performance degradation of UMTS receivers due to UWB emissions", *IEEE Communications Letters*, Vol. 9(5), pp. 441-443, 2005.
- [47] A. Das, A. Nkansah, N.J.Gomes, I.J. Garcia, J.C. Batchelor, D. Wake, "Design of low-cost multimode fibre-fed indoor wireless networks", *IEEE Transactions on Microwave Theory and Techniques*, Vol. 54(8), pp. 3426-3432, 2006.
- [48] T. Marozsak, and E. Udvary, "Vertical cavity surface emitting lasers in radio over fibre applications", 14th International Conference on Microwaves, Radar and Wireless Communications 2002, MIKON-2002, Vol.1, pp. 41-44, 2002.
- [49] R. Alemany, J. Perez, R. Llorente, V. Polo, J. Marti, "Coexistence of WiMAX 802.16d and MB-OFDM UWB in radio over multi-mode fiber indoor systems," In proceedings of the International Topics Meeting on Microwave Photonics MWP'08, pp. 74-77, October 2008.
- [50] J. Mitola III and G. Q. Maguire, "Cognitive radio: making software radios more personal", *IEEE Personal Communications*, Vol. 6, Issue 4, pp. 13-18, Aug 1999.
- [51] C. Duan, G. Pekhteryev, J. Fang, Y. Nakache, J. Zhang, K. Tajima, Y. Nishioka, H. Hirai, "Transmitting multiple HD video streams over UWB links", in Proc. CCNC'06, Las Vegas, Vol. 2, pp. 691-695, 2006.
- [52] M. Jazayerifar, B. Cabon, and J. A. Salehi, "Transmission of multi-band OFDM and impulse radio ultra-wideband signals over single mode fibre", *IEEE JLT*, vol. 26 (15), pp. 2594-2603, Aug. 2008.
- [53] A. Kaszubowska-Anandarajah, P. Perry and L.P. Barry, "Hybrid radio over fibre system for generation and distribution of UWB signals", *ICTON*, p.82-85, June 2008.
- [54] VirtualPhotonics VPI Transmission Maker GUI version 7.5 Build: 344.
- [55] R. A. Shafik, M.S. Rahman, A.H.M.R. Islam, "On the extended relationships among EVM, BER and SNR as performance metrics" in Proc. ICECE'06, Bangladesh, pp. 408-411, Dec. 2006.
- [56] Y. Shoji, C. Choi, S. Kato, I. Toyoda, K. Kawasaki, Y. Oishi, K. Takahashi, H. Nakas, "Re-summarization of merged usage model definitions parameters", *IEEE doc. 802.15-06-0379-02-003c*, 2006.
- [57] M. Beltrán, R. Llorente, R. Sambaraju, and J. Martí, "60 GHz UWB-over-fiber system for in-flight communications," 2009 IEEE MTT-S Int. Microwave Symposium, pp. 5-8, June 2009.
- [58] LCD-TV Hitachi Wooo UT-series Available: www.hitachi.com and http://av.hitachi.co.jp/tv/l_lcd/ut/index.html.
- [59] Lenovo ThinkPad T61p mobile workstations, Available at: www.lenovo.com.
- [60] K. A. Janjua, S.A. Khan, "A comparative economic analysis of different FTTH Architectures", *Wireless Communications, Networking and Mobile Computing WICOM2007*, pp. 4979-4982, Sept. 2007.
- [61] R.B. Ellis, F. Weiss, and O. M. Anton, "HFC and PON-FTTH networks using higher SBS threshold singlemode optical fibre", *Electronics Letters*, Vol. 43 No. 7, pp. 405-407, March 2007.
- [62] C. Lee, K. Choi, "Fibre to the Home", *Lasers and Electro-Optics Society LEOS 2007. The 20th Annual Meeting of the IEEE*, pp. 937-938, 2007.
- [63] H. Schmuck, "Comparison of optically millimeter-wave system concepts with regard to chromatic dispersion," *Electron. Lett.*, vol. 31, no. 21, pp. 1848-1849, 1995.
- [64] S.Kartalopoulos, "Consumer communications in the next generation access network", *Consumer Communications Networking Conf.* 2004.
- [65] J. Prat, "High-density passive fibre-to-the-home networks", *Proc. 7th Intl Conference Transparent Optical Networks*, vol. 2, pp.33 37, 2005.
- [66] A.J. Lowery, L. B. Du, J. Armstrong, "Performance of optical OFDM in ultralong-haul WDM lightwave systems" *IEEE JLT*, vol. 25 (1), pp.131 138, Jan. 2007.
- [67] Corning ClearCurve single-mode optical fibre. available at http://www.corning.com/opticalfibre/products/clearcurve_single_mode_fibre.aspx, 2008.
- [68] L.G. Kazovsky, Wei-Tao Shaw, D. Gutierrez, Ning Cheng, Shing-Wa Wong, "Next-generation optical access networks", *Journal of Lightwave Technology*, Vol. 25 (11), pp. 3428-3442, 2007.
- [69] T. Alves, A. Cartaxo, "Performance degradation due to OFDM-UWB radio signal transmission along dispersive single-mode fiber," *IEEE Photonics Technology Letters*, vol.21, no.3, pp. 158-160, February 2009.

- [70] Q. Chang, J. Gao, Q. Li, Y.i Su, "Simultaneous transmission of point-to-point data and selective delivery of video services in a WDM-PON using ASK/SCM modulation format," In proceedings of the Optical Fiber Communication Conference and Exposition (OFC), February 2008.
- [71] Electronic Communications Committee (ECC), ECC/DEC/(07)02, "ECC Decision of 30 March 2007 on availability of frequency bands between 3400 3800 MHz for the harmonised implementation of Broadband Wireless Access systems (BWA)".
- [72] General Photonics "Reset-free polarization stabilizer - PolaStay™", available at: <http://www.generalphotonics.com/pdf/PolaStay.pdf>
- [73] R. H. Walden, "Analog-to-digital converter survey and analysis", IEEE Journal on selected areas in comm., Vol. 17, No. 4, April 1999.
- [74] A.S. Bhushan, et al., "130-GSa/s photonic analog-to-digital converter with time stretch preprocessor", IEEE Photonics Technology Letters, Vol. 14, Issue 5, pp. 684-484, May 2002.
- [75] J. R. Long, et al., "Energy-efficient wireless front-end concepts for ultra lower power radio", IEEE 2008 Custom Intergrated Circuits Conference (CICC), pp. 587-590, 2008.
- [76] Y. Han, B. Jalali, "Photonic time-stretched analog-to-digital converter: fundamental concepts and practical considerations", Journal of Lightwave Technology, Vol. 21. Issue 12, pp. 3085- 3103, December 2003.
- [77] G. C. Valley, J. P. Hurrell, and G. A. Sefler, "Photonics analog-to-digital converters: fundamental and practical limits," SPIE European Symp. on Optics and Photonics in Security and Defence, Oct. 2004.
- [78] B. Asuri, Y. Han, and B. Jalali, "Time-stretched ADC arrays," IEEE Trans. Circuits Syst. II, Analog Digit. Signal Process., vol. 49, no. 7, pp. 521-524, Jul. 2002.
- [79] J. Azaña and M. A. Muriel, "Real-time optical spectrum analysis based on the time-space duality in chirped fiber gratings," IEEE J. Quantum Electron., vol. 36, pp. 517-526, 2000.
- [80] V. Le Nir, T. van Waterschoot, M. Moonen and J. Duplcy, "Spectral monitoring and parameter estimation for ZP-OFDM signals," Proc. 17th European Signal Processing Conf. (EUSIPCO '09), Aug 2009.
- [81] G. Shen and R. Zetik and R.S. Thoma, "Performance comparison of TOA and TDoA based location estimation algorithms in LOS environment," WPNC 08, 2008.
- [82] M. Laaraiedh, S. Avrillon, B. Uguen, "Overcoming singularities in TDoA based location estimation using total least square" International Conf. on Signals, Circuits & Systems, Djerba (Tunisia), Nov. 2009.
- [83] K. Bronk, J. Stefanski, "Bad geometry influence on positioning accuracy in wireless network," International Conference on Computer as a Tool (EUROCON2007), Sept. 2007.
- [84] Chun-Ting Lin; J. Chen, Peng-Chun Peng, Cheng-Feng Peng, Wei-Ren Peng, Bi-Shiou Chiou, S. Chi, "Hybrid optical access network integrating fiber-to-the-home and radio-over-fiber systems," IEEE Photonics Technology Letters, Vol.19(8), pp.610-612, 2007.
- [85] C. Snow, L. Lampe, R. Schober, "Impact of WiMAX interference on MB-OFDM UWB systems: analysis and mitigation," IEEE Transactions on Communications, Vol. 57, Issue 9, pp. 2818-2827, Sept. 2009.
- [86] B. Quijano, A. Álvarez, M. Lobeira, J.L.García. "Compatibility measurement campaign between IR-UWB and UMTS," IST Mobile and Wireless Communications Summit, 2005.
- [87] J.C. Chen, "Comparison and linearization of LiNbO3 and semiconductor modulators," Journal of optical communications, Vol. 22, No. 1, pp. 2-8, 2001.
- [88] R. F. Tavlykaev, R.V Ramaswamy, "Highly linear Y-fed directional coupler modulator with low intermodulation distorsion". Journal of Lightwave Techn., Vol. 17, No. 2, pp.282-291, Feb 1999.
- [89] K. Higum, S. Oikawa, Y. Hashimoto, H. Nagata and M. Izutsu, "X-cut lithium niobate optical single sideband modulator", Electronics Letters, Vol. 37, No. 8, pp. 515-516, 2001.
- [90] H. Kogelnik and R. V. Schmidt, "Switched directional couplers with alternating," IEEE J. Quantum Electron., vol. 12, pp. 396-401, 1976.
- [91] J. Pham and A. Chan Carusone, "A time-interleaved 16-DAC architecture clocked at the Nyquist rate", IEEE Transactions on Circuits and Systems II: Express Briefs, Vol. 55 (9), pp. 858-862, 2008.
- [92] Y.H. You, I.T. Hwang, C.K. Song, H.K. Song, "PAPR analysis for multi-band OFDM signals", Electronics Letters, Vol. 41 (5), pp. 261-262, 2005.
- [93] S. K. Kim, J. Lee and J. Jeong, "Transmission Performance of 10-Gb/s optical duobinary transmission systems considering adjustable chirp of nonideal LiNbO3 Mach-Zehnder modulators due to

applied voltage ratio and filter bandwidth", *IEEE Journal of Lightwave Technology (JLT)*, Vol. 19 (4), 2001.

[94] K. Siwiak, D. McKeow, "Ultra-wideband radio technology", Ed. John Wiley & Sons, pp. 40-50, 2004.

[95] A.M.J. Koonen, H.P.A. van den Boom, E. Ortego Martinez, Ph. Guignard, E. Tangdiongga, "Cost optimization of optical in-building networks", *Proc. ECOC 2011*, Geneva, paper We.10.P1.114, Sep. 2011.

[96] C. M. Okonkwo, E. Tangdiongga, H. Yang, D. Visani, S. Loquai, R. Kruglov, B. Charbonnier, M. Ouzzif, I. Greiss, O. Ziemann, R. Gaudino and A.M.J. Koonen, "Recent Results from the EU POF-PLUS Project: Multi-Gigabit Transmission over 1 mm Core Diameter Plastic Optical Fibers". *J. Lightw. Technol.*, Vol 29 (2), pp. 186-193, Feb. 2011.

[97] D. Visani et al, "Record 5.3 Gbit/s Transmission over 50m 1mm Core Diameter Graded-Index Plastic Optical Fiber," in *Proc. OFC/NFOEC 2010*, paper PDP A3, 2010.

[98] "Ultra-wide band (UWB technology). Enabling high-speed wireless personal area networks", white paper by Intel [Online]. Available: <http://www.intel.com/technology/comms/uwb/download/ultra-wideband.pdf>

[99] H. Yang, D. Visani, C.M. Okonkwo, Y. Shi, G. Tartarini, E. Tangdiongga, A.M.J. Koonen, "Multi-standard transmission of converged wired and wireless services over 100m plastic optical fibre", *Proc. ECOC2010*, paper We.7.B.3, Sept. 19-23, 2010.

[100] Y. Shi, D. Visani, C.M. Okonkwo, H. Yang, H.P.A. van den Boom, G. Tartarini, E. Tangdiongga, A.M.J. Koonen, "First demonstration of HD video distribution over large-core POF employing UWB for in-home networks", *Proc. OFC2011*, paper OWB5, March 2011.

[101] AccepTV Video Quality Analyzer Software. <http://www.acceptv.com/>

[102] P. D. Townsend, G. Talli, E. K. MacHale, and C. Antony Cork, "Long reach PONs", in *Proceedings of International Conference on Optical Internet (COIN2008)*, 2008.

[103] T. Alves, and A. Cartaxo, "Extension of the exhaustive Gaussian approach for BER estimation in experimental direct-detection OFDM setups," *Microwave and Optic. Technology Letters* Vol. 52, pp. 2772-2775, 2010.

LIST OF ACRONYMS

3GPP: 3rd Generation Partnership Project
3PLAY: Triple-play
4G: Fourth generation
ADC: Analog-to-digital converter
AGC: Automatic gain control
AWG: Arbitrary waveform generator
B2B: Back-to-back
BER: Bit-error rate
BW: Bandwidth
BWA: Broadband wireless access
CH: Channel
CO: Central office
CWDM: Coarse wavelength division multiplexing
DCA: Digital communication analyser
DCM: Dual-carrier modulation
DD: Dual-drive
DH: Distribution hubs
DMOS: Differential mean opinion score
DOP: Degree of polarization
DS: Downstream
DSA: Digital signal analyser
DSL: Digital subscriber lines
DSP: Digital signal processing
E-ADC: Electronic analog-to-digital converters
EDFA: Erbium doped fibre amplifier
EGA: Exhaustive Gaussian approach
EIRP: Effective isotropic radiated power
EOM: Electro-optic modulators
EVM: Error vector magnitude
FBG: Fibre Bragg grating
FEC: Forward error correction
FFI: Fixed frequency interleaving
FFL: Femtosecond fibre laser
FFT: Fast Fourier transform
FPGA: Field programmable gate array
FTTB: Fibre-to-the-building
FTTC: Fibre-to-the-curb
FTTH: Fibre-to-the-home
FTTN: Fibre-to-the-node
GI: Guard interval
GI-POF: Graded index plastic optical fibre
HD: High-definition
HDTV: High-definition television
HFC: Hybrid-fibre coaxial
HFR: Hybrid fibre-radio

IF: Intermediate frequency
IFFT: Inverse fast Fourier transform
IL: Inline
IR: Impulse radio
LR-PON: Long-reach passive optical networks
LTE: Long term evolution
MIMO: Multiple-input multiple-output
MLL: Mode-locked laser
MMF: Multi-mode fibre
MOS: Mean opinion score
MZ-EOM: Mach-Zehnder electro-optic modulators
NoE: Network of excellence
NRZ: Non-return to zero
OFDM: Orthogonal frequency division multiplexing
OL: Optical oscillator
OLT: Optical line termination
ONT: Optical network terminator
OOK: On-off keying
OSNR: Optical signal-to-noise ratio
PAN: Personal area network
PAPR: Peak-to-average power ratio
PBC: Polarization beam combiner
PBS: Polarization beam splitter
PC: Polarization controller
Ph-ADC: Photonic analog-to-digital converter
PM: Polarization-multiplexed
PMMA: Polymethyl-metacrylate
POF: Plastic optical fibre
PON: Passive optical network
PRBS: Pseudo-random bit stream
PSD: Power spectrum density
QAM: Quadrature amplitude modulation
QB: Quadrature bias
QPSK: Quadrature-phase shift keying
R-EAT: Reflective electro-absorption transceiver
RF: Radio-frequency
RMS: Root mean square
RN: Remote node
S/P: Serial-to-parallel
SBS: Stimulated Brillouin scattering
SCM: Sub-carrier multiplexing
SFDR: Spurious free dynamic range
Si-APD: Silicon avalanche photodetector
SNR: Signal-to-noise ratio
SOP: States of polarization
SSB: Single-side band
SSMF: Standard single mode fibre

TDoA: Time difference of arrival
TFC: Time frequency codes
TFI: Time-frequency interleaving
UB-MMF: Ultra-bendable multi-mode fibre
UB-SMF: Ultra-bendable single mode fibre
UP: Upstream
UWB: Ultra-wide band
UWE: UWB wireless extractor
VCSEL: Vertical cavity surface emitting laser
VQA: Video quality analyser
WDM: Wavelength-division multiplexing
WiMAX: Worldwide interoperability for microwave access
WLAN: Wireless local area networks
WPAN: Wireless personal area networks
WUSB: Wireless universal serial bus

LIST OF FIGURES

Figure 1. Simple concept of radio-over-fibre application in FTTH networks	2
Figure 2. Different FTTx deployments.....	3
Figure 3. Main elements in a radio-over-fibre link. Only one direction of communication (downlink/uplink) is shown for simplicity	4
Figure 4. Multi-band OFDM channelization defined by ECMA-368 [6].....	7
Figure 5. Example of TFC with: (a) frequency hopping (TFI), or fixed frequency (FFI)	7
Figure 6. 128 Sub-carriers of OFDM-UWB signal representation [6]	8
Figure 7. OFDM encoder block diagram	8
Figure 8. Band Interleaving, zero Prefix and guard intervals of MB-OFDM UWB signal [6] .	8
Figure 9. Spectral mask defined by FCC [5]	13
Figure 10. UWB radio-over-fibre optical link analysis configuration: (a) Mach-Zehnder external modulation. (b) VCSEL direct modulation	15
Figure 11. (a) VCSEL characteristics. (b) IR-UWB monocycle	15
Figure 12. BER vs. launch power vs. SSMF length in IR-UWB at 480Mbit/s bitrate for (a) external modulation, and (b) direct modulation.....	16
Figure 13. BER vs. launch power vs. SSMF length in OFDM-UWB at 480 Mbit/s with (a) external modulation and (b) direct modulation.....	17
Figure 14. (a) Concept of UWB on FTTH for distribution of high definition audio/video. (b) Proposed sub-carrier multiplexing (SCM) channelization. (c) Proposed UWB wireless extractor (UWE) architecture	18
Figure 15. UWB on FTTH demonstrator setup block diagram. The receiver emulates the UWB wireless extractor	19
Figure 16. OFDM-UWB and IR-UWB transmitter block from Figure 15.....	19
Figure 17. (a) OFDM-UWB electrical spectrum at point (1a) of transmitter in Figure 15; (b) IR-UWB RF spectrum (RBW=1 MHz), and (c) Electrical IR-UWB signal and pulse profile at point (1b) of Figure 15	20
Figure 18. (a) Received OFDM-UWB (QPSK carriers) constellation (784 symbols shown) after pilot compensation, at point (4) of Figure 15. Aggregated bit-rate 1.25 Gbit/s. (b) IR-UWB received eye diagram, at point (4) in Figure 15	21
Figure 19. Experimental BER comparison of UWB implementations at 1.25 Gbit/s for the three FTTH SSMF paths. Filled symbols and dashed lines: OFDM-UWB three channels SCM group (QPSK per carrier); Blank symbols and dotted lines: IR-UWB signal results	21
Figure 20. Diagram of the band group allocation in ECMA-368 [6]	22
Figure 21. FTTH architectures: (a) configuration A (fibre path without optical amplification) [60], and (b) configuration B (fibre paths with inline optical amplification) [61].....	23
Figure 22. Experimental set-up for OFDM-UWB transmission over four different FTTH paths: Path #1= 25 km, Path#2= 50 km, Path#3= 75 km and Path#4= 100 km.....	23
Figure 23. Experimental set-up of the 3-channel QPSK-OFDM transmitter. The centre channel is centred at $f_{OL2}= 6.5$ GHz and is surrounded by two adjacent channels centred at frequencies $f_{OL1}=5$ GHz and $f_{OL3}= 8$ GHz.....	24
Figure 24. Experimental set-up of the five-channel BPSK-OFDM transmitter where the centre channel is centred at $f_{OL2}= 6.5$ GHz. Using mixer frequencies $f_{OL1}= 1.25$ GHz and $f_{OL3}= 2.5$ GHz, neighboring channels centred at frequencies 4 GHz, 5.25 GHz, 7.75 GHz and 9 GHz are obtained.....	25
Figure 25. Electrical spectrum for (a) 3-channel QPSK-OFDM and (b) 5-channel BPSK-OFDM configuration (RBW=1 MHz)	25

Figure 26. (a) Received BPSK constellation, (b) received QPSK constellation (both for 6 dBm received optical power after 75 km fibre transmission (Path#3)), and the resulting constellations after equalization for (c) BPSK and (d) QPSK	26
Figure 27. EVM experimental results: three channels QPSK-OFDM in B2B and after 25 km, 50 km, 75 km and 100 km SSMF transmission. Dashed line indicates the EVM threshold and Greyed area indicates the saturation zone	27
Figure 28. EVM experimental results: five channels BPSK-OFDM in B2B and after 25 km, 50 km, 75 km and 100 km SSMF. Dashed line indicates the EVM threshold and greyed area the saturation zone.....	28
Figure 29. Experimental set-up used to evaluate the performance of OFDM-UWB signals with the number of pilots (S/P: serial-to-parallel; (I)FFT: (inverse) fast Fourier transform; GI: guard interval insertion)	29
Figure 30. Channel configuration block implementation for: (a) one OFDM-UWB channel, (b) three OFDM-UWB channels, and (c) five OFDM-UWB channels, with electrical spectrum captures insets.....	30
Figure 31. Representation of the k-th pilot subcarrier equalization performed through the FTTH link transfer function estimation for the i-th OFDM symbol. $X_{\text{OFDM},i}(f_k)$ and $Y_{\text{OFDM},i}(f_k)$ are the k-th received and compensated pilot subcarrier, respectively, and $E_{\text{FTTH},i}(f_k)$ is the estimated distortion compensation transfer function of the k-th pilot subcarrier	30
Figure 32. BER as a function of the fibre length for 1, 3 and 5 channels and different pilot compensation process for 0 dBm received optical power.....	31
Figure 33. BER vs. number of pilots for 5 BPSK: (○)25 km, (□)50 km, (●)75 km, (◇)100 km of fibre. Continuous lines: $P_{\text{opt}}=10$ dBm, dashed 3 dBm.....	32
Figure 34. Experimental BER comparison using 6, 14, and 26 pilots for compensation process, for 1 channel (squares), 3 channels (circles) and 5 channels (triangles), transmitted through SSMF of 25, 50, 75 and 100 km	33
Figure 35. Proposed concept for UWB wireless-integration in FTTH networks. At subscriber premises the UWB signals are extracted and in Case A feed into an enabled receiver, and in Case B radiated to a user device	34
Figure 36. Experimental setup for OFDM-UWB combined performance evaluation of optical and wireless transmission in hybrid access networks.....	35
Figure 37. EVM vs. fibre vs. optical power before photodetection (a) Ch 1,(b)Ch 2.....	36
Figure 38. UWB spectrum measured (a) after 25 km SSMF transmission, photodetection and amplification -point (1) in Figure 36-; and (b) after $d=1.5$ m radio propagation -point (2) in Figure 36- (RBW = 1 MHz)	36
Figure 39. Received constellations for: (a) Ch 1, (b) Ch 2 after 25 km SSMF point (1) in Figure 36; (c) Ch 1,(d) Ch 2 after $d=1.5$ m radio propagation point (2) in Figure 36.....	37
Figure 40. EVM vs. wireless distance vs. fibre length transmission with optical power before photodetection of -34.3 dBm for (a) Ch 1 and (b) Ch 2	37
Figure 41. Measured EVM vs. radio distance from 0 to 3 meters with optical power of -34.3 dBm for different FTTH configurations (a) Ch 1 and (b) Ch 2.....	38
Figure 42. SCM-UWB multi-user configurations using two polarizations	39
Figure 43. Experimental setup for SCM-UWB transmission with polarization multiplexing	39
Figure 44. Cross-polarization residual measurements after 10 km of SSMF with RF-spectrum for both polarizations at: (a) point (5), (b) point (6) of Figure 43	40
Figure 45. PM-UWB EVM performance of each UWB channel in different multi-user configurations (Figure 42) vs. L: (a) 5 km, (b) 10 km, (c) 25 km	41

Figure 46. Constellations of the center channel TFC6 with different multi-user configurations using or not PM for L: (a) 5 km, (b) 25 km	41
Figure 47. EVM performance using PM measured after 25 and 50 km SSMF for: (a-b) user#1 TFC5, (c-d) user#2 TFC6, (e-f) user#3 TFC7	42
Figure 48. EVM performance using PM measured for different fibre lengths using 7 dBm optical launch power for: (a) user#1 TFC5, (b) user#2 TFC6, (c) user#3 TFC7	42
Figure 49. Evaluation setup for joint wireless services distribution by polarization multiplexing in hybrid radio-fibre on PON.....	43
Figure 50. (a) Polarization multiplexing schemes for co-channel and adjacent-channel UWB and WiMAX transmission. (b) Polarization measurement in Poincaré sphere	44
Figure 51. RF received spectrum after 25 km SSMF transmission measured with in-band coexistence in (a) point (5) pol. A, and (b) point (6) of Figure 49 pol. B (RBW = 1 MHz)	46
Figure 52. EVM vs. fibre length vs. optical launch power for (a) UWB Ch 1 and Ch 2 in pol. A, and (b) WiMAX (10 MHz BW) in pol. B.....	46
Figure 53. RF received spectrum after 25 km SSMF transmission measured with out-of-band coexistence at (a) point (5) pol. A, (b) point (6) of Figure 49 pol. B (RBW = 1 MHz)	47
Figure 54. EVM vs. fibre length vs. optical launch power for (a) UWB Ch2 and Ch3 in pol. A, and (b) WiMAX (10 MHz BW) in pol. B.....	47
Figure 55. WiMAX EVM vs. WiMAX BW vs. optical launch power at 25 km for: (a) co-channel, and (b) adjacent channel interferer case	48
Figure 56. In-building distribution to several UWB access nodes.....	51
Figure 57. In-home distribution providing service to UWB PAN pico-cells	52
Figure 58. Simulation schematic for OFDM-UWB radio-over-fibre evaluation over SSMF and MMF.....	53
Figure 59. Simulated UWB electrical spectrum at the input of the system	53
Figure 60. (a) Simulated electrical spectrum and demodulated constellations after 300 m SSMF at $P_{\text{Launch}}=2$ dBm for (b) TFC5, (c) TFC6, (d) TFC7	54
Figure 61. (a) Simulated electrical spectrum and demodulated constellations after 300 m MMF at $P_{\text{Launch}}=2$ dBm for (b) TFC5, (c) TFC6, (d) TFC7	54
Figure 62. Experimental setup for OFDM-UWB radio-over-fibre evaluation	55
Figure 63. Experimental electrical spectrum at the input of the system (RBW= 1 MHz)...	55
Figure 64. (a) Experimental electrical spectrum. Demodulated constellations after 300 m SSMF at $P_{\text{Launch}}=2$ dBm for (b) TFC5, (c) TFC6, (d) TFC7	56
Figure 65. (a) Experimental electrical spectrum. Demodulated constellations after 300 m MMF at $P_{\text{Launch}}=2$ dBm for (b) TFC5, (c) TFC6, (d) TFC7	56
Figure 66. Experimental vs. simulated EVM results for indoor SSMF distribution as a function of the launch power: (a) TFC5, (b) TFC6, (c) TFC7	57
Figure 67. Experimental vs. simulated EVM results for indoor MMF distribution with different launch power for (a) TFC5, (b) TFC6, (c) TFC7	58
Figure 68. Experimental setup for performance evaluation of OFDM- and impulse-radio UWB distribution over fibre for indoor range	59
Figure 69. Experimental setup for OFDM-UWB distribution	60
Figure 70. (a) Measured EVM and (b) calculated BER for OFDM-UWB performance after 300 m SSMF distribution. ECMA EVM threshold in dashed line	61
Figure 71. (a) Measured EVM and (b) calculated BER for OFDM-UWB performance after 300 m MMF distribution. ECMA EVM threshold in dashed line.....	61
Figure 72. Experimental setup for impulse-radio UWB distribution	62

Figure 73. Baseband monocycle generator. BPG: bit pattern generator, MLL: Mode-locked laser, ODL: Optical delay line, TIA: Transimpedance amplifier, EDL: Electrical delay line	63
Figure 74. (a) Baseband monocycle eye diagram and (b) electrical spectrum at Figure 72 point (6).....	63
Figure 75. Impulse-radio UWB performance for SSMF distribution compared with optical back-to-back configuration. BER limits in dashed lines	64
Figure 76. Eye diagrams of the down-converted impulse-radio UWB monocycles after 300 m SSMF distribution at point (5) in Figure 72. (a) P2= 13.7 dBm, P3= 4.7 dBm. (b) P2= 13.7 dBm, P3= -3 dBm	64
Figure 77. Impulse-radio UWB performance for MMF distribution compared with optical back-to-back configuration. BER limits in dashed lines	65
Figure 78. Eye diagrams of the down-converted IR-UWB monocycles at point (5) in Figure 72 after 300 m MMF: (a) P2=12 dBm and P3=3.2 dBm. (b) P2=12 dBm and P3= -4.9 dBm	65
Figure 79. Spectral interference management in pico-cells cluster architectures	66
Figure 80. Radiometry of UWB signals in a home environment	67
Figure 81. Time-stretch process in time and frequency domain in a single-channel Ph-ADC	68
Figure 82. Time-stretch process in time and frequency domain	68
Figure 83. Block diagram of the single channel Ph-ADC evaluated by simulation.....	70
Figure 84. Simulated time signal and electrical spectrum results for the Ph-ADC with RF input carrier at 3.146 GHz and: (a-b) -59 dBm, (c-d) -65 dBm power respectively	71
Figure 85. Experimental single channel photonic ADC setup	71
Figure 86. Measured electrical spectrum of the Ph-ADC system with RF input carrier at 3.146 GHz and: (a) -59 dBm, (b) -65 dBm power (RBW=1 MHz).....	72
Figure 87. Captured time signal by the E ADC for an RF input power of: (a) -39 dBm, (b) -51 dBm, (c) -59 dBm, (d) -65 dBm	72
Figure 88. (a) Processed results and (b) zoom of estimated signal with RF input power of -65 dBm	73
Figure 89. SNR inside the optical pulse period for an RF input power of: (a) -39 dBm, (b) -51 dBm, (c) -59 dBm, (d) -65 dBm	73
Figure 90. Maximum SNR values obtained by simulation and experimentally vs. RF input power	73
Figure 91. Multi-channel time-multiplexed photonic ADC experimental setup with optical pulse time-multiplexing scheme. Inset (a) Time interleaved optical pulses coming from the different branches combined before the E-ADC.....	75
Figure 92. Spectrum of TFC1 UWB transmission at 0.5 m range the sensor (RBW=50 kHz). M stands for the Ph-ADC stretching factor	76
Figure 93. Spectrogram to the received signal from two optical channels to show the delay estimation based on matching measured power and the known hopping sequence: (a) channel 1 and (b) channel 2	77
Figure 94. TDoA examples for: (a) 2D and (b) 3D positioning	77
Figure 95. Example of fingerprinting processing result of a UWB signal using time frequency code 3 ($f_1, f_1, f_2, f_2, f_3, f_3$).....	78
Figure 96. Example of optically sampled signal with the time-multiplexed photonic-ADC architecture and computed spectrogram.....	78
Figure 97. Localization accuracy from the experimental measurements. The red square represents the real position and the green dot the estimated	79

Figure 98. Sensing and UWB distribution concept	80
Figure 99. In-building UWB -over-fibre and sensing scenario.....	80
Figure 100. Optical access network UWB radio-over-fibre and sensing scenario	81
Figure 101. Laboratory setup for Ph-ADC and UWB distribution	81
Figure 102. Pulsed laser optical spectrum employed.....	82
Figure 103. Time stretched signal for (a) $D2 \approx -2500$ ps/nm and (b) $D2 \approx -3600$ ps/nm...	83
Figure 104. EVM and constellations measured for (a) $D2 \approx -2500$ ps/nm without second EDFA2, (b) $D2 \approx -2500$ ps/nm with EDFA2 at $P_{out}=2$ dBm, (c) $D2 \approx -3600$ ps/nm with EDFA2 at $P_{out}=2$ dBm	83
Figure 105. Measured EVM for different $D2$, length L and amplification	84
Figure 106. Proposed dual parallel Y-coupled device structure.....	86
Figure 107. Laboratory setup with a single Y-coupled linearized modulator	87
Figure 108. Measured electrical spectrum with single Y-coupled linearized modulation (RBW=50 kHz).....	87
Figure 109. Laboratory setup with a single Mach-Zehnder modulator	87
Figure 110. Measured electrical spectrum with a Mach-Zehnder modulator (RBW=50 kHz)	88
Figure 111. Laboratory setup for dual-parallel Y-coupled linearized modulation	88
Figure 112. Measured electrical spectrum for dual-parallel Y-coupled linearized electro-optical modulation (RBW=50 kHz)	89
Figure 113. Laboratory setup for dual-parallel MZ-EOM evaluation.....	89
Figure 114. Measured electrical spectrum for dual-parallel MZ-EOM (RBW=50 kHz)	89
Figure 115. Laboratory setup for the evaluation of the effect of optical fibre transmission	90
Figure 116. Measured electrical spectrum of dual-parallel linearized modulation after 25 km single-mode fibre (RBW=50 kHz).....	91
Figure 117. Measured electrical spectrum of dual-parallel linearized modulation after high dispersive fibre of -1500 ps/nm (RBW=50 kHz).....	91
Figure 118. Scheme of the designed dual drive modulator	92
Figure 119. (a) Experimental setup for two-tone distortion evaluation of the dual-drive modulator. (b) Output optical power and SFDR experimental results of the DD-MZ compared with a conventional single MZ.....	93
Figure 120. Experimental setup for UWB-over-fibre transmission using: (a) DD-MZ, (b) single MZ-EOM.....	93
Figure 121. Measured EVM for both single and DD-MZ in back-to-back for different optical power arriving at the PIN photodiode	94
Figure 122. Measured EVM of Dual-Drive MZ compared with Single MZ after different fibre transmission lengths (L). EVM improvement of the DD-MZ labelled for reference.....	94
Figure 123. DCM OFDM-UWB constellations comparison	94
Figure 124. (a) Typical FTTH architecture, (b) proposed integrated FTTH, optical in-building and radio transmission	97
Figure 125. Schematic blocks for FTTH architectures (a) with R-EAT, and (b) with MZ-EOM	99
Figure 126. Simulation schematics for FTTH architectures analysis (a) with R-EAT, and (b) with MZ-EOM.....	100
Figure 127. Combined 3PLAY electrical spectrum obtained (a) experimentally, and (b) by simulation.....	100

Figure 128. Experimental characterization in filled symbols and simulation approximation in dashed lines for 3PLAY transmission in back-to-back received: (a) absorbed with R-EAT, and (b) by a photodiode PIN	101
Figure 129. Simulation results for FTTH architecture using R-EAT for the (a) reflected 1550 nm path and (b) absorbed 1300 nm path	102
Figure 130. Simulation results for CWDM with MZ-EOM working at (a) 1550 nm and (b) 1300 nm	102
Figure 131. Experimental setup of reflective architecture	103
Figure 132. Time domain plot of the triple format signal	104
Figure 133. Constellation diagrams of triple format RF signal	104
Figure 134. EVM performance of R-EAT for 1360 nm path at L=0km	105
Figure 135. EVM vs fibre length 1360 nm path	105
Figure 136. Constellations obtained at (a) 20.2 km and (b) 25.3 km	105
Figure 137. EVM performance of R-EAT for the upstream 1557 nm path in B2B (L=0 km)	106
Figure 138. R-EAT system range capability	107
Figure 139. Constellations obtained at (a) 15 km and (b) 20 km	107
Figure 140. (a) Downstream 1300 nm signal (b) Upstream 1500 nm and crosstalk (lower)	107
Figure 141. (a) Upstream RF spectrum and (b) optical spectrum of laser and at circ. port 3	108
Figure 142. Spectrum measured after L=20.2 km at: (a) circulator port 2 and (b) CW output with the same fibre length (RBW=3 MHz)	108
Figure 143. Experimental setup for 3PLAY distribution in CWDM architecture	109
Figure 144.(a) Generated electrical spectrum (RF _{in}), (b) spectrogram of signals coexistence	109
Figure 145. LTE, WiMAX and UWB EVM performance with launch power at (a) 1550 nm and (b) 1300 nm	110
Figure 146. Constellations and EVM of the received LTE, WiMAX and UWB signals in B2B configuration: (a) P _{Launch} =-2 dBm at 1550 nm, and (b) P _{Launch} =-1 dBm at 1300 nm	110
Figure 147. Measured EVM on LTE, WiMAX and UWB signals on the (a) 1550 nm and (b) 1300 nm path	110
Figure 148. Constellations and EVM of the received LTE, WiMAX and UWB signals at 1550 nm with P _{Launch} =14.5 dBm after: (a) L=101.8 km, (b) L=121 km	111
Figure 149. Constellations and EVM of the received LTE, WiMAX and UWB signals at 1300 nm with P _{Launch} =14.5 dBm after: (a) L=50.6 km, (b) L=63.3 km	111
Figure 150. Electrical spectrum and signal-to-noise ratio received at (a) 1550 nm (L=101.8 and 121 km) and (b) 1300 nm (L=50.6 and 63.3 km)	111
Figure 151. (a) Application scenario of 3PLAY bidirectional radio distribution after FTTH access networks, and (b) wireless coverage investigation	112
Figure 152. Experimental setup for bidirectional LTE, WiMAX and UWB distribution in FTTH networks and radio propagation at user premises	112
Figure 153. Electrical spectrums measured at different points of Figure 152. Downstream 1550 nm path (a) before MZ-EOM, (b) after 20.2 km SSMF before the antenna, and (c) after 3 m radio propagation. Upstream 1300 nm path (d) before the antenna, (e) before the MZ-EOM after 3 m radio propagation and (f) after 20.2 km SSMF	113
Figure 154. Radio channel response measured with the antennas used for the experiment	113

Figure 155. Constellations and EVM values for the downstream path at 1550 nm at: (a) input of the MZ-EOM [Point (1) in Figure 152], (b) after 20.2 km SSMF and before antenna [Point (2) in Figure 152], (c) after 3 m radio propagation [Point (3) in Figure 152]	114
Figure 156. EVM vs. radio distance d for the downstream path at 1550 nm for (a) LTE, (b) WiMAX and UWB working at (c) DCM and (d) QPSK	114
Figure 157. EVM vs. radio distance d for the upstream path at 1300 nm for (a) LTE, (b) WiMAX and UWB working at (c) DCM and (d) QPSK	115
Figure 158. Constellations and EVM values for the upstream path at 1300 nm at (a) input of the antenna [Point (4) in Figure 152], (b) before the MZ-EOM after 3 m radio [Point (5) in Figure 152] and (c) after 3 m radio and 20.2 km SSMF [Point (6) in Figure 152]	115
Figure 159. Radio services range extension using in-home optical networks.....	116
Figure 160. Application scenarios for FTTH access and in-building distribution using (a) bi-directional SMF and (b) unidirectional MMF	116
Figure 161. LTE, WiMAX and UWB 3PLAY (a) RF generated spectrum and (b) constellations	117
Figure 162. Experimental setup for SMF in-building distribution.....	117
Figure 163. Experimental setup for MMF in-building distribution	117
Figure 164. Back-to-back evaluation for receiver: (a) SMF at 1550 nm, (b) SMF at 1300 nm, (c) MMF at 1550 nm, (d) MMF at 1300 nm	118
Figure 165. EVM vs. in-building distribution length for (a) 1550 nm and (b) 1300 nm ...	118
Figure 166. EVM for SMF in-building distribution length at (a) 1550 nm and (b) 1300 nm	118
Figure 167. LTE received constellations for Corning and Fibercore fibres at 1300 nm.....	119
Figure 168. Constellations and EVM values for LTE, WiMAX and UWB for SMF at 1550 nm	119
Figure 169. Constellations and EVM values for LTE, WiMAX and UWB for SMF at 1300 nm	120
Figure 170. Constellations and EVM values for LTE, WiMAX and UWB for MMF	120
Figure 171. Experimental setup for radio-over-fibre transmission of UWB, WiMAX and LTE over 50 m GI-POF	121
Figure 172. Normalized system response in B2B and after 50 m POF	121
Figure 173. Electrical spectra of: (a) combined signals inserted into VCSEL at point (1) of Figure 171; (b) detected signals after APD at point (2) of Figure 171; and (c) up converted UWB and WiMAX at point (3)	122
Figure 174. Constellation diagrams of LTE, WiMAX, and UWB signals: (a) generated and (b) received after 50 m POF transmission	122
Figure 175. Experimental setup for in-home distribution of HD video using UWB in coexistence with LTE and WiMAX services in a POF network and radio path.....	124
Figure 176. Normalized electrical response of the POF system in back-to-back and after 25 m POF. The IF WiMAX, LTE and IF UWB bands are included for reference.....	124
Figure 177. Measured electrical spectrum (RBW=1 MHz) at different point of Figure 175: (a) Combined signals before VCSEL (point (1)), (b) received signals after 25 m GI-POF at APD output (point (2)), (c) radiated LTE signal (point (3)), and (d) radiated WiMAX and UWB signals with UWB spectral mask (point (4))	125
Figure 178. Measured EVM of each signal for different radio links being transmitted alone or in coexistence with the other radio services	126

Figure 179. Measured constellations and EVM for LTE, WiMAX and UWB after 25 m POF and 2 m radio link transmission: (a) alone, (b) in coexistence with the other services...	126
Figure 180. Measured packet loss in UWB video transmission in coexistence with LTE and WiMAX services for different radio links	127
Figure 181. UWB received DMOS video quality in coexistence for different radio links ...	127
Figure 182. Quality analysis of the video at different points of Figure 181: (a) difference between received and transmitted video for 1 m radio (frame 927, point (1)), (b) difference for 3 m radio (frame 750, point (2)), and (c) delay between the received and transmitted video due to packet loss at 4 m radio (point (3)).....	128
Figure 183. Experimental setup for radio-over-fibre end-to-end transmission with POF in-home distribution	129
Figure 184. Electrical spectrum (RBW=1 MHz) measured at: (a) received signals after SMF link at point (2) of Figure 184; (b) signals inserted to VCSEL at point (3) of Figure 184.	129
Figure 185. Electrical spectrum (RBW=1 MHz) measured at transmitting antenna site at point (4) of Figure 184 for: (a) LTE, and (b) WiMAX and UWB	130
Figure 186. Electrical spectrum (RBW=1 MHz) measured at receiving antenna site at point (5) of Figure 184 for: (a) LTE, and (b) WiMAX and UWB	130
Figure 187. Photos of the experimental setup showing: (a) POF and receiver and (b) wireless link with UWB video transmission	130
Figure 188. EVM measured at: (a) point (2) of Figure 183 with different optical power arriving at PIN. (b) point (4) with different VCSEL output power.....	131
Figure 189. Constellation diagrams of the received signals at end user measured at point (5) in Figure 183 for: (a) LTE, (b) WiMAX, (c) UWB	131
Figure 190. Measured EVM performance: (a) at various locations in Figure 183, (b) LTE alone and in coexistence, (c) WiMAX alone and in coexistence, (d) UWB alone and in coexistence. (e) HD 1080i video transmission packet loss measured in coexistence	132
Figure 191. UWB video captured at: (a) point (4) and (b) point (5) in coexistence with LTE and WiMAX	132
Figure 192. Proposed channel sounding scheme	135
Figure 193. Access network architecture with centralized compensation	135
Figure 194. Channel sounding implementation scheme.....	136
Figure 195. Extra RF-pilots insertion in the free spectrum of the multi-format OFDM-based signals	137
Figure 196. Capture of Matlab processing for digitizing the received signal at the DSO .	138
Figure 197. Experimental setup for impairment compensation subsystem performance evaluation	139
Figure 198. Frequency allocation of extra RF-pilots up to 11 pilots.....	139
Figure 199. Electrical spectrum (RBW=1 MHz) measured at the input of the modulator and after the photodiode after a 100 km SSMF network for: (a) configuration A without pilot compensation, (b) configuration B with 3 pilots, (c) configuration C with 5 pilots, (d) configuration D with 7 pilots, (e) configuration E with 9 pilots and (f) configuration F with 11 pilots.....	141
Figure 200. EVM results of GbE-OFDM, LTE, WiMAX and UWB using different number of pilots for the compensation approach.....	141
Figure 201. Amplitude frequency response estimated from DSP methods: (a) interpolation and (b) 1 st order, (c) 2 nd order and (d) 3 rd order regression. Results obtained from: DSP method (line) and measured pilots amplitude (marks)	142

Figure 202. Electrical spectrum (RBW=1 MHz) measured at the input of the modulator and after the photodiode after a 100 km SSMF network for Configuration E with 9 pilots and: (a) interpolation, (b) 1st order, (c) 2nd order and (d) 3rd order regression methods.....	143
Figure 203. EVM results of GbE-OFDM, LTE, WiMAX and UWB using different estimation methods of the channel response	143
Figure 204. Measured EVM and electrical spectrum for UWB channel 2 when: (a) transmitted alone, (b) transmitted with the extra RF-pilots	144
Figure 205. RF-pilots insertion in the free-spectrum of multi-OFDM services	145
Figure 206. Downstream path evaluated in the proof-of-concept	145
Figure 207. Experimental setup for multi-OFDM transmission along LR-PON applying pre-distortion at the OLT	146
Figure 208. Pictures of (a) the experimental setup for downstream compensation proof-of-concept and (b) spools of fibre combination example for 100 km of SSMF network reach	146
Figure 209. Experimental setup for back-to-back evaluation of multi-OFDM transmission along LR-PON applying pre-distortion at the OLT	146
Figure 210. Measured EVM in back-to-back (a) without and (b) with pilot compensation (selected modulation index marked for reference)	147
Figure 211. Electrical measured spectrums (RBW=1 MHz) of the signal at the OLT and ONT after 125 km SSMF: (a-b) without compensation and (c-d) with compensation for 125 km	147
Figure 212. Optical spectrum measured before the photodiode at the ONT after 125 km: (a) without impairment compensation and (b) with applied compensation	148
Figure 213. Experimental EVM vs. total fibre length between OLT and ONT obtained with and without pilot compensation for: (a) GbE-OFDM, (b) LTE, (c) WiMAX, (d) UWB channel 2 and (e) UWB channel 3 with constellations at 100 km of SSMF.....	148
Figure 214. Experimental setup for multi-OFDM transmission along LR-PON applying pre-distortion at the OLT and optical dispersion compensation at the remote node	149
Figure 215. Electrical measured spectrums (RBW=1 MHz) for: (a) Signal at the OLT with compensation from RF-pilots for 125 km including FBG for compensating 100 km SSMF dispersion and (b) corresponding received signal at ONT after 125 km	150
Figure 216. Experimental EVM vs. total fibre length between OLT and ONT using in-line dispersion compensation by FBG, obtained with and without pilot compensation for: (a) GbE, (b) LTE, (c) WiMAX, (d) UWB channel 2 and (e) UWB channel 3	151
Figure 217. Upstream path evaluated in the proof-of-concept	152
Figure 218. Triple-format OFDM signal and RF-pilots in the free-spectrum for upstream evaluation	152
Figure 219. Experimental setup for upstream evaluation in LR-PON with post-compensation at the OLT.....	152
Figure 220. Pictures of (a) the experimental setup for upstream compensation proof-of-concept and (b) DML caption.....	153
Figure 221. Measured EVM in a long-reach PON using DML of 100 km with different modulation indexes (selected modulation index marked for reference)	153
Figure 222. Electrical spectrum (RBW=1 MHz): (a) transmitted at the DML, and received at the OLT after (a) 75 km and (b) 125 km network	154
Figure 223. Experimental EVM vs. total fibre length between ONT and OLT obtained with and without pilot post-compensation for: (a) GbE, (b) LTE, and (c) WiMAX	154
Figure 224. Delay estimation algorithm block diagram	169

Figure 225. Example of weight estimation output for 120 snapshots. The confident of the measured state is evaluated. The redder the state is the more confident in the measure	171
Figure 226. Example of operation of the two steps PDE algorithm: The prediction steps by applying a modulus on the PDF at rank $n-1$, and the update of this PDF thanks to the weight vector and normalization before iterate the process at rank n	171
Figure 227. Root Mean Square Error as a function of number of snapshot for 5000 uniformly distributed random τ values	173
Figure 228. Cumulative density function for 80 snapshots and 5000 uniformly distributed random τ values for different percentages of error	173
Figure 229. Root mean square error of positioning for 5 sensors located in different configuration: (a-b) the middle of the walls, (c-d) the edges of the room	174
Figure 230. Root mean square error of 2D positioning for 5 sensors located at different heights: (a) configuration E, and (b) configuration F	175
Figure 231. Root mean square error of 3D positioning for 5 sensors located using configuration F: (a) on position depth y as a function of width x , and (b) on position height, z , as a function of depth y	175
Figure 232. (a) Structure of a single linearized Y-fed coupler modulator chip and (b) principle of operation	177
Figure 233. (a) Factor of merit depending on the active coupling length of first and second section normalized by the coupling length (by simulation). Red color corresponds to the highest linearity. (b) Zoom of the fabrication-target parameters.....	178
Figure 234. (a) Fabricated gold electroplated RF electrodes, and (b) packaged device...	179
Figure 235. E/O response characterization for: (a) Y-junction UCELLS5 and (b) Y-junction UCELLS21 fabricated devices	179
Figure 236. (a) Scheme of the designed dual drive modulator chip in top view and cross section. (b) NRZ output eye diagrams for measured for 10 Gbps and 20 Gbps	180
Figure 237. (a) Bandwidths (lower traces) and electric back-reflections at the inputs for both RF-lines measured with the packaged DD-MZ modulators; (b) IP3 measurements on DD-MZ RF+ at 5 GHz	180
Figure 238. Experimental set up for frequency chirp control and measurement	181
Figure 239. 20 Gbps output temporally responses with three positions of the optical filter (left) and corresponding frequency excursion (right) for: (a-b) $V+=V_n$, $V-=0$, (c-d) $V+=V_n/2$, $V=-V_n/2$, and (e-f) $V+=0$, $V=-V_n$	182

LIST OF TABLES

Table 1. Maximum EIRP levels stated by FCC for UWB emissions [5].....	6
Table 2. ECMA-368 frequency information of band group #1 channels	7
Table 3. ECMA-368 time frequency codes for band group #1	7
Table 4. UWB radio-over-fibre simulation parameters.....	14
Table 5. UWB radio-over-fibre simulated reach summary.....	17
Table 6. OFDM-UWB parameters and device specifications.....	35
Table 7. Baseline EVM measured without optical transmission	36
Table 8. EVM penalty due to optical transmission.....	38
Table 9. WiMAX signal parameters.....	45
Table 10. Simulation parameters of the Ph-ADC	70
Table 11. Device Specifications of multi-channel Ph-ADC	75
Table 12. Position estimation from the experimental data	79
Table 13. Device specifications of setup for Ph-ADC and UWB-over fibre.....	81
Table 14. Accumulated Dispersion in SSMF Paths.....	82
Table 15. SFDR comparison of linearized modulator	90
Table 16. Simulation parameters according to experimental devices	101
Table 17. Summary of simulation results obtained for 3PLAY distribution in FTTH	103
Table 18. EVM performance of 3PLAY after 50 m POF.....	122
Table 19. RF-pilots frequency (GHz) used for evaluating the performance of the channel response estimation with different number of pilots	140
Table 20. Frequency of the RF-pilots used for channel response estimation.....	145
Table 21. Frequency of the RF-pilots used for upstream channel response estimation ...	152
Table 22. Sensors position (x, y ,z meters) for each configuration	174
Table 23. Positioning absolute error (calculated).....	175
Table 24. Fabricated Y-junction specifications.....	179